The Dissertation Committee for Adam S. Goldsmith Certifies that this is the approved version of the following Dissertation:

The effects of radiation damage and annealing on the diffusion of helium from zircon

Committee:

Daniel F. Stockli, Supervisor

Richard A. Ketcham, Co-Supervisor

Jung-Fu Lin

John I. Garver

Cécile Gautheron

THE EFFECTS OF RADIATION DAMAGE AND ANNEALING ON THE DIFFUSION OF HELIUM FROM ZIRCON

by

Adam S. Goldsmith

Dissertation

Presented to the Faculty of the Graduate School of
The University of Texas at Austin
in Partial Fulfillment
of the Requirements
for the Degree of

Doctor of Philosophy

The University of Texas at Austin
December 2018

Dedication

I dedicate this work to the memory of my grandfather, Ray Goldsmith, and to my parents, Ed and Kathy, and my grandmother Jeanette, for their unwavering support.

Acknowledgements

I would like to thank everyone from the Stockli research group, past and present, for their support, knowledge, conversations, and general company. In particular, I am grateful to Spencer Seman, Mike Prior, Edgardo Pujols-Vazquez, Nikki Seymour, Margo Odlum, Emily Goldstein-Cooperdock, Cody Colleps, Kelly Thomson, Josh Feldman, Renas Koshnaw, Doug Barber, Rudra Chatterjee, Josh Burrus, Charlie Verdel, Ali MacNamee, Megan Flansburg, Eirini Poulaki, Catherine Ross, Dan Arnost, Nicole Hart, and Tim Shin for their friendship. Other members, past and present, of the UT graduate student and postdoc body I would like to thank are: Jake Makis, Tomas Capaldi, Alissa Kotowski, Michelle Gevedon, Travis Clow, Sol Cooperdock, Mariya Levina, Amy Atwater, Evan Ramos, Christine O'Neil, Ed Marshall, Chelsea Mackaman-Lofland, Sarah George, Lily Jackson, Gabriela Gutierrez, Rachel Bernard, Meredith Bush, Peter Gold, Steffi Wafforn, and Sudip Chakraborti. I apologize if I have left anyone out. I sincerely appreciate all the good times we had, and I look forward to seeing you all again at conferences and in general around the world.

I am grateful to my lab managers, Des Patterson, Roman Kislitsyn, and Lisa Stockli for being sources of guidance and knowledge within mass spectrometry, troubleshooting, and more… especially to Des, from whom I have inherited a great working knowledge of very complex machinery (and yet, somehow, am only still scratching the tip of the iceberg). I am grateful to Andy Smye and Luc Lavier on their guidance in learning MATLAB, without which my dissertation would not look nearly as good or be nearly as comprehensive. Those skills enabled me to envision my data on a completely different level than before, and it has helped propel me even further as I I am also grateful to Julie Fosdick and her research group at UConn for their support and feedback, and for being a part of the next phase of my career as a lab manager. Thanks to Sarah Arabi-Katbi for helping with mineral separations.

I am deeply grateful and thankful to my advisors, Danny Stockli and Rich Ketcham, for everything that they have done for me—the sum of which cannot fit on this page, but that ranges from general guidance and personal advice to traveling Europe. Thank you so, so very much. Last but not least, I am grateful to my committee, Cécile Gautheron, John Garver, and Afu Lin, for lending their very specific set of expertises to a very confounding problem that is now, hopefully, significantly less confounding for thermochronologists everywhere.

I take a great deal of pride in what I have accomplished in these pages, but I will never forget everyone whose time, knowledge, and support made it possible.

Abstract

The effects of radiation damage and annealing on the diffusion of helium from zircon

Adam S. Goldsmith, Ph.D.

The University of Texas at Austin, 2018

Supervisor: Daniel Stockli, Co-Supervisor: Richard Ketcham

The relationship between radiogenic ^{4}He in zircon, and its associated radiation damage to the crystal lattice, have been of scientific interest since the earliest attempts at geochronology, and remain an active topic of research today in the pursuit of understanding the timing of low-temperature geological processes. Recently, the complex interrelationships between ^{4}He diffusion kinetics, time, temperature, and radiation damage were quantified into a complete model for the zircon (U-Th)/He (ZHe) thermochronometric system: the Zircon Radiation Damage Accumulation and Annealing Model (ZRDAAM). Many researchers have taken issue with the predictions of this model, however, particularly at moderate to high radiation doses ($\sim 3 \times 10^{17} - 2 \times 10^{19}$ α/g). In this submission, the relationship between radiation damage and ^{4}He diffusion kinetics are examined in greater detail to identify sources of discrepancy between observations and model predictions. Using zircons from three geologically distinct localities, this work represents the largest study on the diffusion kinetics of ^{4}He from zircon to date, including 26 cycled step-heating analyses. A new behavior is observed in diffusion kinetics behavior, termed ‘rollover’: a thermally activated decrease in diffusivities, interpreted as low-temperature annealing.

Comparing the results of modeled and observed ZHe dating and step-heating analyses, we find significant discrepancies with model predictions in agreement with previous research. The source of these discrepancies is identified as low-temperature annealing, a process distinct from epitaxial recrystallization, resulting in significant effects on diffusional behavior, and not accounted for in the ZRDAAM. Results reveal that the damage threshold beyond which model diffusivities increase is too high, likely as a result of extensive prior geological annealing of the high-damage Sri Lankan zircons used to calibrate the ZRDAAM. Furthermore, the use of a single alpha dose appears inappropriate for capturing the full complexity of the ZHe system. Lastly, these results strongly suggest that the diffusion of ^{4}He from zircon proceeds in a manner similar to a homogeneous gas, in spite of the fact that natural ^{4}He concentrations are often strongly heterogeneous. This work is a significant step forward in the improvement of ZHe thermochronology, and will yield to the recovery of more accurate and robust thermal histories.

Table of Contents

Introductory Notes

This dissertation is a collection of three chapters that discuss how radiation damage and annealing affects the crystalline structure of zircon, which in turn affect the kinetics of thermally activated He loss. These results are interpreted in the context of their implications for interpreting zircon (U-Th)/He (or ZHe) thermochronology, with the goal of helping to develop a newer, more robust ZHe model capable of recovery of more accurate, robust thermal histories.

Chapter 1 uses 1D finite difference diffusional modeling to predict the effects of radiation damage annealing on He diffusion rates, as well as exploring the effects of heterogeneous He concentrations within zircons which are thought to be a source of significant but unknown error. These results show that models fail to match basic traits of real experiments, calling into question fundamental aspects of our knowledge of He diffusional mechanics. Chapter 2 explores the diffusion kinetics of He using real zircons from three locations around the world—the Sinai Peninsula of Egypt; the Hall Peninsula of Baffin Island, Nunavut, Canada; and the Grasberg Igneous Complex of New Guinea, Indonesia. Our results define a relationship between diffusion and damage that is markedly different from the current model, and furthermore, a careful interpretation of annealing behaviors offers a coherent explanation for these discrepancies—the critical difference between annealing and recyrstallization. Chapter 3 explores the relationship between ZHe age and radiation damage, showing in different terms how and why the current forward model fails to explain trends observed in ZHe ages, using a comprehensive inverse modeling approach.

Chapter 1: Finite difference modeling of the effects of ^{4}He concentration profiles on whole-grain step-heating diffusivity estimations[1]

ABSTRACT

The retrieval of accurate thermal histories recorded by the (U-Th)/He system relies on empirical estimates of diffusion kinetics from natural minerals, although the difficulty in obtaining samples with homogeneous gas concentrations (required for accurate diffusivities) has limited the collection of such datasets. Whole-grain analyses are relatively time- and cost-effective, but natural ^{4}He concentration heterogeneities caused by α-ejection, diffusional rounding, and/or parent nuclide zonation present an unquantified source of error. We employ a 1D spherical finite difference diffusion model to simulate effects of natural sources of He concentration heterogeneities, with a focus on the zircon (U-Th)/He (ZHe) system. Using He concentration profiles affected by various natural heterogeneities, models consistently predict that diffusion kinetics are strongly underestimated using such methods, especially at low gas release fractions. These underestimations are driven by He depletion near the grain boundary caused by α-ejection, and exacerbated by U and Th depletion. Conversely, models with parent nuclide (and therefore He) enrichment near the grain boundary compensate for ejection-based loss, yielding more accurate diffusion kinetics overall. A comparison of these results to real step-heating data yields few similarities, however, with real zircons being linear or having overestimated diffusivities at low gas releases. Radiation damage and its annealing are also significant factors affecting He diffusional mechanics. Using diffusivities and annealing as predicted by the current ZHe forward model, cycled step-heating temperatures at high doses ($>1 \times 10^{18}$ α/g) predict diffusion decreases

---

[1] Goldsmith, A.S., Ketcham, R. A., Stockli, D.F. (in review) *Finite difference modeling of the effects of ^{4}He concentration profiles on whole-grain step-heating diffusivity estimations.* Geochimica et Cosmochimica Acta. R. Ketcham provided major assistance understanding the math, direction in how best to calculate and plot results, and extensive review. D. Stockli has also contributed to model interpretations and review. The models are my original work; example code is found in Appendix A.

consistently with increased heating temperatures, similar to real data. Annealing above this threshold dose predicts increases in diffusivity which are not observed in real data, however. Results suggest that step-heating data may provide a reasonable proxy for empirically measuring damage annealing kinetics. Major discrepancies between model results and real data reveal the need for more cycled-step heating data to understand the full complexities of He diffusion dynamics.

1.1 INTRODUCTION

For decades, (U-Th)/He low-temperature thermochronology has been used to shed light on the timing of tectonism, erosion, and other geological processes. As researchers work to understand the natural complexities of the (U-Th)/He system, to obtain more accurate thermal histories, and to explore the expansion of 'He dating' to new mineral systems, many employ cycled step-heating experiments as a means of empirically estimating the kinetics of He diffusion. These experiments use the fraction of total He released during heating over a range of temperatures to approximate diffusivities. Such calculations presume a diffusant with an initially homogeneous ('square') concentration profile, however, and natural ^{4}He concentrations in minerals are inherently heterogeneous. Although the effects of heterogeneous He distributions due to ejection, rounding, and parent nuclide zonation have been extensively discussed and quantified with respect to obtaining more accurate ages or thermal histories (Meesters and Dunai, 2002; Hourigan et al., 2005; Gautheron and Tassan-Got, 2010; Ketcham et al., 2011; Ault and Flowers, 2012; Gautheron et al., 2012; Danišík et al., 2017), its effects on approximations of empirical diffusion kinetics remains unquantified. 1×10^{18} α/g

To side-step the effects of He concentration heterogeneities, some researchers analyze interior shards or polished slabs of megacrystic specimens (e.g. Durango apatite, Farley et al., 1996; and Sri Lankan zircons, Guenthner et al., 2013 and references therein). Although this approach effectively minimizes ^{4}He heterogeneity, the availability of natural mineral specimens of such size and quality is restricted to a few localities worldwide. Furthermore, such minerals may be less than ideal for thermochronometric calibration in more insidious ways: the host rocks of the Sri Lankan zircons, for example, have experienced significant damage and partial annealing to their crystalline structures (Nasdala et al., 2004). Results from Chapter 2 suggest that such partial annealing exerts a distinct effect on He diffusion rates which cannot be achieved by damage accumulation alone. For the large majority of localities and ^{4}He-dateable mineral systems, researchers are restricted to trace minerals which are far smaller (<<1 mm) and less ideal.

Today, researchers may opt for the ^{4}He/^{3}He method, in which mineral separates undergo proton-irradiation to induce a miniscule (~10^{-12} cc) but homogeneous concentration of ^{3}He (Shuster and Farley, 2005 and references therein). This approach, in theory, yields accurate diffusion kinetics and offers a more robust thermal history from single grains. While ^{4}He/^{3}He has numerous advantages relative to whole-grain ^{4}He analyses, it is also significantly more costly and time-consuming: researchers must book time with instruments intended for cancer treatment, and may wait a year or more between shipping samples and the start of analyses due irradiation schedules and the health risks imposed by latent radiation. Conversely, zircons may be prepped from mineral separates for ^{4}He only analyses within a single day. ^{4}He/^{3}He analyses also require more elaborate instrumentation than is commonly used for ^{4}He analyses. Many researchers use quadrupole mass spectrometry to measure ^{4}He (QMS), and calibrate unknown volumes to an internal ^{3}He reference standard; however, the amount of ^{3}He produced by proton irradiation is typically well below the blank levels caused by residual standard ^{3}He, and is impossible to distinguish from hydrogen-deuteride without the use of a magnetic sector machine.

These complications have limited the collection of diffusional datasets, which in turn restricts our understanding of the full complexities and/or viability of (U-Th)/He thermochronology for various mineral systems. Using a 1D spherical finite difference diffusion model, this study provides a quantitative assessment of the shortcomings of empirical estimates of diffusion kinetics based on fractional losses from whole grains with heterogeneous ^{4}He concentrations, using zircon as an example. These results complement those of Chapter 2, in which we present the results of 26 cycled step-heating experiments on natural zircon. Additionally, we have explored the effects of in-situ radiation damage annealing, which results from Chapter 2 suggest play a significant and underappreciated role in diffusional mechanics.

1.2 ESTIMATING DIFFUSIVITIES USING RELATIVE LOSSES

The design of a typical step-heating experiment involves a single or multiple mineral grains, heated together in an ultra-high vacuum furnace. The sample is held at constant temperatures for set periods of time, after each of which the volume of gas released is analyzed. After a final phase of degassing, the fraction of total gas released, *f*, is used to approximate the diffusivity for each step, denoted D_f. Assuming a spherical geometry, commonly used to approximate diffusion in many He-bearing minerals (Meesters and Dunai, 2002; Gautheron and Tassan-Got, 2010), D_f is calculated by

$$\left(\frac{D_f}{a^2}\right)_{i+1} = \begin{cases} for\ f < 0.85 & \dfrac{1}{\pi^2 \Delta t_{i,i+1}}\left[-\dfrac{\pi^2}{3}(f_{i+1}-f_i) - 2\pi\left(\sqrt{1-\dfrac{\pi}{3}f_{i+1}} - \sqrt{1-\dfrac{\pi}{3}f_i}\right)\right] \\ for\ f > 0.85 & \dfrac{1}{\pi^2 \Delta t_{i,i+1}} ln\left(\dfrac{1-f_i}{1-f_{i+1}}\right) \end{cases}$$

(Equations 1.1 and 1.2)

where a is the radial width of the diffusion domain, $\Delta t_{i+1,i}$ is the length of heating step $i+1$, and f_{i+1} is the cumulative fractional release at step $i+1$ (Fechtig and Kalbitzer, 1966; McDougall and Harrison, 1999). Equations 1.1 – 1.2 are presented visually in Figure 1.1. Ideally, results forms a

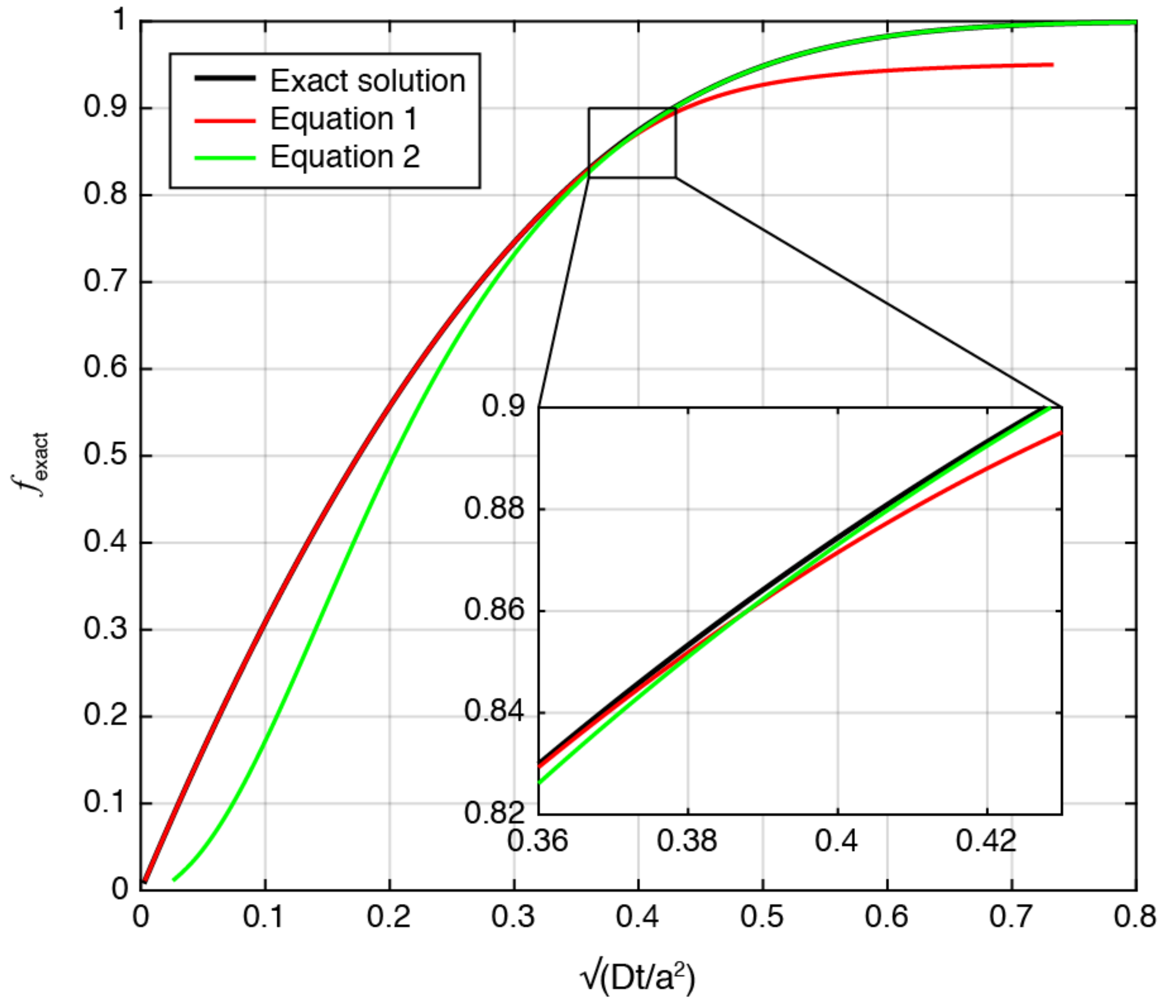

Figure 1.1 A visual representation of Equations 1.1 - 1.2 (red and green lines; McDougall and Harrison, 1999) relative to the exact solution (black line; Carslaw & Jaeger, 1959). Equation 1 provides a perfect fit to the exact solution from f > 0 up to f ≈ 0.83; Equation 2 provides a perfect fit to the exact solution beyond about f = 0.9. Between 0.83 – 0.9, neither equation provides a perfect fit although the degree of difference is small. While McDougall and Harrison (1999) chose to place the crossover threshold at 0.85, we find that a value of 0.86 yields slightly smaller errors.

linear trend on an Arrhenius plot, from which activation energy (E_A) and frequency factor (D_0) may be empirically measured from the slope and intercept, respectively, using

$$\ln\left(\frac{D_f}{a^2}\right) = \ln\left(\frac{D_0}{a^2}\right) - E_A/RT$$

where R is the gas constant, and T is absolute temperature. The variables a, E_A, D_0 collectively describe the kinetics of diffusion, from which researchers extrapolate measurements to geologically relevant time-temperature conditions.

1.3 METHODOLOGY AND RESULTS

1.3.1 Base model description and errors

This study is based on a 1D spherical finite difference diffusion model as described by Ketcham (2005). Unlike thermal history models which simulate heating over 10^8 - 10^9 yr, step-heating experiments typically require <1 month. This allows the model to be simplified by omitting the negligible ^{4}He production rate, and to achieve lower errors using parameters which would otherwise demand excessive computing power. Models use 60 grid nodes per 1 µm of radial width and time-step lengths of 10 seconds. Each model 'grain' is heated on a cycled, stepped prograde/retrograde schedule similar to real experiments (e.g. Chapter 2) until <1% of the original He volume remains. Volumes are calculated from He concentration profiles after each heating step by integration over a cubic piecewise spline.

Experiments are separated into three categories: (1) heterogeneous ^{4}He concentrations and constant diffusion kinetics (Sections 1.3.2 – 1.3.3); (2) homogeneous ^{4}He concentration and variable diffusion kinetics (Section 1.3.4); (3) heterogeneous ^{4}He concentrations *and* variable diffusion kinetics (Section 1.3.5). The 'constant kinetics' experiments (1) are isolate and explore the effects of gas heterogeneities on diffusion kinetics estimates. In annealing experiments (2), we explore the effects of radiation damage annealing during the Tt conditions of step-heating. Finally, we combine the effects of heterogeneous ^{4}He and annealing (3), and compare the results to real diffusion data. Constant kinetics models use E_A = 40.1 kcal/mol and D_0 = 0.46 cm^{2}s^{-1} to approximate moderately crystalline zircon (e.g. Reiners, 2005), and any offsets due to heterogeneity are measured against these known values. Variable kinetics models use the ZRDAAM to calculate *D* (Guenthner et al., 2013).

The model was tested for accuracy against an analogous exact solution, f_{exact} (Carslaw and Jaeger, 1959), under isothermal heating from a square profile (Fig. 1.2A). Modeled *f* is low by approx. 0.016% for the first hours of heating, rapidly approach zero with increasing gas release. These errors are the result of discretization of the extremely steep concentration curve produced near the grain boundary by low losses from a homogeneous concentration profile. For ^{4}He concentration profiles that feature initial depletion near the grain boundary, this is not expected to be a significant source of error. Errors on diffusivities calculated from model *f* under isothermal and cycled step-heating conditions are presented as:

$$ln\left({}^{a_m}/_{a}\right) = \frac{1}{2}\left(\ln\left(\frac{D}{a^2}\right)_{true} - \ln\left(\frac{D_f}{a^2}\right)_{model}\right)$$

(e.g. Lovera and Richter, 1989) (Fig. 1.2B). A positive ln(a_m/a) indicates that the model diffusivity, D_f, is an underestimation of true *D* and vice versa for negative values. The major source of error is a small (ln(a_m/a) ≈ -0.0046) overestimation of diffusivities near the Eq. 1.1 – Eq. 1.2 threshold, which we have placed at $f = 0.86$ to minimize error (Fig. 1.1).

1.3.2 α-ejection and diffusional rounding

As α-particles in zircon travel ~18 μm from their parent nuclide upon ejection, some ^{4}He produced near the grain boundary is ejected from the grain, resulting in low

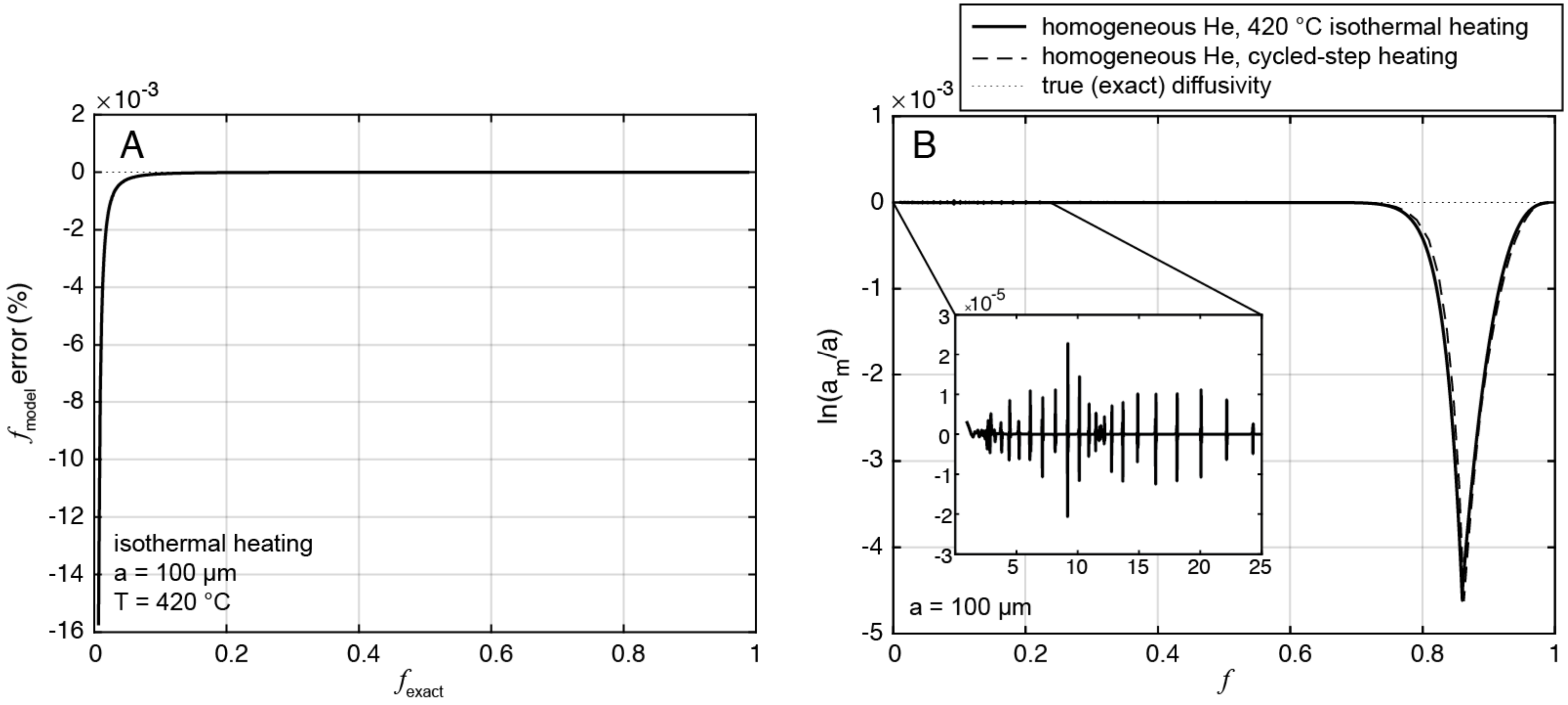

Figure 1.2 Model errors on cumulative fraction of gas lost, *f*, compared to an exact isothermal solution (A), and D_f estimates (B) using fractional losses from A. Models use 60 nodes/μm, and a time-step length of 10 sec. Errors are evaluated at 1 hr intervals. (A) Differences between modeled gas losses (f_{model}) and exact losses (f_{exact}) are presented as $100 \times (1 - f_{\text{model}}/f_{\text{exact}})$. The exact solution is only valid under isothermal heating (Carslaw and Jaeger, 1959). The highest errors, approx. -0.016%, occur at low *f* and rapidly diminish with increasing release. These errors result from discretization of the square profile at low losses, and are not expected to significantly afflict heterogeneous profiles. (B) Deviations of model D_f estimates from true diffusivity (dotted line) as $\ln(a_m/a) = ½\,(\ln(D/a^2)_{\text{true}} - \ln(D_f/a^2)_{\text{model}})$. Negative $\ln(a_m/a)$ values indicate that D_f is an overestimation of true diffusivity. Both isothermal (solid line) and cycled step-heating (dashed line) conditions are closely matched, showing a small ($\ln(a_m/a) \approx 0.0046$) dip in errors near the crossover point between Eqs. 1.1 – 1.2, reflecting that neither equation provides an exact fit in this region (Fig. 1.1). Smaller ($\ln(a_m/a) \approx \pm 2 \times 10^{-5}$) spikes in errors during isothermal heating are also present (B, inset), particularly in the first 25% of gas release.

^{4}He concentrations near the grain boundary (Farley et al., 1996; Hourigan et al., 2005; Ketcham et al., 2011; Danišík et al., 2017). When applied to model concentration profiles (Figs. 1.3 and 1.4, Tables 1.1 and 1.2), this 'missing' He causes D_f and the diffusion kinetics estimated from it to be underestimated. Activation energies are low by 2-3 kcal/mol and D_0 is low by approximately one order of magnitude, causing a fluctuation in resulting T_C estimates with increasing gas release. Closure temperatures are low by more than 10 °C at all grain sizes, with larger grains yielding lower errors overall.

These 'simple' α-ejection profiles, however, apply exclusively to chemically homogeneous zircons from host rocks which experience effectively immediate cooling and no post-crystallization heating (e.g., un-buried volcanic tuffs). Most zircon-bearing rocks experience Tt conditions at which He actively diffuses within (and out of) the grain, rounding the concentration profile and further depleting He near the grain boundary. Forward model-generated He profiles representing severe, moderate, and light rounding are tested for errors with results provided in Figures 1.5 and 1.6, and in Tables 1.3 and 1.4. Severe and moderate rounding show very similar error structures, with light rounding having lower errors overall. Further He depletion near the grain boundary exacerbates the underestimation of diffusivities observed with α-ejection (Fig. 3), with $\ln(a_m/a) > 2$ and closure temperature estimates low by >25 °C at low f. Activation energies are underestimated by up to 12 kcal/mol, with D_0 underestimated by almost 5 orders of magnitude at low f for severe and moderate rounding.

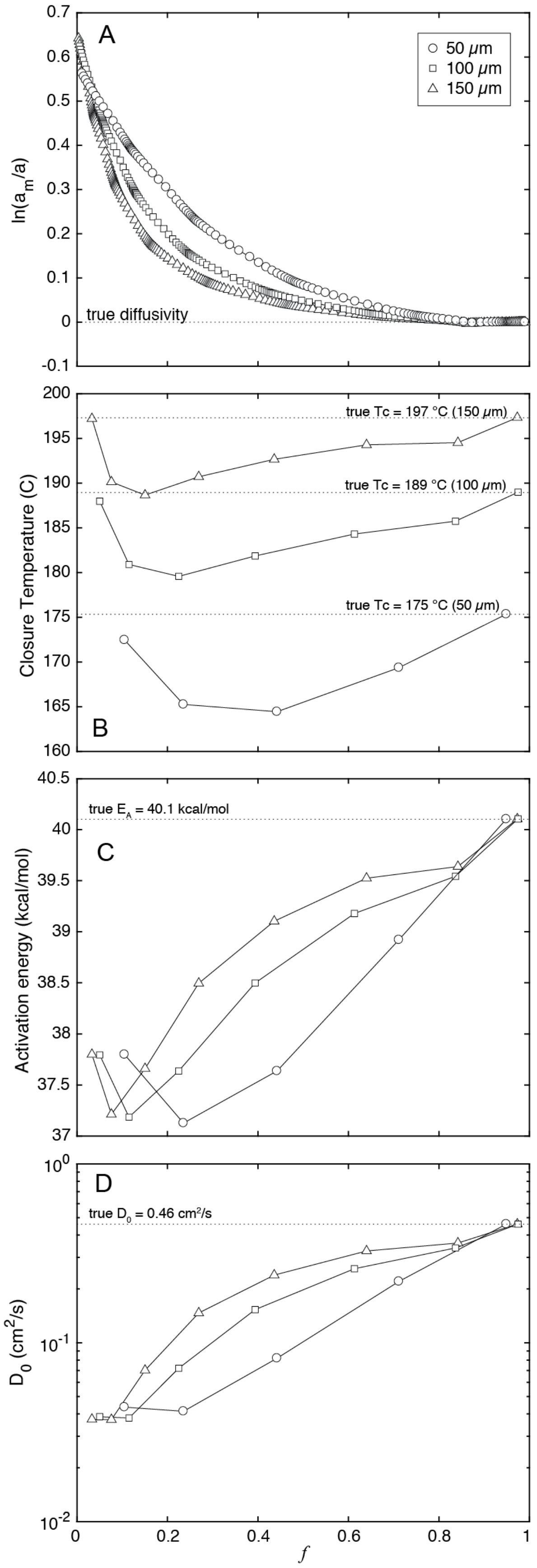

Figure 1.3 The effects of ^{4}He concentration profiles affected by α-ejection (e.g. Farley, 1996) on diffusivities and diffusion kinetics modeled with various grain sizes (50, 100, 150 μm). Diffusion kinetics (B,C,D) are estimated over the course of the experiment by regressing retrograde heating portions of Arrhenius relationships, similar to Chapter 2. Results are plotted against the average *f* over the regressed data. (A) Errors are highest at low *f*, but drop with increasing gas release and diffusional smoothing of the concentration profile. Smaller grains yield lower initial errors, but $\ln(a_m/a)$ approaches zero more slowly. Closure temperatures are for monotonic cooling at 10 °C/m.y. Tc is underestimated by >10 °C in all grains at moderate *f* (0.1 – 0.5), with larger grains approaching true values faster. Initial closure temperature estimates at low *f* are only coincidentally close to true values: both activation energy (C) and D_0 (D) are underestimated. As E_A and D_0 rise closer to true values, closure temperatures drop and rise again.

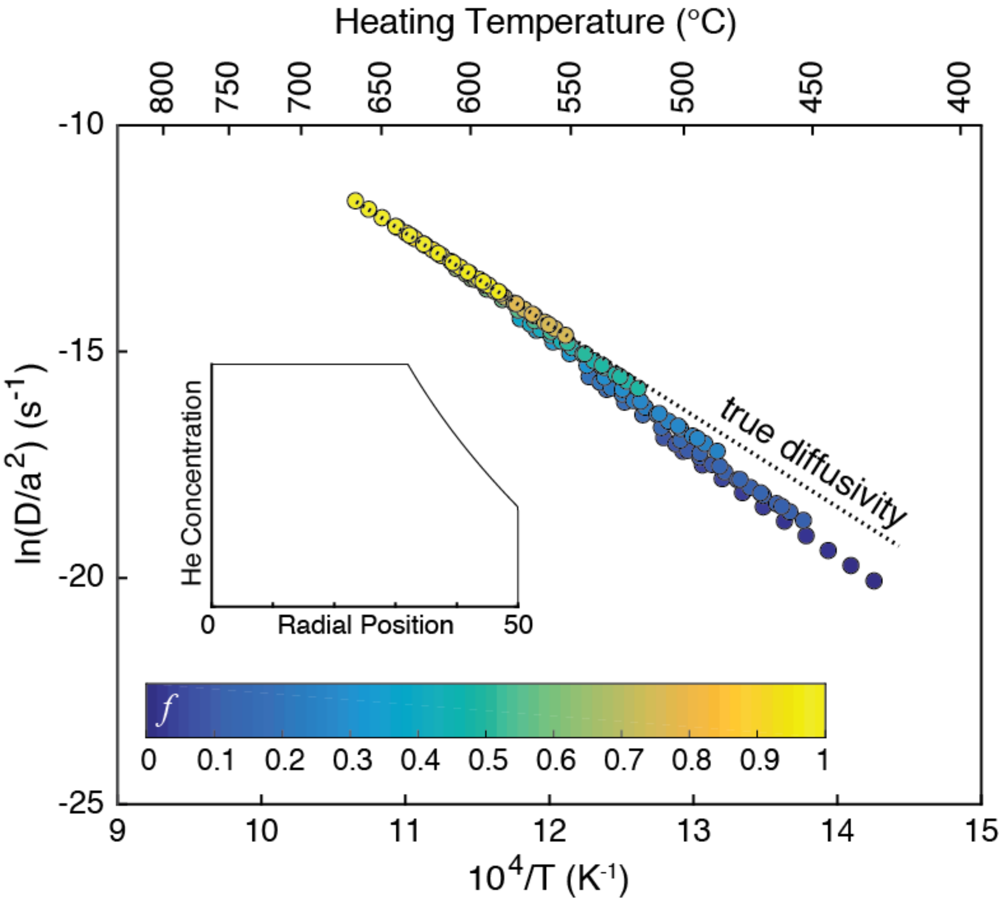

Figure 1.4 The Arrhenius relationship produced by D_f estimates from a 50 µm radius zircon having a ^{4}He and a 20 µm ejection radius (inset) in Arrhenius space (Fig. 1.3, Table 1.2). Data are colored to represent *f*. D_f is underestimated at $f < 0.1$, as the ejection-related depletion near the grain boundary causes less ^{4}He to be released during each step than 'expected' by Eqs. 1.1 – 1.2. With increasing *f*, D_f rises up to near true values (dotted line).

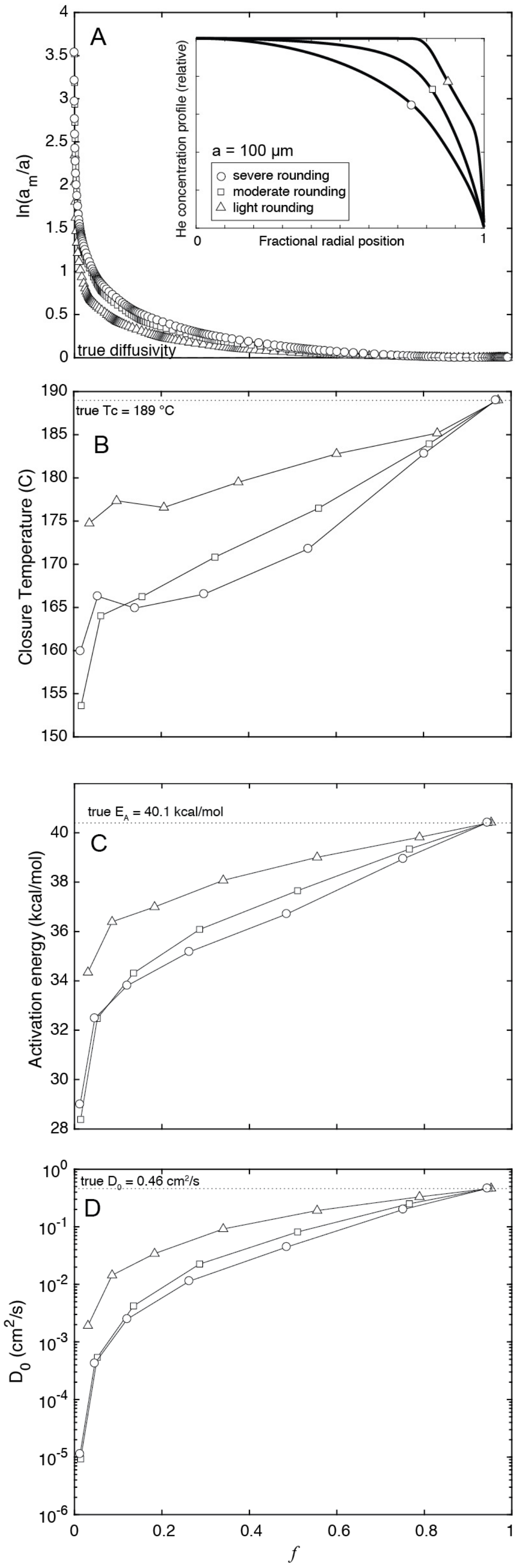

Figure 1.5 The effects on diffusivities and diffusion kinetics estimated from 4He concentration profiles with α-ejection and various degrees of diffusional rounding (A, inset). (A) Light rounding yields lower errors and faster recovery relative to moderate and severe rounding, with the latter two profiles showing closely matched and sometimes overlapping errors. Errors caused by diffusional rounding are significantly higher than from alpha ejection alone (Fig. 1.3), due to a higher degree of 4He depletion near the grain boundary. (B) Nominal closure temperature estimates are significantly low relative to the true value of 189 °C, with moderate and high rounding yielding results as low as 165 °C. (B) Activation energy estimates for moderate to severe rounding are low by as much as 10 kcal/mol, and by 6 kcal/mol with light rounding. (D) D0 estimates are low by and increase over two to almost five orders of magnitude.

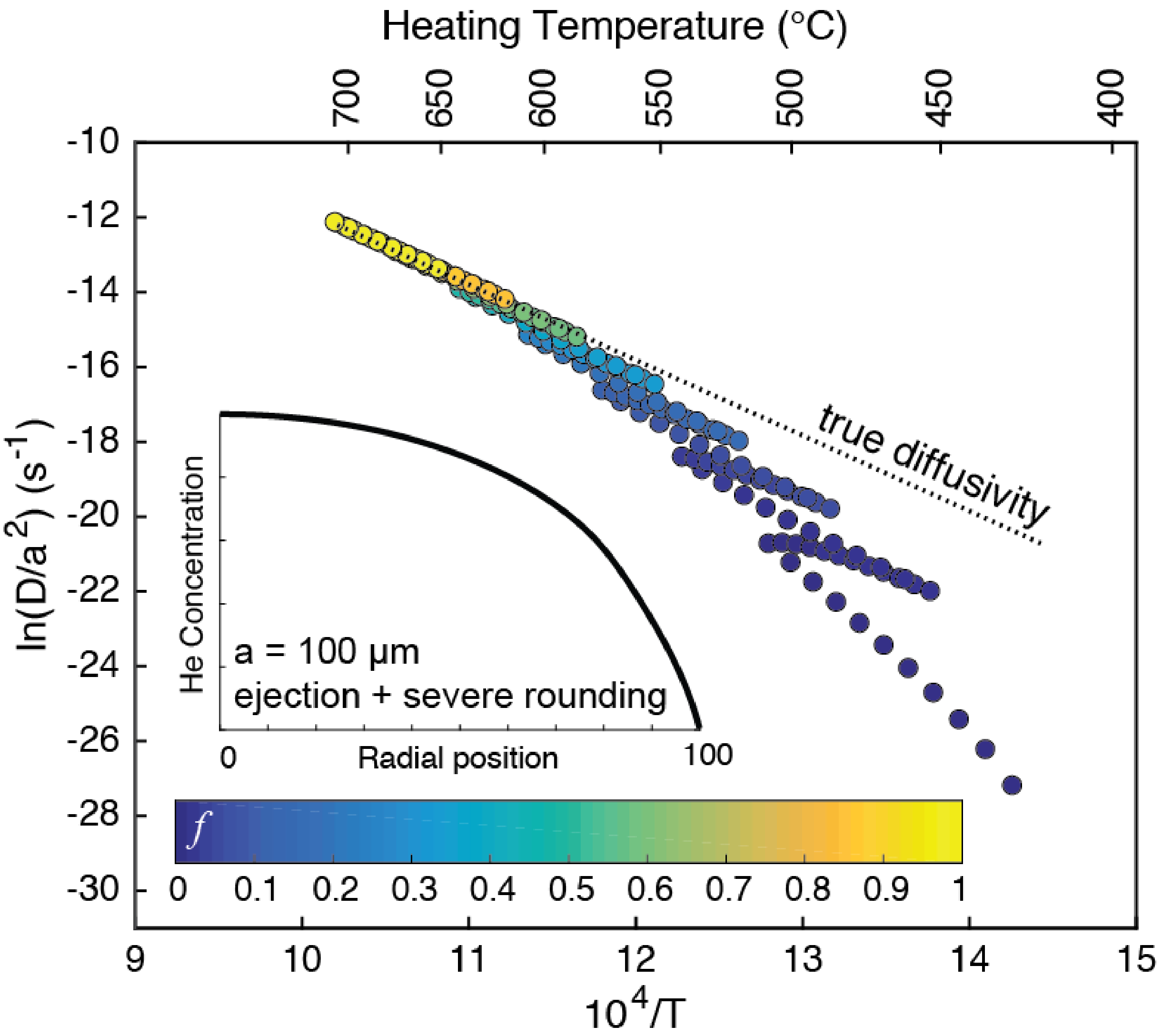

Figure 1.6 The Arrhenius relationship produced by D_f estimates from a severely rounded ^{4}He concentration profile (inset). D_f is significantly underestimated at low gas releases ($f < 0.1$), but rises quickly to true values beyond $f > 0.15$.

Table 1.1 Effects of alpha ejection on estimated diffusivities for various diffusional radii. All heating steps simulated were 1 hr. Diffusivities from the first step are omitted using Equations 1.1-1.2.

		50 µm				100 µm				150 µm			
Total Time (hr)	**Heating Temperature (°C)**	***f***	**Df (cm2/s)**	**ln(Df/a2)**	**ln(am/a)**	***f***	**Df (cm2/s)**	**ln(Df/a2)**	**ln(am/a)**	***f***	**Df (cm2/s)**	**ln(Df/a2)**	**ln(am/a)**
1	420	0.007	--	--	--	0.003	--	--	--	0.002	--	--	--
2	428	0.012	4.73E-14	-20.09	0.56	0.005	4.18E-14	-21.60	0.62	0.004	4.03E-14	-22.44	0.64
3	436	0.016	6.64E-14	-19.75	0.56	0.007	5.87E-14	-21.26	0.62	0.005	5.66E-14	-22.10	0.64
4	444	0.020	9.26E-14	-19.41	0.55	0.009	8.19E-14	-20.92	0.61	0.006	7.90E-14	-21.77	0.63
5	452	0.024	1.28E-13	-19.09	0.54	0.012	1.13E-13	-20.60	0.60	0.008	1.09E-13	-21.44	0.62
6	460	0.030	1.77E-13	-18.77	0.53	0.014	1.56E-13	-20.28	0.59	0.009	1.51E-13	-21.12	0.61
7	468	0.036	2.43E-13	-18.45	0.52	0.017	2.15E-13	-19.96	0.58	0.011	2.07E-13	-20.81	0.60
8	476	0.042	3.32E-13	-18.14	0.51	0.020	2.93E-13	-19.65	0.57	0.013	2.83E-13	-20.49	0.59
9	484	0.050	4.51E-13	-17.83	0.50	0.024	4.00E-13	-19.34	0.56	0.016	3.86E-13	-20.18	0.58
10	492	0.059	6.13E-13	-17.52	0.49	0.028	5.42E-13	-19.03	0.55	0.018	5.23E-13	-19.88	0.56
11	500	0.069	8.29E-13	-17.22	0.47	0.033	7.34E-13	-18.73	0.53	0.022	7.09E-13	-19.58	0.55
12	508	0.081	1.12E-12	-16.92	0.45	0.038	9.92E-13	-18.43	0.52	0.025	9.57E-13	-19.28	0.53
13	503	0.090	9.76E-13	-17.06	0.44	0.043	8.65E-13	-18.57	0.50	0.028	8.35E-13	-19.41	0.52
14	498	0.097	8.44E-13	-17.20	0.43	0.046	7.48E-13	-18.71	0.49	0.030	7.21E-13	-19.56	0.51
15	493	0.102	7.24E-13	-17.36	0.42	0.049	6.42E-13	-18.86	0.48	0.032	6.19E-13	-19.71	0.50
16	488	0.107	6.17E-13	-17.52	0.41	0.051	5.47E-13	-19.02	0.47	0.034	5.28E-13	-19.87	0.49
17	483	0.110	5.24E-13	-17.68	0.41	0.053	4.64E-13	-19.19	0.47	0.035	4.48E-13	-20.03	0.49
18	478	0.113	4.43E-13	-17.85	0.40	0.054	3.92E-13	-19.36	0.46	0.036	3.79E-13	-20.20	0.48
19	473	0.116	3.72E-13	-18.02	0.40	0.055	3.30E-13	-19.53	0.46	0.036	3.19E-13	-20.38	0.48
20	468	0.118	3.12E-13	-18.20	0.40	0.056	2.77E-13	-19.71	0.46	0.037	2.67E-13	-20.55	0.47
21	463	0.119	2.61E-13	-18.38	0.39	0.057	2.31E-13	-19.89	0.45	0.038	2.23E-13	-20.73	0.47
22	458	0.121	2.17E-13	-18.56	0.39	0.058	1.92E-13	-20.07	0.45	0.038	1.86E-13	-20.92	0.47
23	453	0.122	1.80E-13	-18.75	0.39	0.058	1.60E-13	-20.26	0.45	0.038	1.54E-13	-21.10	0.47
24	461	0.123	2.45E-13	-18.44	0.39	0.059	2.17E-13	-19.95	0.45	0.039	2.09E-13	-20.80	0.47
25	469	0.125	3.31E-13	-18.14	0.39	0.060	2.93E-13	-19.65	0.45	0.040	2.83E-13	-20.50	0.46
26	477	0.128	4.44E-13	-17.85	0.38	0.061	3.94E-13	-19.35	0.44	0.040	3.80E-13	-20.20	0.46
27	485	0.131	5.95E-13	-17.55	0.38	0.063	5.27E-13	-19.06	0.44	0.041	5.09E-13	-19.91	0.46
28	493	0.136	7.94E-13	-17.27	0.37	0.065	7.03E-13	-18.77	0.43	0.043	6.79E-13	-19.62	0.45
29	501	0.141	1.06E-12	-16.98	0.37	0.068	9.35E-13	-18.49	0.43	0.045	9.02E-13	-19.33	0.45
30	509	0.148	1.40E-12	-16.70	0.36	0.071	1.24E-12	-18.20	0.42	0.047	1.20E-12	-19.05	0.44
31	517	0.157	1.86E-12	-16.42	0.35	0.076	1.64E-12	-17.92	0.41	0.050	1.59E-12	-18.77	0.43
32	525	0.168	2.46E-12	-16.14	0.34	0.081	2.18E-12	-17.64	0.40	0.053	2.10E-12	-18.49	0.42
33	533	0.181	3.25E-12	-15.86	0.32	0.088	2.88E-12	-17.36	0.38	0.058	2.77E-12	-18.21	0.40

Table 1.1 cont

34	541	0.197	4.30E-12	-15.58	0.31	0.096	3.81E-12	-17.08	0.37	0.063	3.67E-12	-17.93	0.38
35	536	0.210	3.81E-12	-15.70	0.29	0.102	3.37E-12	-17.21	0.35	0.067	3.25E-12	-18.05	0.37
36	531	0.221	3.35E-12	-15.83	0.28	0.107	2.96E-12	-17.34	0.34	0.071	2.85E-12	-18.18	0.36
37	526	0.229	2.92E-12	-15.96	0.27	0.112	2.58E-12	-17.47	0.33	0.074	2.49E-12	-18.32	0.35
38	521	0.237	2.53E-12	-16.11	0.26	0.116	2.24E-12	-17.62	0.32	0.076	2.15E-12	-18.46	0.34
39	516	0.243	2.18E-12	-16.25	0.25	0.119	1.93E-12	-17.76	0.31	0.079	1.86E-12	-18.61	0.33
40	511	0.248	1.88E-12	-16.41	0.25	0.121	1.66E-12	-17.92	0.31	0.080	1.60E-12	-18.76	0.33
41	506	0.252	1.60E-12	-16.56	0.24	0.123	1.42E-12	-18.07	0.30	0.082	1.36E-12	-18.92	0.32
42	501	0.256	1.37E-12	-16.72	0.24	0.125	1.21E-12	-18.23	0.30	0.083	1.16E-12	-19.08	0.32
43	496	0.259	1.16E-12	-16.88	0.23	0.127	1.03E-12	-18.40	0.30	0.084	9.87E-13	-19.24	0.32
44	491	0.261	9.83E-13	-17.05	0.23	0.128	8.68E-13	-18.56	0.29	0.085	8.35E-13	-19.41	0.31
45	486	0.263	8.30E-13	-17.22	0.23	0.129	7.32E-13	-18.73	0.29	0.085	7.05E-13	-19.58	0.31
46	494	0.266	1.10E-12	-16.94	0.23	0.130	9.70E-13	-18.45	0.29	0.086	9.34E-13	-19.30	0.31
47	502	0.269	1.45E-12	-16.66	0.23	0.132	1.28E-12	-18.17	0.29	0.088	1.23E-12	-19.02	0.31
48	510	0.274	1.91E-12	-16.39	0.22	0.134	1.68E-12	-17.90	0.28	0.089	1.62E-12	-18.75	0.30
49	518	0.280	2.50E-12	-16.12	0.22	0.137	2.20E-12	-17.63	0.28	0.091	2.12E-12	-18.48	0.30
50	526	0.287	3.26E-12	-15.85	0.21	0.141	2.87E-12	-17.37	0.27	0.094	2.76E-12	-18.21	0.29
51	534	0.296	4.24E-12	-15.59	0.20	0.146	3.74E-12	-17.10	0.27	0.097	3.60E-12	-17.95	0.29
52	542	0.307	5.51E-12	-15.33	0.20	0.152	4.86E-12	-16.84	0.26	0.101	4.68E-12	-17.69	0.28
53	550	0.321	7.15E-12	-15.07	0.19	0.159	6.30E-12	-16.58	0.25	0.106	6.06E-12	-17.43	0.27
54	558	0.338	9.27E-12	-14.81	0.17	0.168	8.16E-12	-16.32	0.24	0.112	7.85E-12	-17.17	0.26
55	566	0.359	1.20E-11	-14.55	0.16	0.179	1.06E-11	-16.06	0.23	0.119	1.01E-11	-16.91	0.25
56	574	0.383	1.55E-11	-14.29	0.15	0.192	1.36E-11	-15.81	0.21	0.128	1.31E-11	-16.66	0.23
57	569	0.402	1.38E-11	-14.41	0.13	0.203	1.21E-11	-15.92	0.20	0.135	1.17E-11	-16.78	0.22
58	564	0.419	1.22E-11	-14.53	0.12	0.212	1.07E-11	-16.05	0.19	0.141	1.03E-11	-16.90	0.21
59	559	0.432	1.07E-11	-14.66	0.12	0.219	9.43E-12	-16.18	0.18	0.146	9.05E-12	-17.03	0.20
60	554	0.443	9.38E-12	-14.80	0.11	0.225	8.25E-12	-16.31	0.17	0.151	7.92E-12	-17.16	0.19
61	549	0.453	8.17E-12	-14.93	0.11	0.231	7.18E-12	-16.45	0.17	0.154	6.89E-12	-17.30	0.19
62	544	0.461	7.09E-12	-15.08	0.10	0.235	6.23E-12	-16.59	0.17	0.157	5.98E-12	-17.44	0.19
63	539	0.468	6.13E-12	-15.22	0.10	0.239	5.39E-12	-16.74	0.16	0.160	5.17E-12	-17.59	0.18
64	534	0.473	5.28E-12	-15.37	0.09	0.242	4.65E-12	-16.88	0.16	0.162	4.46E-12	-17.74	0.18
65	529	0.478	4.54E-12	-15.52	0.09	0.245	3.99E-12	-17.04	0.16	0.164	3.83E-12	-17.89	0.18
66	524	0.482	3.89E-12	-15.68	0.09	0.247	3.42E-12	-17.19	0.15	0.166	3.29E-12	-18.04	0.18
67	519	0.485	3.33E-12	-15.83	0.09	0.249	2.93E-12	-17.35	0.15	0.167	2.81E-12	-18.20	0.17
68	527	0.490	4.31E-12	-15.57	0.09	0.252	3.79E-12	-17.09	0.15	0.169	3.64E-12	-17.94	0.17
69	535	0.495	5.55E-12	-15.32	0.09	0.255	4.88E-12	-16.83	0.15	0.171	4.69E-12	-17.69	0.17
70	543	0.502	7.13E-12	-15.07	0.08	0.259	6.27E-12	-16.58	0.15	0.174	6.02E-12	-17.44	0.17
71	551	0.511	9.12E-12	-14.82	0.08	0.264	8.02E-12	-16.34	0.14	0.177	7.70E-12	-17.19	0.16
72	559	0.521	1.16E-11	-14.58	0.08	0.270	1.02E-11	-16.10	0.14	0.181	9.82E-12	-16.95	0.16

Table 1.1 cont

73	567	0.534	1.48E-11	-14.34	0.07	0.278	1.30E-11	-15.86	0.14	0.187	1.25E-11	-16.71	0.16
74	575	0.550	1.87E-11	-14.10	0.07	0.287	1.65E-11	-15.62	0.13	0.193	1.58E-11	-16.47	0.15
75	583	0.568	2.37E-11	-13.87	0.06	0.298	2.08E-11	-15.38	0.12	0.201	2.00E-11	-16.24	0.14
76	591	0.590	2.98E-11	-13.64	0.05	0.311	2.63E-11	-15.15	0.12	0.210	2.52E-11	-16.00	0.14
77	599	0.615	3.75E-11	-13.41	0.05	0.327	3.31E-11	-14.92	0.11	0.222	3.17E-11	-15.77	0.13
78	607	0.643	4.69E-11	-13.19	0.04	0.346	4.15E-11	-14.69	0.10	0.235	3.98E-11	-15.55	0.12
79	602	0.666	4.17E-11	-13.30	0.03	0.361	3.70E-11	-14.81	0.09	0.246	3.55E-11	-15.66	0.11
80	597	0.685	3.69E-11	-13.43	0.03	0.374	3.28E-11	-14.93	0.09	0.255	3.14E-11	-15.78	0.11
81	592	0.701	3.25E-11	-13.55	0.02	0.385	2.89E-11	-15.06	0.08	0.263	2.77E-11	-15.91	0.10
82	587	0.713	2.85E-11	-13.68	0.02	0.394	2.54E-11	-15.18	0.08	0.269	2.44E-11	-16.04	0.10
83	582	0.724	2.50E-11	-13.82	0.02	0.402	2.23E-11	-15.32	0.08	0.275	2.14E-11	-16.17	0.10
84	577	0.733	2.18E-11	-13.95	0.02	0.408	1.95E-11	-15.45	0.07	0.280	1.87E-11	-16.30	0.09
85	572	0.741	1.90E-11	-14.09	0.02	0.414	1.70E-11	-15.59	0.07	0.284	1.63E-11	-16.44	0.09
86	567	0.747	1.65E-11	-14.23	0.02	0.419	1.48E-11	-15.72	0.07	0.287	1.42E-11	-16.58	0.09
87	562	0.752	1.44E-11	-14.37	0.01	0.423	1.29E-11	-15.87	0.07	0.290	1.24E-11	-16.72	0.09
88	557	0.757	1.24E-11	-14.51	0.01	0.427	1.12E-11	-16.01	0.07	0.293	1.07E-11	-16.86	0.09
89	552	0.761	1.07E-11	-14.66	0.01	0.430	9.65E-12	-16.15	0.07	0.295	9.26E-12	-17.01	0.09
90	560	0.765	1.36E-11	-14.42	0.01	0.433	1.22E-11	-15.92	0.07	0.298	1.17E-11	-16.77	0.09
91	568	0.771	1.71E-11	-14.19	0.01	0.438	1.54E-11	-15.68	0.06	0.301	1.48E-11	-16.54	0.08
92	576	0.778	2.15E-11	-13.96	0.01	0.444	1.94E-11	-15.45	0.06	0.305	1.86E-11	-16.31	0.08
93	584	0.787	2.69E-11	-13.74	0.01	0.451	2.43E-11	-15.23	0.06	0.311	2.33E-11	-16.08	0.08
94	592	0.797	3.36E-11	-13.52	0.01	0.459	3.04E-11	-15.01	0.06	0.317	2.91E-11	-15.86	0.08
95	600	0.809	4.17E-11	-13.30	0.01	0.470	3.78E-11	-14.79	0.06	0.325	3.63E-11	-15.64	0.08
96	608	0.823	5.16E-11	-13.09	0.01	0.482	4.69E-11	-14.57	0.05	0.334	4.50E-11	-15.42	0.07
97	616	0.838	6.36E-11	-12.88	0.00	0.497	5.80E-11	-14.36	0.05	0.345	5.57E-11	-15.21	0.07
98	624	0.855	7.83E-11	-12.67	0.00	0.513	7.16E-11	-14.15	0.05	0.358	6.87E-11	-15.00	0.07
99	632	0.874	9.60E-11	-12.47	0.00	0.533	8.80E-11	-13.94	0.04	0.372	8.45E-11	-14.79	0.06
100	640	0.893	1.17E-10	-12.28	0.00	0.555	1.08E-10	-13.74	0.04	0.390	1.04E-10	-14.59	0.06
101	635	0.908	1.03E-10	-12.40	0.00	0.574	9.64E-11	-13.85	0.03	0.404	9.26E-11	-14.70	0.05
102	630	0.919	9.11E-11	-12.52	0.00	0.589	8.57E-11	-13.97	0.03	0.416	8.24E-11	-14.82	0.05
103	625	0.928	8.05E-11	-12.65	0.00	0.602	7.61E-11	-14.09	0.03	0.427	7.31E-11	-14.94	0.05
104	620	0.935	7.09E-11	-12.77	0.00	0.613	6.74E-11	-14.21	0.03	0.435	6.48E-11	-15.06	0.05
105	615	0.940	6.25E-11	-12.90	0.00	0.623	5.95E-11	-14.33	0.02	0.443	5.72E-11	-15.18	0.04
106	610	0.945	5.49E-11	-13.03	0.00	0.631	5.25E-11	-14.46	0.02	0.450	5.05E-11	-15.31	0.04
107	605	0.948	4.82E-11	-13.16	0.00	0.638	4.62E-11	-14.59	0.02	0.455	4.44E-11	-15.44	0.04
108	600	0.951	4.23E-11	-13.29	0.00	0.643	4.05E-11	-14.72	0.02	0.460	3.90E-11	-15.57	0.04
109	595	0.954	3.70E-11	-13.42	0.00	0.648	3.55E-11	-14.85	0.02	0.464	3.42E-11	-15.70	0.04
110	590	0.956	3.23E-11	-13.56	0.00	0.653	3.11E-11	-14.98	0.02	0.468	2.99E-11	-15.83	0.04
111	585	0.958	2.82E-11	-13.69	0.00	0.657	2.72E-11	-15.12	0.02	0.471	2.62E-11	-15.97	0.04

Table 1.1 cont

112	593	0.960	3.51E-11	-13.48	0.00	0.661	3.38E-11	-14.90	0.02	0.475	3.26E-11	-15.75	0.04
113	601	0.962	4.34E-11	-13.26	0.00	0.667	4.19E-11	-14.69	0.02	0.480	4.04E-11	-15.53	0.04
114	609	0.965	5.35E-11	-13.05	0.00	0.673	5.17E-11	-14.47	0.02	0.485	4.98E-11	-15.32	0.04
115	617	0.968	6.57E-11	-12.85	0.00	0.682	6.37E-11	-14.27	0.02	0.492	6.14E-11	-15.12	0.03
116	625	0.971	8.04E-11	-12.65	0.00	0.691	7.81E-11	-14.06	0.01	0.500	7.53E-11	-14.91	0.03
117	633	0.975	9.80E-11	-12.45	0.00	0.702	9.54E-11	-13.86	0.01	0.510	9.20E-11	-14.71	0.03
118	641	0.979	1.19E-10	-12.25	0.00	0.715	1.16E-10	-13.66	0.01	0.521	1.12E-10	-14.51	0.03
119	649	0.983	1.44E-10	-12.06	0.00	0.730	1.41E-10	-13.47	0.01	0.534	1.36E-10	-14.32	0.03
120	657	0.987	1.74E-10	-11.87	0.00	0.747	1.71E-10	-13.28	0.01	0.550	1.65E-10	-14.12	0.03
121	665	0.990	2.10E-10	-11.69	0.00	0.765	2.06E-10	-13.09	0.01	0.567	2.00E-10	-13.93	0.02
122	673					0.786	2.48E-10	-12.91	0.01	0.587	2.41E-10	-13.75	0.02
123	668					0.803	2.22E-10	-13.02	0.00	0.603	2.16E-10	-13.86	0.02
124	663					0.816	1.99E-10	-13.13	0.00	0.617	1.93E-10	-13.97	0.02
125	658					0.828	1.78E-10	-13.24	0.00	0.629	1.73E-10	-14.08	0.02
126	653					0.837	1.58E-10	-13.36	0.00	0.639	1.54E-10	-14.20	0.01
127	648					0.845	1.41E-10	-13.47	0.00	0.648	1.37E-10	-14.31	0.01
128	643					0.852	1.25E-10	-13.59	0.00	0.656	1.22E-10	-14.43	0.01
129	638					0.858	1.11E-10	-13.71	0.00	0.662	1.08E-10	-14.55	0.01
130	633					0.863	9.86E-11	-13.83	0.00	0.668	9.57E-11	-14.67	0.01
131	628					0.867	8.71E-11	-13.95	0.00	0.673	8.47E-11	-14.79	0.01
132	623					0.871	7.68E-11	-14.08	0.00	0.677	7.48E-11	-14.92	0.01
133	618					0.874	6.77E-11	-14.21	0.00	0.680	6.60E-11	-15.04	0.01
134	626					0.877	8.28E-11	-14.00	0.00	0.685	8.07E-11	-14.84	0.01
135	634					0.882	1.01E-10	-13.81	0.00	0.690	9.85E-11	-14.64	0.01
136	642					0.887	1.22E-10	-13.61	0.00	0.697	1.20E-10	-14.45	0.01
137	650					0.892	1.48E-10	-13.42	0.00	0.704	1.45E-10	-14.25	0.01
138	658					0.899	1.79E-10	-13.23	0.00	0.713	1.75E-10	-14.07	0.01
139	666					0.906	2.15E-10	-13.05	0.00	0.723	2.11E-10	-13.88	0.01
140	674					0.915	2.57E-10	-12.87	0.00	0.734	2.54E-10	-13.70	0.01
141	682					0.923	3.08E-10	-12.69	0.00	0.747	3.04E-10	-13.52	0.01
142	690					0.933	3.67E-10	-12.52	0.00	0.762	3.62E-10	-13.34	0.01
143	698					0.942	4.35E-10	-12.34	0.00	0.778	4.31E-10	-13.16	0.00
144	706					0.952	5.16E-10	-12.17	0.00	0.796	5.12E-10	-12.99	0.00
145	701					0.959	4.64E-10	-12.28	0.00	0.811	4.62E-10	-13.10	0.00
146	696					0.965	4.17E-10	-12.39	0.00	0.823	4.16E-10	-13.20	0.00
147	691					0.969	3.74E-10	-12.50	0.00	0.833	3.74E-10	-13.31	0.00
148	686					0.973	3.36E-10	-12.60	0.00	0.842	3.36E-10	-13.42	0.00
149	681					0.976	3.01E-10	-12.71	0.00	0.849	3.01E-10	-13.52	0.00
150	676					0.978	2.69E-10	-12.83	0.00	0.856	2.70E-10	-13.63	0.00

Table 1.1 cont

151	671	0.980	2.40E-10	-12.94	0.00	0.861	2.42E-10	-13.74	0.00
152	666	0.981	2.14E-10	-13.05	0.00	0.866	2.16E-10	-13.86	0.00
153	661	0.982	1.91E-10	-13.17	0.00	0.870	1.92E-10	-13.97	0.00
154	656	0.983	1.70E-10	-13.28	0.00	0.873	1.71E-10	-14.09	0.00
155	651	0.984	1.51E-10	-13.40	0.00	0.876	1.52E-10	-14.21	0.00
156	659	0.985	1.82E-10	-13.21	0.00	0.880	1.83E-10	-14.02	0.00
157	667	0.986	2.19E-10	-13.03	0.00	0.884	2.20E-10	-13.84	0.00
158	675	0.988	2.63E-10	-12.85	0.00	0.889	2.64E-10	-13.66	0.00
159	683	0.989	3.14E-10	-12.67	0.00	0.894	3.15E-10	-13.48	0.00
160	691	0.990	3.74E-10	-12.50	0.00	0.900	3.75E-10	-13.30	0.00
161	699					0.907	4.46E-10	-13.13	0.00
162	707					0.914	5.28E-10	-12.96	0.00
163	715					0.922	6.23E-10	-12.80	0.00
164	723					0.931	7.34E-10	-12.63	0.00
165	731					0.940	8.62E-10	-12.47	0.00
166	739					0.949	1.01E-09	-12.31	0.00
167	734					0.955	9.15E-10	-12.41	0.00
168	729					0.961	8.28E-10	-12.51	0.00
169	724					0.965	7.48E-10	-12.61	0.00
170	719					0.969	6.76E-10	-12.72	0.00
171	714					0.972	6.10E-10	-12.82	0.00
172	709					0.974	5.49E-10	-12.92	0.00
173	704					0.976	4.95E-10	-13.03	0.00
174	699					0.978	4.45E-10	-13.13	0.00
175	694					0.979	3.99E-10	-13.24	0.00
176	689					0.980	3.58E-10	-13.35	0.00
177	684					0.981	3.21E-10	-13.46	0.00
178	692					0.982	3.83E-10	-13.28	0.00
179	700					0.983	4.54E-10	-13.11	0.00
180	708					0.985	5.38E-10	-12.94	0.00
181	716					0.986	6.35E-10	-12.78	0.00
182	724					0.988	7.48E-10	-12.61	0.00
183	732					0.989	8.79E-10	-12.45	0.00
184	740					0.991	1.03E-09	-12.29	0.00

Table 1.2 Model estimates of diffusion kinetics from grains with alpha ejection. f values reported are the average release percent over the regression corresponding to the kinetic values reported.

True activation energy: 40.1 kcal/mol
True D0: 0.46 cm2/s

50 µm			**True Tc: 175.3 °C**
f	**Closure temperature (°C)**	**Activation energy (kcal/mol)**	**D0 (cm2/s)**
0.105	172.5	37.8	4.36E-02
0.235	165.3	37.1	4.14E-02
0.442	164.4	37.6	8.19E-02
0.712	169.4	38.9	2.20E-01
0.949	175.3	40.1	4.61E-01

100 µm			**True closure temp: 189.0 °C**
f	**Closure temperature (°C)**	**Activation energy (kcal/mol)**	**D0 (cm2/s)**
0.050	188.0	37.8	3.86E-02
0.115	180.9	37.2	3.79E-02
0.225	179.6	37.6	7.20E-02
0.394	181.9	38.5	1.53E-01
0.613	184.3	39.2	2.59E-01
0.837	185.7	39.5	3.39E-01
0.975	189.0	40.1	4.61E-01

150 µm			**True closure temp: 197.3 °C**
f	**Closure temperature (°C)**	**Activation energy (kcal/mol)**	**D0 (cm2/s)**
0.033	197.2	37.8	3.73E-02
0.076	190.1	37.2	3.72E-02
0.150	188.7	37.7	7.02E-02
0.269	190.7	38.5	1.47E-01
0.436	192.7	39.1	2.39E-01
0.640	194.3	39.5	3.26E-01
0.842	194.5	39.6	3.61E-01
0.973	197.3	40.1	4.61E-01

Table 1.3 Model Tt conditions and Df estimates from grains with alpha ejection and diffusionally rounded profiles.

		Low degree of rounding				**Moderate degree of rounding**				**High degree of rounding**			
Total Time (hr)	**Heating Temperature (°C)**	*f*	**Df (cm2/s)**	**ln(Df/a2)**	**ln(am/a)**	*f*	**Df (cm2/s)**	**ln(Df/a2)**	**ln(am/a)**	*f*	**Df (cm2/s)**	**ln(Df/a2)**	**ln(am/a)**
1	420	3.90E-04	--	--	--	1.18E-04	--	--	--	1.17E-04	--	--	--
2	428	0.001	1.63E-15	-24.84	2.25	2.81E-04	1.58E-16	-27.18	3.41	2.76E-04	1.52E-16	-27.21	3.43
3	436	0.002	4.16E-15	-23.90	1.94	0.001	4.22E-16	-26.19	3.08	4.92E-04	4.01E-16	-26.24	3.11
4	444	0.002	8.91E-15	-23.14	1.72	0.001	9.54E-16	-25.38	2.84	0.001	8.91E-16	-25.44	2.87
5	452	0.004	1.73E-14	-22.47	1.54	0.001	1.97E-15	-24.65	2.63	0.001	1.82E-15	-24.73	2.67
6	460	0.005	3.17E-14	-21.87	1.39	0.002	3.86E-15	-23.98	2.44	0.002	3.50E-15	-24.08	2.49
7	468	0.007	5.53E-14	-21.32	1.26	0.002	7.28E-15	-23.34	2.28	0.002	6.49E-15	-23.46	2.33
8	476	0.009	9.27E-14	-20.80	1.15	0.003	1.33E-14	-22.74	2.12	0.003	1.17E-14	-22.87	2.19
9	484	0.012	1.50E-13	-20.32	1.05	0.005	2.37E-14	-22.16	1.97	0.004	2.04E-14	-22.31	2.05
10	492	0.016	2.36E-13	-19.86	0.96	0.006	4.12E-14	-21.61	1.84	0.006	3.51E-14	-21.77	1.92
11	500	0.020	3.63E-13	-19.43	0.88	0.008	7.04E-14	-21.07	1.70	0.008	5.90E-14	-21.25	1.79
12	508	0.025	5.44E-13	-19.03	0.81	0.011	1.18E-13	-20.56	1.58	0.010	9.76E-14	-20.75	1.67
13	503	0.029	5.12E-13	-19.09	0.76	0.013	1.22E-13	-20.53	1.48	0.012	9.96E-14	-20.73	1.58
14	498	0.032	4.63E-13	-19.19	0.73	0.015	1.18E-13	-20.56	1.41	0.013	9.56E-14	-20.77	1.52
15	493	0.034	4.10E-13	-19.31	0.70	0.016	1.09E-13	-20.63	1.36	0.015	8.84E-14	-20.85	1.47
16	488	0.036	3.57E-13	-19.45	0.69	0.017	9.90E-14	-20.73	1.33	0.016	7.97E-14	-20.95	1.44
17	483	0.038	3.08E-13	-19.60	0.67	0.018	8.79E-14	-20.85	1.30	0.017	7.06E-14	-21.07	1.41
18	478	0.039	2.64E-13	-19.75	0.66	0.019	7.69E-14	-20.99	1.28	0.017	6.16E-14	-21.21	1.39
19	473	0.040	2.24E-13	-19.92	0.65	0.020	6.65E-14	-21.13	1.26	0.018	5.32E-14	-21.35	1.37
20	468	0.041	1.89E-13	-20.09	0.65	0.020	5.70E-14	-21.29	1.25	0.018	4.55E-14	-21.51	1.36
21	463	0.042	1.59E-13	-20.26	0.64	0.021	4.84E-14	-21.45	1.24	0.019	3.87E-14	-21.67	1.35
22	458	0.043	1.33E-13	-20.44	0.64	0.021	4.09E-14	-21.62	1.23	0.019	3.26E-14	-21.84	1.34
23	453	0.043	1.11E-13	-20.62	0.63	0.022	3.43E-14	-21.79	1.22	0.019	2.74E-14	-22.02	1.33
24	461	0.044	1.51E-13	-20.31	0.63	0.022	4.72E-14	-21.47	1.21	0.020	3.76E-14	-21.70	1.32
25	469	0.045	2.05E-13	-20.01	0.63	0.023	6.47E-14	-21.16	1.20	0.020	5.15E-14	-21.39	1.32
26	477	0.046	2.77E-13	-19.70	0.62	0.023	8.88E-14	-20.84	1.19	0.021	7.06E-14	-21.07	1.30
27	485	0.048	3.74E-13	-19.40	0.61	0.024	1.22E-13	-20.52	1.17	0.022	9.68E-14	-20.76	1.29
28	493	0.050	5.04E-13	-19.11	0.60	0.026	1.68E-13	-20.21	1.15	0.023	1.33E-13	-20.44	1.27
29	501	0.052	6.78E-13	-18.81	0.59	0.028	2.32E-13	-19.88	1.12	0.025	1.84E-13	-20.12	1.24
30	509	0.056	9.11E-13	-18.51	0.57	0.030	3.22E-13	-19.55	1.09	0.027	2.55E-13	-19.79	1.21
31	517	0.060	1.23E-12	-18.22	0.56	0.033	4.50E-13	-19.22	1.06	0.029	3.55E-13	-19.46	1.18
32	525	0.065	1.65E-12	-17.92	0.54	0.036	6.33E-13	-18.88	1.01	0.033	4.98E-13	-19.12	1.13
33	533	0.071	2.22E-12	-17.62	0.51	0.041	8.94E-13	-18.53	0.97	0.037	7.02E-13	-18.77	1.09
34	541	0.079	2.99E-12	-17.33	0.49	0.047	1.27E-12	-18.18	0.92	0.042	9.95E-13	-18.43	1.04
35	536	0.085	2.68E-12	-17.43	0.46	0.052	1.20E-12	-18.24	0.87	0.046	9.37E-13	-18.49	0.99
36	531	0.091	2.38E-12	-17.55	0.45	0.056	1.10E-12	-18.33	0.83	0.050	8.61E-13	-18.57	0.96
37	526	0.095	2.09E-12	-17.68	0.43	0.059	9.92E-13	-18.43	0.81	0.053	7.77E-13	-18.67	0.93
38	521	0.098	1.82E-12	-17.82	0.42	0.062	8.83E-13	-18.55	0.78	0.055	6.92E-13	-18.79	0.91
39	516	0.101	1.58E-12	-17.96	0.41	0.064	7.78E-13	-18.67	0.77	0.057	6.10E-13	-18.92	0.89
40	511	0.104	1.36E-12	-18.11	0.41	0.066	6.79E-13	-18.81	0.75	0.059	5.33E-13	-19.05	0.88
41	506	0.106	1.17E-12	-18.26	0.40	0.068	5.89E-13	-18.95	0.74	0.061	4.62E-13	-19.19	0.86

Table 1.3 cont

42	501	0.108	9.99E-13	-18.42	0.39	0.070	5.07E-13	-19.10	0.73	0.062	3.98E-13	-19.34	0.85
43	496	0.109	8.50E-13	-18.58	0.39	0.071	4.35E-13	-19.25	0.73	0.063	3.41E-13	-19.50	0.85
44	491	0.111	7.21E-13	-18.75	0.39	0.072	3.71E-13	-19.41	0.72	0.064	2.91E-13	-19.65	0.84
45	486	0.112	6.09E-13	-18.92	0.38	0.073	3.15E-13	-19.58	0.71	0.065	2.47E-13	-19.82	0.84
46	494	0.113	8.08E-13	-18.63	0.38	0.074	4.20E-13	-19.29	0.71	0.066	3.30E-13	-19.53	0.83
47	502	0.115	1.07E-12	-18.36	0.38	0.075	5.58E-13	-19.00	0.70	0.067	4.39E-13	-19.24	0.82
48	510	0.117	1.41E-12	-18.08	0.37	0.077	7.41E-13	-18.72	0.69	0.069	5.83E-13	-18.96	0.81
49	518	0.120	1.85E-12	-17.81	0.37	0.079	9.83E-13	-18.44	0.68	0.071	7.74E-13	-18.68	0.80
50	526	0.124	2.42E-12	-17.54	0.36	0.083	1.30E-12	-18.16	0.67	0.073	1.03E-12	-18.39	0.79
51	534	0.128	3.16E-12	-17.27	0.35	0.087	1.73E-12	-17.87	0.65	0.077	1.36E-12	-18.11	0.77
52	542	0.134	4.13E-12	-17.00	0.34	0.091	2.30E-12	-17.59	0.63	0.081	1.82E-12	-17.82	0.75
53	550	0.141	5.38E-12	-16.74	0.33	0.098	3.07E-12	-17.30	0.61	0.087	2.43E-12	-17.53	0.73
54	558	0.150	7.02E-12	-16.47	0.31	0.105	4.09E-12	-17.01	0.58	0.094	3.25E-12	-17.24	0.70
55	566	0.161	9.15E-12	-16.21	0.30	0.115	5.48E-12	-16.72	0.55	0.102	4.36E-12	-16.95	0.67
56	574	0.173	1.19E-11	-15.94	0.28	0.126	7.35E-12	-16.43	0.52	0.113	5.87E-12	-16.65	0.63
57	569	0.184	1.07E-11	-16.05	0.26	0.136	6.77E-12	-16.51	0.49	0.121	5.44E-12	-16.73	0.60
58	564	0.193	9.51E-12	-16.17	0.25	0.144	6.15E-12	-16.60	0.47	0.129	4.96E-12	-16.82	0.57
59	559	0.200	8.40E-12	-16.29	0.24	0.151	5.52E-12	-16.71	0.45	0.135	4.46E-12	-16.92	0.55
60	554	0.207	7.37E-12	-16.42	0.23	0.156	4.91E-12	-16.83	0.43	0.140	3.98E-12	-17.04	0.54
61	549	0.212	6.44E-12	-16.56	0.22	0.161	4.33E-12	-16.96	0.42	0.145	3.52E-12	-17.16	0.53
62	544	0.216	5.60E-12	-16.70	0.22	0.165	3.80E-12	-17.09	0.41	0.149	3.10E-12	-17.29	0.51
63	539	0.220	4.86E-12	-16.84	0.21	0.169	3.32E-12	-17.22	0.40	0.152	2.71E-12	-17.42	0.51
64	534	0.223	4.19E-12	-16.99	0.21	0.172	2.88E-12	-17.36	0.40	0.155	2.36E-12	-17.56	0.50
65	529	0.226	3.61E-12	-17.14	0.21	0.175	2.49E-12	-17.51	0.39	0.157	2.04E-12	-17.71	0.49
66	524	0.228	3.10E-12	-17.29	0.20	0.177	2.15E-12	-17.66	0.39	0.159	1.76E-12	-17.86	0.49
67	519	0.230	2.65E-12	-17.45	0.20	0.179	1.84E-12	-17.81	0.38	0.161	1.51E-12	-18.01	0.48
68	527	0.233	3.44E-12	-17.19	0.20	0.181	2.40E-12	-17.55	0.38	0.163	1.97E-12	-17.74	0.48
69	535	0.236	4.44E-12	-16.93	0.20	0.184	3.11E-12	-17.29	0.38	0.166	2.56E-12	-17.48	0.47
70	543	0.240	5.70E-12	-16.68	0.19	0.188	4.02E-12	-17.03	0.37	0.169	3.31E-12	-17.22	0.47
71	551	0.245	7.31E-12	-16.43	0.19	0.192	5.18E-12	-16.77	0.36	0.174	4.28E-12	-16.97	0.46
72	559	0.251	9.35E-12	-16.19	0.19	0.198	6.68E-12	-16.52	0.35	0.179	5.53E-12	-16.71	0.45
73	567	0.259	1.19E-11	-15.94	0.18	0.206	8.60E-12	-16.27	0.34	0.186	7.14E-12	-16.46	0.44
74	575	0.268	1.52E-11	-15.70	0.17	0.215	1.11E-11	-16.02	0.33	0.195	9.22E-12	-16.20	0.42
75	583	0.279	1.92E-11	-15.46	0.16	0.226	1.42E-11	-15.77	0.31	0.205	1.19E-11	-15.94	0.40
76	591	0.293	2.44E-11	-15.23	0.15	0.239	1.83E-11	-15.51	0.30	0.217	1.54E-11	-15.69	0.38
77	599	0.309	3.08E-11	-14.99	0.14	0.255	2.35E-11	-15.26	0.28	0.232	1.99E-11	-15.43	0.36
78	607	0.328	3.89E-11	-14.76	0.13	0.273	3.02E-11	-15.01	0.26	0.250	2.58E-11	-15.17	0.34
79	602	0.343	3.48E-11	-14.87	0.12	0.289	2.75E-11	-15.11	0.24	0.265	2.37E-11	-15.26	0.32
80	597	0.356	3.09E-11	-14.99	0.12	0.302	2.48E-11	-15.21	0.23	0.278	2.15E-11	-15.35	0.30
81	592	0.367	2.74E-11	-15.11	0.11	0.313	2.22E-11	-15.32	0.22	0.289	1.93E-11	-15.46	0.29
82	587	0.377	2.42E-11	-15.24	0.10	0.323	1.97E-11	-15.44	0.21	0.298	1.72E-11	-15.57	0.27
83	582	0.384	2.12E-11	-15.37	0.10	0.331	1.75E-11	-15.56	0.20	0.306	1.53E-11	-15.69	0.26
84	577	0.391	1.86E-11	-15.50	0.10	0.338	1.54E-11	-15.69	0.19	0.313	1.35E-11	-15.82	0.26
85	572	0.397	1.63E-11	-15.63	0.09	0.344	1.35E-11	-15.82	0.19	0.318	1.19E-11	-15.94	0.25
86	567	0.402	1.42E-11	-15.77	0.09	0.349	1.18E-11	-15.95	0.18	0.323	1.04E-11	-16.07	0.24
87	562	0.406	1.23E-11	-15.91	0.09	0.353	1.03E-11	-16.09	0.18	0.328	9.13E-12	-16.21	0.24

Table 1.3 cont

88	557	0.410	1.07E-11	-16.05	0.09	0.357	8.98E-12	-16.23	0.18	0.331	7.96E-12	-16.35	0.24
89	552	0.413	9.24E-12	-16.20	0.09	0.360	7.79E-12	-16.37	0.17	0.334	6.91E-12	-16.49	0.23
90	560	0.417	1.17E-11	-15.96	0.09	0.364	9.90E-12	-16.13	0.17	0.338	8.80E-12	-16.25	0.23
91	568	0.421	1.48E-11	-15.73	0.08	0.369	1.25E-11	-15.89	0.17	0.343	1.12E-11	-16.01	0.23
92	576	0.427	1.86E-11	-15.50	0.08	0.375	1.58E-11	-15.66	0.16	0.349	1.41E-11	-15.77	0.22
93	584	0.434	2.34E-11	-15.27	0.08	0.382	2.00E-11	-15.43	0.16	0.357	1.79E-11	-15.54	0.21
94	592	0.443	2.92E-11	-15.05	0.08	0.392	2.51E-11	-15.20	0.15	0.366	2.25E-11	-15.31	0.21
95	600	0.454	3.65E-11	-14.82	0.07	0.403	3.15E-11	-14.97	0.15	0.377	2.84E-11	-15.08	0.20
96	608	0.466	4.53E-11	-14.61	0.07	0.416	3.94E-11	-14.75	0.14	0.390	3.57E-11	-14.85	0.19
97	616	0.481	5.62E-11	-14.39	0.07	0.431	4.93E-11	-14.52	0.13	0.406	4.49E-11	-14.62	0.18
98	624	0.499	6.95E-11	-14.18	0.06	0.450	6.15E-11	-14.30	0.12	0.424	5.63E-11	-14.39	0.17
99	632	0.519	8.57E-11	-13.97	0.06	0.471	7.67E-11	-14.08	0.11	0.446	7.06E-11	-14.16	0.15
100	640	0.541	1.05E-10	-13.76	0.05	0.495	9.53E-11	-13.86	0.10	0.470	8.85E-11	-13.94	0.14
101	635	0.560	9.43E-11	-13.87	0.04	0.516	8.62E-11	-13.96	0.09	0.491	8.05E-11	-14.03	0.12
102	630	0.576	8.40E-11	-13.99	0.04	0.533	7.74E-11	-14.07	0.08	0.509	7.28E-11	-14.13	0.11
103	625	0.590	7.47E-11	-14.11	0.04	0.547	6.93E-11	-14.18	0.07	0.523	6.54E-11	-14.24	0.10
104	620	0.601	6.62E-11	-14.23	0.03	0.560	6.17E-11	-14.30	0.07	0.536	5.85E-11	-14.35	0.10
105	615	0.611	5.86E-11	-14.35	0.03	0.570	5.48E-11	-14.42	0.07	0.547	5.21E-11	-14.47	0.09
106	610	0.619	5.17E-11	-14.48	0.03	0.579	4.85E-11	-14.54	0.06	0.556	4.62E-11	-14.59	0.09
107	605	0.626	4.55E-11	-14.60	0.03	0.587	4.29E-11	-14.66	0.06	0.564	4.09E-11	-14.71	0.08
108	600	0.632	4.00E-11	-14.73	0.03	0.593	3.78E-11	-14.79	0.06	0.571	3.61E-11	-14.83	0.08
109	595	0.637	3.51E-11	-14.86	0.03	0.599	3.32E-11	-14.92	0.05	0.577	3.18E-11	-14.96	0.08
110	590	0.642	3.07E-11	-15.00	0.03	0.604	2.91E-11	-15.05	0.05	0.582	2.79E-11	-15.09	0.07
111	585	0.646	2.68E-11	-15.13	0.02	0.608	2.55E-11	-15.18	0.05	0.586	2.45E-11	-15.22	0.07
112	593	0.650	3.34E-11	-14.91	0.02	0.613	3.18E-11	-14.96	0.05	0.592	3.05E-11	-15.00	0.07
113	601	0.656	4.14E-11	-14.70	0.02	0.620	3.94E-11	-14.75	0.05	0.598	3.80E-11	-14.78	0.07
114	609	0.663	5.12E-11	-14.49	0.02	0.627	4.88E-11	-14.53	0.05	0.606	4.71E-11	-14.57	0.06
115	617	0.671	6.30E-11	-14.28	0.02	0.636	6.03E-11	-14.32	0.04	0.616	5.82E-11	-14.36	0.06
116	625	0.681	7.73E-11	-14.07	0.02	0.647	7.42E-11	-14.11	0.04	0.627	7.18E-11	-14.15	0.06
117	633	0.693	9.46E-11	-13.87	0.02	0.660	9.11E-11	-13.91	0.04	0.640	8.84E-11	-13.94	0.05
118	641	0.706	1.15E-10	-13.67	0.02	0.674	1.11E-10	-13.71	0.03	0.655	1.08E-10	-13.73	0.05
119	649	0.721	1.40E-10	-13.48	0.01	0.691	1.36E-10	-13.51	0.03	0.673	1.33E-10	-13.53	0.04
120	657	0.739	1.70E-10	-13.29	0.01	0.710	1.66E-10	-13.31	0.03	0.693	1.62E-10	-13.33	0.04
121	665	0.758	2.05E-10	-13.10	0.01	0.731	2.01E-10	-13.12	0.02	0.715	1.98E-10	-13.13	0.03
122	673	0.779	2.47E-10	-12.91	0.01	0.755	2.43E-10	-12.93	0.02	0.740	2.40E-10	-12.94	0.02
123	668	0.796	2.22E-10	-13.02	0.01	0.774	2.19E-10	-13.03	0.01	0.760	2.16E-10	-13.04	0.02
124	663	0.810	1.98E-10	-13.13	0.00	0.789	1.96E-10	-13.14	0.01	0.777	1.94E-10	-13.15	0.02
125	658	0.822	1.77E-10	-13.24	0.00	0.803	1.75E-10	-13.25	0.01	0.791	1.74E-10	-13.26	0.01
126	653	0.832	1.58E-10	-13.36	0.00	0.813	1.56E-10	-13.37	0.01	0.802	1.55E-10	-13.37	0.01
127	648	0.840	1.41E-10	-13.48	0.00	0.823	1.39E-10	-13.48	0.01	0.812	1.39E-10	-13.49	0.01
128	643	0.847	1.25E-10	-13.59	0.00	0.830	1.24E-10	-13.60	0.00	0.820	1.23E-10	-13.61	0.01
129	638	0.853	1.11E-10	-13.71	0.00	0.837	1.10E-10	-13.72	0.00	0.827	1.09E-10	-13.72	0.01
130	633	0.858	9.84E-11	-13.83	0.00	0.843	9.76E-11	-13.84	0.00	0.833	9.71E-11	-13.84	0.00
131	628	0.863	8.71E-11	-13.95	0.00	0.847	8.64E-11	-13.96	0.00	0.838	8.60E-11	-13.97	0.00
132	623	0.866	7.68E-11	-14.08	0.00	0.851	7.64E-11	-14.08	0.00	0.842	7.60E-11	-14.09	0.00
133	618	0.869	6.77E-11	-14.21	0.00	0.855	6.74E-11	-14.21	0.00	0.846	6.71E-11	-14.21	0.00

Table 1.3 cont

134	626	0.873	8.28E-11	-14.00	0.00	0.859	8.26E-11	-14.01	0.00	0.851	8.22E-11	-14.01	0.00
135	634	0.878	1.01E-10	-13.81	0.00	0.864	1.01E-10	-13.81	0.00	0.856	1.00E-10	-13.81	0.00
136	642	0.883	1.22E-10	-13.61	0.00	0.870	1.22E-10	-13.61	0.00	0.862	1.22E-10	-13.61	0.00
137	650	0.889	1.48E-10	-13.42	0.00	0.877	1.48E-10	-13.42	0.00	0.869	1.48E-10	-13.42	0.00
138	658	0.896	1.79E-10	-13.23	0.00	0.884	1.79E-10	-13.24	0.00	0.877	1.79E-10	-13.24	0.00
139	666	0.903	2.15E-10	-13.05	0.00	0.893	2.15E-10	-13.05	0.00	0.886	2.15E-10	-13.05	0.00
140	674	0.912	2.57E-10	-12.87	0.00	0.902	2.57E-10	-12.87	0.00	0.896	2.57E-10	-12.87	0.00
141	682	0.921	3.08E-10	-12.69	0.00	0.912	3.08E-10	-12.69	0.00	0.907	3.08E-10	-12.69	0.00
142	690	0.931	3.67E-10	-12.52	0.00	0.923	3.66E-10	-12.52	0.00	0.918	3.66E-10	-12.52	0.00
143	698	0.941	4.35E-10	-12.34	0.00	0.934	4.35E-10	-12.34	0.00	0.930	4.35E-10	-12.34	0.00
144	706	0.951	5.16E-10	-12.17	0.00	0.945	5.16E-10	-12.17	0.00	0.942	5.16E-10	-12.17	0.00
145	701	0.958	4.64E-10	-12.28	0.00	0.953	4.64E-10	-12.28	0.00	0.951	4.64E-10	-12.28	0.00
146	696	0.964	4.17E-10	-12.39	0.00	0.960	4.17E-10	-12.39	0.00	0.957	4.17E-10	-12.39	0.00
147	691	0.968	3.74E-10	-12.50	0.00	0.965	3.74E-10	-12.50	0.00	0.963	3.74E-10	-12.50	0.00
148	686	0.972	3.36E-10	-12.60	0.00	0.969	3.36E-10	-12.60	0.00	0.967	3.36E-10	-12.60	0.00
149	681	0.975	3.01E-10	-12.71	0.00	0.972	3.01E-10	-12.71	0.00	0.970	3.01E-10	-12.71	0.00
150	676	0.977	2.69E-10	-12.83	0.00	0.974	2.69E-10	-12.83	0.00	0.973	2.69E-10	-12.83	0.00
151	671	0.979	2.40E-10	-12.94	0.00	0.977	2.40E-10	-12.94	0.00	0.975	2.40E-10	-12.94	0.00
152	666	0.980	2.14E-10	-13.05	0.00	0.978	2.14E-10	-13.05	0.00	0.977	2.14E-10	-13.05	0.00
153	661	0.982	1.91E-10	-13.17	0.00	0.980	1.91E-10	-13.17	0.00	0.978	1.91E-10	-13.17	0.00
154	656	0.983	1.70E-10	-13.28	0.00	0.981	1.70E-10	-13.28	0.00	0.980	1.70E-10	-13.28	0.00
155	651	0.984	1.51E-10	-13.40	0.00	0.982	1.51E-10	-13.40	0.00	0.981	1.51E-10	-13.40	0.00
156	659	0.985	1.82E-10	-13.21	0.00	0.983	1.82E-10	-13.21	0.00	0.982	1.82E-10	-13.21	0.00
157	667	0.986	2.19E-10	-13.03	0.00	0.984	2.19E-10	-13.03	0.00	0.983	2.19E-10	-13.03	0.00
158	675	0.987	2.63E-10	-12.85	0.00	0.986	2.63E-10	-12.85	0.00	0.985	2.63E-10	-12.85	0.00
159	683	0.989	3.14E-10	-12.67	0.00	0.987	3.14E-10	-12.67	0.00	0.986	3.14E-10	-12.67	0.00
160	691	0.990	3.74E-10	-12.50	0.00	0.989	3.74E-10	-12.50	0.00	0.988	3.74E-10	-12.50	0.00
161	699	0.991	4.45E-10	-12.32	0.00	0.990	4.45E-10	-12.32	0.00	0.990	4.45E-10	-12.32	0.00
162	707	0.986	4.52E-10	-12.31	0.00	0.984	4.52E-10	-12.31	0.00	0.992	5.27E-10	-12.15	0.00
163	715	0.988	5.34E-10	-12.14	0.00	0.987	5.34E-10	-12.14	0.00	0.986	5.34E-10	-12.14	0.00
164	723	0.991	6.30E-10	-11.97	0.00	0.990	6.30E-10	-11.97	0.00	0.989	6.30E-10	-11.97	0.00
165	731					0.992	7.41E-10	-11.81	0.00	0.992	7.41E-10	-11.81	0.00

Table 1.4 Diffusion kinetics estimated from rounded He concentration profiles.

True closure temperature: 189.0 °C
True activation energy: 40.1 kcal/mol
True D0: 0.46 cm2/s
Radius: 100 µm

Low degree of rounding			
f	**Closure temperature (°C)**	**Activation energy (kcal/mol)**	**D0 (cm2/s)**
0.036	174.7	34.3	2.43E-03
0.098	177.3	36.1	1.56E-02
0.206	176.6	36.9	4.05E-02
0.376	179.5	38.0	1.07E-01
0.601	182.8	38.9	2.15E-01
0.831	185.2	39.4	3.20E-01
0.970	189.0	40.1	4.61E-01

Moderate degree of rounding			
f	**Closure temperature (°C)**	**Activation energy (kcal/mol)**	**D0 (cm2/s)**
0.02	153.6	28.3	1.23E-05
0.06	164.0	32.4	7.10E-04
0.16	166.2	34.3	5.73E-03
0.32	170.8	36.1	2.94E-02
0.56	176.5	37.7	1.01E-01
0.81	183.9	39.2	2.80E-01
0.97	189.0	40.1	4.61E-01

High degree of rounding			
f	**Closure temperature (°C)**	**Activation energy (kcal/mol)**	**D0 (cm2/s)**
0.02	159.9	28.8	1.43E-05
0.05	166.3	32.3	5.30E-04
0.14	164.9	33.8	3.25E-03
0.30	166.5	35.2	1.47E-02
0.54	171.8	36.8	5.85E-02
0.80	182.8	39.0	2.48E-01
0.97	189.0	40.1	4.61E-01

1.3.3 Parent nuclide zonation

Parent nuclide concentrations in zircon are commonly heterogeneous, resulting in an uneven ^{4}He production rate and distribution (Hanchar and Miller, 1993; Hourigan et al., 2005; Danišík et al., 2017). We use two approaches to investigate the effects of U and Th zonation on D_f estimates: a set of simplified zonation profiles, and profiles based on measurements of U and Th zonation from real zircons.

The simplified approach simulates parent nuclide zonation with six synthetic U and Th profiles over which concentrations increase or decrease from 10 to 100 ppm concentrically (Fig. 1.7A). Forward modeling of 100 µm radius grains with these concentration profiles, employing a rapid-cooling thermal history to minimize diffusional rounding, yields a variety of highly heterogeneous He profiles (Fig. 1.7B). Results of cycled step-heating for these grains are provided in Figures 1.8 and 1.9, and in Tables S1.5 and 1.6. Errors are significantly lower in rim-enriched models overall, with high He concentrations compensating for ejection-based depletion. Enriched rims yield activation energies within +2/-3 kcal/mol of true values, and D_0 estimates within one order of magnitude. Closure temperatures in enriched rim experiments are off from the true value (189 °C) by approx. +10/-15 °C. By contrast, rim-depleted profiles consistently underestimate diffusivities and kinetic parameters, with T_C underestimated by up to 65 °C in the most extreme case. Convex (enriched-depleted-enriched) and concave (depleted-enriched-depleted) profiles behave nearly identically to rim-enriched and rim-depleted models respectively, suggesting that interior heterogeneities are far less significant than those near the grain boundary. The sharp zoning, depleted rim model yields the highest deviations from true values, having the most strongly depleted profile near the grain boundary.

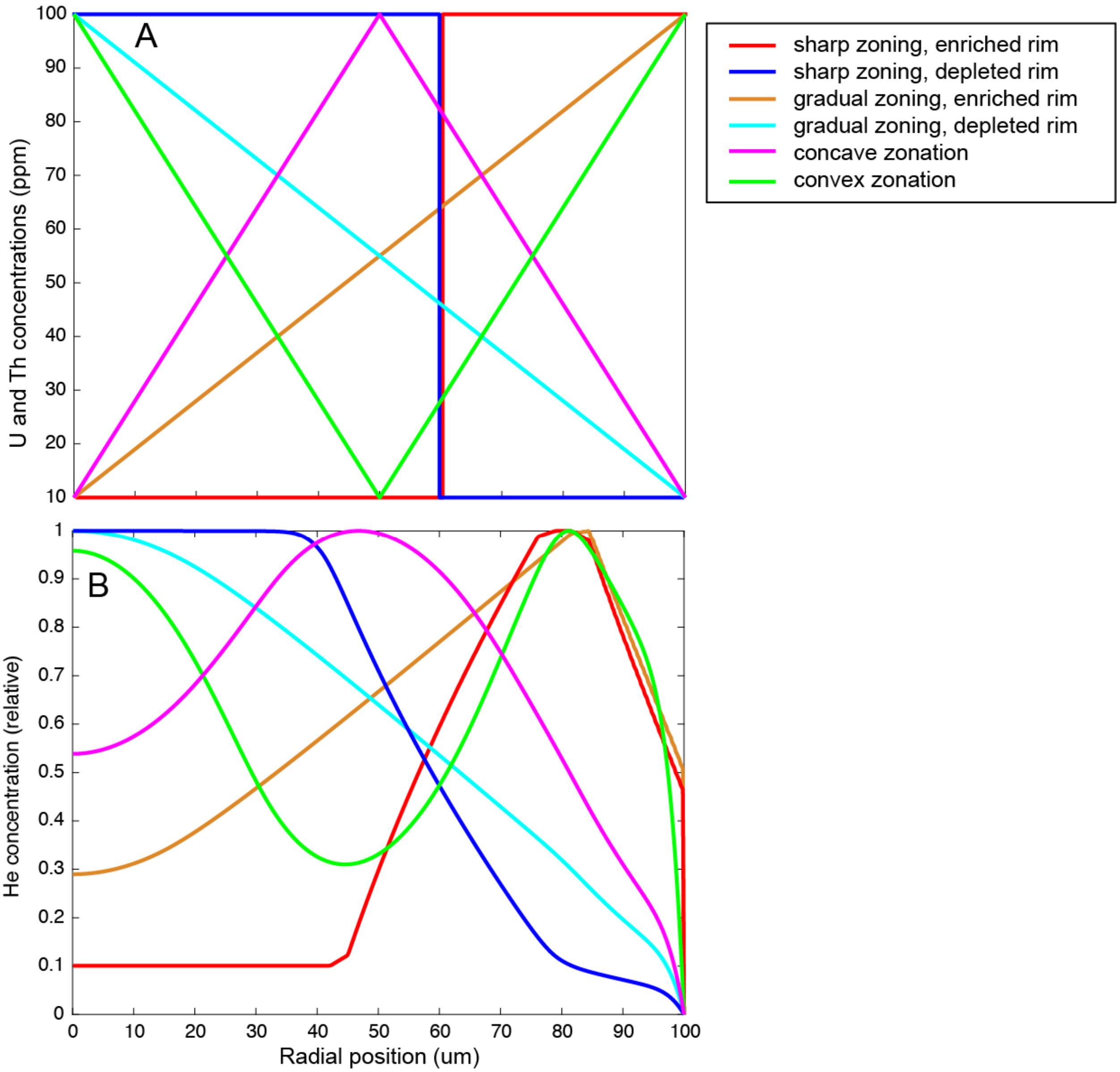

Figure 1.7 (A) Simple parent nuclide zonation schemes. U and Th concentrations increase, decrease, or both, from 10 ppm to 100 ppm. ‘Gradual’ profiles have an even slope across the grain, whereas ‘sharp’ profiles change concentration abruptly at 60 µm. Concave and convex profiles have a peak or valley at 50 µm. Because of the 1D nature of the model, concentration heterogeneities are concentric. (B) He concentration profiles produced from forward modeling of the above parent nuclide zonation schemes under rapid cooling to minimize rounding and maximize heterogeneity. The thermal history used begins at 151 Ma at 300 °C/m.y. and immediately cools at a rate of 300 °C/m.y., followed by isothermal holding at 20 °C for 150 m.y.

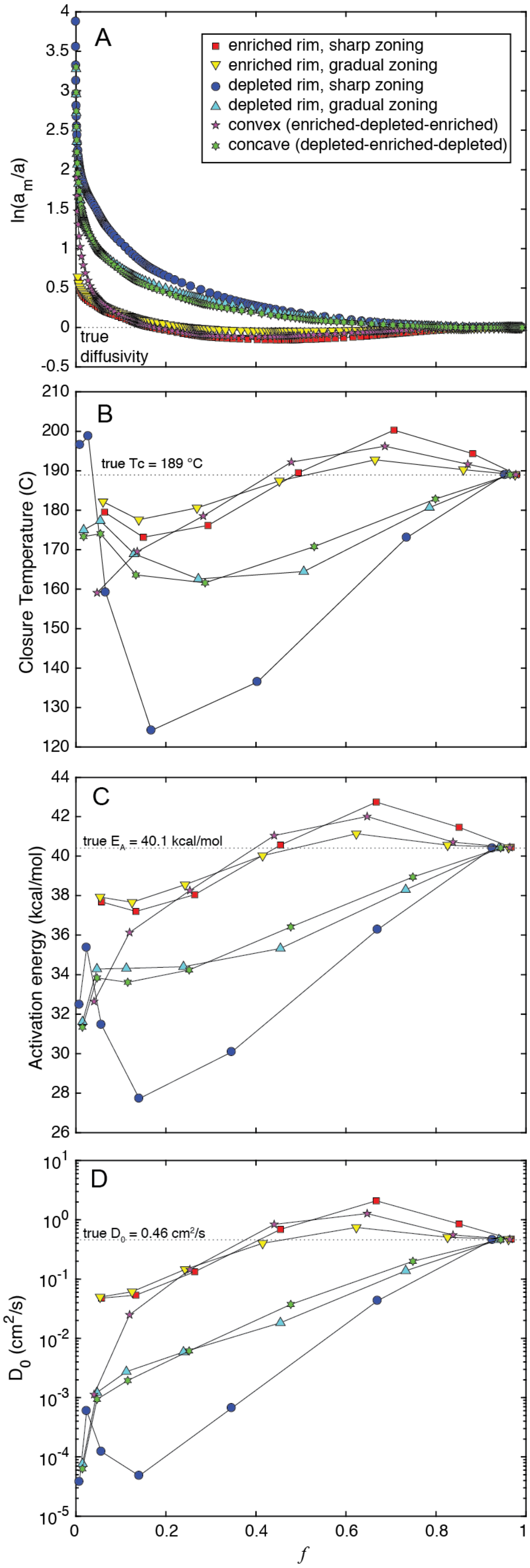
A
B
C
D
enriched rim, sharp zoning
enriched rim, gradual zoning
depleted rim, sharp zoning
depleted rim, gradual zoning
convex (enriched-depleted-enriched)
concave (depleted-enriched-depleted)
$\ln(a_m/a)$
4
3.5
3
2.5
2
1.5
1
0.5
0
-0.5
true
diffusivity
Closure Temperature (C)
210
200
190
180
170
160
150
140
130
120
true Tc = 189 °C
Activation energy (kcal/mol)
44
42
40
38
36
34
32
30
28
26
true E_A = 40.1 kcal/mol
D_0 (cm^2/s)
10^1
10^0
10^{-1}
10^{-2}
10^{-3}
10^{-4}
10^{-5}
true D_0 = 0.46 cm^2/s
0
0.2
0.4
0.6
0.8
1
f

Figure 1.8

Figure 1.8 The effects of various U and Th zonation schemes (Fig. 1.7) on diffusivities and diffusion kinetics. (A) Errors on depleted and concave profiles show a similar pattern to previous experiments, with rounded profiles (Fig. 1.5) showing high errors at low *f* and approaching zero with increasing release. Enriched and convex profiles yield lower initial errors, and also low negative $\ln(a_m/a)$ values at $0.2 < f < 0.8$, indicating slight overestimations of diffusivities. Enriched rim profiles have lower errors overall than depleted rim profiles. The highest errors arise from a parent-depleted rim sharp zonation ('depleted, sharp zoning'), and the lowest errors arising from the enriched, gradual profile. (B) Although He profiles were produced with rapid cooling (dT/dt = 300 °C/m.y.), closure temperatures are presented for dT/dt = 10 °C/m.y for consistency with previous results. (C) Activation energies from U and Th depleted rims are underestimated by up to 12 kcal/mol, but for enriched rims are off by only +2/-3 kcal/mol. (D) D_0 results yield a similar topology to activation energy, with overestimations less than one order of magntidue for enriched rims at high *f*. Depleted rims underestimate D_0 by up nearly five orders of magntiude at low *f*.

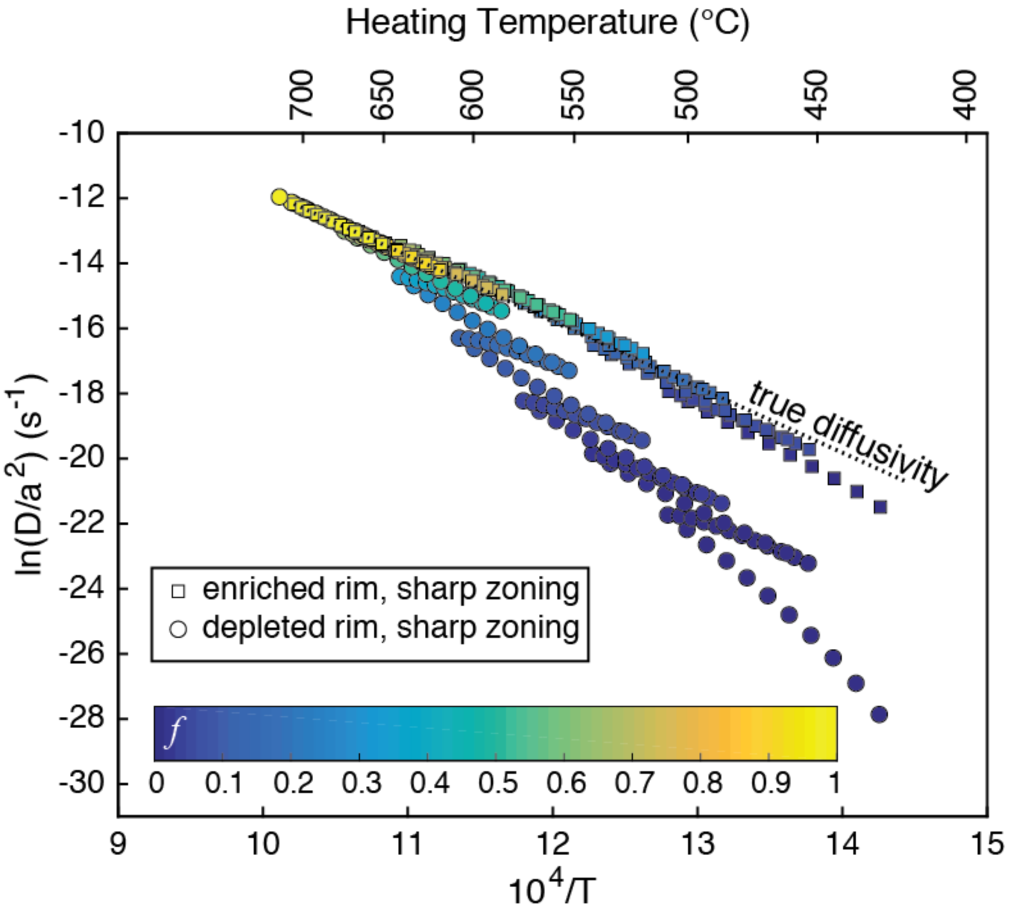

Figure 1.9 The Arrhenius relationships produced by parent nuclide-enriched and -depleted rims (sharp zoning, Fig. 1.8, Table 1.6). Although depleted rims show a significant underestimation of D_f similar to previous results (Figs. 1.3 and 1.5), the enriched rim model yields a slight overestimation of diffusivities at $f > \sim 40$ with lower errors overall.

Table 1.6 Diffusion kinetics estimated from He concentration profiles, arising from simple parent nuclide zonation and rapid cooling (Fig. 1.6B, Table S1.5).

True closure temperature: 189.0 °C
True activation energy: 40.1 kcal/mol
True D0: 0.46 cm2/s
Radius: 100 µm

Sharp zoning, depleted rim

f	**Closure temperature (°C)**	**Activation energy (kcal/mol)**	**D0 (cm2/s)**
0.009	196.6	32.5	5.26E-05
0.028	198.8	34.8	5.57E-04
0.066	159.2	30.2	8.06E-05
0.168	124.2	27.5	6.18E-05
0.403	136.5	30.9	1.43E-03
0.735	173.1	37.3	9.42E-02
0.953	189.0	40.1	4.59E-01

Sharp zoning, enriched rim

f	**Closure temperature (°C)**	**Activation energy (kcal/mol)**	**D0 (cm2/s)**
0.064	179.5	37.2	4.37E-02
0.150	173.2	36.9	5.51E-02
0.293	176.1	38.1	1.71E-01
0.494	189.5	40.8	9.31E-01
0.707	200.3	42.5	2.09E+00
0.882	194.3	41.1	8.07E-01
0.979	189.0	40.1	4.63E-01

Gradual zoning, depleted rim

f	**Closure temperature (°C)**	**Activation energy (kcal/mol)**	**D0 (cm2/s)**
0.015	179.2	31.6	7.68E-05
0.047	182.5	34.3	1.22E-03
0.112	173.8	34.3	2.74E-03
0.239	166.6	34.4	5.87E-03
0.454	166.1	35.3	1.83E-02
0.733	180.6	38.3	1.38E-01
0.940	192.4	40.4	4.61E-01

Table 1.6 cont

Gradual zoning, enriched rim			
f	**Closure temperature (°C)**	**Activation energy (kcal/mol)**	**D0 (cm2/s)**
0.054	186.9	37.9	4.97E-02
0.125	181.5	37.7	6.11E-02
0.243	183.0	38.6	1.46E-01
0.415	189.5	40.0	4.01E-01
0.623	195.6	41.1	7.43E-01
0.826	193.1	40.6	5.08E-01
0.961	192.5	40.4	4.68E-01

Convex			
f	**Closure temperature (°C)**	**Activation energy (kcal/mol)**	**D0 (cm2/s)**
0.040	162.1	32.6	1.13E-03
0.119	172.7	36.1	2.49E-02
0.253	179.7	38.3	1.45E-01
0.441	193.4	41.0	8.36E-01
0.647	199.9	42.0	1.27E+00
0.838	193.9	40.7	5.55E-01
0.964	192.5	40.4	4.68E-01

Concave			
f	**Closure temperature (°C)**	**Activation energy (kcal/mol)**	**D0 (cm2/s)**
0.01	177.8	31.3	6.29E-05
0.05	179.6	33.8	9.36E-04
0.12	168.6	33.6	1.94E-03
0.25	164.2	34.2	6.13E-03
0.48	171.8	36.4	3.73E-02
0.75	184.3	38.9	1.99E-01
0.94	192.4	40.4	4.63E-01

1.3.4 Radiation damage annealing

Although the relationship between high radiation doses and He loss in zircon has long been recognized (e.g. Strutt, 1908; Hurley, 1952), only recently was the relationship quantified by Guenthner and others (2013). Their Zircon Radiation Damage Accumulation and Annealing Model (ZRDAAM; Fig 1.10) predicts that diffusivity is high at low doses, decreasing with damage-induced blockage of c-axis fast-diffusion pathways; at doses above ~1 × 10^{18} α/g, diffusivity rapidly increases with the increasing interconnection of FT damage zones (Ketcham et al., 2013). While the effects of radiation damage have received the bulk of attention, these models are concerned with understanding the predicted effects of annealing at the temperature-time conditions of cycled step-heating. Results from Chapter 2 suggest that low-temperature annealing plays a critical and underappreciated role in shaping He diffusion kinetics.

In these models, diffusivities are calculated as a function of dose (Fig. 1.10), which changes over the course of the experiment due to annealing. As a zircon is damaged or annealed, it is moved either forward or backwards along the curve defined in Figure 1.10. We use a square He profile to isolate annealing effects from heterogeneities, and anneal all damage as a single population from an unannealed starting point for simplicity. Figure 1.11 and Table 1.7 show two distinct forms of annealing behavior: at starting doses < 1 × 10^{18} α/g, and at temperatures above ~600 °C, annealing predicts gentle increases in diffusivity; above 1 × 10^{18} α/g, and at temperatures as low as 420 °C, annealing causes significant decreases to diffusivity. Kinetics calculated from these results are given in Figure 1.12 and Table 1.8: below 1 × 10^{18} α/g, all kinetics parameters (Ea, D_0, T_C) are decreased as a result of annealing effects. Above this threshold, increasing E_A yields an increase in T_C while D_0 remains constant.

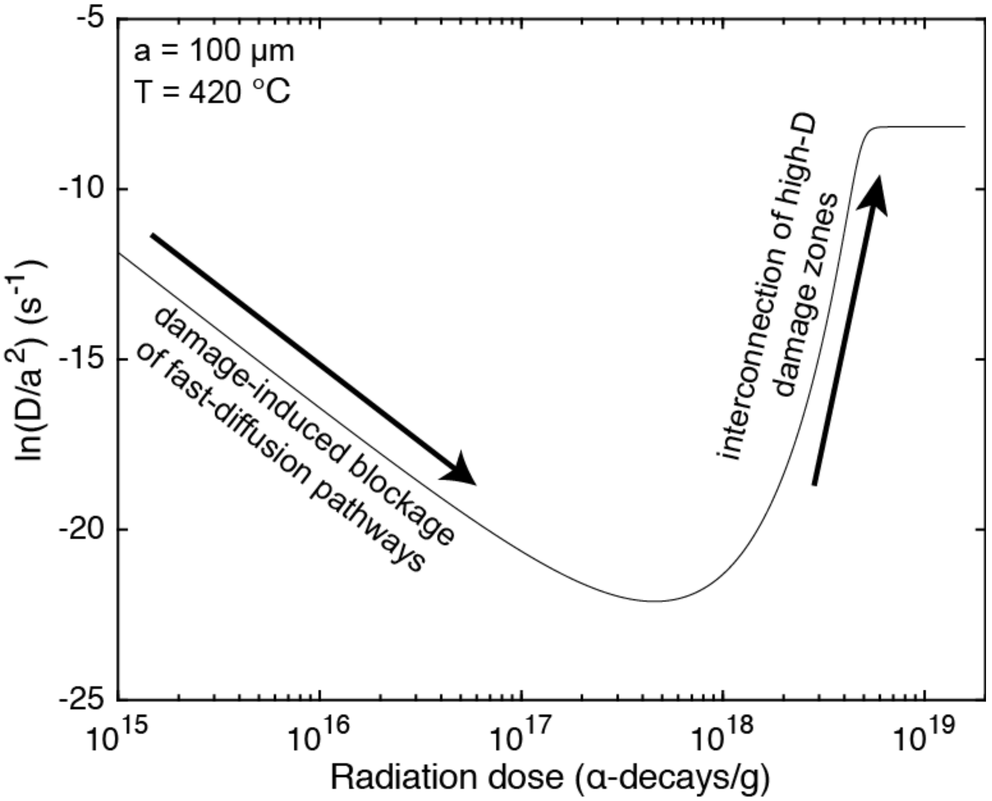

Figure 1.10 The Zircon Radiation Damage Accumulation and Annealing Model (ZRDAAM, Guenthner et al., 2013) describes He diffusion rates as a function of radiation dose. Diffusivities are shown for a 100 µm radius grain at 420 °C. At low doses, He diffusion rates are high due to the presence of fast-diffusion pathways along the c-axis. These pathways become blocked with increasing damage, forcing diffusion through more tortuous, low-diffusivity pathways. At a threshold dose just below 1 × 10^{18} α/g, fission track damage zones form interconnected pathways through the zircon, rapidly increasing diffusivity with increasing damage.

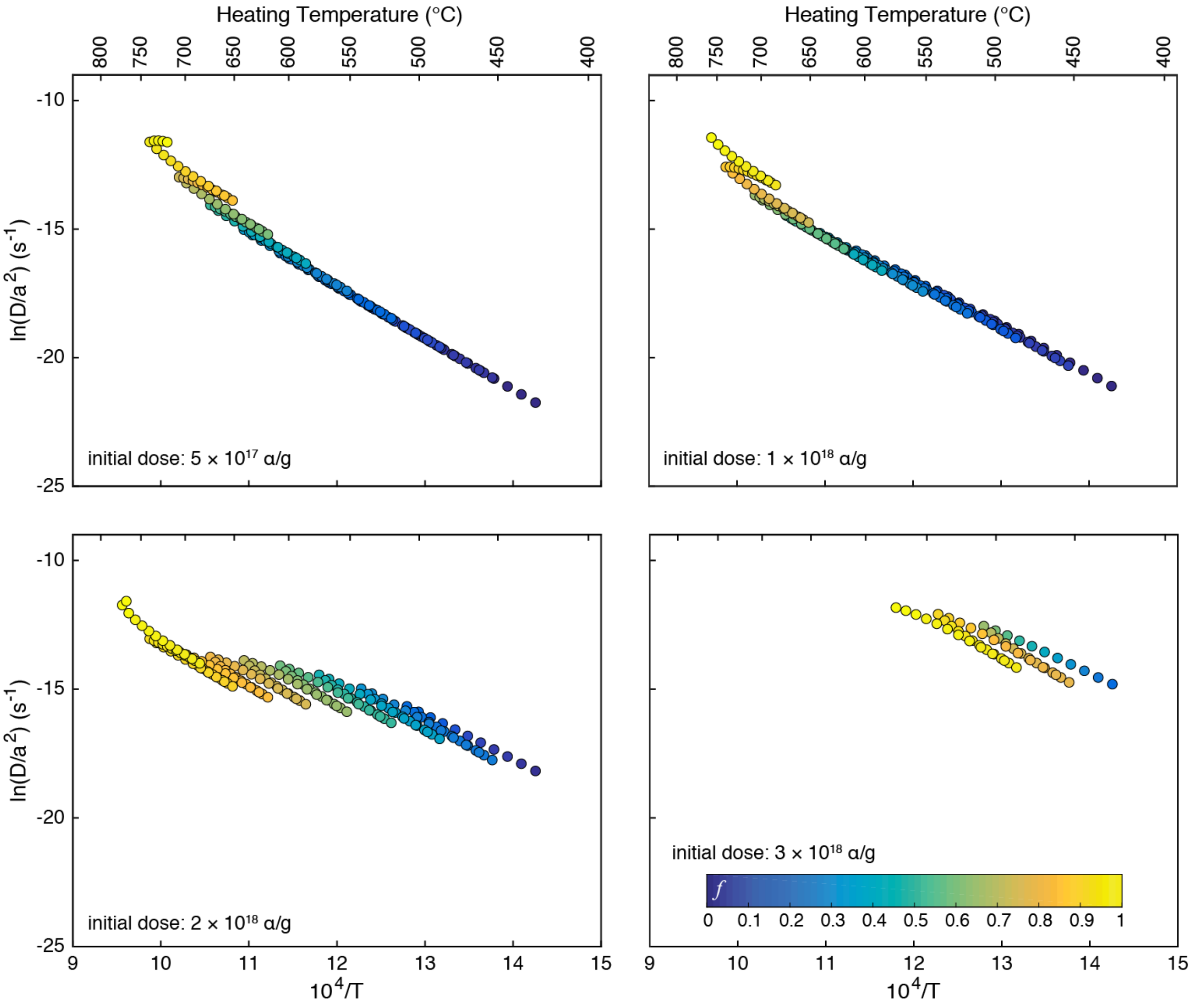

Figure 1.11 The effect of fission track damage annealing on diffusivities, as predicted by the ZRDAAM (Fig. 12; Guenthner et al., 2013), as a response to cycled step-heating temperatures. Models use a 100 µm radial width, and a square initial He profile to isolate annealing effects. Damage is annealed as a single population. At temperatures ~600 – 650 °C and doses below ~1 × 10^{18} α/g, diffusivity increases with restoration of crystallinity (Fig. 1.10). Above ~1 × 10^{18} α/g, annealing decreases diffusivities, with effects starting at the lowest heating temperature (420 °C).

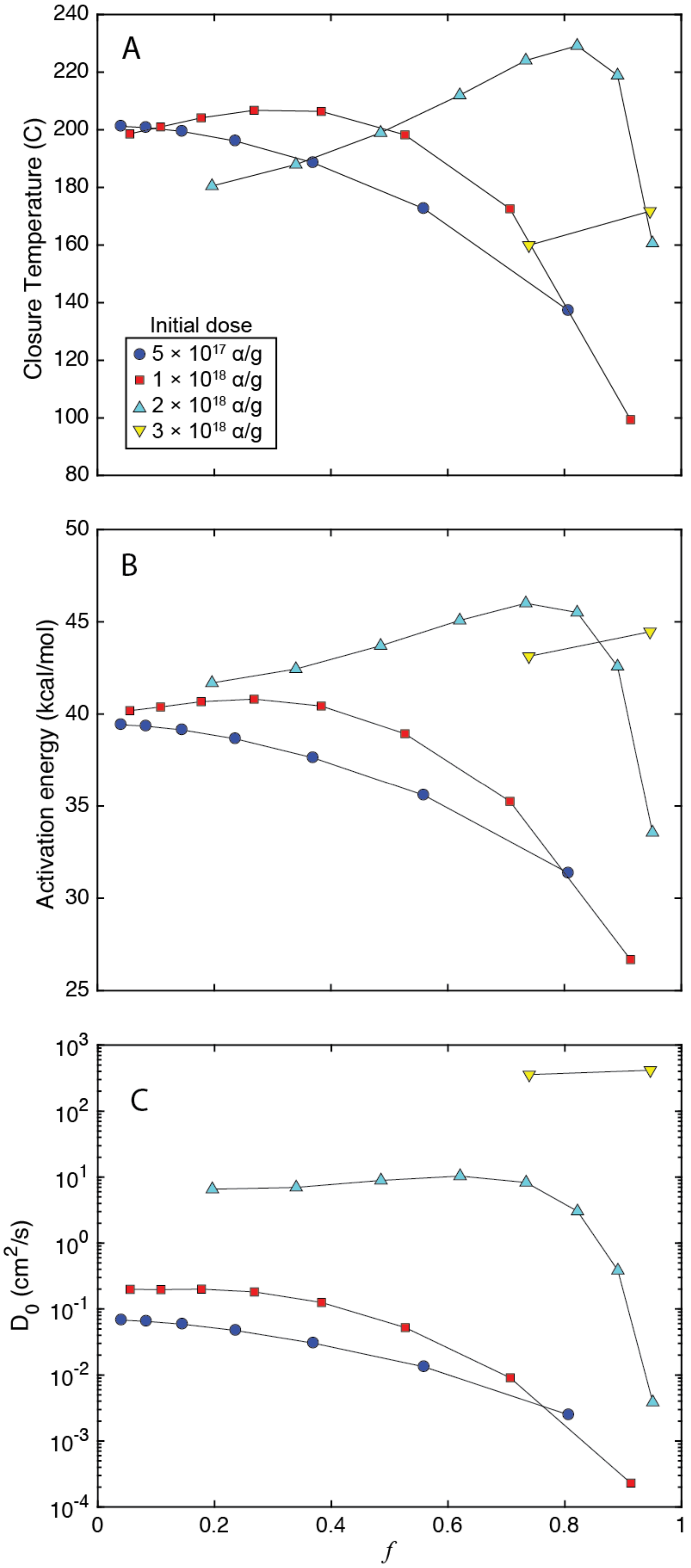

Figure 1.12 Changes in diffusion kinetics caused by annealing during step-heating. Because these experiments use a homogeneous initial ^{4}He concentration, and have 'true' diffusion kinetics values that change with annealing, these calculations are distinct from previous analyses of errors from heterogeneous ^{4}He concentrations. Because $D_f = D_{true}$, no $\ln(a_m/a)$ plot is necessary. All plots show similar relationships: annealing at low doses (<1× 10^{18} α/g) yields decreases in activation energy (B) and D_0 (C) which cause decreases in closure temperature (A). Above these doses, the model dictates that annealing yields an opposite effect of increasing kinetic parameters and increasing Tc.

Table 1.7 Effects of in-situ damage annealing on diffusivities and dose. These experiments use a homogeneous initial concentration, so that $D_f = D_{true}$.

		5E17 α/g			1E18 α/g			2E18 α/g			3E18 α/g		
Total Time (hr)	**Heating Temperature (°C)**	***f***	**ln(Df/a2)**	**Dose (α/g)**		**ln(Df/a2)**	**Dose (α/g)**	***f***	**ln(Df/a2)**	**Dose (α/g)**	***f***	**ln(Df/a2)**	**Dose (α/g)**
1	420	0.003	--	4.87E+17	0.005	--	9.75E+17	0.021	--	1.95E+18	0.115	--	2.92E+18
2	428	0.005	-21.8	4.85E+17	0.007	-21.0322	9.69E+17	0.031	-18.20	1.94E+18	0.163	-14.83	2.91E+18
3	436	0.007	-21.5	4.82E+17	0.010	-20.726	9.64E+17	0.040	-17.92	1.93E+18	0.208	-14.57	2.89E+18
4	444	0.008	-21.1	4.80E+17	0.012	-20.4251	9.59E+17	0.050	-17.64	1.92E+18	0.252	-14.31	2.88E+18
5	452	0.010	-20.8	4.77E+17	0.015	-20.1308	9.54E+17	0.060	-17.36	1.91E+18	0.298	-14.06	2.86E+18
6	460	0.013	-20.5	4.74E+17	0.018	-19.8434	9.49E+17	0.071	-17.10	1.90E+18	0.345	-13.81	2.85E+18
7	468	0.015	-20.2	4.72E+17	0.021	-19.5632	9.43E+17	0.083	-16.84	1.89E+18	0.395	-13.58	2.83E+18
8	476	0.018	-20.0	4.69E+17	0.025	-19.2901	9.37E+17	0.097	-16.59	1.87E+18	0.446	-13.35	2.81E+18
9	484	0.021	-19.7	4.65E+17	0.029	-19.024	9.30E+17	0.111	-16.35	1.86E+18	0.498	-13.14	2.79E+18
10	492	0.024	-19.4	4.61E+17	0.034	-18.7648	9.23E+17	0.127	-16.12	1.85E+18	0.551	-12.94	2.77E+18
11	500	0.028	-19.1	4.57E+17	0.039	-18.5126	9.15E+17	0.144	-15.90	1.83E+18	0.604	-12.75	2.74E+18
12	508	0.032	-18.9	4.53E+17	0.044	-18.2672	9.06E+17	0.162	-15.69	1.81E+18	0.656	-12.57	2.72E+18
13	503	0.035	-19.0	4.50E+17	0.048	-18.4498	9.01E+17	0.175	-15.91	1.80E+18	0.690	-12.83	2.70E+18
14	498	0.038	-19.2	4.49E+17	0.052	-18.6265	8.98E+17	0.185	-16.11	1.80E+18	0.715	-13.05	2.69E+18
15	493	0.040	-19.4	4.48E+17	0.054	-18.8016	8.95E+17	0.192	-16.30	1.79E+18	0.733	-13.25	2.69E+18
16	488	0.041	-19.5	4.47E+17	0.056	-18.9766	8.94E+17	0.199	-16.48	1.79E+18	0.747	-13.45	2.68E+18
17	483	0.043	-19.7	4.46E+17	0.058	-19.1524	8.93E+17	0.204	-16.67	1.79E+18	0.758	-13.64	2.68E+18
18	478	0.044	-19.9	4.46E+17	0.059	-19.3296	8.92E+17	0.208	-16.85	1.78E+18	0.767	-13.82	2.68E+18
19	473	0.045	-20.1	4.46E+17	0.060	-19.5084	8.91E+17	0.211	-17.03	1.78E+18	0.774	-14.01	2.67E+18
20	468	0.045	-20.2	4.45E+17	0.061	-19.6891	8.91E+17	0.214	-17.21	1.78E+18	0.780	-14.20	2.67E+18
21	463	0.046	-20.4	4.45E+17	0.062	-19.872	8.90E+17	0.216	-17.40	1.78E+18	0.784	-14.38	2.67E+18
22	458	0.046	-20.6	4.45E+17	0.063	-20.057	8.90E+17	0.218	-17.59	1.78E+18	0.788	-14.57	2.67E+18
23	453	0.047	-20.8	4.45E+17	0.063	-20.2445	8.90E+17	0.219	-17.77	1.78E+18	0.791	-14.76	2.67E+18
24	461	0.047	-20.5	4.45E+17	0.064	-19.9471	8.90E+17	0.221	-17.48	1.78E+18	0.795	-14.46	2.67E+18
25	469	0.048	-20.2	4.45E+17	0.065	-19.6563	8.89E+17	0.224	-17.19	1.78E+18	0.800	-14.17	2.67E+18
26	477	0.049	-19.9	4.44E+17	0.066	-19.3721	8.88E+17	0.227	-16.91	1.78E+18	0.807	-13.89	2.67E+18
27	485	0.050	-19.6	4.44E+17	0.067	-19.0945	8.87E+17	0.232	-16.63	1.77E+18	0.815	-13.62	2.66E+18
28	493	0.052	-19.4	4.43E+17	0.069	-18.8234	8.86E+17	0.237	-16.37	1.77E+18	0.825	-13.36	2.66E+18
29	501	0.054	-19.1	4.42E+17	0.072	-18.5592	8.83E+17	0.244	-16.11	1.77E+18	0.837	-13.11	2.65E+18
30	509	0.056	-18.8	4.40E+17	0.075	-18.302	8.80E+17	0.253	-15.86	1.76E+18	0.852	-12.87	2.64E+18
31	517	0.059	-18.6	4.38E+17	0.078	-18.0522	8.75E+17	0.263	-15.63	1.75E+18	0.868	-12.65	2.63E+18
32	525	0.062	-18.3	4.35E+17	0.083	-17.8102	8.69E+17	0.275	-15.40	1.74E+18	0.885	-12.45	2.61E+18
33	533	0.067	-18.1	4.31E+17	0.088	-17.5761	8.61E+17	0.289	-15.20	1.72E+18	0.903	-12.27	2.58E+18
34	541	0.072	-17.8	4.26E+17	0.094	-17.35	8.52E+17	0.306	-15.00	1.70E+18	0.920	-12.11	2.56E+18

Table 1.7 cont

35	536	0.076	-18.0	4.23E+17	0.099	-17.5197	8.46E+17	0.318	-15.21	1.69E+18	0.931	-12.36	2.54E+18
36	531	0.079	-18.1	4.21E+17	0.103	-17.6841	8.42E+17	0.327	-15.40	1.68E+18	0.939	-12.58	2.53E+18
37	526	0.082	-18.3	4.19E+17	0.106	-17.8466	8.39E+17	0.335	-15.58	1.68E+18	0.945	-12.77	2.52E+18
38	521	0.084	-18.5	4.18E+17	0.109	-18.0086	8.37E+17	0.341	-15.76	1.67E+18	0.949	-12.96	2.51E+18
39	516	0.086	-18.6	4.18E+17	0.111	-18.171	8.35E+17	0.347	-15.93	1.67E+18	0.953	-13.14	2.51E+18
40	511	0.087	-18.8	4.17E+17	0.113	-18.3343	8.34E+17	0.351	-16.10	1.67E+18	0.956	-13.31	2.50E+18
41	506	0.089	-18.9	4.17E+17	0.114	-18.4989	8.33E+17	0.355	-16.27	1.67E+18	0.958	-13.49	2.50E+18
42	501	0.090	-19.1	4.16E+17	0.116	-18.665	8.33E+17	0.358	-16.44	1.67E+18	0.959	-13.66	2.50E+18
43	496	0.091	-19.3	4.16E+17	0.117	-18.8328	8.32E+17	0.360	-16.61	1.66E+18	0.961	-13.83	2.50E+18
44	491	0.091	-19.4	4.16E+17	0.118	-19.0026	8.32E+17	0.362	-16.78	1.66E+18	0.962	-14.01	2.50E+18
45	486	0.092	-19.6	4.16E+17	0.118	-19.1743	8.32E+17	0.364	-16.95	1.66E+18	0.963	-14.18	2.50E+18
46	494	0.093	-19.3	4.16E+17	0.119	-18.9022	8.31E+17	0.366	-16.68	1.66E+18	0.964	-13.91	2.49E+18
47	502	0.094	-19.1	4.15E+17	0.121	-18.636	8.31E+17	0.369	-16.42	1.66E+18	0.966	-13.65	2.49E+18
48	510	0.095	-18.8	4.15E+17	0.122	-18.3757	8.30E+17	0.373	-16.16	1.66E+18	0.967	-13.40	2.49E+18
49	518	0.097	-18.5	4.14E+17	0.124	-18.1213	8.28E+17	0.377	-15.91	1.66E+18	0.970	-13.15	2.48E+18
50	526	0.099	-18.3	4.13E+17	0.127	-17.873	8.26E+17	0.383	-15.67	1.65E+18	0.972	-12.91	2.48E+18
51	534	0.102	-18.0	4.12E+17	0.130	-17.631	8.23E+17	0.391	-15.43	1.65E+18	0.975	-12.69	2.47E+18
52	542	0.105	-17.8	4.09E+17	0.134	-17.3957	8.19E+17	0.399	-15.21	1.64E+18	0.978	-12.48	2.46E+18
53	550	0.110	-17.6	4.06E+17	0.139	-17.1674	8.13E+17	0.410	-15.00	1.63E+18	0.981	-12.29	2.44E+18
54	558	0.115	-17.3	4.02E+17	0.144	-16.9467	8.05E+17	0.422	-14.81	1.61E+18	0.985	-12.12	2.41E+18
55	566	0.120	-17.1	3.97E+17	0.151	-16.7339	7.95E+17	0.436	-14.63	1.59E+18	0.988	-11.98	2.38E+18
56	574	0.128	-16.9	3.91E+17	0.159	-16.5291	7.83E+17	0.451	-14.47	1.57E+18	0.990	-11.86	2.35E+18
57	569	0.133	-17.0	3.87E+17	0.165	-16.6903	7.75E+17	0.463	-14.68	1.55E+18			
58	564	0.138	-17.1	3.85E+17	0.170	-16.8451	7.69E+17	0.472	-14.87	1.54E+18			
59	559	0.142	-17.3	3.83E+17	0.174	-16.9971	7.66E+17	0.480	-15.04	1.53E+18			
60	554	0.146	-17.4	3.81E+17	0.178	-17.1481	7.63E+17	0.486	-15.21	1.53E+18			
61	549	0.148	-17.6	3.80E+17	0.181	-17.2989	7.61E+17	0.491	-15.37	1.52E+18			
62	544	0.151	-17.7	3.80E+17	0.183	-17.4502	7.59E+17	0.496	-15.53	1.52E+18			
63	539	0.153	-17.9	3.79E+17	0.186	-17.6023	7.58E+17	0.500	-15.69	1.52E+18			
64	534	0.155	-18.0	3.79E+17	0.187	-17.7557	7.57E+17	0.503	-15.85	1.51E+18			
65	529	0.156	-18.2	3.78E+17	0.189	-17.9105	7.56E+17	0.505	-16.01	1.51E+18			
66	524	0.157	-18.3	3.78E+17	0.190	-18.0668	7.56E+17	0.508	-16.17	1.51E+18			
67	519	0.159	-18.5	3.78E+17	0.191	-18.2248	7.56E+17	0.509	-16.33	1.51E+18			
68	527	0.160	-18.2	3.78E+17	0.193	-17.9749	7.55E+17	0.512	-16.08	1.51E+18			
69	535	0.162	-18.0	3.77E+17	0.195	-17.7304	7.54E+17	0.515	-15.84	1.51E+18			
70	543	0.164	-17.8	3.76E+17	0.197	-17.4912	7.53E+17	0.519	-15.60	1.51E+18			
71	551	0.166	-17.5	3.75E+17	0.200	-17.2574	7.51E+17	0.523	-15.38	1.50E+18			
72	559	0.170	-17.3	3.74E+17	0.203	-17.0292	7.48E+17	0.529	-15.16	1.50E+18			
73	567	0.174	-17.1	3.72E+17	0.207	-16.807	7.44E+17	0.536	-14.95	1.49E+18			

Table 1.7 cont

74	575	0.179	-16.8	3.69E+17	0.212	-16.591	7.38E+17	0.544	-14.75	1.48E+18
75	583	0.185	-16.6	3.65E+17	0.219	-16.3819	7.31E+17	0.554	-14.56	1.46E+18
76	591	0.192	-16.4	3.60E+17	0.226	-16.1798	7.20E+17	0.565	-14.39	1.44E+18
77	599	0.200	-16.2	3.54E+17	0.234	-15.9853	7.08E+17	0.577	-14.24	1.42E+18
78	607	0.210	-16.0	3.46E+17	0.244	-15.7981	6.93E+17	0.590	-14.11	1.39E+18
79	602	0.218	-16.1	3.41E+17	0.252	-15.95	6.83E+17	0.601	-14.33	1.37E+18
80	597	0.225	-16.2	3.38E+17	0.258	-16.0948	6.76E+17	0.609	-14.52	1.35E+18
81	592	0.231	-16.3	3.35E+17	0.264	-16.2364	6.71E+17	0.616	-14.69	1.34E+18
82	587	0.237	-16.5	3.33E+17	0.268	-16.3767	6.67E+17	0.621	-14.85	1.33E+18
83	582	0.241	-16.6	3.32E+17	0.272	-16.5166	6.64E+17	0.626	-15.00	1.33E+18
84	577	0.245	-16.7	3.31E+17	0.276	-16.6568	6.62E+17	0.630	-15.16	1.32E+18
85	572	0.248	-16.9	3.30E+17	0.279	-16.7976	6.61E+17	0.633	-15.31	1.32E+18
86	567	0.251	-17.0	3.30E+17	0.281	-16.9394	6.59E+17	0.636	-15.45	1.32E+18
87	562	0.253	-17.1	3.29E+17	0.283	-17.0824	6.59E+17	0.639	-15.60	1.32E+18
88	557	0.255	-17.3	3.29E+17	0.285	-17.2267	6.58E+17	0.641	-15.75	1.32E+18
89	552	0.257	-17.4	3.29E+17	0.287	-17.3725	6.57E+17	0.643	-15.90	1.31E+18
90	560	0.259	-17.2	3.28E+17	0.289	-17.1422	6.57E+17	0.645	-15.67	1.31E+18
91	568	0.262	-17.0	3.28E+17	0.291	-16.9167	6.55E+17	0.648	-15.45	1.31E+18
92	576	0.265	-16.7	3.27E+17	0.294	-16.696	6.54E+17	0.651	-15.23	1.31E+18
93	584	0.269	-16.5	3.26E+17	0.298	-16.4801	6.51E+17	0.655	-15.02	1.30E+18
94	592	0.274	-16.3	3.24E+17	0.302	-16.2693	6.48E+17	0.660	-14.82	1.30E+18
95	600	0.280	-16.1	3.21E+17	0.308	-16.0638	6.42E+17	0.666	-14.63	1.28E+18
96	608	0.287	-15.9	3.18E+17	0.314	-15.8639	6.35E+17	0.673	-14.46	1.27E+18
97	616	0.295	-15.7	3.13E+17	0.322	-15.67	6.26E+17	0.681	-14.29	1.25E+18
98	624	0.305	-15.5	3.07E+17	0.331	-15.4821	6.14E+17	0.690	-14.15	1.23E+18
99	632	0.317	-15.3	2.99E+17	0.341	-15.3004	5.99E+17	0.699	-14.02	1.20E+18
100	640	0.331	-15.0	2.90E+17	0.352	-15.1244	5.81E+17	0.710	-13.91	1.16E+18
101	635	0.343	-15.1	2.84E+17	0.362	-15.2616	5.69E+17	0.718	-14.12	1.14E+18
102	630	0.353	-15.3	2.80E+17	0.370	-15.3931	5.61E+17	0.724	-14.30	1.12E+18
103	625	0.361	-15.4	2.77E+17	0.377	-15.5223	5.55E+17	0.729	-14.47	1.11E+18
104	620	0.369	-15.5	2.75E+17	0.383	-15.6506	5.50E+17	0.734	-14.62	1.10E+18
105	615	0.375	-15.6	2.73E+17	0.388	-15.779	5.47E+17	0.738	-14.77	1.09E+18
106	610	0.381	-15.7	2.72E+17	0.392	-15.9079	5.44E+17	0.741	-14.91	1.09E+18
107	605	0.386	-15.8	2.71E+17	0.396	-16.0376	5.42E+17	0.744	-15.05	1.08E+18
108	600	0.390	-16.0	2.70E+17	0.400	-16.1683	5.41E+17	0.746	-15.19	1.08E+18
109	595	0.394	-16.1	2.70E+17	0.403	-16.3002	5.40E+17	0.748	-15.33	1.08E+18
110	590	0.397	-16.2	2.69E+17	0.405	-16.4333	5.39E+17	0.750	-15.47	1.08E+18
111	585	0.400	-16.4	2.69E+17	0.407	-16.5678	5.38E+17	0.752	-15.61	1.08E+18
112	593	0.403	-16.1	2.69E+17	0.410	-16.3547	5.37E+17	0.754	-15.40	1.07E+18

Table 1.7 cont

113	601	0.407	-15.9	2.68E+17	0.413	-16.1456	5.36E+17	0.756	-15.19	1.07E+18
114	609	0.412	-15.7	2.67E+17	0.417	-15.9407	5.34E+17	0.759	-14.99	1.07E+18
115	617	0.418	-15.5	2.65E+17	0.422	-15.7398	5.31E+17	0.762	-14.80	1.06E+18
116	625	0.425	-15.3	2.63E+17	0.427	-15.5431	5.26E+17	0.766	-14.62	1.05E+18
117	633	0.434	-15.1	2.60E+17	0.434	-15.3505	5.21E+17	0.770	-14.44	1.04E+18
118	641	0.444	-14.9	2.56E+17	0.442	-15.1621	5.12E+17	0.776	-14.28	1.02E+18
119	649	0.455	-14.7	2.51E+17	0.451	-14.9778	5.02E+17	0.782	-14.13	1.00E+18
120	657	0.469	-14.5	2.44E+17	0.461	-14.7972	4.88E+17	0.788	-14.00	9.77E+17
121	665	0.485	-14.3	2.36E+17	0.474	-14.6197	4.72E+17	0.795	-13.88	9.44E+17
122	673	0.504	-14.1	2.26E+17	0.487	-14.4442	4.52E+17	0.803	-13.77	9.04E+17
123	668	0.520	-14.2	2.20E+17	0.499	-14.5564	4.39E+17	0.809	-13.97	8.78E+17
124	663	0.534	-14.2	2.15E+17	0.509	-14.6675	4.30E+17	0.814	-14.14	8.60E+17
125	658	0.547	-14.3	2.12E+17	0.518	-14.7792	4.23E+17	0.818	-14.29	8.47E+17
126	653	0.558	-14.4	2.09E+17	0.525	-14.8922	4.19E+17	0.822	-14.43	8.37E+17
127	648	0.567	-14.5	2.07E+17	0.532	-15.0067	4.15E+17	0.825	-14.56	8.30E+17
128	643	0.575	-14.6	2.06E+17	0.538	-15.1227	4.12E+17	0.827	-14.70	8.24E+17
129	638	0.582	-14.8	2.05E+17	0.543	-15.2402	4.10E+17	0.830	-14.83	8.20E+17
130	633	0.589	-14.9	2.04E+17	0.547	-15.3594	4.08E+17	0.831	-14.95	8.17E+17
131	628	0.594	-15.0	2.03E+17	0.551	-15.48	4.07E+17	0.833	-15.08	8.14E+17
132	623	0.599	-15.1	2.03E+17	0.554	-15.6022	4.06E+17	0.835	-15.21	8.12E+17
133	618	0.603	-15.2	2.03E+17	0.557	-15.7259	4.05E+17	0.836	-15.34	8.11E+17
134	626	0.608	-15.0	2.02E+17	0.561	-15.5274	4.04E+17	0.838	-15.14	8.08E+17
135	634	0.614	-14.8	2.01E+17	0.565	-15.3321	4.03E+17	0.839	-14.95	8.05E+17
136	642	0.620	-14.6	2.00E+17	0.570	-15.1399	4.00E+17	0.842	-14.77	8.00E+17
137	650	0.629	-14.4	1.98E+17	0.576	-14.9506	3.97E+17	0.844	-14.59	7.94E+17
138	658	0.638	-14.2	1.96E+17	0.583	-14.7638	3.92E+17	0.847	-14.41	7.85E+17
139	666	0.650	-14.1	1.93E+17	0.591	-14.579	3.86E+17	0.851	-14.25	7.72E+17
140	674	0.663	-13.9	1.89E+17	0.601	-14.3957	3.78E+17	0.855	-14.09	7.55E+17
141	682	0.678	-13.7	1.83E+17	0.612	-14.2129	3.67E+17	0.859	-13.94	7.33E+17
142	690	0.696	-13.4	1.76E+17	0.625	-14.0293	3.53E+17	0.864	-13.81	7.06E+17
143	698	0.716	-13.2	1.68E+17	0.639	-13.8432	3.36E+17	0.870	-13.68	6.72E+17
144	706	0.739	-13.0	1.58E+17	0.656	-13.6524	3.17E+17	0.875	-13.56	6.33E+17
145	701	0.760	-13.0	1.52E+17	0.671	-13.7222	3.04E+17	0.880	-13.72	6.07E+17
146	696	0.778	-13.1	1.47E+17	0.683	-13.8004	2.95E+17	0.884	-13.85	5.89E+17
147	691	0.793	-13.1	1.44E+17	0.695	-13.8856	2.88E+17	0.888	-13.98	5.76E+17
148	686	0.806	-13.2	1.41E+17	0.705	-13.9764	2.83E+17	0.891	-14.10	5.66E+17
149	681	0.818	-13.3	1.40E+17	0.713	-14.0719	2.79E+17	0.893	-14.22	5.59E+17
150	676	0.827	-13.4	1.38E+17	0.721	-14.1713	2.76E+17	0.895	-14.33	5.53E+17
151	671	0.836	-13.5	1.37E+17	0.727	-14.274	2.74E+17	0.897	-14.45	5.49E+17

Table 1.7 cont

152	666	0.843	-13.6	1.36E+17	0.733	-14.3796	2.73E+17	0.899	-14.56	5.45E+17
153	661	0.849	-13.7	1.36E+17	0.738	-14.4877	2.71E+17	0.901	-14.68	5.43E+17
154	656	0.855	-13.8	1.35E+17	0.743	-14.5982	2.70E+17	0.902	-14.80	5.40E+17
155	651	0.859	-13.9	1.35E+17	0.747	-14.7106	2.69E+17	0.903	-14.91	5.39E+17
156	659	0.865	-13.7	1.34E+17	0.751	-14.5239	2.68E+17	0.904	-14.73	5.37E+17
157	667	0.871	-13.5	1.33E+17	0.757	-14.3392	2.67E+17	0.906	-14.55	5.33E+17
158	675	0.878	-13.3	1.32E+17	0.763	-14.156	2.64E+17	0.908	-14.37	5.29E+17
159	683	0.886	-13.2	1.31E+17	0.770	-13.9734	2.61E+17	0.910	-14.20	5.22E+17
160	691	0.895	-13.0	1.28E+17	0.779	-13.7905	2.57E+17	0.913	-14.03	5.13E+17
161	699	0.905	-12.8	1.25E+17	0.789	-13.6059	2.50E+17	0.916	-13.87	5.01E+17
162	707	0.916	-12.6	1.21E+17	0.800	-13.4176	2.42E+17	0.919	-13.71	4.85E+17
163	715	0.928	-12.4	1.16E+17	0.812	-13.2231	2.32E+17	0.923	-13.55	4.64E+17
164	723	0.940	-12.1	1.10E+17	0.827	-13.0192	2.19E+17	0.927	-13.39	4.39E+17
165	731	0.953	-11.9	1.02E+17	0.843	-12.8015	2.04E+17	0.931	-13.23	4.08E+17
166	739	0.966	-11.6	9.32E+16	0.862	-12.5608	1.86E+17	0.936	-13.06	3.73E+17
167	734	0.975	-11.6	8.73E+16	0.878	-12.5577	1.75E+17	0.940	-13.13	3.49E+17
168	729	0.982	-11.6	8.31E+16	0.892	-12.5793	1.66E+17	0.944	-13.21	3.33E+17
169	724	0.987	-11.6	8.01E+16	0.904	-12.6192	1.60E+17	0.948	-13.28	3.20E+17
170	719	0.991	-11.6	7.79E+16	0.914	-12.6729	1.56E+17	0.950	-13.36	3.11E+17
171	714				0.923	-12.7376	1.52E+17	0.953	-13.44	3.05E+17
172	709				0.930	-12.811	1.50E+17	0.955	-13.53	2.99E+17
173	704				0.936	-12.8915	1.48E+17	0.957	-13.62	2.95E+17
174	699				0.941	-12.9778	1.46E+17	0.959	-13.72	2.92E+17
175	694				0.945	-13.0689	1.45E+17	0.960	-13.82	2.90E+17
176	689				0.949	-13.1641	1.44E+17	0.961	-13.92	2.88E+17
177	684				0.952	-13.2629	1.43E+17	0.962	-14.02	2.86E+17
178	692				0.955	-13.0839	1.42E+17	0.964	-13.84	2.84E+17
179	700				0.959	-12.9045	1.41E+17	0.965	-13.67	2.81E+17
180	708				0.963	-12.7234	1.38E+17	0.967	-13.49	2.77E+17
181	716				0.968	-12.5385	1.35E+17	0.969	-13.32	2.71E+17
182	724				0.972	-12.3473	1.31E+17	0.971	-13.14	2.63E+17
183	732				0.977	-12.1462	1.26E+17	0.973	-12.96	2.52E+17
184	740				0.982	-11.9303	1.19E+17	0.976	-12.76	2.38E+17
185	748				0.986	-11.6932	1.10E+17	0.979	-12.56	2.20E+17
186	756				0.991	-11.4261	9.93E+16	0.982	-12.33	1.99E+17
187	764							0.985	-12.07	1.73E+17
188	772							0.989	-11.76	1.43E+17
189	767							0.992	-11.61	1.24E+17

Table 1.8 Diffusion kinetics results for models with homogeneous initial ^{4}He concentrations, and diffusivities determined by ZRDAAM, with in-situ annealing.

5E17 α/g

f	Closure temperature (°C)	Activation energy (kcal/mol)	D0 (cm2/s)
0.04	201.2	39.4	6.78E-02
0.08	200.7	39.3	6.50E-02
0.15	199.4	39.1	5.88E-02
0.24	196.1	38.7	4.72E-02
0.37	188.5	37.6	3.03E-02
0.56	172.6	35.6	1.33E-02
0.81	137.2	31.4	2.48E-03

1E18 α/g

f	Closure temperature (°C)	Activation energy (kcal/mol)	D0 (cm2/s)
0.056	198.6	40.2	1.99E-01
0.108	201.0	40.4	1.97E-01
0.178	204.1	40.7	2.00E-01
0.268	206.7	40.8	1.82E-01
0.383	206.4	40.4	1.26E-01
0.527	198.2	38.9	5.24E-02
0.707	172.6	35.2	9.06E-03
0.913	99.4	26.7	2.29E-04

2E18 α/g

f	Closure temperature (°C)	Activation energy (kcal/mol)	D0 (cm2/s)
0.196	180.5	41.7	6.56E+00
0.340	187.9	42.4	6.97E+00
0.485	198.9	43.7	8.90E+00
0.621	212.0	45.1	1.04E+01
0.734	224.0	46.0	8.28E+00
0.822	229.1	45.5	3.03E+00
0.891	218.9	42.6	3.84E-01
0.951	160.6	33.6	3.86E-03

Table 1.8 cont

3E18 α/g			
f	**Closure temperature (°C)**	**Activation energy (kcal/mol)**	**D0 (cm2/s)**
0.739	159.9	43.1	3.57E+02
0.947	171.7	44.5	4.17E+02

1.3.5 Comparisons with real step-heating data

Lastly, the effects of both heterogeneous ^{4}He concentrations and in-situ annealing are combined, and the results are compared to empirically measured diffusivities from real zircons. For these comparisons, two zircons from Chapter 2 are selected—C015-14 and C015-28 from the Hall Peninsula of Baffin Island, Nunavut, Canada. Laser ablation ICP-MS pit profiling on these zircons (Fig. 1.13 inset) reveals rims with parent isotope concentrations that are both enriched (C015-14) and depleted (C015-28). The former displays a relatively linear Arrhenius trend, whereas the latter shows a trend indicative of annealing (Fig. 1.13, triangles). Model radii are set to the measured equivalent spherical radii of the real zircons and are subjected to the same Tt schedules as their complementary experiments. As a first-order approximation to ^{4}He concentrations, profiles from Figure 1.7B are used: 'sharp zoning, enriched rim' for C015-14, and 'sharp zoning, depleted rim' for C015-28. Although the zircons chosen for these comparisons yield the strongest degree of enrichment or depletion relative to bulk concentrations measured in Chapter 2—approx 1.5 – 2.5x—profiles from Fig. 1.7B involve a significantly stronger change in U and Th concentration by 10x. Initial radiation doses are based on total damage retention since 1610 Ma, the youngest msc K/Ar age measured on the Hall Peninsula (T_C = 420 °C), and are likely an overestimation as fission track damage is known to anneal at lower temperatures (Chapter 2 and references therein).

Comparing real and model experiments (Table 1.9; Fig. 1.13, circles) yields mixed results. For C015-14 (Fig. 1.13A), although both model and empirical measurements are relatively linear above 300 °C, ZRDAAM predicts diffusivities which are significantly lower than those observed. This may be due to difficulties in calculating an appropriate dosage for the zircon; however, our dose estimate is likely overestimated (Chapter 2), and decreasing the initial dose would decrease

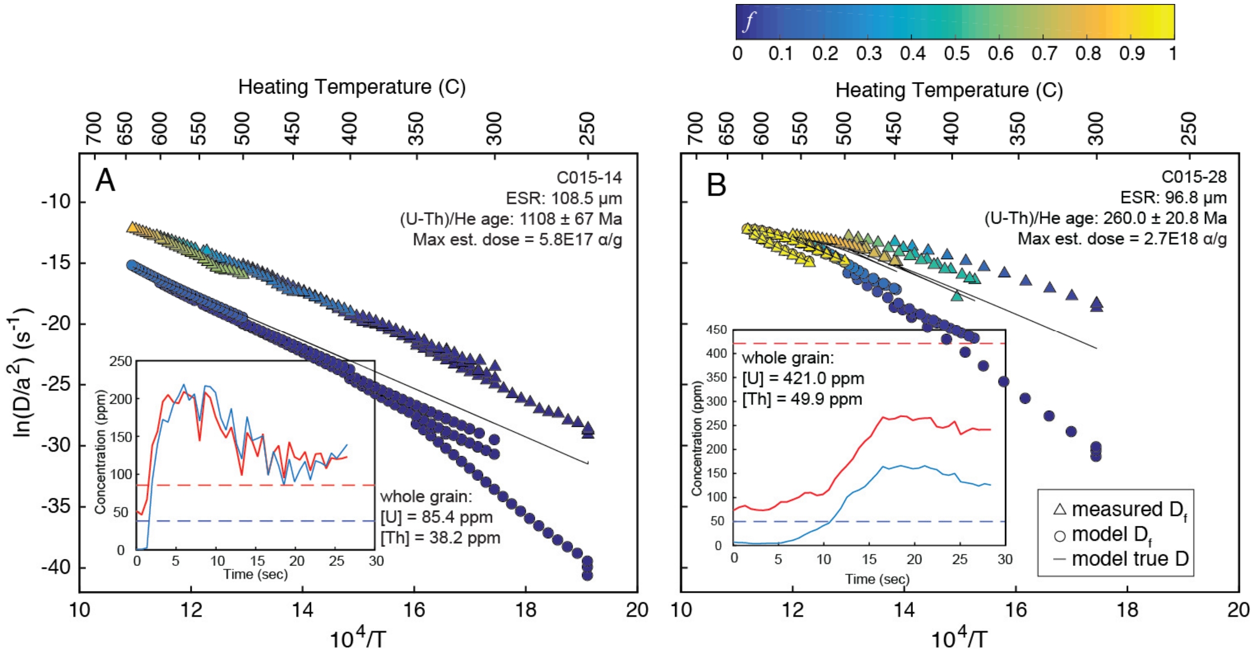

Figure 1.13 Comparisons of real zircon step-heating results (triangles) to model results (circles) using the same step-heating schedule. The thin black line shows the model results for a homogeneous gas concentration under similar conditions (e.g. as an ideal ^{3}He reference in proton irradiation). Inset figures show U and Th concentrations measured by laser ablation ICP-MS pit profiling at the grain rim (solid lines) relative to bulk average concentrations (dashed lines; see Chapter 2). Zircon C015-14 (A) shows a rim enriched in U and Th relative to bulk concentrations; C015-28 (B) shows a relative depletion in U and Th. To compare these results to a relevant model, we have used the 'sharp zoning, enriched' and 'sharp zoning, depleted' profiles from Fig. 1.7B. (A) Although both trends appear relatively linear, diffusivities predicted by ZRDAAM at these doses are much lower than their empirically measured counterparts. The effects of ^{4}He depletion near the grain boundary in causing initially low diffusivities as predicted by the model are much more severe than the subtle effects observed in the measured data. (B) Although models and real results are in strong agreement at high releases, they diverge significantly at low fractional releases. The strongly depleted ^{4}He rim of the model yields severely underestimated initial diffusivities, however, measured results do not appear to show any of the expected effects of ^{4}He depletion near the grain boundary whatsoever, in spite of its U and Th depleted rim. Relative to the homogeneous model reference (thin black line), initial diffusivities are high. Annealing effects appear more aggressive in measured results vs model results.

Table 1.9 Comparisons between real and modeled diffusion experiments, using the same time-temperature schedules.

C015-14	**U,Th enriched rim**	**measured**	**measured**	**modeled**	**modeled**	**modeled**	**C015-14**	**U,Th enriched rim**	**measured**	**measured**	**modeled**	**modeled**	**modeled**
Time (hr)	**Temperature (°C)**	***f***	**$\ln(D_f/a^2)$**	***f***	**$\ln(D_f/a^2)$**	**Dose (α/g)**	**Time (hr)**	**Temperature (°C)**	***f***	**$\ln(D_f/a^2)$**	***f***	**$\ln(D_f/a^2)$**	**Dose (α/g)**
1.0	250	9.78E-05	-29.109	1.53E-07	--	5.76E+17	1.0	300	0.018	-18.682	0.003	--	2.656E+18
3.0	250	1.93E-04	-28.733	4.54E-07	-40.660	5.76E+17	2.0	300	0.028	-18.340	0.005	-22.038	2.654E+18
5.0	250	2.53E-04	-28.761	7.51E-07	-39.979	5.76E+17	3.0	300	0.035	-18.322	0.006	-22.045	2.653E+18
8.1	250	3.34E-04	-28.590	1.20E-06	-39.502	5.76E+17	4.1	300	0.041	-18.352	0.007	-22.050	2.652E+18
9.1	255	3.69E-04	-28.152	1.41E-06	-38.853	5.76E+17	5.1	315	0.050	-17.730	0.008	-21.170	2.65E+18
10.1	260	4.08E-04	-27.939	1.71E-06	-38.321	5.76E+17	6.1	329	0.064	-17.108	0.011	-20.393	2.647E+18
11.1	265	4.70E-04	-27.381	2.14E-06	-37.767	5.76E+17	7.1	345	0.083	-16.533	0.016	-19.551	2.642E+18
12.1	270	0.001	-27.254	2.75E-06	-37.193	5.75E+17	8.1	360	0.109	-15.868	0.023	-18.807	2.636E+18
13.1	275	0.001	-27.029	3.57E-06	-36.607	5.75E+17	9.1	375	0.141	-15.346	0.033	-18.103	2.628E+18
14.1	280	0.001	-26.456	4.73E-06	-36.011	5.75E+17	10.1	389	0.181	-14.841	0.046	-17.483	2.62E+18
15.1	285	0.001	-26.168	6.29E-06	-35.411	5.75E+17	11.1	404	0.229	-14.389	0.063	-16.849	2.609E+18
16.1	290	0.001	-25.789	8.43E-06	-34.812	5.75E+17	12.1	420	0.283	-13.993	0.087	-16.210	2.595E+18
17.1	295	0.001	-25.335	1.13E-05	-34.216	5.74E+17	13.2	434	0.342	-13.659	0.116	-15.692	2.58E+18
18.1	300	0.001	-24.995	1.52E-05	-33.625	5.74E+17	14.2	450	0.407	-13.282	0.153	-15.126	2.56E+18
19.1	305	0.002	-24.666	2.05E-05	-33.038	5.74E+17	15.2	442	0.440	-13.767	0.173	-15.502	2.552E+18
20.1	310	0.002	-24.288	2.74E-05	-32.462	5.74E+17	16.2	432	0.459	-14.256	0.186	-15.923	2.549E+18
21.1	315	0.002	-24.002	3.64E-05	-31.897	5.73E+17	17.2	421	0.470	-14.695	0.193	-16.382	2.547E+18
22.2	320	0.003	-23.705	4.85E-05	-31.340	5.73E+17	18.2	412	0.478	-15.115	0.197	-16.763	2.546E+18
23.2	325	0.003	-23.361	6.40E-05	-30.796	5.73E+17	19.2	401	0.482	-15.532	0.200	-17.239	2.545E+18
24.2	330	0.004	-23.024	8.40E-05	-30.267	5.72E+17	20.2	392	0.485	-15.974	0.202	-17.639	2.545E+18
25.2	335	0.005	-22.726	1.10E-04	-29.747	5.72E+17	21.2	382	0.487	-16.401	0.203	-18.095	2.545E+18
26.2	340	0.005	-22.391	1.43E-04	-29.240	5.71E+17	22.3	386	0.489	-16.272	0.205	-17.912	2.545E+18
27.2	345	0.006	-22.076	1.85E-04	-28.747	5.71E+17	23.3	396	0.490	-17.810	0.207	-17.463	2.544E+18
28.2	350	0.007	-21.813	2.37E-04	-28.269	5.70E+17	24.3	406	0.494	-15.514	0.210	-17.027	2.544E+18
29.2	340	0.008	-22.239	2.68E-04	-28.636	5.70E+17	25.3	415	0.501	-15.154	0.215	-16.647	2.543E+18
30.2	330	0.008	-22.668	2.85E-04	-29.096	5.70E+17	26.3	426	0.510	-14.771	0.222	-16.197	2.541E+18
31.3	320	0.008	-23.234	2.95E-04	-29.611	5.70E+17	27.3	436	0.522	-14.448	0.233	-15.804	2.537E+18
32.3	310	0.009	-23.804	3.01E-04	-30.163	5.70E+17	28.3	446	0.538	-14.134	0.247	-15.427	2.532E+18
33.3	300	0.009	-24.473	3.04E-04	-30.745	5.70E+17	29.3	456	0.559	-13.789	0.265	-15.067	2.524E+18
34.3	305	0.009	-24.129	3.08E-04	-30.435	5.70E+17	30.3	466	0.589	-13.335	0.289	-14.728	2.513E+18
35.3	310	0.009	-23.894	3.13E-04	-30.128	5.70E+17	31.4	476	0.622	-13.131	0.317	-14.409	2.498E+18
36.3	315	0.009	-23.474	3.21E-04	-29.822	5.70E+17	32.4	486	0.657	-12.955	0.351	-14.113	2.479E+18
37.3	320	0.009	-23.220	3.31E-04	-29.515	5.70E+17	33.4	496	0.693	-12.797	0.390	-13.838	2.457E+18
38.3	325	0.009	-22.885	3.43E-04	-29.208	5.70E+17	34.4	488	0.714	-13.239	0.414	-14.187	2.446E+18
39.3	330	0.010	-22.664	3.60E-04	-28.898	5.70E+17	35.4	478	0.726	-13.702	0.429	-14.571	2.44E+18

Table 1.9 cont

40.3	335	0.010	-22.401	3.81E-04	-28.585	5.70E+17	36.4	468	0.734	-14.124	0.439	-14.946	2.437E+18
41.4	340	0.011	-22.109	4.09E-04	-28.267	5.70E+17	37.5	458	0.738	-14.533	0.446	-15.322	2.436E+18
42.4	345	0.011	-21.852	4.45E-04	-27.944	5.69E+17	38.5	448	0.742	-14.927	0.450	-15.704	2.435E+18
43.4	350	0.012	-21.590	4.90E-04	-27.616	5.69E+17	39.5	450	0.745	-14.872	0.455	-15.631	2.434E+18
43.9	355	0.012	-21.285	0.001	-27.304	5.69E+17	40.5	460	0.750	-14.545	0.462	-15.260	2.432E+18
44.4	360	0.013	-21.040	0.001	-27.006	5.69E+17	41.5	470	0.756	-14.216	0.471	-14.902	2.43E+18
44.9	365	0.014	-20.783	0.001	-26.705	5.68E+17	42.5	480	0.764	-13.912	0.484	-14.557	2.425E+18
45.4	370	0.015	-20.544	0.001	-26.400	5.68E+17	43.6	485	0.773	-13.786	0.498	-14.400	2.419E+18
46.0	375	0.016	-20.315	0.001	-26.093	5.68E+17	44.6	490	0.783	-13.665	0.513	-14.249	2.412E+18
46.5	380	0.017	-20.050	0.001	-25.784	5.67E+17	45.6	495	0.793	-13.579	0.530	-14.104	2.404E+18
47.0	385	0.018	-19.959	0.001	-25.475	5.67E+17	46.6	500	0.803	-13.480	0.549	-13.966	2.394E+18
47.5	390	0.020	-19.846	0.001	-25.167	5.66E+17	47.6	505	0.814	-13.397	0.568	-13.835	2.382E+18
48.0	395	0.021	-19.609	0.001	-24.863	5.66E+17	48.6	510	0.826	-13.248	0.589	-13.711	2.37E+18
48.5	400	0.023	-19.371	0.001	-24.565	5.65E+17	49.7	515	0.837	-13.168	0.610	-13.594	2.356E+18
49.0	390	0.024	-19.672	0.001	-24.953	5.64E+17	50.7	520	0.849	-13.115	0.632	-13.485	2.34E+18
49.6	380	0.025	-19.919	0.002	-25.381	5.64E+17	51.7	525	0.860	-13.040	0.655	-13.382	2.323E+18
50.1	370	0.026	-20.350	0.002	-25.836	5.64E+17	52.7	530	0.871	-12.982	0.678	-13.286	2.304E+18
50.6	360	0.026	-20.791	0.002	-26.313	5.64E+17	53.7	535	0.882	-12.926	0.700	-13.197	2.284E+18
51.1	350	0.027	-21.229	0.002	-26.810	5.64E+17	54.7	540	0.892	-12.891	0.723	-13.115	2.263E+18
51.6	375	0.027	-20.134	0.002	-25.572	5.64E+17	55.8	545	0.902	-12.856	0.745	-13.039	2.24E+18
52.1	360	0.028	-20.795	0.002	-26.287	5.64E+17	56.8	550	0.911	-12.816	0.766	-12.969	2.216E+18
52.6	345	0.028	-21.413	0.002	-27.042	5.64E+17	57.8	555	0.920	-12.763	0.787	-12.905	2.19E+18
53.1	330	0.028	-22.150	0.002	-27.839	5.64E+17	58.8	560	0.928	-12.712	0.807	-12.848	2.163E+18
53.7	315	0.028	-23.055	0.002	-28.677	5.64E+17	59.8	550	0.933	-13.117	0.819	-13.227	2.15E+18
54.2	300	0.028	-23.541	0.002	-29.559	5.64E+17	60.8	540	0.936	-13.487	0.827	-13.568	2.142E+18
54.7	309	0.028	-23.055	0.002	-29.024	5.64E+17	61.8	530	0.939	-13.834	0.833	-13.897	2.138E+18
55.2	315	0.028	-23.012	0.002	-28.675	5.64E+17	62.9	520	0.940	-14.185	0.837	-14.222	2.136E+18
55.7	320	0.028	-22.862	0.002	-28.390	5.64E+17	63.9	510	0.941	-14.533	0.840	-14.549	2.134E+18
56.2	325	0.028	-22.433	0.002	-28.110	5.64E+17	64.9	500	0.942	-14.844	0.842	-14.881	2.133E+18
56.7	330	0.028	-22.263	0.002	-27.817	5.64E+17	65.9	510	0.943	-14.574	0.845	-14.555	2.132E+18
57.2	335	0.028	-22.073	0.002	-27.574	5.64E+17	66.9	520	0.944	-14.278	0.848	-14.240	2.13E+18
57.8	340	0.028	-21.857	0.002	-27.293	5.64E+17	67.9	530	0.946	-14.001	0.853	-13.935	2.126E+18
58.3	345	0.029	-21.451	0.002	-27.029	5.64E+17	68.9	540	0.948	-13.711	0.859	-13.643	2.12E+18
58.8	350	0.029	-21.234	0.002	-26.768	5.64E+17	69.9	550	0.950	-13.436	0.867	-13.367	2.11E+18
59.3	355	0.029	-20.988	0.002	-26.510	5.64E+17	70.9	560	0.954	-13.187	0.876	-13.113	2.094E+18
59.8	360	0.029	-20.714	0.002	-26.256	5.64E+17	71.9	570	0.957	-12.964	0.887	-12.884	2.071E+18
60.3	365	0.030	-20.494	0.002	-26.003	5.64E+17	72.9	580	0.962	-12.760	0.899	-12.687	2.04E+18
60.8	370	0.030	-20.256	0.002	-25.754	5.64E+17	73.9	590	0.966	-12.603	0.911	-12.523	1.998E+18
61.3	375	0.031	-20.040	0.002	-25.506	5.64E+17	75.0	600	0.970	-12.468	0.923	-12.398	1.946E+18

Table 1.9 cont

61.8	380	0.032	-19.797	0.002	-25.259	5.63E+17	76.0	610	0.975	-12.332	0.935	-12.313	1.885E+18
62.3	385	0.033	-19.573	0.002	-25.014	5.63E+17	77.0	620	0.979	-12.269	0.945	-12.260	1.815E+18
62.8	390	0.034	-19.407	0.002	-24.771	5.63E+17	78.0	610	0.981	-12.725	0.950	-12.740	1.782E+18
63.3	395	0.035	-19.355	0.002	-24.528	5.63E+17	79.0	600	0.982	-13.097	0.954	-13.102	1.764E+18
63.8	400	0.037	-19.285	0.002	-24.287	5.62E+17	80.0	590	0.983	-13.421	0.956	-13.423	1.754E+18
64.3	405	0.038	-19.059	0.003	-24.047	5.62E+17	81.0	580	0.984	-13.761	0.958	-13.724	1.748E+18
64.8	410	0.040	-18.786	0.003	-23.809	5.61E+17	82.0	570	0.984	-14.074	0.959	-14.018	1.745E+18
65.3	415	0.042	-18.499	0.003	-23.572	5.61E+17	83.0	560	0.984	-14.391	0.960	-14.311	1.743E+18
65.8	420	0.045	-18.199	0.003	-23.337	5.60E+17	84.1	550	0.985	-14.747	0.961	-14.607	1.742E+18
66.4	425	0.049	-17.938	0.003	-23.105	5.59E+17	85.1	540	0.985	-15.002	0.961	-14.907	1.741E+18
66.9	430	0.053	-17.743	0.004	-22.876	5.58E+17							
67.4	435	0.057	-17.549	0.004	-22.650	5.57E+17							
67.9	440	0.063	-17.325	0.005	-22.427	5.56E+17							
68.4	445	0.068	-17.142	0.005	-22.208	5.54E+17							
68.9	450	0.075	-16.956	0.006	-21.993	5.53E+17							
69.4	455	0.082	-16.763	0.006	-21.781	5.51E+17							
69.9	460	0.090	-16.581	0.007	-21.574	5.50E+17							
70.5	465	0.098	-16.390	0.008	-21.370	5.48E+17							
71.0	470	0.108	-16.133	0.009	-21.169	5.46E+17							
71.5	475	0.118	-15.961	0.009	-20.972	5.44E+17							
72.0	480	0.129	-15.804	0.010	-20.778	5.42E+17							
72.5	485	0.140	-15.616	0.012	-20.587	5.39E+17							
73.0	490	0.152	-15.461	0.013	-20.399	5.37E+17							
73.5	495	0.165	-15.323	0.014	-20.214	5.34E+17							
74.0	500	0.179	-15.175	0.015	-20.031	5.32E+17							
74.5	490	0.187	-15.549	0.016	-20.355	5.30E+17							
75.1	480	0.193	-15.942	0.017	-20.692	5.30E+17							
75.6	470	0.197	-16.306	0.017	-21.041	5.29E+17							
76.1	460	0.199	-16.837	0.018	-21.402	5.29E+17							
76.6	450	0.200	-17.363	0.018	-21.773	5.29E+17							
77.1	440	0.201	-17.432	0.018	-22.156	5.29E+17							
77.6	430	0.202	-17.763	0.018	-22.551	5.29E+17							
78.1	420	0.203	-18.198	0.018	-22.957	5.29E+17							
78.7	410	0.203	-18.584	0.018	-23.376	5.29E+17							
79.2	400	0.203	-19.016	0.018	-23.807	5.29E+17							
79.7	405	0.204	-18.778	0.018	-23.590	5.29E+17							
80.2	410	0.204	-18.591	0.018	-23.375	5.29E+17							
80.7	415	0.204	-18.445	0.018	-23.163	5.29E+17							
81.2	420	0.205	-18.242	0.019	-22.955	5.29E+17							

Table 1.9 cont

81.7	425	0.206	-17.986	0.019	-22.749	5.29E+17
82.2	430	0.206	-17.823	0.019	-22.546	5.29E+17
82.7	435	0.207	-17.590	0.019	-22.346	5.29E+17
83.2	440	0.208	-17.417	0.019	-22.148	5.28E+17
83.8	445	0.210	-17.369	0.019	-21.953	5.28E+17
84.3	450	0.211	-17.326	0.019	-21.760	5.28E+17
84.8	455	0.212	-17.234	0.019	-21.570	5.28E+17
85.3	460	0.214	-16.979	0.020	-21.382	5.28E+17
85.8	465	0.216	-16.758	0.020	-21.196	5.28E+17
86.3	470	0.219	-16.476	0.020	-21.012	5.27E+17
86.8	475	0.223	-16.192	0.021	-20.829	5.27E+17
87.3	480	0.227	-16.043	0.021	-20.649	5.26E+17
87.8	485	0.232	-15.881	0.022	-20.470	5.26E+17
88.3	490	0.237	-15.688	0.023	-20.293	5.25E+17
88.9	495	0.244	-15.533	0.024	-20.118	5.24E+17
89.4	500	0.251	-15.367	0.025	-19.944	5.22E+17
89.9	505	0.259	-15.222	0.026	-19.771	5.21E+17
90.4	510	0.268	-15.071	0.027	-19.600	5.19E+17
90.9	515	0.278	-14.901	0.028	-19.430	5.17E+17
91.4	520	0.289	-14.761	0.030	-19.262	5.14E+17
91.9	525	0.301	-14.639	0.031	-19.094	5.11E+17
92.4	530	0.314	-14.484	0.033	-18.927	5.08E+17
93.0	535	0.329	-14.340	0.035	-18.762	5.05E+17
93.5	540	0.344	-14.199	0.038	-18.597	5.01E+17
94.0	545	0.360	-14.070	0.040	-18.433	4.97E+17
94.5	541	0.376	-14.004	0.042	-18.539	4.94E+17
95.0	555	0.395	-13.847	0.046	-18.111	4.89E+17
95.5	560	0.414	-13.747	0.049	-17.948	4.84E+17
96.0	565	0.433	-13.622	0.053	-17.786	4.78E+17
96.5	570	0.454	-13.495	0.057	-17.625	4.73E+17
97.0	575	0.476	-13.407	0.061	-17.463	4.67E+17
97.6	580	0.497	-13.298	0.066	-17.301	4.60E+17
98.1	585	0.520	-13.178	0.071	-17.140	4.54E+17
98.6	590	0.542	-13.083	0.077	-16.979	4.47E+17
99.1	595	0.565	-13.002	0.083	-16.818	4.40E+17
99.6	600	0.589	-12.879	0.090	-16.655	4.33E+17
100.1	590	0.605	-13.173	0.095	-16.891	4.29E+17
100.6	580	0.617	-13.514	0.098	-17.140	4.27E+17
101.1	570	0.625	-13.803	0.101	-17.402	4.25E+17

Table 1.9 cont

101.6	560	0.630	-14.129	0.103	-17.674	4.25E+17
102.1	550	0.634	-14.445	0.104	-17.956	4.24E+17
102.6	540	0.637	-14.910	0.105	-18.247	4.24E+17
103.1	530	0.639	-15.315	0.106	-18.546	4.24E+17
103.7	520	0.640	-15.622	0.107	-18.855	4.24E+17
104.2	510	0.641	-15.658	0.107	-19.172	4.24E+17
104.7	500	0.642	-15.979	0.108	-19.498	4.24E+17
105.2	505	0.643	-15.820	0.108	-19.332	4.24E+17
105.7	510	0.644	-15.666	0.108	-19.168	4.24E+17
106.2	515	0.645	-15.567	0.109	-19.005	4.24E+17
106.7	520	0.646	-15.558	0.109	-18.844	4.24E+17
107.2	525	0.648	-15.514	0.110	-18.685	4.24E+17
107.7	530	0.649	-15.392	0.111	-18.527	4.23E+17
108.2	535	0.651	-15.129	0.112	-18.371	4.23E+17
108.7	540	0.653	-14.919	0.113	-18.216	4.23E+17
109.2	545	0.656	-14.707	0.114	-18.062	4.23E+17
109.8	550	0.660	-14.448	0.115	-17.909	4.22E+17
110.3	555	0.664	-14.323	0.117	-17.758	4.22E+17
110.8	560	0.669	-14.166	0.119	-17.607	4.21E+17
111.3	565	0.674	-14.031	0.121	-17.457	4.20E+17
111.8	570	0.680	-13.889	0.123	-17.308	4.19E+17
112.3	575	0.687	-13.729	0.126	-17.159	4.18E+17
112.8	580	0.695	-13.605	0.129	-17.011	4.16E+17
113.3	585	0.703	-13.441	0.132	-16.863	4.14E+17
113.8	590	0.713	-13.320	0.136	-16.715	4.12E+17
114.3	595	0.723	-13.156	0.141	-16.567	4.09E+17
114.8	600	0.734	-13.051	0.145	-16.419	4.06E+17
115.4	605	0.749	-12.770	0.151	-16.271	4.02E+17
115.9	610	0.762	-12.792	0.157	-16.122	3.97E+17
116.4	615	0.776	-12.662	0.164	-15.973	3.92E+17
116.9	620	0.790	-12.546	0.171	-15.824	3.86E+17
117.4	625	0.805	-12.449	0.179	-15.675	3.79E+17
117.9	630	0.820	-12.358	0.188	-15.524	3.72E+17
118.4	635	0.835	-12.235	0.197	-15.374	3.65E+17
118.9	640	0.850	-12.159	0.208	-15.223	3.57E+17

diffusivities further (Fig. 1.10). Initial diffusivities at low temperatures in the model predict that the low-diffusivity ‘tail,’ resulting from He depletion near the grain boundary, is more prominent than observed in real experiments. Lastly, empirical measurements show a gentle decrease in diffusivities at high temperatures, whereas model results show an opposite trend of gently increasing diffusivities. For C015-28 (Fig. 1.13B), model results are overall similar or overlapping with real values at high releases. At low fractional releases, initial model diffusivities are very low relative to measured values: although the model predicts severely underestimated diffusivities, such effects from a ^{4}He depleted rim appear absent from empirical results from C015-28, or are masked by annealing behavior. Even relative to a homogeneous model reference, initial measured diffusivities are high, and decrease as a result of annealing. Annealing appears slightly more aggressive in real data.

1.4 DISCUSSION

1.4.1 Implications for whole-grain diffusional analyses

The results of modeling common styles of He concentration heterogeneities within the ZHe system, summarized in Table 1.10, suggest that we should observe a consistent underestimation of diffusivities and diffusion kinetics, resulting from natural He depletion near the grain boundary (Figs. 1.3 – 1.6; Tables 1.1 – 1.4). The degree of depletion appears most significant to D_f estimates closest to the grain boundary and at low f, decreasing its effects with increasing depth into the grain and with further diffusional rounding (increasing f). These effects are minimized by: using larger grain sizes, for which the α-ejection profile affects a smaller portion of the interior volume (Fig. 1.3); estimating kinetics at higher f values, which are visibly more linear in Arrhenius space (Figs. 1.2, 1.4, 1.6); and comparing results to real zircons with U and Th enrichment near the grain

Table 1.10 A summary of model experiments.

Location	Diffusivity	He concentration profile
Section 1.3.2, Tables 1.1 - 1.2, Figures 1.3 - 1.4	constant	alpha ejection
Section 1.3.2, Tables 1.3 - 1.4, Figures 1.5 - 1.6	constant	alpha ejection, rounding
Section 1.3.3, Tables S1.5 - 1.6, Figures 1.8 - 1.9	constant	alpha ejection, zonation
Section 1.3.4, Table 1.7, Figures 1.11 - 1.12	variable (ZRDAAM)	homogeneous
Section 1.3.5, Table 1.8, Figure 1.13	variable (ZRDAAM)	alpha ejection, zonation

boundary (Fig. 1.8), with models suggesting that near-boundary He enrichment may (over)compensate for the effects of α-ejection depletion.

A comparison of results to real data, however, yields little similarity. While all models predict that initial diffusivities at low *f* are underestimated (Fig. 1.8), many cycled step-heating experiments on zircon are either linear or show anomalously *high* diffusivities at low *f* (Reiners et al., 2002, 2004; Wolfe and Stockli, 2010; Guenthner et al., 2013; Chapter 2). The real step-heating data from C015-14 do show slightly low diffusivities at low *f*, but this effect is subtle compared to the model predictions (Fig. 1.8). Furthermore, results from Chapter 2 show several step-heating experiments in which ^{4}He diffusivities are closely matched to those from a homogeneous concentration of ^{3}He. Although it is possible that such effects are present in real data but masked by other effects, He appears to diffuse from whole zircon grains in a manner similar to a homogeneous diffusant in spite of recent observations that natural concentrations are more heterogeneous than can be modeled with a 1D sphere (Danišík et al., 2017). The discrepancy between model predictions and real results raises questions about fundamental assumptions of He diffusional mechanics.

One possibility to explain this discrepancy is interconnected fission track damage zones, as described by Ketcham and others (2013), which at high doses may form complete interconnected damage zones through either the whole grain or relatively damaged portions. If damage density is high enough, these paths may provide a nearby escape route to the majority of He in the grain. While radiation damage plays an undeniably critical role in He diffusional mechanics, this explanation cannot explain the anomalously high diffusivities observed in some low- to moderate-damage zircons (Reiners et al., 2002; 2004). Even in the case of young (~3 Ma) volcanic zircons with very low doses (~ 10^{15} α/g), diffusivity begins relatively high and decreases, rather than beginning low and increasing as predicted (Chapter 2). At this point, further investigation into the diffusional mechanics of natural zircon is required to understand these discrepancies.

1.4.2 Implications for damage annealing

Models that incorporate radiation damage annealing show notable similarities with real data, particularly the effects of annealing at doses $>1 \times 10^{18}$ α/g (Fig. 1.11). Chapter 2 presents the results of 26 cycled step-heating experiments, the majority of which display decreasing diffusivities in a similar but more aggressive manner. Although annealing is not always a straightforward process within zircon (Zhang et al., 2000; Geisler et al., 2001; Nasdala et al., 2004; Chapter 2), these results suggest that cycled step-heating diffusivities may be used as a reasonable proxy for estimating and empirically checking rates of FT annealing, combined with etching and track length measurements in zircons with well constrained thermal histories.

At doses below 1×10^{18} α/g, the predicted effects of decreasing diffusion with increasing damage (Fig. 1.11) are reversed as diffusivities increase with annealing. This behavior is not observed in any published cycled step-heating experiments, although few venture above 600 °C. Furthermore, increases in diffusivity during annealing implies restoration of c-axis crystallinity, a process requiring full epitaxial recrystallization; however, previous annealing experiments on zircon observe that damage zones only yield reduced strain at these temperatures, and that heating ≥1000 °C is required to fully restore crystallinity (Colombo and Chrosch, 1998; Geisler, 2002; Nasdala et al., 2004; Marsellos and Garver, 2010). Because data on annealing within the temperature range of 600 – 1000 °C are sparse, these relationships require further investigation.

1.5 CONCLUSIONS AND RECOMMENDATIONS

Although the lack of apparent similarities between real and modeled data with regard to gas heterogeneities imply that these results should be applied cautiously, some recommendations to researchers wishing to undertake cycled step-heating analyses can be made with confidence:

1. Relatively larger grain sizes are preferable and yield more consistent results. (This is also true of (U-Th)/He dating in general.)
2. Avoid measuring diffusion kinetics using D_f values at very low f. Although model results and real data differ on the expression of low-f anomalies, that both often yield non-linear results in this range suggests avoiding D_f where $f < 0.05 - 0.10$ in calculating diffusion kinetics is advisable. Conversely, although some researchers use several hours (3 – 10) isothermal heating to release this gas before cycled step-heating, observing and measuring non-Arrhenian behaviors during the early stages of gas release ($f > 0.05$) may yield helpful insights into diffusional mechanics.
3. Longer and more comprehensive step-heating experiments which cover a wider range of relative temperatures, and cover a large range of fractional gas releases, will either (a) yield results with lower analytical errors due to more well-defined Arrhenius relationships, *or* (b) show anomalous Arrhenius relationships which yield clues to deepen our understanding of diffusional mechanics, ultimately improving the recovery of robust thermal histories using the (U-Th)/He technique.

Because relationships between diffusional mechanics and radiation damage are often complex in natural minerals, more empirical estimates of diffusion kinetics are imperative to improving the recovery of thermal histories. Although approaches to this problem like ^{4}He/^{3}He may be costly and time-consuming, comparisons between model results and real data suggest that the easier approach of analyzing whole-grain zircon ^{4}He diffusivities may provide accurate diffusion kinetics in spite of concentration heterogeneities. Furthermore, our observation of annealing behaviors in cycled step-heating suggest that this approach may provide a boon to researchers wishing to understand or better parameterize the annealing kinetics of fission tracks or diffusivity-alerting radiation damage as a whole.

Chapter 2: The effects of radiation damage and annealing on helium diffusion from zircon, with implications for zircon (U-Th)/He thermochronology[2]

ABSTRACT

Understanding the effects of radiation damage on He diffusion in minerals allows researchers to recover more robust thermal histories from (U-Th)/He thermochronometry. Many high-damage zircon (U-Th)/He (ZHe) datasets, however, reveal significant discrepancies damage-diffusivity relationships and model predictions. An analysis of the diffusion kinetics of 26 zircons with widely varying damage states provides critical insight into the source of these discrepancies—the model's parameterization of radiation damage annealing—and suggests that simplifying damage and annealing into a single α-dose is insufficient to describe the He diffusion kinetics in zircon. Zircons are sampled from a variety of geological settings: a slow-cooled Archean craton along the Hall Peninsula, Baffin Island, Canada; Neoproterozoic basement rock along the Gulf of Suez rift flank, Egypt; and young, rapidly cooled Grasberg Igneous Complex, New Guinea, Indonesia. Analyses include ^{4}He-only and ^{4}He/^{3}He cycled step-heating experiments on whole, natural zircons to obtain diffusion kinetics; Raman spectroscopy to provide an independent measure of crystallinity; annealing experiments to observe changes in crystallinity over the temperature-time (Tt) conditions of step-heating; and trace element analyses to examine the effects of parent nuclide zonation on heterogeneous ^{4}He diffusion rates. A majority of these experiments have yielded a new behavior: a thermally-activated, continuous decrease in expected diffusivities

---

[2] Goldsmith, A.S., Stockli, D.F., Ketcham, R.A. (in review). *The effects of radiation damage and annealing on helium diffusion from zircon, with implicatios for zircon (U-Th)/He thermochronology*. Geochimica et Cosmochimica Acta. D. Stockli helped procure samples from Apache and CNGO, as well as funding and machine time. D. Stockli and R. Ketcham provided critical guidance and key insights through several phases of major revisions and reinterpretations, and extensive discussions. Both also contributed significantly to the overall structure of the paper.

over the course of cycled step-heating analyses, termed ‘rollover’, which we interpret to be low-temperature annealing. This ‘relaxation’ annealing has been observed to reduce inter-atomic stresses in damage zones, and is distinct from epitaxial recrystallization. This distinction raises three major issues with the current forward model: first, rollover occurs at lower doses and Tt conditions than model predictions at high doses; second, diffusivity is predicted to increase with annealing at lower damage states, a behavior which is not observed in our experiments; third, the model’s high damage-diffusivity relationship were based on Sri Lankan zircons which have experienced significant geological low-temperature annealing. Lastly, when interpreted in the context of 1D spherical finite-difference modeling, these results call into question fundamental assumptions about the mechanisms of ^{4}He diffusion and the effects of heterogeneous ^{4}He diffusion. These insights will be critical in the development of a more robust and accurate ZHe thermochronology.

2.1 INTRODUCTION

Zircon ($ZrSiO_4$) is one of the most commonly used minerals in geo- and thermochronology, due to high concentrations of U and Th (up to 10^4 ppm), low initial Pb content, presence as a trace mineral in a variety of crustal rocks, and resistance to chemical and physical weathering. The high preservation potential means that some zircons experience radiation doses which damage the internal crystal structure over geologic time (up to billions of years), although they maintain macro-scale structural and chemical integrity even after a total loss of crystallinity (Woodhead et al., 1991a; Zhang et al., 2000a; Capitani et al., 2000; Nasdala et al., 2001, 2004; Ewing et al., 2003). Today, the accumulation of radiogenic ^{4}He within zircon and its thermally activated volume diffusion forms the basis of zircon (U-Th)/He (or ZHe) thermochronology, however, the effects of radiation damage on the retention of radiogenic ^{4}He has long been of interest to researchers (e.g. Strutt, 1908; Hurley, 1952) and remains an active topic of research in zircon and other minerals

(Flowers et al., 2009; Gautheron et al., 2009; Guenthner et al., 2013; Anderson et al., 2017; Baughman et al., 2017; Danišík et al., 2017; Willett et al., 2017).

In (U-Th)/He thermochronology, a quantitative understanding of He diffusion kinetics combined with ages from a range of different grain geometries, taken from different geographical locations, enables researchers to produce cooling ages and interpret thermal histories (Dunai, 2005; Ketcham, 2005; Stockli, 2005). Cooling ages correspond to a host rock cooling below a closure temperatures (T_C), or the temperature below which bulk ^{4}He is retained within the grain—T_C is a function of diffusion kinetics, grain size and cooling rate (Dodson, 1973). Interpreting samples with consistent and reproducible cooling ages is relatively straightforward; (U-Th)/He datasets of slowly-cooled samples, in contrast, may yield systematic age variations up to hundreds of millions of years from a single host rock (e.g. Flowers et al., 2009; Guenthner et al., 2013; Chapter 3). In zircon (U-Th)/He (ZHe) thermochronology, this age dispersion manifests as decreasing cooling ages with increasing effective U (eU = [U] + 0.232[Th]; here used as a proxy for radiation damage) (Fig 2.1 A,B). In some young zircons with low radiation doses, age-eU correlations positive, similar to the apatite (U-Th)/He system (e.g., Flowers et al., 2009; Guenthner et al., 2013). An understanding of the relationship between damage and diffusion kinetics allow researchers to recover more robust, continuous thermal histories from over-dispersed ages (Chapter 3). A recent forward model for the ZHe system, ZRDAAM (Zircon Radiation Damage Accumulation and Annealing Model; Guenthner et al., 2013), attempted to quantify the relationship between He diffusion, radiation damage accumulation and annealing. The model integrates two sets of zircon He diffusion kinetics, representing diffusivities of crystalline and metamict zircon, and is based on the parameterization of the effects of radiation damage on tortuosity (Guenthner et al., 2013; Ketcham et al., 2013). While the ZRDAAM model represents a valuable initial implementation, multiple studies have noted significant discrepancies between model predictions and geologically feasible thermal histories, or that populations of zircons require impossibly large radiation doses to produce model results (e.g., Pik et al., 2016; Powell et al., 2016; Anderson et al., 2017). These discrepancies suggest fundamental inadequacies in the current understanding of radiation damage and its impact on He diffusion, likely leading to the recovery of geologically unreasonable and inaccurate thermal histories in some cases (Chapter 3).

The goal of this work is to understand the relationship between He diffusion and radiation damage more closely, with the goal of allowing researchers to leverage better thermal histories from by over-dispersed ages (e.g. Flowers et al., 2009). The complexities of this relationship requires a multifaceted approach including: (1) cycled step-heating experiments to obtain empirical estimates of diffusion kinetics; (2) Raman spectroscopic measurements to obtain an independent assessment of radiation damage; (3) annealing experiments based on Raman spectroscopy to observe changes to crystallinity at the Tt conditions of step-heating experiments; (4) trace element analyses to assess the degree and effects of parent nuclide zonation on apparent diffusivities (a heterogeneous diffusant may affect diffusion kinetics estimates; McDougall and Harrison, 1999, Chapter 1); and (5) proton-irradiation to compare ^{4}He diffusion to a homogeneous reference concentration of ^{3}He and to obtain more accurate diffusion kinetics. These data are also interpreted in the context of Chapter 1, which utilizes a 1D spherical finite difference model to predict the effects of U, Th, and He heterogeneities, alpha ejection, rounding, and radiation damage on measured diffusion kinetics from imperfect (non-homogeneous He concentration) samples.

2.1 RADIATION DAMAGE AND ANNEALING

A central concept to radiation damage in zircon is that of *metamictization*, or the total destruction/amorphization of the crystal lattice (Woodhead, Rossman, and Silver, 1991; Salje et al., 1999). Beyond this threshold in zircon—posited to be linked to a percolation transition and estimated to occur in the range of 10^{18}-10^{19} α/g (Murakami et al., 1991; Salje et al., 1999; Geisler et al., 2003; Ketcham et al., 2013)—studies document an inflection in macroscopic swelling, reduction in bulk density, and changes in both X-ray diffraction patterns and Raman spectra (Holland and Gottfried, 1955; Murakami et al., 1991; Nasdala et al., 1995; Salje et al., 1999; Nasdala et al., 2001; Ewing et al., 2003). Some studies have also observed anomalously high concentrations in Ca, Fe, or OH in zircon exceeding a particular dose threshold (Woodhead et al., 1991b; Geisler et al., 2001b, 2003). The threshold dose for metamictization in zircon has been considered equivalent to the α-recoil damage percolation threshold, estimated at 2-4 × 10^{18} α-decays/g, beyond which damage zones form an interconnected network through the whole grain (Holland and Gottfried, 1955; Murakami et al., 1991; Salje et al., 1999; Zhang et al., 2000c; Nasdala et al., 2004). However, geometrical modeling by Ketcham and others (2013) suggested that a more realistic α-dose percolation threshold may only be as low as 2.5 - 3.1 × 10^{16} α/g, whereas the percolation of fission tracks occurs at an equivalent α-dose of ~1.9 × 10^{18} α/g.

Understanding the loss of crystallinity in zircon due to radioactive decay is relatively straightforward relative to understanding its recovery or annealing. While the annealing kinetics of fission tracks comprise a unique and independent low-temperature thermochronometer (ZFT), fission tracks are thought to be affected by α-recoil damage density (Marsellos and Garver, 2010 and references therein). Attempts to understand this effect on fission track annealing have so far been qualitatively insightful, but challenging to quantify (Tagami, 2005; Bernet and Garver, 2005; Marsellos and Garver, 2010). Furthermore, a number of studies have documented that annealing proceeds differently for partially and completely metamict grains and with different stages of recovery at different Tt conditions. For example, in partially metamict zircon, results have shown that low-temperature annealing yields recovery of short-range atomic order and removal of point defects, whereas full epitaxial recrystallization requires significantly higher temperatures (Colombo and Chrosch, 1998; Colombo et al., 1999; Zhang et al., 2000b; Capitani et al., 2000; Geisler et al., 2001a; Geisler, 2002; Geisler and Pidgeon, 2002). X-ray diffraction studies have demonstrated that recovery of crystallinity along the zircon *c*-axis—which acts as a crystallographic He fast-diffusion pathway in zircon (Farley, 2007; Reich et al., 2007; Cherniak et al., 2009; Guenthner et al., 2013)—requires much higher temperatures than recovery along the basal plane (Colombo and Chrosch, 1998a; Colombo et al., 1999). In severely damaged zircon (~10^{19} α/g), annealing involves the relaxation of strain, followed by formation of randomly oriented crystallites of zircon, ZrO_2 and silica glass at higher temperatures (Capitani et al., 2000; Váczi et al., 2009; Geisler and Pidgeon, 2002; Colombo et al., 1999). Furthermore, numerous Raman studies found that spectra do not revert to 'original' pristine crystalline values after heating and annealing, but rather form unique trends with respect to both peak shift and width (Geisler et al., 2001b; Nasdala et al., 2001; Geisler et al., 2001a; Marsellos and Garver, 2010).

In summation, these findings demonstrate that what is called 'annealing' in zircon is not a full reversal of damage, but a complex multi-phase damage-variable process that leaves the crystal lattice in a semi-crystalline state that is impossible to produce by only the accumulation of radiation damage. For the remainder of this text, we use the term 'annealing' to describe a process which relaxes crystalline stresses caused by radiation damage, and 'recrystallization' to describe the (re)formation of crystalline $ZrSiO_4$ within a zircon (Nasdala et al., 2004).

2.3 CASE STUDIES

This study examines the relationship between diffusion of helium from zircon and radiation damage from three geologically distinct localities. The three case studies investigate high-damage (10^{17}-10^{19} α/g) zircons from Precambrian orthogneiss basement rocks of the Hall Peninsula, Baffin Island, Nunavut, Canada, late Neoproterozoic granite from the western coast of the Sinai Peninsula along the Gulf of Suez, Egypt, and a very young Pleistocene granite from western Papua New Guinea, Indonesia. ZHe ages from these regions show a clear negative age-eU correlation, consistent with the expected effects of high radiation doses (Guenthner et al., 2013 and references therein). Granites and orthogneisses were chosen for this study as all zircons will have identical thermal histories and ages should only vary as a function of grain kinetics, in contrast to detrital zircons from sedimentary strata in which multiple source terrains yield a range of inherited crystallization and cooling ages and radiation doses (Guenthner et al., 2015). Zircons from Pleistocene granite from western Papua New Guinea were chosen to constrain the He in very low-damage (10^{15} α/g) zircon. Table 2.1 provides basic sample information such as grain size, relevant concentrations, ZHe ages, and estimated radiation doses.

2.3.1 Hall Peninsula

This study presents data from 18 zircons from the Hall Peninsula of Baffin Island, Nunavut, Canada. Rock samples were collected by the Canada Nunavut Geoscience Office (CNGO), during the 2012 Hall Peninsula Integrated Geoscience Project, from transects intended to characterize the long-term exhumation history of the Hall Peninsula (Creason, 2015). ZHe ages are shown as a function of eU on Figure 2.1A, with location and lithology are provided in Figure 2.2.

These rocks are part of an Archaean tonalite-orthogneiss complex (Scott, 1996), dated by zircon laser ablation ICP-MS U-Pb and Pb-Pb geochronology at 2.9-2.8 Ga (Scott, 1999) and were metamorphosed during the Trans-Hudson orogeny (~2.0 - 1.8 Ga; St-Onge et al., 2009 and references therein). K/Ar ages range from ~1.7 – 1.6 Ga and suggest that the Archean rocks experienced either very slowly cooling or reheating, but likely remained at temperatures >420°C for 140 myr after peak metamorphism at ~1.8 Ga (Skipton and St-Onge, 2013; Skipton et al., 2015). Although few constraints exist for the post 1.8 Ga thermal history of the rock on Hall Peninsula, Zhang and Pell (2014) used Ordovician conodonts recovered from limestone xenoliths in kimberlite to estimate max. Jurassic burial depths of 270–305 m. Apatite fission track (AFT)

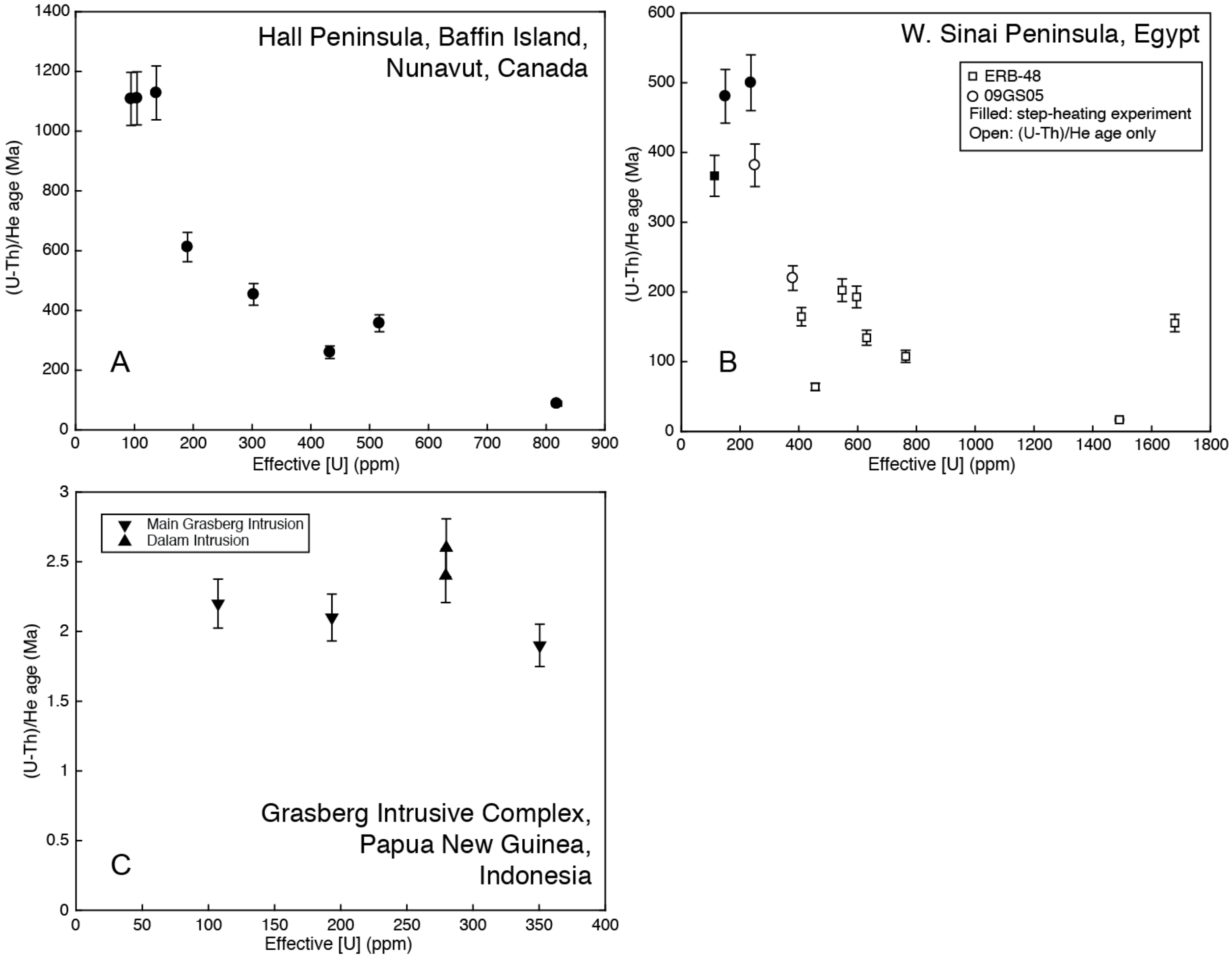

Figure 2.1 Zircon (U-Th)/He ages for the samples in this study. Additional ages from zircons not analyzed by step-heating (white) have been included for the Sinai Peninsula zircons to highlight the strong negative age-eU trend observed in both sample sets (Chapter 3). This correlation is typical for high-damage zircon (Guenthner et al., 2013 and references therein). Low damage, rapidly-cooled zircons from the Grasberg Intrusive Complex (bottom) lack an age-eU correlation, but provide an opportunity to study very low-damage (~10^{15} α/g) zircon.

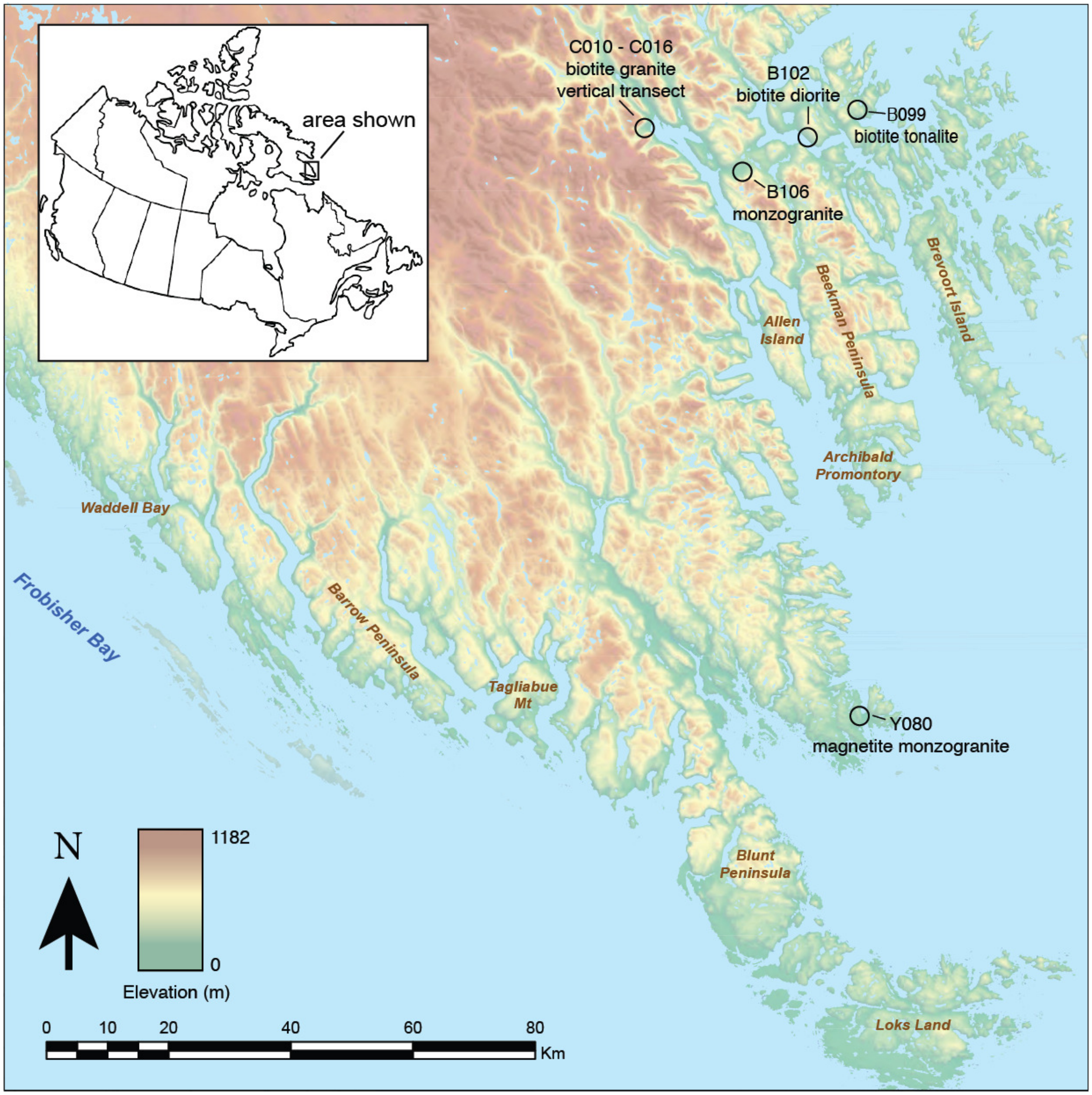

Figure 2.2 A topographic map of the Hall Peninsula of Baffin Island, Nunavut, Canada (inset), with sample names, locations, and lithologies. Samples C013 and C015 are from a vertical transect. Modified from Creason, 2015.

Table 2.1 Ages and aliquot information for zircons analyzed for diffusion kinetics in this study. Doses in intalics are estimated maximums: for Hall Peninsula zircons, doses are based on total damage retention since the youngest K/Ar age of 1610 Ma (Skipton et al., 2015, and references therein). Sinai Peninsula zircon doses are estimated using the U-Pb age of 610 Ma.

Aliquot	Locale	Experiment Type	^{4}He (ncc)	U (ppm)	Th (ppm)	ESR (um)	(U-Th)/He age (Ma)	Dose (α/g)	FWHM (cm-1)	+/-	v3 peak shift (cm-1)	+/-
09GS05-3	Sinai Peninsula	^{4}He only	14.3	105.6	113.2	39.9	366	*2.82E+17*	6.6	0.8	1004.9	0.1
ERB-48-1	Sinai Peninsula	^{4}He only	286.8	237.2	58.7	76.9	500	*5.38E+17*	10.8	0.4	1000.4	0.7
ERB-48-2	Sinai Peninsula	^{4}He only	660.7	131.1	83.0	125.7	480	*3.22E+17*	8.7	0.9	1002.7	0.6
B099-7	Hall Peninsula	^{4}He only	935.6	N/A	N/A	101.4	N/A		5.9	2.2	1003.6	0.7
B099-11	Hall Peninsula	^{4}He only	416.5	N/A	N/A	102.0	N/A		no peak		no peak	
C013-11	Hall Peninsula	^{4}He only	162.6	91.2	56.9	80.9	1110	*6.38E+17*	7.2	1.2	1001.8	1.2
C015-14	Hall Peninsula	^{4}He only	193.3	85.4	38.2	108.5	1108	*5.78E+17*	8.8	1.0	1000.7	0.8
C015-20	Hall Peninsula	^{4}He only	1142.5	499.9	72.2	106.2	357	*3.19E+18*	12.8	1.6	992.6	1.6
C015-21	Hall Peninsula	^{4}He only	756.2	285.6	74.6	99.3	454	*1.87E+18*	11.0	1.9	995.5	2.2
C015-24	Hall Peninsula	^{4}He only	441.4	789.6	124.2	108.3	88	*5.05E+18*	11.8	1.4	994.1	1.9
C015-27	Hall Peninsula	^{4}He only	499.7	182.8	32.1	94.1	612	*1.17E+18*	9.4	1.6	993.1	2.2
C015-28	Hall Peninsula	^{4}He only	539.4	421.0	49.9	96.8	260	*2.67E+18*	10.7	2.1	992.7	2.3
Y080-1	Hall Peninsula	^{4}He/^{3}He	215.4	487.2	10.3	93.6	120	3.03E+18	N/A		N/A	
Y080-2	Hall Peninsula	^{4}He/^{3}He	578.5	578.5	6.5	114.0	713	6.47E+17	N/A		N/A	
B106-1	Hall Peninsula	^{4}He/^{3}He	1176.5	756.9	253.8	132.0	125	5.02E+18	N/A		N/A	
B106-2	Hall Peninsula	^{4}He/^{3}He	449.4	800.8	302.2	115.8	70	5.35E+18	N/A		N/A	
B106-3	Hall Peninsula	^{4}He/^{3}He	112.5	1682.8	431.2	127.2	6.4	1.10E+19	N/A		N/A	
B106-6	Hall Peninsula	^{4}He/^{3}He	351.7	695.1	126.8	89.1	130	4.29E+18	N/A		N/A	
C015-2	Hall Peninsula	^{4}He/^{3}He	982.8	320.7	154.1	113.2	369	2.19E+18	N/A		N/A	
C015-3	Hall Peninsula	^{4}He/^{3}He	430.1	81.6	42.3	93.4	973	5.60E+17	N/A		N/A	
C015-4	Hall Peninsula	^{4}He/^{3}He	526.4	610.8	439.7	83.0	277	4.35E+18	N/A		N/A	
MGI-1	Grasberg Intrusive Complex	^{4}He only	18.9	313.2	162.2	151.2	1.9	3.65E+15	N/A		N/A	
MGI-2	Grasberg Intrusive Complex	^{4}He only	6.2	172.4	91.2	126.5	2.1	2.01E+15	N/A		N/A	
MGI-3	Grasberg Intrusive Complex	^{4}He only	2.0	98.7	37.6	105.6	2.2	1.12E+15	N/A		N/A	
Dalam-1	Grasberg Intrusive Complex	^{4}He only	5.8	245.9	145.8	102.0	2.4	3.00E+15	N/A		N/A	
Dalam-2	Grasberg Intrusive Complex	^{4}He only	5.7	244.8	152.3	103.2	2.6	3.01E+15	N/A		N/A	

analyses from farther north, at 66-68°N along the eastern coast, yielded ages ranging from 200-440 Ma that have been interpreted to reflect a history of slow exhumation from variable topography and paleotemperatures (McGregor et al., 2013). For a more thorough description of these samples and their geologic context, the reader is directed to (Creason, 2015).

2.3.2 Sinai Peninsula

The study utilizes three zircons from two samples of undeformed late Pan-African granitic basement rock from the western Sinai Peninsula. Granite samples were taken from surface outcrops at Gebel Samra (09GS05) and an industry borehole near Gebel Samra (ERB-48 from the ERB-B-2X borehole, courtesy of Apache Egypt) along the central eastern margin of the Gulf of Suez (Fig. 2.3). These undeformed granitic samples are likely from the same pluton, offset by faulting. Ages are shown as a function of eU in Figure 2.1B.

The Phanerozoic structural and sedimentary history of the Gulf of Suez has been extensively studied and documented in light of >100 years of hydrocarbon exploration motivated academic and industry research (e.g., Bosworth and McClay, 2001; Bosworth et al., 2005). The regional basement rock consists of orthogneisses, metavolcanics and metasedimentary rocks, granites, and granodiorites formed and variably metamorphosed during the East African orogeny (700-570 Ma) (Bosworth et al., 2005). Zircon U-Pb LA-ICP-MS data from the two samples used in this study both yielded an intrusion age of 610 Ma (Stockli, own unpublished data). After emplacement, these rocks were rapidly exhumed to the surface as they are overlain by lower Paleozoic strata. Subsequently they), with post-tectonic dikes yielding Rb-Sr ages of 591 ± 9 Ma (Stern and Manton, 1987). These rocks also experienced several low-temperature events, including Hercynian tectonism during the Late Devonian-Early Carboniferous (e.g. Frizon de Lamotte et al., 2013), Neo-Tethyan rifting in the early Mesozoic (Bosworth and McClay, 2001), and Santonian

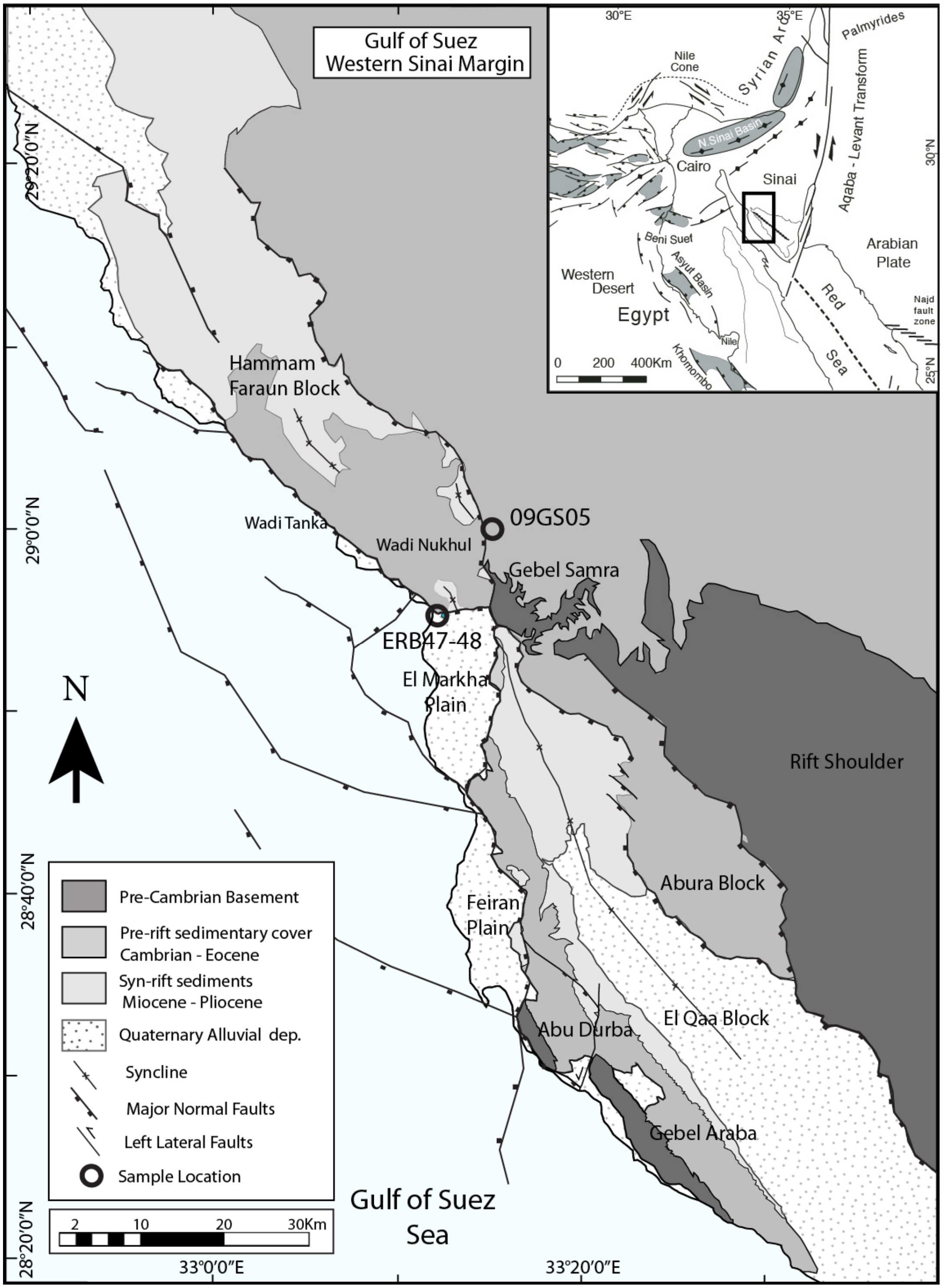
Gulf of Suez
Western Sinai Margin
30°E
35°E
Palmyrides
Syrian Arc
Nile Cone
N.Sinai Basin
Cairo
30°N
Sinai
Aqaba - Levant Transform
Beni Suef
Asyut Basin
Western Desert
Egypt
Arabian Plate
Red Sea
Najd fault zone
Nile
Khomombo
0 200 400Km
25°N
29°20'0"N
Hammam Faraun Block
09GS05
Wadi Tanka
Wadi Nukhul
29°0'0"N
Gebel Samra
ERB47-48
El Markha Plain
N
Rift Shoulder
28°40'0"N
Abura Block
Feiran Plain
Pre-Cambrian Basement
Pre-rift sedimentary cover Cambrian - Eocene
Syn-rift sediments Miocene - Pliocene
Quaternary Alluvial dep.
Syncline
Major Normal Faults
Left Lateral Faults
Sample Location
Abu Durba
El Qaa Block
Gebel Araba
Gulf of Suez Sea
28°20'0"N
2 10 20 30Km
33°0'0"E
33°20'0"E

Figure 2.3

Figure 2.3 A geologic map of the Sinai Peninsula, Egypt, showing sample locations and associated formations. Samples ERB47-48 are regional basement samples from the ERB-B-2X borehole, taken from ~1621 m depth. Sample 09GS05 is a surface sample, presumably from the same granite.

inversion (Guiraud and Bosworth, 1997; Guiraud, 1998; Bosworth and McClay, 2001; Bosworth et al., 2005). The current tectonic architecture is the result of latest Oligocene to middle Miocene magma-poor continental rifting in the Gulf of Suez as part of the Red Sea rift between the African and Arabian plates (Bosworth et al., 2015; Bosworth and Stockli, 2016). Rift flank exhumation initiated at ~23 Ma and ceased by 14 Ma (Kohn et al., 1993; Omar and Steckler, 1995; Omar et al., 1989; Bosworth and McClay, 2001; Bojar et al., 2002; Bosworth et al., 2005). For a more thorough description of these samples and their geologic context, the reader is directed to Pujols (2011).

2.3.3 Grasberg Igneous Complex

In order to study the diffusion kinetics of low-damage zircon, five zircon grains were selected from the very young and rapidly-cooled Grasberg Igneous Complex (GIC), located on the island of New Guinea, Indonesia, composed of the Main Grasberg Intrusion (MGI) and the slightly older Dalam intrusion (Fig. 2.4). Samples are from the tops of two boreholes (0 m depth). ZHe ages are presented against eU in Figure 2.1C.

Magmatism in this region arose from decompression melting of asthenospheric mantle, due to the breakoff of the oceanic portion of the Australian plate (Cloos et al., 2005). Although the geometry and structure of the regional intrusive bodies have been extensively investigated as they host world-class Au and Cu deposits (Cloos, 1997; Leys et al., 2012), the timing of magmatism and cooling has only been recently characterized in detail (Wafforn, 2017). Wafforn (2017) determined the larger Dalam body to be a multi-phase intrusion emplaced from 3.6-3.3 Ma and with the MGI following at 3.2 Ma (zircon U-Pb). ZHe cooling ages are indistinguishable from U-Pb ages, with apatite (U-Th)/He (AHe) ages being slightly younger (2.9 – 2.1 Ma). These results illustrate rapid cooling from post-magmatic to ambient temperatures (Wafforn, 2017).

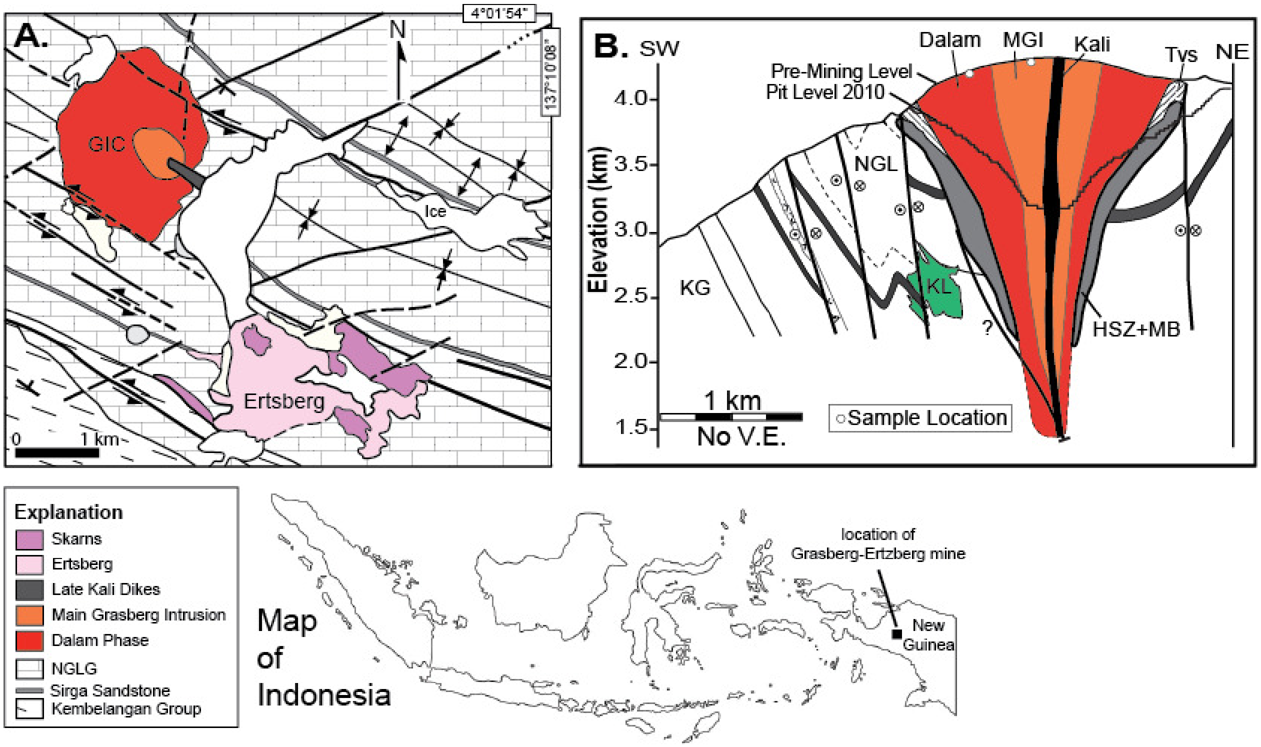

Figure 2.4 Modified from Wafforn (2017). (A) A simplified geologic map of the Grasberg-Ertsberg mining district on the island of New Guinea (below). (B) A schematic cross section showing sample locations within the Main Grasberg Intrusion (MGI) and the surrounding Dalam intrusion. Samples are taken from the tops of boreholes.

2.4 METHODOLOGY

2.4.1 Raman Spectroscopy

Raman spectroscopy has been used extensively to characterize the degree of crystalline disorder in zircon—the primary source of which is radiation damage—by measuring changes in the ν3 anti-symmetric SiO_4 stretching peak shift ('peak shift' is the center of the peak in wavenumber, cm^{-1}) and full-width at half-maximum (FWHM). With increasing crystalline disorder, the ν3 peak shift decreases and the FWHM increases (Fig. 2.5; Nasdala et al., 1995, 2001; Palenik et al., 2003; Nasdala et al., 2004; Marsellos and Garver, 2010). For this study, Raman spectroscopy provides an independent assessment of damage in the older and high-dose Hall and Sinai Peninsula zircons, for which radiation dose calculations are best estimates. Because accurate doses for Grasberg zircons can be calculated easily in light of tight constraints on the thermal history—and because other results suggest that U concentration, not radiation damage, is the primary factor in shaping Raman spectra at low doses (Marsellos and Garver, 2010)—this technique was not applied to GIC zircons.

Raman spectral measurements were carried out at the Mineral Physics Laboratory at the University of Texas at Austin, using an Andor Solis spectrometer with 1800 grooves/mm with a laser wavelength of 532 nm and a square spot size of ~30 μm. Reported measurements of ν3 peak shift and FWHM are the mean of three or more 5-10 sec collection periods from random locations on the zircon's prism crystal faces, with uncertainties reported as 1σ. The peak shift and FWHM of the ν3 peak were calculated using the program *fityk* (Wojdyr, 2010) using a mixed Lorentzian-Gaussian peak fitting routing after manual baseline subtraction for the 800 to 1200 cm^{-1} region to minimize fluorescence effects or background noise. FWHM peaks were corrected for the system's spectral resolution of 1.5 cm^{-1} following Nasdala and others (2001 and references therein).

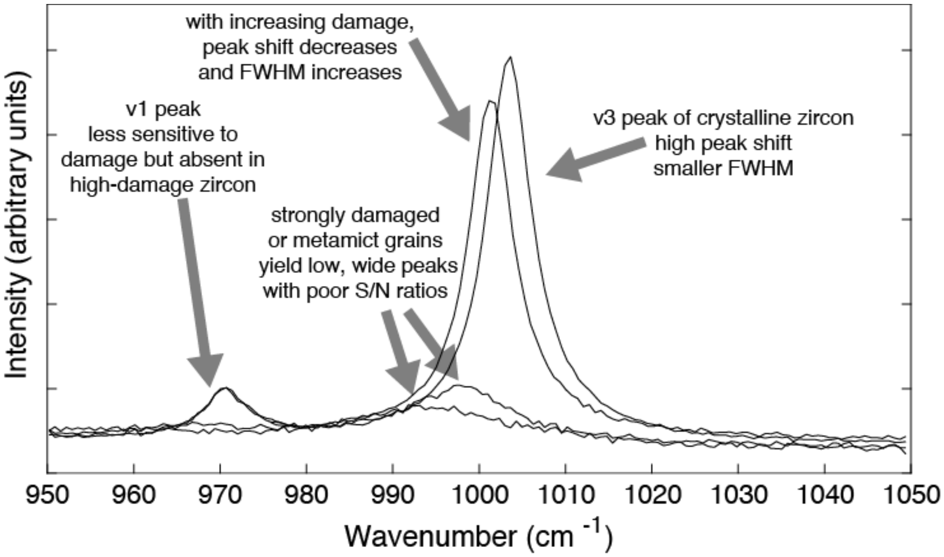

Figure 2.5 Example Raman spectra from this study. Most notable are the strong v3 peaks for low-to-moderately damaged zircon, with a relatively high peak shift (wavenumber at peak center) and lower FWHM than those spectra representing high damage, which are relatively shorter, wider, and noisier, with lower peak shifts. This plot also shows spectra for v1, which is less sensitive to atomic disorder but not present in high-damage samples.

2.4.2 Trace element laser ablation ICP-MS

U and Th concentrations in natural zircon are commonly non-uniform and display concentric, sector, or complex zonation, resulting in both spatially heterogeneous ^{4}He ingrowth and radiation damage. In addition to causing variations in diffusion kinetics and retentivity, these spatial parent nuclide heterogeneities also affect the alpha ejection correction, thermochronometric age, and the resulting thermal histories (Hourigan et al., 2005; Farley et al., 2011; Ault and Flowers, 2012; Guenthner et al., 2013; Anderson et al., 2017; Danišík et al., 2017). Several studies have employed laser ablation ICP-MS depth-profiling or imaging of internal surfaces to resolve either 1D or 2D parent nuclide distributions (Ault and Flowers, 2012; Smye and Stockli, 2014; Danišík et al., 2017; Anderson et al., 2017). In order to assess the possible effects on parent nuclide zonation on apparent diffusion kinetics, zircons from Hall Peninsula were LA-ICP-MS depth profiled prior to diffusion experiments using methodology described by Marsh and Stockli (2015). Bulk. These data were later combined with whole-grain average U and Th concentrations to access grain-scale heterogeneity.

Depth-profile trace element LA-ICP-MS analyses were performed on unpolished whole zircon grains mounted parallel to the c-axis on double-sided tape using an Analyte.G2 193 nm ArF excimer laser in a large format HELEX cell with <0.3s washout time (Smye and Stockli, 2014). The ablated dry aerosol was analyzed using a ThermoFisher Element 2 single-collector magnetic sector ICP-MS to determine concentrations of U, Th, and other trace elements with a down-hole resolution of <1 µm. Ablation pits were 30 µm in diameter and ~18-25 µm in depth and were ablated at a rate of ~0.6 µm/s. LA-ICP-MS trace element for samples B099-7, C013-11, C013-13, and C015-14 were calibrated using NIST612 glass and for all other samples using GJ-1 zircon standard (Jackson et al., 2004). While multi-year analyses of GJ-1 zircon at the UTChron Laboratory utilizing NIST612 glass have shown variations of up to 60 ppm in U and Th spatially within GJ-1, this variation only affects the absolute, but not the relative 1D U and Th concentration depth profiles. However, down-hole U and Th concentrations calibrated using GJ-1 were labeled as “approximate concentration”. In some cases, multiple LA-ICP-MS measurements were carried out on the same zircon grain to examine the first-order consistency of zonation patterns.

2.4.3 Step-heating experiments and (U-Th)/He analyses

The evolution of diffusivity of a noble gas within a crystalline solid as a function of temperature is an Arrhenius function:

$$D = D_0 e^{-E_A/RT}$$

where D is diffusivity, D_0 is the pre-exponential ‘frequency’ factor, E_A is activation energy, R is the gas constant, and T is absolute temperature. The variables D_0, a, and E_A collectively describe the kinetics of diffusion. D_0 and can be determined E_A and are measured empirically by cycled step-heating experiments. A sample is exposed to an array of heating steps and the released gas volume is measured by mass spectrometry, from which diffusivities (D_f) at each step are estimated. Ideally, the gas release is controlled by single-site volume diffusion, with the resulting data array forming a linear trend from which E_A and D_0 can be calculated from the slope and intercept, respectively, and from which diffusivity may be extrapolated from laboratory to geologic temperatures and timescales, and to other diffusion domain sizes. Using fractional losses to estimate diffusivities from ^{4}He may be problematic, as equations assume a homogeneous concentration while natural ^{4}He concentrations are always heterogeneous. In Chapter 1, we use a 1D spherical diffusion model to assess the effects of these heterogeneities on diffusivity estimates.

^{4}He-only step-heating experiments

Zircons were selected for ^{4}He step-heating analyses on the basis of gain size, quality, lack of U and Th zonation inferred from LA-ICP-MS profile, and degree of radiation damage as quantified by Raman spectroscopy. Single grains were placed in Pt foil tubes, wrapped in larger Cu foil envelopes, and folded around a K-type thermocouple. Samples were heated in-vacuo for ^{4}He step-heating analyses using a halogen-bulb light furnace (Farley et al., 1999), consisting of an ELH-type halogen bulb atop a stainless-steel cell with a sapphire window under ultra-high vacuum (<1E-9 torr). Common temperature standard deviations over most heating steps were <1°C. The liberated ^{4}He released was spiked with ^{3}He, cryogenically purified/concentrated, and measured by isotope dilution using a Balzers Prisma 200 quadrupole mass spectrometer. Heating schedules were adjusted on the basis of grain size and Raman-estimated damage to optimize He gas yields per step. After step-heating experiments, zircon crystals were retrieved for total gas extraction by diode laser heating to ~1300°C and noble gas He analysis to ensure >99% He recovery from each zircon grain.

^{4}He/^{3}He step-heating experiments

Using fractional losses of a heterogeneously distributed diffusant might be problematic to estimating diffusion kinetics (Chapter 1; McDougall and Harrison, 1999; Fechtig and Kalbitzer, 1966). This problem can be alleviated through the creation of a homogeneous reference diffusant by proton irradiation, inducing small amounts of spallogenic ^{3}He *in situ* within the crystal lattice (e.g. Shuster and Farley, 2005). Diffusivities from homogeneously distributed ^{3}He are ideal for direct comparisons with ^{4}He-based diffusion data. Zircon grains from a subset of the Hall Peninsula samples were proton irradiated at Harvard Medical Center at 230 MeV, and selected by size and crystal quality. Samples were heated in-vacuo using a PhotonMachine 75W diode laser and the released ^{4}He and ^{3}He were cryogenically purified and measured using a ThermoFisher Helix SFT high-resolution magnetic sector split flight tube mass spectrometer with a mass resolution of >700. ^{4}He and ^{3}He concentrations were calibrated against a manometrically-calibrated ^{4}He/^{3}He standard. In these experiments, heating schedules started at higher temperatures

(400°C) and decreased heating-step temperatures (retrograde heating), rather than increasing temperatures (prograde heating) as was done in most ^{4}He-only experiments.

2.4.4 (U-Th)/He ages

After step-heating analysis, all zircons were subjected to (U-Th)/He analytical techniques following the procedures described by Wolfe and Stockli (2010). All remaining He was extracted by diode laser heating at ~1300°C at least 2 times to ensure >99% cumulative He release . After total degassing, zircon grains were dissolved in high-pressure digestion vessels with an isotopically enriched ^{235}U, ^{230}Th, and ^{149}Sm spike. U and Th concentrations were determined by isotope dilution using a ThermoFisher Element2 single-collector magnetic sector ICP-MS with the help of gravimetric standard solution. Uncertainties on U and Th concentrations are <1%.

2.4.5 Annealing experiments

We performed annealing experiments monitored by Raman spectroscopy to quantify possible changes in zircon crystallinity that might occur during prograde step-heating in diffusion experiments. Zircons selected were from Hall Peninsula samples featured in this study, and similar samples with the same negative age-eU correlations (Chapter 3). Fish Canyon Tuff zircons were also analyzed as a low-damage reference material (Reiners et al., 2004). All grains were analyzed by Raman spectroscopy at the University of Texas Mineral Physics laboratory before and after trace element analysis. Analysis spots were arbitrarily chosen on the same prism-face surface as trace element analyses, at least 15 µm away from laser ablation pits to avoid potential perturbations. Each measurement presented is an average of nine ten-second collection periods over a 30 µm square spot size using a 532 nm laser. After initial, pre-heating Raman measurements, zircon grains were inserted into a Pt foil packets and step-heated using a halogen bulb furnace analogous to ^{4}He-only step-heating experiments between 400°C and 600°C. Zircons in experiment

5 underwent an additional phase of heating by diode laser at 700°C for one hour analogous to ^{4}He/^{3}He experiments. After each phase of heating, zircons were unpacked and re-analyzed in the same spot to observe changes in ν3 peak shift and shape.

2.5 RESULTS

2.5.1 Step-heating experiments

Step-heating times and temperatures, fractional and absolute losses, and estimated diffusivities are provided in Table 2.2 for ^{4}He experiments, with diffusion kinetics and closure temperatures calculated from linear ($R \geq 0.995$) Arrhenius regressions (below) are in Table 2.3. The steps and regressions chosen to best approximate the initial, undisturbed diffusion kinetics (T_C, E_A, and $\ln(D_0/a^2)$) of each experiment, denoted D_{init}, are bolded. Similar data and results for ^{4}He/^{3}He experiments are provided in Tables 2.4 and 2.5; D_{init} is the first regression in all cases. All uncertainties for step-heating results are analytical or propagated from analytical uncertainties, with regressions calculated using a York II regression (York and others, 2004).

In Chapter 1, we produce a series of 'best practices' recommendations for step-heating experiment design, one of which is that low gas releases should be avoided when calculating diffusion kinetics from results. Diffusivities calculated from initial heating steps often show anomalous Arrhenius relationships, both in modeling and in empirical studies, which in turn yield anomalous diffusion kinetics when fitted (Chapter 1, and references therein). Readers may notice, however, that we have failed to take our own advice on this point, often including the first steps of the experiment in D_{init}. This is because our Arrhenius relationships are somewhat opposite of 'typical' results regarding such anomalies: they appear linear at low gas releases, but yield changing diffusion kinetics at higher releases which obscure measurement of the 'initial' kinetics. Changes in diffusion kinetics beyond the initial heating steps are discussed at length in this

Table 2.2 Step heating times, temperatures, and He releases from ^{4}He-only experiments. Bold steps are those used to calculate D_{init}. Italicized data are excluded from regressions, either due to halogen bulb instabilities (high temperature errors), or ^{4}He measured at/below blank levels.

Aliquot 09GS05-3

Location Sinai Peninsula

Step #	**Time (min)**	**Average T (°C)**	**±**	**He (ncc)**	**±**	**f**	**ln(D/a^2)**	**±**
1	60	400	1.5	0.091	0.0014	0.006	-20.73	2.089
2	61	400	1.5	0.033	0.0013	0.009	-20.88	2.908
3	120	400	1.5	0.048	0.0014	0.012	-20.88	2.185
4	121	400	1.5	0.037	0.0013	0.015	-20.89	2.190
5	240	400	1.5	0.057	0.0017	0.019	-20.92	1.717
6	241	400	1.5	0.046	0.0013	0.022	-20.94	1.743
7	361	400	1.5	0.059	0.0014	0.026	-20.94	1.362
8	361	400	1.5	0.050	0.0014	0.030	-20.94	1.390
9	481	400	1.5	0.056	0.0015	0.033	-20.98	1.234
10	**241**	**420**	**1.5**	**0.061**	**0.0014**	**0.038**	**-20.09**	**1.118**
11	**121**	**430**	**1.5**	**0.043**	**0.0012**	**0.041**	**-19.66**	**1.213**
12	**61**	**440**	**1.5**	**0.029**	**0.0012**	**0.043**	**-19.29**	**1.333**
13	**61**	**450**	**1.5**	**0.043**	**0.0015**	**0.046**	**-18.85**	**1.102**
14	**61**	**460**	**1.5**	**0.058**	**0.0016**	**0.050**	**-18.45**	**0.965**
15	**61**	**470**	**1.5**	**0.076**	**0.0015**	**0.055**	**-18.09**	**0.791**
16	**61**	**480**	**1.5**	**0.100**	**0.0018**	**0.062**	**-17.70**	**0.643**
17	**61**	**490**	**1.5**	**0.121**	**0.0016**	**0.071**	**-17.38**	**0.541**
18	**60**	**500**	**1.5**	**0.146**	**0.0021**	**0.081**	**-17.04**	**0.460**
19	**61**	**510**	**1.5**	**0.175**	**0.0020**	**0.093**	**-16.73**	**0.391**
20	**60**	**520**	**1.5**	**0.201**	**0.0014**	**0.107**	**-16.42**	**0.296**
21	60	530	1.5	0.227	0.0019	0.123	-16.14	0.241
22	60	540	1.5	0.263	0.0023	0.141	-15.84	0.219
23	60	550	1.5	0.287	0.0020	0.162	-15.60	0.189
24	60	560	1.5	0.305	0.0024	0.183	-15.39	0.162
25	60	570	1.5	0.342	0.0024	0.207	-15.13	0.138
26	60	580	3	0.417	0.0020	0.236	-14.78	0.103
27	60	590	1.5	0.438	0.0021	0.267	-14.57	0.088
28	121	565	1.5	0.361	0.0054	0.292	-15.33	0.118
29	120	555	1.5	0.236	0.0025	0.309	-15.66	0.149
30	121	545	1.5	0.167	0.0016	0.320	-15.95	0.116
31	120	535	1.5	0.112	0.0015	0.328	-16.30	0.120
32	120	525	1.5	0.081	0.0016	0.334	-16.60	0.141
33	121	515	1.5	0.057	0.0014	0.338	-16.94	0.172

Table 2.2 cont

34	121	505	1.5	0.041	0.0016	0.341	-17.24	0.211
35	120	495	1.5	0.028	0.0013	0.342	-17.61	0.275
36	121	485	1.5	0.022	0.0012	0.344	-17.87	0.286
37	120	475	1.5	0.015	0.0012	0.345	-18.23	0.371
38	180	482	1.5	0.028	0.0013	0.347	-18.01	0.229
39	180	492	1.5	0.037	0.0013	0.350	-17.72	0.193
40	180	502	1.5	0.047	0.0014	0.353	-17.45	0.161
41	181	512	1.5	0.063	0.0013	0.357	-17.15	0.127
42	180	522	1.5	0.083	0.0017	0.363	-16.86	0.112
43	180	532	1.5	0.106	0.0018	0.371	-16.58	0.103
44	181	542	1.5	0.144	0.0015	0.381	-16.25	0.078
45	181	552	1.5	0.191	0.0018	0.394	-15.92	0.063
46	181	562	1.5	0.248	0.0024	0.411	-15.60	0.059
47	181	572	1.5	0.298	0.0021	0.432	-15.34	0.053
48	*181*	*575*	*16.5*	*0.304*	*0.0023*	*0.453*	*-15.25*	*0.050*
49	*181*	*576*	*27*	*0.309*	*0.0026*	*0.475*	*-15.15*	*0.048*
50	*181*	*577*	*36*	*0.313*	*0.0022*	*0.497*	*-15.06*	*0.044*
51	180	535	1.5	0.071	0.0016	0.502	-16.49	0.125
52	181	545	1.5	0.089	0.0012	0.508	-16.25	0.061
53	181	555	1.5	0.115	0.0017	0.516	-15.97	0.052
54	181	565	1.5	0.151	0.0020	0.527	-15.67	0.049
55	181	574	4.5	0.180	0.0013	0.539	-15.45	0.040
56	*181*	*578*	*18*	*0.210*	*0.0018*	*0.554*	*-15.25*	*0.034*
57	*181*	*577*	*31.5*	*0.211*	*0.0019*	*0.569*	*-15.19*	*0.037*
58	*181*	*574*	*39*	*0.187*	*0.0021*	*0.582*	*-15.26*	*0.040*
59	*181*	*556*	*105*	*0.161*	*0.0015*	*0.593*	*-15.36*	*0.039*

Aliquot ERB48-1
Location Sinai Peninsula

Step #	**Time (min)**	**Average T (°C)**	**±**	**He (ncc)**	**±**	**f**	**ln(D/a^2)**	**±**
1	61	400	1.5	2.633	0.0062	0.009	-20.03	0.644
2	61	400	1.5	2.104	0.0071	0.017	-19.21	0.678
3	121	400	1.5	3.697	0.0034	0.029	-18.74	0.258
4	121	400	1.5	3.593	0.0054	0.042	-18.32	0.184
5	241	400	1.5	6.297	0.0081	0.064	-18.04	0.103
6	241	400	1.5	5.676	0.0091	0.084	-17.79	0.100
7	360	400	1.5	7.503	0.0120	0.110	-17.62	0.067
8	361	400	1.5	6.634	0.0143	0.133	-17.50	0.068
9	481	400	1.5	7.972	0.0084	0.161	-17.39	0.044

Table 2.2 cont

10	**240**	**420**	**1.5**	**7.885**	**0.0123**	**0.188**	**-16.51**	**0.037**
11	**121**	**430**	**1.5**	**5.446**	**0.0074**	**0.207**	**-16.05**	**0.041**
12	**60**	**440**	**1.5**	**3.764**	**0.0066**	**0.220**	**-15.62**	**0.037**
13	**61**	**450**	**1.5**	**5.332**	**0.0066**	**0.239**	**-15.20**	**0.024**
14	**61**	**460**	**1.5**	**7.020**	**0.0095**	**0.263**	**-14.82**	**0.021**
15	**61**	**470**	**1.5**	**9.042**	**0.0120**	**0.295**	**-14.43**	**0.019**
16	**61**	**480**	**1.5**	**11.112**	**0.0166**	**0.334**	**-14.06**	**0.017**
17	**61**	**490**	**1.5**	**13.309**	**0.0163**	**0.380**	**-13.71**	**0.014**
18	**61**	**500**	**1.5**	**14.966**	**0.0114**	**0.432**	**-13.40**	**0.010**
19	**61**	**510**	**1.5**	**16.074**	**0.0253**	**0.488**	**-13.13**	**0.009**
20	61	520	1.5	16.607	0.0220	0.546	-12.89	0.008
21	61	530	1.5	16.825	0.0187	0.605	-12.67	0.006
22	61	540	1.5	16.737	0.0250	0.663	-12.46	0.005
23	60	550	1.5	17.053	0.0799	0.723	-12.20	0.007
24	61	560	1.5	14.776	0.0163	0.774	-12.13	0.006
25	61	570	1.5	12.621	0.0130	0.818	-12.05	0.003
26	61	580	1.5	10.670	0.0109	0.855	-11.98	0.002
27	61	590	1.5	9.409	0.0126	0.888	-11.84	0.002
28	121	565	1.5	6.119	0.0072	0.910	-12.73	0.000
29	121	555	1.5	3.194	0.0056	0.921	-13.21	0.000
30	121	545	1.5	1.966	0.0069	0.928	-13.58	0.000
31	121	535	1.5	1.280	0.0042	0.932	-13.94	0.000
32	121	525	1.5	0.843	0.0040	0.935	-14.30	0.000
33	121	515	1.5	0.573	0.0035	0.937	-14.65	0.000
34	121	505	1.5	0.393	0.0033	0.938	-15.00	0.000
35	121	495	1.5	0.279	0.0027	0.939	-15.32	0.000
36	121	485	1.5	0.190	0.0021	0.940	-15.69	0.000
37	121	475	1.5	0.131	0.0021	0.940	-16.06	0.000
38	181	482	1.5	0.239	0.0021	0.941	-15.84	0.000
39	180	492	1.5	0.325	0.0023	0.942	-15.52	0.000
40	180	502	1.5	0.441	0.0034	0.944	-15.19	0.000
41	181	512	1.5	0.577	0.0037	0.946	-14.89	0.000
42	181	522	1.5	0.749	0.0033	0.949	-14.59	0.000
43	181	532	1.5	0.935	0.0027	0.952	-14.31	0.000
44	181	542	1.5	1.135	0.0038	0.956	-14.04	0.000
45	181	552	1.5	1.343	0.0048	0.960	-13.77	0.000
46	181	562	1.5	1.489	0.0047	0.966	-13.54	0.000
47	180	572	1.5	1.557	0.0041	0.971	-13.34	0.000
48	180	582	1.5	1.546	0.0058	0.976	-13.16	0.000

Table 2.2 cont

49	180	590	1.5	1.371	0.0035	0.981	-13.06	0.000
50	180	600	1.5	1.218	0.0033	0.985	-12.94	0.000
51	181	610	1.5	1.012	0.0044	0.989	-12.86	0.000
52	181	620	1.5	0.789	0.0035	0.992	-12.83	0.000
53	180	630	1.5	0.597	0.0034	0.994	-12.81	0.000
54	180	639	4.5	0.465	0.0034	0.995	-12.77	0.000
55	*180*	*641*	*16.5*	*0.283*	*0.0021*	*0.996*	*-12.99*	*0.000*
56	181	625	1.5	0.108	0.0023	0.997	-13.78	0.000
57	181	610	1.5	0.059	0.0020	0.997	-14.29	0.000
58	180	600	1.5	0.041	0.0018	0.997	-14.59	0.000
59	181	595	1.5	0.034	0.0018	0.997	-14.75	0.000

Aliquot ERB48-2

Location Sinai Peninsula

Step #	Time (min)	Average T (°C)	±	He (ncc)	±	f	$\ln(D/a^2)$	±
1	61	400	1.5	5.290	0.0120	0.008	-20.30	0.662
2	61	400	1.5	2.956	0.0085	0.012	-19.93	0.836
3	121	400	1.5	4.808	0.0107	0.020	-19.67	0.390
4	121	400	1.5	4.142	0.0128	0.026	-19.47	0.381
5	241	400	1.5	7.262	0.0162	0.037	-19.27	0.214
6	241	400	1.5	6.345	0.0166	0.047	-19.11	0.212
7	361	400	1.5	8.332	0.0110	0.059	-19.00	0.123
8	361	400	1.5	7.435	0.0112	0.070	-18.90	0.104
9	481	400	1.5	8.862	0.0208	0.084	-18.83	0.090
10	**241**	**420**	**1.5**	**9.262**	**0.0161**	**0.098**	**-17.92**	**0.082**
11	**120**	**430**	**1.5**	**6.370**	**0.0195**	**0.108**	**-17.46**	**0.096**
12	**61**	**440**	**1.5**	**4.616**	**0.0113**	**0.115**	**-17.02**	**0.097**
13	**61**	**450**	**1.5**	**6.500**	**0.0109**	**0.124**	**-16.60**	**0.054**
14	**61**	**460**	**1.5**	**8.887**	**0.0147**	**0.138**	**-16.18**	**0.044**
15	**61**	**470**	**1.5**	**11.748**	**0.0141**	**0.156**	**-15.78**	**0.036**
16	**61**	**480**	**1.5**	**14.874**	**0.0190**	**0.178**	**-15.39**	**0.031**
17	**61**	**490**	**1.5**	**18.175**	**0.0228**	**0.206**	**-15.03**	**0.027**
18	**61**	**500**	**1.5**	**21.560**	**0.0260**	**0.238**	**-14.68**	**0.022**
19	**61**	**510**	**1.5**	**24.585**	**0.0294**	**0.275**	**-14.37**	**0.019**
20	**61**	**520**	**1.5**	**27.461**	**0.0313**	**0.317**	**-14.07**	**0.016**
21	61	530	1.5	30.735	0.0240	0.364	-13.77	0.012
22	61	540	1.5	32.785	0.0264	0.413	-13.52	0.009
23	61	550	1.5	34.120	0.0287	0.465	-13.29	0.008

Table 2.2 cont

24	60	560	1.5	34.578	0.0225	0.517	-13.07	0.006
25	60	570	1.5	35.152	0.0504	0.570	-12.87	0.006
26	61	580	1.5	34.778	0.0404	0.623	-12.70	0.006
27	60	590	1.5	32.920	0.0347	0.673	-12.55	0.004
28	121	565	1.5	23.571	0.0184	0.709	-13.43	0.004
29	120	555	1.5	14.301	0.0227	0.730	-13.80	0.004
30	121	545	1.5	8.963	0.0175	0.744	-14.20	0.005
31	121	535	1.5	5.868	0.0153	0.753	-14.57	0.005
32	121	525	1.5	3.990	0.0141	0.759	-14.93	0.006
33	121	515	1.5	2.766	0.0109	0.763	-15.27	0.007
34	121	505	1.5	1.912	0.0084	0.766	-15.62	0.007
35	121	495	1.5	1.327	0.0091	0.768	-15.97	0.009
36	121	485	1.5	0.935	0.0088	0.769	-16.32	0.011
37	121	475	1.5	0.652	0.0085	0.770	-16.67	0.015
38	180	482	1.5	1.176	0.0087	0.772	-16.47	0.008
39	181	492	1.5	1.596	0.0090	0.774	-16.16	0.007
40	181	502	1.5	2.177	0.0088	0.778	-15.84	0.005
41	181	512	1.5	2.913	0.0109	0.782	-15.53	0.004
42	181	522	1.5	3.852	0.0099	0.788	-15.22	0.004
43	181	532	1.5	4.936	0.0128	0.795	-14.94	0.003
44	181	542	1.5	6.172	0.0122	0.805	-14.67	0.003
45	181	552	1.5	7.518	0.0194	0.816	-14.42	0.003
46	181	562	1.5	8.847	0.0144	0.829	-14.18	0.002
47	180	572	1.5	10.223	0.0173	0.845	-13.94	0.002
48	180	582	1.5	11.184	0.0194	0.862	-13.74	0.002
49	180	590	1.5	10.944	0.0156	0.878	-13.63	0.002
50	180	600	1.5	10.929	0.0177	0.895	-13.48	0.001
51	181	610	1.5	10.453	0.0127	0.911	-13.39	0.000
52	181	620	1.5	11.727	0.0206	0.929	-13.09	0.000
53	180	615	1.5	6.003	0.0127	0.938	-13.57	0.000
54	180	600	1.5	3.204	0.0103	0.942	-14.09	0.000
55	180	595	1.5	2.493	0.0105	0.946	-14.27	0.000
56	181	590	1.5	1.903	0.0082	0.949	-14.48	0.000
57	180	580	1.5	1.309	0.0093	0.951	-14.80	0.000
58	180	585	1.5	1.408	0.0100	0.953	-14.69	0.000
59	180	580	1.5	1.121	0.0094	0.955	-14.87	0.000

Table 2.2 cont

Aliquot B099-7

Location Hall Peninsula

Step #	Time (min)	Average T (°C)	±	He (ncc)	±	f	ln(D/a²)	±
1	61	250	1.5	0.296	0.0066	0.000	-26.76	5.008
2	120	250	1.5	0.319	0.0050	0.001	-26.24	4.584
3	121	250	1.5	0.263	0.0037	0.001	-25.94	4.017
4	180	250	1.5	0.344	0.0074	0.001	-25.73	3.640
5	60	255	1.5	0.208	0.0022	0.002	-24.90	3.765
6	60	260	1.5	0.249	0.0025	0.002	-24.56	2.803
7	60	265	1.5	0.253	0.0050	0.002	-24.40	3.057
8	60	270	1.5	0.280	0.0068	0.002	-24.16	3.234
9	60	275	1.5	0.345	0.0056	0.003	-23.81	2.955
10	60	280	1.5	0.459	0.0057	0.003	-23.37	2.479
11	60	285	1.5	0.619	0.0127	0.004	-22.89	2.476
12	60	290	1.5	0.768	0.0039	0.005	-22.49	2.046
13	60	295	1.5	0.900	0.0026	0.006	-22.14	1.165
14	61	300	1.5	1.079	0.0019	0.007	-21.79	0.801
15	60	305	1.5	1.259	0.0029	0.008	-21.43	0.684
16	60	310	1.5	1.479	0.0029	0.010	-21.09	0.608
17	60	315	1.5	1.749	0.0029	0.012	-20.75	0.487
18	60	320	1.5	1.999	0.0030	0.014	-20.44	0.403
19	60	325	1.5	2.319	0.0042	0.016	-20.12	0.358
20	61	330	1.5	2.699	0.0044	0.019	-19.82	0.314
21	61	335	1.5	3.139	0.0046	0.022	-19.50	0.258
22	61	340	1.5	3.579	0.0050	0.026	-19.21	0.218
23	61	345	1.5	4.049	0.0048	0.031	-18.93	0.181
24	61	350	1.5	4.569	0.0051	0.036	-18.66	0.149
25	61	340	1.5	2.799	0.0049	0.039	-19.03	0.196
26	61	330	1.5	1.729	0.0037	0.040	-19.45	0.219
27	60	320	1.5	1.059	0.0026	0.041	-19.88	0.236
28	60	310	1.5	0.679	0.0115	0.042	-20.30	0.515
29	60	300	1.5	0.338	0.0040	0.043	-20.99	0.865
30	60	305	1.5	0.432	0.0087	0.043	-20.73	0.625
31	60	310	1.5	0.602	0.0134	0.044	-20.39	0.718
32	60	315	1.5	0.761	0.0038	0.044	-20.13	0.507
33	61	320	1.5	0.928	0.0030	0.045	-19.93	0.223
34	60	325	1.5	1.109	0.0031	0.047	-19.71	0.180
35	61	330	1.5	1.379	0.0036	0.048	-19.48	0.161
36	61	335	1.5	1.669	0.0040	0.050	-19.26	0.149

Table 2.2 cont

37	61	340	1.5	2.029	0.0048	0.052	-19.02	0.140
38	61	345	1.5	2.419	0.0040	0.055	-18.80	0.121
39	61	350	1.5	2.889	0.0050	0.058	-18.56	0.105
40	31	355	3	1.799	0.0040	0.060	-18.32	0.150
41	31	360	3	2.169	0.0036	0.062	-18.09	0.104
42	31	365	3	2.609	0.0029	0.065	-17.86	0.083
43	31	370	3	3.089	0.0038	0.068	-17.64	0.074
44	31	375	3	3.569	0.0054	0.072	-17.44	0.077
45	31	380	3	4.149	0.0068	0.076	-17.23	0.078
46	31	385	3	4.829	0.0056	0.082	-17.02	0.068
47	31	390	3	5.519	0.0046	0.087	-16.81	0.054
48	30	395	3	6.119	0.0058	0.094	-16.60	0.049
49	31	400	3	7.119	0.0065	0.102	-16.40	0.045
50	**31**	**390**	**3**	**4.479**	**0.0050**	**0.106**	**-16.79**	**0.060**
51	**30**	**380**	**3**	**2.849**	**0.0047**	**0.109**	**-17.17**	**0.066**
52	**31**	**370**	**3**	**1.859**	**0.0045**	**0.111**	**-17.61**	**0.078**
53	**30**	**360**	**3**	**1.189**	**0.0027**	**0.113**	**-18.00**	**0.087**
54	**31**	**350**	**3**	**0.780**	**0.0035**	**0.113**	**-18.45**	**0.103**
55	**30**	**375**	**3**	**2.009**	**0.0032**	**0.116**	**-17.46**	**0.047**
56	**30**	**360**	**3**	**1.109**	**0.0028**	**0.117**	**-18.03**	**0.080**
57	**30**	**345**	**3**	**0.530**	**0.0094**	**0.117**	**-18.76**	**0.224**
58	**30**	**330**	**3**	**0.267**	**0.0038**	**0.118**	**-19.44**	**0.402**
59	31	315	3	0.183	0.0020	0.118	-19.85	0.279
60	31	300	3	0.095	0.0022	0.118	-20.51	0.369
61	31	310	3	0.140	0.0019	0.118	-20.12	0.253
62	31	315	3	0.173	0.0022	0.118	-19.90	0.214
63	31	320	3	0.203	0.0018	0.119	-19.74	0.186
64	30	325	3	0.242	0.0013	0.119	-19.53	0.130
65	31	330	3	0.254	0.0061	0.119	-19.51	0.254
66	30	335	3	0.268	0.0060	0.119	-19.43	0.364
67	31	340	3	0.323	0.0049	0.120	-19.27	0.288
68	31	345	3	0.441	0.0111	0.120	-18.95	0.302
69	31	350	3	0.560	0.0113	0.121	-18.71	0.325
70	31	355	3	0.774	0.0046	0.122	-18.38	0.187
71	31	360	3	0.927	0.0030	0.123	-18.19	0.090
72	30	365	3	1.129	0.0030	0.124	-17.95	0.065
73	31	370	3	1.399	0.0033	0.125	-17.76	0.058
74	30	375	3	1.669	0.0030	0.127	-17.53	0.051
75	30	380	3	2.019	0.0034	0.129	-17.33	0.045

Table 2.2 cont

76	31	385	3	2.479	0.0048	0.132	-17.13	0.045
77	30	390	3	2.889	0.0037	0.135	-16.92	0.042
78	31	395	3	3.509	0.0050	0.139	-16.73	0.037
79	30	400	3	4.329	0.0072	0.143	-16.46	0.038
80	30	405	3	4.809	0.0061	0.148	-16.31	0.037
81	31	410	3	5.579	0.0052	0.154	-16.15	0.030
82	31	415	3	6.489	0.0082	0.161	-15.96	0.029
83	31	420	3	7.409	0.0050	0.169	-15.77	0.026
84	31	425	3	8.489	0.0086	0.178	-15.58	0.023
85	31	430	3	9.319	0.0085	0.188	-15.42	0.023
86	30	435	3	10.199	0.0091	0.199	-15.23	0.021
87	*31*	*432*	*52.5*	*11.299*	*0.0100*	*0.211*	*0.00*	*0.000*
88	30	445	3	13.099	0.0145	0.225	-14.84	0.019
89	31	450	3	14.299	0.0083	0.241	-14.70	0.017
90	31	455	3	15.299	0.0095	0.257	-14.55	0.014
91	31	460	3	16.199	0.0094	0.274	-14.41	0.013
92	30	465	3	16.599	0.0144	0.292	-14.27	0.013
93	31	470	3	17.599	0.0104	0.311	-14.17	0.012
94	30	475	3	17.999	0.0105	0.330	-14.03	0.010
95	31	480	3	18.999	0.0058	0.350	-13.92	0.008
96	31	485	3	19.299	0.0103	0.371	-13.83	0.008
97	31	490	3	19.999	0.0099	0.392	-13.71	0.007
98	30	495	3	20.499	0.0101	0.414	-13.57	0.007
99	31	500	3	21.699	0.0114	0.437	-13.46	0.006
100	30	490	3	13.499	0.0118	0.452	-13.83	0.008
101	30	480	3	8.509	0.0087	0.461	-14.25	0.009
102	31	470	3	5.689	0.0067	0.467	-14.66	0.009
103	30	460	3	3.769	0.0040	0.471	-15.02	0.009
104	31	450	3	2.589	0.0042	0.474	-15.42	0.010
105	31	440	3	1.709	0.0039	0.476	-15.82	0.012
106	30	430	3	1.129	0.0032	0.477	-16.20	0.014
107	31	420	3	0.786	0.0043	0.478	-16.59	0.019
108	31	410	3	0.430	0.0058	0.478	-17.19	0.040
109	31	400	3	0.255	0.0049	0.478	-17.71	0.067
110	31	405	3	0.305	0.0051	0.479	-17.53	0.052
111	31	410	3	0.395	0.0086	0.479	-17.27	0.055
112	31	415	3	0.525	0.0093	0.480	-16.99	0.054
113	30	420	3	0.734	0.0098	0.481	-16.62	0.042
114	31	425	3	0.859	0.0021	0.481	-16.49	0.024

Table 2.2 cont

115	30	430	3	1.039	0.0031	0.483	-16.26	0.011
116	31	435	3	1.269	0.0036	0.484	-16.09	0.011
117	30	440	3	1.539	0.0038	0.486	-15.86	0.011
118	31	445	3	1.939	0.0031	0.488	-15.65	0.009
119	31	449	3	2.409	0.0044	0.490	-15.43	0.008
120	31	455	3	2.859	0.0048	0.493	-15.25	0.008
121	31	460	3	3.269	0.0040	0.497	-15.10	0.007
122	31	465	3	3.889	0.0055	0.501	-14.92	0.007
123	31	470	3	4.519	0.0069	0.506	-14.75	0.007
124	31	475	3	5.239	0.0215	0.511	-14.58	0.011
125	31	480	3	6.009	0.0065	0.518	-14.42	0.009
126	30	485	3	7.039	0.0055	0.525	-14.21	0.005
127	31	490	3	7.989	0.0063	0.534	-14.09	0.005
128	30	495	3	8.929	0.0068	0.543	-13.91	0.005
129	30	500	3	9.899	0.0074	0.554	-13.77	0.004
130	31	505	3	11.499	0.0096	0.566	-13.61	0.004
131	31	510	3	12.099	0.0083	0.579	-13.52	0.004
132	30	515	3	12.699	0.0092	0.593	-13.39	0.004
133	30	520	3	13.599	0.0085	0.607	-13.27	0.004
134	30	525	3	14.099	0.0092	0.622	-13.18	0.003
135	30	530	3	15.599	0.0093	0.639	-13.02	0.003
136	30	535	3	15.499	0.0123	0.656	-12.97	0.003
137	31	540	3	17.299	0.0105	0.674	-12.82	0.003
138	30	545	3	17.399	0.0116	0.693	-12.71	0.003
139	*31*	*539*	*72*	*18.099*	*0.0104*	*0.712*	*0.00*	*0.000*
140	31	555	3	19.199	0.0103	0.733	-12.49	0.002
141	31	560	3	19.499	0.0092	0.753	-12.38	0.002
142	31	565	3	19.399	0.0118	0.774	-12.29	0.002
143	31	570	3	18.999	0.0153	0.794	-12.21	0.002
144	31	575	3	17.999	0.0144	0.814	-12.16	0.002
145	31	580	3	17.099	0.0123	0.832	-12.10	0.002
146	31	585	3	16.599	0.0113	0.850	-12.02	0.001
147	30	590	3	14.099	0.0085	0.865	-12.03	0.001
148	31	595	3	13.199	0.0074	0.879	-12.02	0.001
149	31	600	3	12.899	0.0069	0.893	-11.91	0.001
150	31	590	3	8.569	0.0063	0.902	-12.23	0.000
151	31	580	3	6.099	0.0057	0.908	-12.50	0.000
152	31	570	3	4.279	0.0046	0.913	-12.79	0.000
153	31	560	3	2.889	0.0039	0.916	-13.14	0.000

Table 2.2 cont

154	31	550	3	1.999	0.0036	0.918	-13.48	0.000
155	31	540	3	1.409	0.0022	0.920	-13.80	0.000
156	30	530	3	0.958	0.0030	0.921	-14.14	0.000
157	31	520	3	0.662	0.0122	0.921	-14.53	0.000
158	31	510	3	0.379	0.0085	0.922	-15.08	0.000
159	31	500	3	0.263	0.0035	0.922	-15.44	0.000
160	30	505	3	0.292	0.0051	0.922	-15.30	0.000
161	31	510	3	0.362	0.0076	0.923	-15.12	0.000
162	31	515	3	0.436	0.0055	0.923	-14.92	0.000
163	31	520	3	0.544	0.0104	0.924	-14.70	0.000
164	31	525	3	0.675	0.0128	0.925	-14.47	0.000
165	30	530	3	0.815	0.0037	0.925	-14.24	0.000
166	30	535	3	0.943	0.0027	0.926	-14.08	0.000
167	30	540	3	1.099	0.0027	0.928	-13.91	0.000
168	31	545	3	1.289	0.0026	0.929	-13.77	0.000
169	31	550	3	1.489	0.0036	0.931	-13.60	0.000
170	31	555	3	1.739	0.0039	0.932	-13.42	0.000
171	31	560	3	1.989	0.0040	0.935	-13.26	0.000
172	31	565	3	2.229	0.0046	0.937	-13.11	0.000
173	30	570	3	2.529	0.0038	0.940	-12.91	0.000
174	31	575	3	2.929	0.0043	0.943	-12.75	0.000
175	30	580	3	3.169	0.0044	0.946	-12.58	0.000
176	31	584	3	3.339	0.0051	0.950	-12.50	0.000
177	30	590	3	3.459	0.0067	0.953	-12.36	0.000
178	31	595	3	3.729	0.0041	0.957	-12.23	0.000
179	30	600	3	4.019	0.0045	0.962	-12.03	0.000
180	31	605	3	4.549	0.0056	0.967	-11.81	0.000
181	31	610	3	4.459	0.0063	0.971	-11.69	0.000
182	30	615	3	4.459	0.0067	0.976	-11.49	0.000
183	31	620	3	4.129	0.0051	0.981	-11.41	0.000
184	30	625	3	4.089	0.0049	0.985	-11.15	0.000
185	31	630	3	4.239	0.0052	0.989	-10.85	0.000
186	31	635	3	4.289	0.0035	0.994	-10.38	0.000
187	30	640	3	4.239	0.0076	0.999	-9.43	0.000

Aliquot B099-11

Location Hall Peninsula

Step #	**Time (min)**	**Average T (°C)**	**±**	**He (ncc)**	**±**	**f**	**ln(D/a^2)**	**±**
1	*91*	*298*	*27*	*35.333*	*0.0746*	*0.085*	*17.51*	*0.869*

Table 2.2 cont

2	91	300	4.5	13.039	0.0193	0.116	17.45	0.138
3	91	300	4.5	10.054	0.0212	0.140	17.45	0.138
4	**91**	**315**	**3**	**14.851**	**0.0345**	**0.176**	**17.00**	**0.087**
5	**90**	**330**	**1.5**	**21.258**	**0.0441**	**0.227**	**16.58**	**0.041**
6	**91**	**345**	**3**	**27.715**	**0.0441**	**0.294**	**16.18**	**0.079**
7	**91**	**360**	**1.5**	**34.821**	**0.0740**	**0.377**	**15.79**	**0.038**
8	**91**	**375**	**1.5**	**39.232**	**0.0673**	**0.471**	**15.43**	**0.036**
9	**91**	**390**	**1.5**	**40.647**	**0.0666**	**0.569**	**15.08**	**0.034**
10	60	405	1.5	28.462	0.0420	0.637	14.75	0.033
11	61	420	1.5	29.548	0.0532	0.708	14.43	0.031
12	61	435	1.5	27.709	0.0419	0.775	14.12	0.030
13	61	450	1.5	23.193	0.0510	0.830	13.83	0.029
14	61	440	1.5	9.851	0.0197	0.854	14.02	0.030
15	60	430	1.5	5.170	0.0113	0.867	14.22	0.030
16	60	420	1.5	3.160	0.0087	0.874	14.43	0.031
17	60	410	1.5	1.992	0.0065	0.879	14.64	0.032
18	60	400	1.5	1.288	0.0055	0.882	14.86	0.033
19	61	415	1.5	1.955	0.0106	0.887	14.53	0.032
20	61	430	1.5	2.930	0.0078	0.894	14.22	0.030
21	61	445	1.5	4.136	0.0084	0.904	13.92	0.029
22	61	460	1.5	5.399	0.0125	0.917	13.64	0.028
23	61	475	1.5	6.095	0.0173	0.931	13.37	0.027
24	61	490	1.5	6.023	0.0103	0.946	13.10	0.026
25	60	505	1.5	5.252	0.0161	0.958	12.85	0.025
26	61	520	1.5	4.360	0.0127	0.969	12.61	0.024
27	61	510	1.5	1.870	0.0055	0.973	12.77	0.025
28	90	500	1.5	1.386	0.0046	0.977	12.93	0.025
29	91	490	1.5	0.759	0.0032	0.978	13.10	0.026
30	91	480	1.5	0.453	0.0026	0.980	13.28	0.026
31	91	470	1.5	0.281	0.0018	0.980	13.46	0.027
32	91	460	1.5	0.185	0.0033	0.981	13.64	0.028
33	90	450	1.5	0.126	0.0013	0.981	13.83	0.029
34	91	440	1.5	0.085	0.0012	0.981	14.02	0.030
35	91	430	1.5	0.057	0.0009	0.981	14.22	0.030
36	90	420	1.5	0.039	0.0010	0.981	14.43	0.031
37	*60*	*0*	*1.5*	*0.013*	*0.0032*	*0.981*	*0.00*	*0.000*
38	61	435	1.5	0.041	0.0009	0.982	14.12	0.030
39	61	450	1.5	0.069	0.0014	0.982	13.83	0.029
40	61	465	1.5	0.111	0.0013	0.982	13.55	0.028

Table 2.2 cont

41	60	480	1.5	0.170	0.0033	0.982	13.28	0.026
42	61	495	1.5	0.261	0.0017	0.983	13.02	0.025
43	61	510	1.5	0.373	0.0016	0.984	12.77	0.025
44	60	525	1.5	0.497	0.0026	0.985	12.53	0.024
45	61	540	1.5	0.596	0.0021	0.987	12.30	0.023
46	61	555	1.5	0.629	0.0032	0.988	12.08	0.022
47	61	570	1.5	0.623	0.0040	0.990	11.86	0.021
48	61	585	1.5	0.617	0.0026	0.991	11.65	0.020
49	61	600	1.5	0.460	0.0024	0.992	11.45	0.020
50	61	615	1.5	0.386	0.0023	0.993	11.26	0.019
51	90	605	1.5	0.250	0.0023	0.994	11.39	0.019
52	90	595	1.5	0.138	0.0017	0.994	11.52	0.020
53	90	585	1.5	0.083	0.0013	0.994	11.65	0.020
54	91	575	1.5	0.051	0.0010	0.994	11.79	0.021
55	91	565	1.5	0.032	0.0010	0.994	11.93	0.021
56	90	555	1.5	0.021	0.0008	0.994	12.08	0.022
57	91	545	1.5	0.014	0.0007	0.994	12.22	0.022
58	91	535	1.5	0.010	0.0005	0.994	12.37	0.023
59	91	525	1.5	0.007	0.0006	0.994	12.53	0.024
60	121	535	1.5	0.011	0.0007	0.995	12.37	0.023
61	121	540	1.5	0.014	0.0007	0.995	12.30	0.023
62	121	555	1.5	0.023	0.0007	0.995	12.08	0.022
63	121	570	1.5	0.035	0.0008	0.995	11.86	0.021
64	120	585	1.5	0.061	0.0010	0.995	11.65	0.020
65	121	600	1.5	0.094	0.0013	0.995	11.45	0.020
66	120	615	1.5	0.146	0.0022	0.995	11.26	0.019
67	120	605	1.5	0.088	0.0012	0.996	11.39	0.019
68	121	595	1.5	0.060	0.0010	0.996	11.52	0.020
69	121	585	1.5	0.037	0.0009	0.996	11.65	0.020
70	121	575	1.5	0.023	0.0009	0.996	11.79	0.021
71	121	565	1.5	0.016	0.0007	0.996	11.93	0.021
72	121	555	1.5	0.012	0.0006	0.996	12.08	0.022
73	120	545	1.5	0.007	0.0006	0.996	12.22	0.022
74	121	535	1.5	0.006	0.0006	0.996	12.37	0.023
75	121	525	1.5	0.004	0.0005	0.996	12.53	0.024
76	121	515	1.5	0.003	0.0005	0.996	12.69	0.024

Table 2.2 cont

Aliquot C013-11

Location Hall Peninsula

Step #	**Time (min)**	**Average T (°C)**	**±**	**He (ncc)**	**±**	**f**	**ln(D/a^2)**	**±**
1	60	150	1.5	0.001	0.0014	0.000	-34.35	12.786
2	120	150	1.5	0.001	0.0013	0.000	-34.50	13.091
3	*121*	*150*	*1.5*	*0.000*	*0.0011*	*0.000*	*0.00*	*0.000*
4	*61*	*160*	*1.5*	*0.000*	*0.0011*	*0.000*	*0.00*	*0.000*
5	*61*	*170*	*1.5*	*0.000*	*0.0008*	*0.000*	*0.00*	*0.000*
6	61	180	1.5	0.001	0.0016	0.000	-33.16	0.000
7	61	190	1.5	0.003	0.0017	0.000	-31.51	10.934
8	60	200	1.5	0.000	0.0015	0.000	-33.41	12.844
9	60	210	1.5	0.004	0.0015	0.000	-30.40	9.777
10	61	220	1.5	0.250	0.0075	0.002	-23.52	4.059
11	60	230	1.5	0.007	0.0016	0.002	-26.39	6.943
12	61	240	1.5	0.008	0.0015	0.002	-26.27	5.666
13	61	250	1.5	0.011	0.0016	0.002	-25.88	5.300
14	60	260	1.5	0.016	0.0018	0.002	-25.48	5.004
15	61	270	1.5	0.024	0.0021	0.002	-25.01	4.660
16	61	280	1.5	0.032	0.0023	0.002	-24.63	4.416
17	60	290	1.5	0.047	0.0021	0.003	-24.12	3.934
18	60	300	1.5	0.064	0.0022	0.003	-23.68	3.497
19	60	310	1.5	0.084	0.0024	0.003	-23.26	3.171
20	60	320	1.5	0.115	0.0025	0.004	-22.77	2.796
21	60	330	1.5	0.153	0.0021	0.005	-22.28	2.334
22	60	340	1.5	0.200	0.0021	0.006	-21.80	1.882
23	61	350	1.5	0.236	0.0039	0.008	-21.44	1.833
24	61	335	1.5	0.113	0.0023	0.008	-22.03	2.335
25	61	320	1.5	0.054	0.0022	0.009	-22.72	2.630
26	61	305	1.5	0.020	0.0018	0.009	-23.68	3.395
27	61	290	1.5	0.010	0.0020	0.009	-24.38	4.014
28	60	275	1.5	0.005	0.0019	0.009	-25.05	4.696
29	61	260	1.5	0.002	0.0014	0.009	-26.09	5.544
30	61	245	1.5	0.002	0.0017	0.009	-26.11	5.500
31	*61*	*230*	*3*	*0.000*	*0.0111*	*0.009*	*0.00*	*0.000*
32	*61*	*215*	*3*	*0.000*	*0.0012*	*0.009*	*0.00*	*0.000*
33	61	200	1.5	0.002	0.0019	0.009	-26.24	0.000
34	60	210	1.5	0.001	0.0015	0.009	-27.00	6.478
35	*61*	*220*	*1.5*	*0.000*	*0.0013*	*0.009*	*0.00*	*0.000*
36	*61*	*230*	*3*	*0.000*	*0.0013*	*0.009*	*0.00*	*0.000*

Table 2.2 cont

37	*61*	*240*	*3*	*0.000*	*0.0008*	*0.009*	*0.00*	*0.000*
38	61	250	1.5	0.000	0.0015	0.009	-27.42	0.000
39	60	260	1.5	0.001	0.0017	0.009	-26.34	5.779
40	61	270	1.5	0.003	0.0021	0.009	-25.40	5.003
41	61	280	1.5	0.005	0.0017	0.009	-25.03	4.638
42	60	290	1.5	0.007	0.0020	0.009	-24.63	4.232
43	31	300	3	0.009	0.0018	0.009	-23.82	4.096
44	31	310	3	0.012	0.0020	0.009	-23.44	3.740
45	31	320	3	0.021	0.0018	0.009	-22.91	3.244
46	31	330	3	0.036	0.0024	0.010	-22.33	2.804
47	31	340	3	0.062	0.0020	0.010	-21.76	2.337
48	31	350	3	0.094	0.0020	0.011	-21.29	1.881
49	30	360	3	0.138	0.0020	0.011	-20.81	1.553
50	**30**	**370**	**3**	**0.207**	**0.0019**	**0.013**	**-20.32**	**1.210**
51	**31**	**380**	**3**	**0.226**	**0.0066**	**0.014**	**-20.15**	**1.583**
52	***30***	***390***	***3***	***1.039***	***0.0023***	***0.020***	***0.00***	***0.000***
53	**31**	**400**	**3**	**0.518**	**0.0090**	**0.024**	**-18.82**	**0.970**
54	**30**	**410**	**3**	**0.728**	**0.0039**	**0.028**	**-18.28**	**0.713**
55	**30**	**420**	**3**	**0.882**	**0.0037**	**0.034**	**-17.91**	**0.426**
56	**31**	**430**	**3**	**1.063**	**0.0029**	**0.040**	**-17.58**	**0.310**
57	**31**	**440**	**3**	**1.268**	**0.0043**	**0.048**	**-17.22**	**0.254**
58	**31**	**450**	**3**	**1.468**	**0.0038**	**0.057**	**-16.89**	**0.214**
59	31	435	3	0.738	0.0032	0.061	-17.45	0.299
60	30	420	3	0.298	0.0063	0.063	-18.27	0.570
61	31	405	3	0.215	0.0035	0.065	-18.60	0.663
62	31	390	3	0.122	0.0023	0.065	-19.15	0.685
63	30	375	3	0.068	0.0025	0.066	-19.70	0.868
64	31	360	3	0.032	0.0023	0.066	-20.47	1.321
65	30	345	3	0.016	0.0018	0.066	-21.14	1.738
66	30	330	3	0.008	0.0019	0.066	-21.79	2.199
67	31	315	3	0.004	0.0017	0.066	-22.52	2.807
68	31	300	3	0.004	0.0017	0.066	-22.50	2.719
69	31	310	3	0.006	0.0016	0.066	-22.13	2.337
70	31	320	3	0.006	0.0019	0.066	-22.22	2.489
71	30	330	3	0.008	0.0019	0.066	-21.83	2.246
72	31	340	3	0.011	0.0023	0.066	-21.52	2.035
73	30	350	3	0.020	0.0021	0.066	-20.90	1.587
74	31	360	3	0.028	0.0022	0.067	-20.60	1.314
75	30	370	3	0.044	0.0022	0.067	-20.11	1.023

Table 2.2 cont

76	31	380	3	0.075	0.0020	0.067	-19.61	0.713
77	30	390	3	0.107	0.0022	0.068	-19.21	0.559
78	31	400	3	0.170	0.0034	0.069	-18.76	0.487
79	31	410	3	0.224	0.0049	0.070	-18.47	0.527
80	31	420	3	0.235	0.0064	0.072	-18.40	0.625
81	31	430	3	0.379	0.0076	0.074	-17.89	0.503
82	31	440	3	0.607	0.0140	0.078	-17.38	0.472
83	31	450	3	0.848	0.0034	0.083	-16.98	0.305
84	30	460	3	1.135	0.0034	0.090	-16.58	0.132
85	31	470	3	1.461	0.0038	0.099	-16.27	0.111
86	31	480	3	1.822	0.0041	0.110	-15.94	0.095
87	31	490	3	2.252	0.0025	0.124	-15.60	0.072
88	31	500	3	2.890	0.0042	0.142	-15.21	0.058
89	31	510	3	4.448	0.0067	0.169	-14.60	0.047
90	30	520	3	4.195	0.0050	0.195	-14.44	0.047
91	31	530	3	4.657	0.0070	0.224	-14.21	0.037
92	31	540	3	4.429	0.0052	0.251	-14.10	0.035
93	*31*	*543*	*54*	*4.683*	*0.0200*	*0.280*	*-13.91*	*0.038*
94	31	560	3	5.431	0.0060	0.313	-13.61	0.031
95	30	570	3	5.960	0.0080	0.350	-13.34	0.020
96	30	580	3	6.722	0.0087	0.391	-13.06	0.018
97	31	590	3	6.606	0.0081	0.432	-12.95	0.016
98	30	600	3	7.285	0.0096	0.477	-12.66	0.013
99	30	585	3	4.019	0.0052	0.501	-13.14	0.017
100	31	570	3	2.485	0.0043	0.517	-13.58	0.015
101	31	555	3	1.456	0.0029	0.525	-14.07	0.016
102	31	540	3	0.916	0.0030	0.531	-14.51	0.017
103	31	525	3	0.535	0.0118	0.534	-15.03	0.044
104	30	510	3	0.263	0.0090	0.536	-15.70	0.104
105	31	495	3	0.216	0.0023	0.537	-15.92	0.070
106	31	480	3	0.135	0.0025	0.538	-16.39	0.052
107	31	465	3	0.079	0.0019	0.539	-16.93	0.076
108	31	450	3	0.052	0.0026	0.539	-17.33	0.108
109	31	460	3	0.065	0.0022	0.539	-17.11	0.092
110	30	470	3	0.089	0.0020	0.540	-16.76	0.062
111	31	480	3	0.123	0.0025	0.541	-16.47	0.049
112	31	490	3	0.172	0.0024	0.542	-16.13	0.040
113	31	500	3	0.225	0.0023	0.543	-15.86	0.031
114	30	510	3	0.231	0.0060	0.545	-15.80	0.049

Table 2.2 cont

115	30	520	3	0.310	0.0048	0.546	-15.50	0.047
116	31	530	3	0.492	0.0068	0.549	-15.06	0.033
117	31	540	3	0.722	0.0032	0.554	-14.66	0.022
118	30	550	3	0.925	0.0030	0.560	-14.36	0.013
119	31	560	3	1.228	0.0029	0.567	-14.09	0.011
120	31	570	3	1.599	0.0042	0.577	-13.79	0.010
121	*31*	*572*	*58.5*	*1.933*	*0.0049*	*0.589*	*-13.57*	*0.010*
122	30	590	3	2.484	0.0048	0.604	-13.23	0.009
123	30	600	3	3.041	0.0056	0.623	-12.97	0.008
124	31	610	3	3.655	0.0049	0.645	-12.74	0.007
125	31	620	3	4.283	0.0057	0.672	-12.49	0.006

Aliquot C015-14

Location Hall Peninsula

Step #	Time (min)	Average T (°C)	±	He (ncc)	±	f	ln(D/a^2)	±
1	61	250	1.5	0.019	0.0023	0.000	-29.11	7.865
2	121	250	1.5	0.018	0.0022	0.000	-28.73	7.667
3	120	250	1.5	0.012	0.0020	0.000	-28.76	7.630
4	181	250	1.5	0.016	0.0024	0.000	-28.59	7.079
5	61	255	1.5	0.007	0.0020	0.000	-28.15	7.717
6	60	260	1.5	0.008	0.0021	0.000	-27.94	7.455
7	61	265	1.5	0.012	0.0021	0.000	-27.38	6.915
8	61	270	1.5	0.012	0.0024	0.001	-27.25	6.849
9	60	275	1.5	0.013	0.0021	0.001	-27.03	6.636
10	61	280	1.5	0.020	0.0024	0.001	-26.46	6.054
11	60	285	1.5	0.023	0.0022	0.001	-26.17	5.808
12	60	290	1.5	0.028	0.0024	0.001	-25.79	5.450
13	60	295	1.5	0.037	0.0025	0.001	-25.33	5.065
14	60	300	1.5	0.044	0.0021	0.001	-24.99	4.677
15	61	305	1.5	0.052	0.0019	0.002	-24.66	4.237
16	60	310	1.5	0.062	0.0025	0.002	-24.29	3.975
17	60	315	1.5	0.070	0.0024	0.002	-24.00	3.803
18	61	320	1.5	0.081	0.0030	0.003	-23.70	3.592
19	60	325	1.5	0.095	0.0025	0.003	-23.36	3.300
20	60	330	1.5	0.113	0.0023	0.004	-23.02	2.890
21	61	335	1.5	0.131	0.0024	0.005	-22.72	2.597
22	61	340	1.5	0.156	0.0027	0.005	-22.39	2.372
23	61	345	1.5	0.181	0.0029	0.006	-22.07	2.190
24	61	350	1.5	0.201	0.0023	0.007	-21.81	1.934

Table 2.2 cont

25	61	340	1.5	0.117	0.0020	0.008	-22.23	2.144
26	60	330	1.5	0.071	0.0025	0.008	-22.66	2.489
27	61	320	1.5	0.039	0.0029	0.008	-23.23	3.100
28	60	310	1.5	0.021	0.0023	0.009	-23.80	3.612
29	61	300	1.5	0.011	0.0022	0.009	-24.47	4.090
30	61	305	1.5	0.016	0.0023	0.009	-24.12	3.749
31	61	310	1.5	0.019	0.0020	0.009	-23.89	3.486
32	61	315	1.5	0.029	0.0018	0.009	-23.47	2.974
33	61	320	1.5	0.037	0.0021	0.009	-23.21	2.775
34	60	325	1.5	0.049	0.0027	0.009	-22.88	2.671
35	60	330	1.5	0.060	0.0022	0.010	-22.66	2.506
36	60	335	1.5	0.075	0.0025	0.010	-22.39	2.251
37	61	340	1.5	0.098	0.0021	0.011	-22.10	1.983
38	60	345	1.5	0.118	0.0027	0.011	-21.84	1.838
39	61	350	1.5	0.147	0.0025	0.012	-21.58	1.687
40	31	355	3	0.096	0.0028	0.012	-21.28	2.003
41	31	360	3	0.117	0.0024	0.013	-21.03	1.760
42	31	365	3	0.144	0.0025	0.014	-20.77	1.537
43	31	370	3	0.173	0.0025	0.015	-20.53	1.401
44	31	375	3	0.203	0.0021	0.016	-20.30	1.209
45	31	380	3	0.246	0.0027	0.017	-20.04	1.079
46	31	385	3	0.250	0.0048	0.018	-19.94	1.271
47	31	390	3	0.260	0.0058	0.020	-19.83	1.396
48	31	395	3	0.307	0.0064	0.021	-19.59	1.319
49	31	400	3	0.359	0.0063	0.023	-19.35	1.193
50	30	390	3	0.240	0.0065	0.024	-19.65	1.427
51	31	380	3	0.185	0.0027	0.025	-19.90	1.338
52	31	370	3	0.117	0.0021	0.026	-20.33	1.222
53	30	360	3	0.071	0.0026	0.026	-20.77	1.500
54	31	350	3	0.047	0.0024	0.027	-21.21	1.822
55	31	375	3	0.138	0.0028	0.027	-20.11	1.063
56	31	360	3	0.070	0.0022	0.028	-20.77	1.533
57	30	345	3	0.036	0.0024	0.028	-21.39	1.943
58	31	330	3	0.018	0.0025	0.028	-22.13	2.585
59	31	315	3	0.007	0.0020	0.028	-23.03	3.346
60	31	300	3	0.004	0.0019	0.028	-23.52	3.675
61	31	309	3	0.007	0.0019	0.028	-23.03	3.164
62	31	315	3	0.007	0.0017	0.028	-22.99	3.080
63	30	320	3	0.008	0.0022	0.028	-22.84	3.042

Table 2.2 cont

64	30	325	3	0.013	0.0019	0.028	-22.41	2.692
65	31	330	3	0.016	0.0024	0.028	-22.24	2.567
66	31	335	3	0.019	0.0020	0.028	-22.05	2.403
67	31	340	3	0.023	0.0025	0.028	-21.83	2.234
68	30	345	3	0.034	0.0028	0.029	-21.43	2.052
69	30	350	3	0.042	0.0022	0.029	-21.21	1.833
70	31	355	3	0.055	0.0022	0.029	-20.97	1.528
71	30	360	3	0.069	0.0019	0.029	-20.69	1.307
72	31	365	3	0.087	0.0024	0.030	-20.47	1.179
73	30	370	3	0.105	0.0027	0.030	-20.23	1.157
74	31	375	3	0.132	0.0029	0.031	-20.02	1.058
75	31	380	3	0.165	0.0030	0.032	-19.77	0.955
76	30	385	3	0.194	0.0026	0.033	-19.55	0.836
77	30	390	3	0.222	0.0041	0.034	-19.38	0.837
78	**31**	**395**	**3**	**0.233**	**0.0045**	**0.035**	**-19.33**	**0.921**
79	**30**	**400**	**3**	**0.234**	**0.0045**	**0.037**	**-19.26**	**0.925**
80	**30**	**405**	**3**	**0.282**	**0.0050**	**0.038**	**-19.03**	**0.829**
81	**30**	**410**	**3**	**0.355**	**0.0068**	**0.040**	**-18.75**	**0.797**
82	**30**	**415**	**3**	**0.449**	**0.0064**	**0.042**	**-18.47**	**0.712**
83	**30**	**420**	**3**	**0.570**	**0.0127**	**0.045**	**-18.16**	**0.734**
84	**31**	**425**	**3**	**0.711**	**0.0050**	**0.049**	**-17.90**	**0.583**
85	**30**	**430**	**3**	**0.773**	**0.0041**	**0.053**	**-17.70**	**0.365**
86	**31**	**435**	**3**	**0.893**	**0.0041**	**0.057**	**-17.50**	**0.298**
87	**30**	**440**	**3**	**0.994**	**0.0035**	**0.063**	**-17.28**	**0.254**
88	**31**	**445**	**3**	**1.130**	**0.0040**	**0.068**	**-17.09**	**0.218**
89	**31**	**450**	**3**	**1.244**	**0.0042**	**0.075**	**-16.90**	**0.202**
90	**31**	**455**	**3**	**1.379**	**0.0039**	**0.082**	**-16.70**	**0.176**
91	**31**	**460**	**3**	**1.510**	**0.0037**	**0.090**	**-16.51**	**0.151**
92	**31**	**465**	**3**	**1.668**	**0.0040**	**0.098**	**-16.31**	**0.134**
93	**31**	**470**	**3**	**1.807**	**0.0050**	**0.108**	**-16.13**	**0.126**
94	**31**	**475**	**3**	**1.945**	**0.0046**	**0.118**	**-15.96**	**0.115**
95	**31**	**480**	**3**	**2.065**	**0.0052**	**0.129**	**-15.80**	**0.103**
96	**30**	**485**	**3**	**2.193**	**0.0050**	**0.140**	**-15.62**	**0.094**
97	**30**	**490**	**3**	**2.330**	**0.0049**	**0.152**	**-15.46**	**0.083**
98	**31**	**495**	**3**	**2.515**	**0.0055**	**0.165**	**-15.32**	**0.075**
99	**31**	**500**	**3**	**2.657**	**0.0056**	**0.179**	**-15.17**	**0.069**
100	30	490	3	1.644	0.0050	0.187	-15.55	0.089
101	31	480	3	1.096	0.0030	0.193	-15.94	0.088
102	31	470	3	0.740	0.0033	0.197	-16.31	0.091

Table 2.2 cont

103	31	460	3	0.427	0.0071	0.199	-16.84	0.166
104	31	450	3	0.250	0.0064	0.200	-17.36	0.286
105	31	440	3	0.231	0.0034	0.201	-17.43	0.228
106	30	430	3	0.160	0.0027	0.202	-17.76	0.214
107	31	420	3	0.107	0.0029	0.203	-18.20	0.271
108	31	410	3	0.072	0.0023	0.203	-18.58	0.344
109	31	400	3	0.047	0.0026	0.203	-19.02	0.458
110	31	405	3	0.059	0.0028	0.204	-18.78	0.399
111	30	410	3	0.069	0.0026	0.204	-18.59	0.352
112	31	415	3	0.082	0.0024	0.204	-18.44	0.290
113	31	420	3	0.101	0.0023	0.205	-18.24	0.239
114	30	425	3	0.125	0.0023	0.206	-17.99	0.196
115	31	430	3	0.152	0.0029	0.206	-17.82	0.184
116	30	435	3	0.185	0.0035	0.207	-17.59	0.186
117	30	440	3	0.218	0.0025	0.208	-17.42	0.155
118	31	445	3	0.235	0.0055	0.210	-17.37	0.183
119	30	450	3	0.236	0.0068	0.211	-17.33	0.253
120	31	455	3	0.265	0.0042	0.212	-17.23	0.209
121	30	460	3	0.328	0.0079	0.214	-16.98	0.189
122	31	465	3	0.418	0.0086	0.216	-16.76	0.196
123	30	470	3	0.529	0.0102	0.219	-16.48	0.178
124	31	475	3	0.713	0.0075	0.223	-16.19	0.133
125	31	480	3	0.811	0.0042	0.227	-16.04	0.092
126	31	485	3	0.930	0.0034	0.232	-15.88	0.064
127	30	490	3	1.062	0.0032	0.237	-15.69	0.055
128	31	495	3	1.242	0.0032	0.244	-15.53	0.049
129	31	500	3	1.415	0.0033	0.251	-15.37	0.045
130	31	505	3	1.574	0.0048	0.259	-15.22	0.046
131	31	510	3	1.755	0.0049	0.268	-15.07	0.046
132	30	515	3	1.924	0.0048	0.278	-14.90	0.042
133	30	520	3	2.107	0.0050	0.289	-14.76	0.039
134	31	525	3	2.334	0.0033	0.301	-14.64	0.034
135	31	530	3	2.578	0.0034	0.314	-14.48	0.029
136	31	535	3	2.802	0.0050	0.329	-14.34	0.029
137	30	540	3	2.934	0.0034	0.344	-14.20	0.027
138	30	545	3	3.131	0.0054	0.360	-14.07	0.025
139	*30*	*541*	*61.5*	*3.135*	*0.0050*	*0.376*	*-14.00*	*0.025*
140	31	555	3	3.542	0.0059	0.395	-13.85	0.022
141	31	560	3	3.647	0.0049	0.414	-13.75	0.021

Table 2.2 cont

142	31	565	3	3.846	0.0044	0.433	-13.62	0.018
143	31	570	3	4.051	0.0060	0.454	-13.49	0.017
144	31	575	3	4.097	0.0055	0.476	-13.41	0.017
145	31	580	3	4.232	0.0040	0.497	-13.30	0.015
146	30	585	3	4.268	0.0058	0.520	-13.18	0.014
147	30	590	3	4.339	0.0041	0.542	-13.08	0.013
148	31	595	3	4.486	0.0045	0.565	-13.00	0.011
149	31	600	3	4.663	0.0078	0.589	-12.88	0.011
150	30	590	3	3.129	0.0053	0.605	-13.17	0.014
151	31	580	3	2.188	0.0047	0.617	-13.51	0.013
152	30	570	3	1.531	0.0039	0.625	-13.80	0.014
153	30	560	3	1.078	0.0043	0.630	-14.13	0.015
154	30	550	3	0.773	0.0042	0.634	-14.44	0.018
155	31	540	3	0.495	0.0095	0.637	-14.91	0.032
156	31	530	3	0.328	0.0065	0.639	-15.32	0.049
157	31	520	3	0.240	0.0058	0.640	-15.62	0.051
158	30	510	3	0.223	0.0032	0.641	-15.66	0.040
159	31	500	3	0.166	0.0027	0.642	-15.98	0.037
160	31	505	3	0.194	0.0026	0.643	-15.82	0.029
161	30	510	3	0.219	0.0025	0.644	-15.67	0.026
162	30	515	3	0.240	0.0047	0.645	-15.57	0.031
163	30	520	3	0.241	0.0076	0.646	-15.56	0.048
164	30	525	3	0.251	0.0058	0.648	-15.51	0.050
165	31	530	3	0.291	0.0105	0.649	-15.39	0.051
166	31	535	3	0.376	0.0103	0.651	-15.13	0.050
167	30	540	3	0.446	0.0074	0.653	-14.92	0.038
168	31	545	3	0.564	0.0130	0.656	-14.71	0.034
169	31	550	3	0.722	0.0085	0.660	-14.45	0.029
170	30	555	3	0.780	0.0046	0.664	-14.32	0.019
171	30	560	3	0.898	0.0026	0.669	-14.17	0.012
172	31	565	3	1.041	0.0037	0.674	-14.03	0.010
173	31	570	3	1.174	0.0040	0.680	-13.89	0.010
174	30	575	3	1.300	0.0035	0.687	-13.73	0.009
175	31	580	3	1.477	0.0032	0.695	-13.61	0.008
176	30	585	3	1.631	0.0035	0.703	-13.44	0.008
177	31	590	3	1.834	0.0036	0.713	-13.32	0.007
178	30	595	3	2.006	0.0040	0.723	-13.16	0.007
179	31	600	3	2.197	0.0063	0.734	-13.05	0.007
180	31	605	3	2.751	0.0050	0.749	-12.77	0.006

Table 2.2 cont

181	31	610	3	2.531	0.0048	0.762	-12.79	0.006
182	31	615	3	2.704	0.0044	0.776	-12.66	0.005
183	30	620	3	2.741	0.0050	0.790	-12.55	0.005
184	31	625	3	2.896	0.0058	0.805	-12.45	0.005
185	31	630	3	2.918	0.0043	0.820	-12.36	0.004
186	30	635	3	2.919	0.0043	0.835	-12.23	0.004
187	31	640	3	2.950	0.0045	0.850	-12.16	0.004

Aliquot C015-20

Location Hall Peninsula

Step #	Time (min)	Average T (°C)	±	He (ncc)	±	f	ln(D/a^2)	±
1	*61*	*296*	*33*	*16.200*	*0.0171*	*0.014*	*-19.16*	*0.319*
2	**61**	**315**	**1.5**	**9.570**	**0.0242**	**0.023**	**-18.72**	**0.447**
3	**61**	**330**	**1.5**	**12.900**	**0.0281**	**0.034**	**-17.98**	**0.254**
4	**61**	**345**	**1.5**	**17.800**	**0.0552**	**0.049**	**-17.26**	**0.191**
5	**61**	**360**	**1.5**	**24.300**	**0.0361**	**0.071**	**-16.56**	**0.119**
6	**61**	**375**	**1.5**	**31.000**	**0.0382**	**0.098**	**-15.96**	**0.069**
7	**61**	**390**	**1.5**	**37.500**	**0.0431**	**0.131**	**-15.44**	**0.048**
8	**60**	**405**	**1.5**	**44.200**	**0.0688**	**0.169**	**-14.96**	**0.039**
9	**61**	**420**	**1.5**	**53.700**	**0.1514**	**0.216**	**-14.49**	**0.037**
10	61	435	1.5	62.200	0.0951	0.271	-14.05	0.028
11	60	450	1.5	70.600	0.1884	0.333	-13.63	0.021
12	61	442	1.5	36.200	0.0740	0.364	-14.12	0.030
13	61	432	1.5	22.500	0.0589	0.384	-14.50	0.023
14	61	422	1.5	12.900	0.0211	0.395	-14.99	0.022
15	61	412	1.5	8.730	0.0136	0.403	-15.35	0.016
16	61	402	1.5	5.740	0.0101	0.408	-15.74	0.016
17	61	392	1.5	4.040	0.0096	0.411	-16.08	0.017
18	61	382	1.5	2.730	0.0047	0.414	-16.46	0.018
19	61	386	1.5	2.910	0.0076	0.416	-16.39	0.014
20	61	396	1.5	3.990	0.0092	0.420	-16.06	0.013
21	61	406	1.5	5.490	0.0073	0.425	-15.72	0.011
22	61	416	1.5	7.550	0.0152	0.431	-15.38	0.011
23	61	426	1.5	9.510	0.0195	0.440	-15.13	0.012
24	61	436	1.5	12.900	0.0159	0.451	-14.79	0.010
25	61	446	3	15.900	0.0215	0.465	-14.53	0.009
26	61	456	1.5	22.400	0.0275	0.484	-14.13	0.008
27	61	466	1.5	27.400	0.0334	0.508	-13.85	0.007
28	61	476	1.5	33.200	0.0376	0.537	-13.56	0.007

Table 2.2 cont

29	60	486	1.5	35.400	0.0273	0.568	-13.37	0.006
30	61	496	1.5	34.600	0.0324	0.599	-13.31	0.005
31	61	488	1.5	22.500	0.0531	0.618	-13.65	0.008
32	61	478	1.5	14.300	0.0175	0.631	-14.04	0.008
33	61	468	3	9.830	0.0165	0.640	-14.38	0.006
34	61	458	1.5	6.600	0.0122	0.645	-14.75	0.007
35	61	448	1.5	4.440	0.0076	0.649	-15.13	0.007
36	61	450	0.75	4.460	0.0078	0.653	-15.11	0.005
37	61	460	1.5	5.840	0.0078	0.658	-14.82	0.004
38	61	470	1.5	7.280	0.0107	0.665	-14.58	0.004
39	61	480	1.5	10.000	0.0180	0.673	-14.23	0.004
40	61	485	1.5	10.800	0.0139	0.683	-14.12	0.004
41	61	490	1.5	10.700	0.0147	0.692	-14.09	0.004
42	61	495	1.5	11.200	0.0200	0.702	-14.01	0.004
43	61	500	1.5	13.300	0.0180	0.714	-13.79	0.004
44	60	505	1.5	12.300	0.0132	0.724	-13.81	0.004
45	60	510	1.5	12.700	0.0209	0.735	-13.73	0.004
46	61	515	1.5	12.000	0.0208	0.746	-13.75	0.004
47	61	520	1.5	12.100	0.0142	0.757	-13.70	0.003
48	61	525	1.5	12.400	0.0167	0.767	-13.62	0.003
49	61	530	3	12.600	0.0163	0.778	-13.56	0.003
50	61	535	3	14.000	0.0190	0.791	-13.39	0.003
51	61	540	1.5	13.400	0.0159	0.802	-13.37	0.003
52	60	545	1.5	11.700	0.0184	0.813	-13.43	0.003
53	61	550	3	12.300	0.0183	0.823	-13.34	0.002
54	61	555	1.5	12.700	0.0148	0.835	-13.24	0.002
55	60	560	1.5	11.100	0.0187	0.844	-13.29	0.002
56	60	550	1.5	7.340	0.0068	0.851	-13.65	0.002
57	61	540	1.5	5.260	0.0113	0.855	-13.96	0.002
58	61	530	1.5	3.650	0.0057	0.859	-14.30	0.003
59	61	520	1.5	3.100	0.0044	0.861	-14.44	0.002
60	61	510	1.5	2.100	0.0040	0.863	-14.81	0.002
61	61	500	1.5	1.540	0.0036	0.864	-15.11	0.002
62	61	510	1.5	1.930	0.0040	0.866	-14.87	0.002
63	61	520	1.5	2.230	0.0052	0.868	-14.71	0.002
64	61	530	1.5	2.630	0.0063	0.870	-14.53	0.002
65	60	540	1.5	3.200	0.0043	0.873	-14.29	0.002
66	61	550	1.5	4.080	0.0063	0.877	-14.04	0.001
67	61	560	1.5	5.770	0.0098	0.882	-13.65	0.001

Table 2.2 cont

68	61	570	3	5.790	0.0102	0.887	-13.60	0.002
69	61	580	3	6.800	0.0095	0.893	-13.39	0.001
70	61	590	3	7.750	0.0075	0.900	-13.19	0.001
71	60	600	1.5	8.160	0.0186	0.907	-13.08	0.000
72	60	610	1.5	9.200	0.0204	0.915	-12.88	0.000
73	60	620	1.5	9.390	0.0109	0.923	-12.77	0.000
74	61	610	1.5	5.510	0.0085	0.928	-13.23	0.000
75	61	600	1.5	3.820	0.0083	0.931	-13.54	0.000
76	61	590	1.5	2.930	0.0044	0.934	-13.77	0.000
77	61	580	1.5	1.850	0.0054	0.935	-14.19	0.000
78	61	570	1.5	1.290	0.0053	0.936	-14.53	0.000
79	61	560	1.5	1.060	0.0027	0.937	-14.71	0.000
80	61	550	1.5	0.828	0.0022	0.938	-14.95	0.000
81	61	540	1.5	0.608	0.0023	0.939	-15.25	0.000

Aliquot C015-21
Location Hall Peninsula

Step #	Time (min)	Average T (°C)	±	He (ncc)	±	f	ln(D/a^2)	±
1	**61**	**300**	**1.5**	**6.140**	**0.0100**	**0.008**	**-20.27**	**0.549**
2	**61**	**314**	**6**	**5.520**	**0.0041**	**0.015**	**-19.30**	**0.439**
3	**61**	**330**	**4.5**	**7.140**	**0.0131**	**0.025**	**-18.50**	**0.250**
4	**61**	**345**	**1.5**	**9.440**	**0.0110**	**0.037**	**-17.78**	**0.172**
5	**61**	**360**	**1.5**	**12.700**	**0.0063**	**0.054**	**-17.09**	**0.091**
6	**61**	**375**	**1.5**	**17.100**	**0.0174**	**0.077**	**-16.41**	**0.063**
7	**61**	**390**	**4.5**	**22.900**	**0.0288**	**0.107**	**-15.76**	**0.052**
8	**61**	**405**	**1.5**	**29.600**	**0.0332**	**0.146**	**-15.15**	**0.038**
9	**60**	**420**	**1.5**	**36.200**	**0.0499**	**0.194**	**-14.60**	**0.029**
10	**61**	**434**	**4.5**	**41.600**	**0.0588**	**0.249**	**-14.16**	**0.023**
11	**61**	**450**	**1.5**	**47.800**	**0.0441**	**0.312**	**-13.72**	**0.015**
12	61	442	1.5	26.700	0.0346	0.348	-14.09	0.018
13	61	432	1.5	15.300	0.0212	0.368	-14.53	0.017
14	61	422	1.5	9.770	0.0107	0.381	-14.92	0.015
15	60	412	4.5	6.110	0.0123	0.389	-15.33	0.016
16	61	402	1.5	4.430	0.0050	0.395	-15.64	0.015
17	61	392	1.5	2.790	0.0047	0.398	-16.08	0.014
18	60	381	4.5	1.790	0.0057	0.401	-16.50	0.019
19	60	386	4.5	2.270	0.0061	0.404	-16.25	0.015
20	61	396	1.5	3.020	0.0050	0.408	-15.97	0.012
21	61	406	1.5	4.360	0.0059	0.413	-15.59	0.009

Table 2.2 cont

22	61	416	1.5	5.850	0.0079	0.421	-15.27	0.009
23	60	426	1.5	7.700	0.0100	0.431	-14.94	0.009
24	60	436	1.5	10.600	0.0144	0.445	-14.58	0.008
25	61	446	1.5	13.400	0.0138	0.463	-14.30	0.007
26	61	456	4.5	16.400	0.0238	0.485	-14.03	0.007
27	61	466	4.5	19.400	0.0254	0.510	-13.78	0.007
28	60	476	1.5	22.700	0.0278	0.540	-13.50	0.006
29	60	486	1.5	26.200	0.0279	0.575	-13.25	0.005
30	61	496	4.5	27.900	0.0360	0.612	-13.07	0.005
31	61	488	4.5	16.300	0.0216	0.634	-13.50	0.007
32	61	478	4.5	10.100	0.0094	0.647	-13.92	0.006
33	61	468	1.5	6.330	0.0119	0.655	-14.34	0.006
34	60	458	1.5	4.090	0.0061	0.661	-14.74	0.006
35	60	448	1.5	2.720	0.0063	0.664	-15.13	0.006
36	61	450	1.5	2.820	0.0047	0.668	-15.10	0.005
37	60	460	1.5	4.030	0.0065	0.673	-14.70	0.004
38	61	470	1.5	5.550	0.0102	0.681	-14.38	0.004
39	61	480	4.5	6.910	0.0087	0.690	-14.12	0.004
40	61	485	1.5	7.560	0.0149	0.700	-14.00	0.004
41	60	490	1.5	8.040	0.0148	0.710	-13.88	0.004
42	61	495	3	8.560	0.0096	0.722	-13.79	0.003
43	61	500	4.5	8.890	0.0134	0.734	-13.70	0.003
44	61	505	1.5	9.350	0.0110	0.746	-13.60	0.003
45	61	510	4.5	9.820	0.0163	0.759	-13.49	0.003
46	60	515	1.5	10.000	0.0121	0.772	-13.39	0.003
47	61	520	1.5	10.100	0.0193	0.785	-13.34	0.003
48	61	525	1.5	10.400	0.0100	0.799	-13.24	0.002
49	61	530	1.5	10.500	0.0146	0.813	-13.15	0.002
50	61	535	1.5	9.940	0.0119	0.826	-13.13	0.002
51	61	540	1.5	9.970	0.0107	0.839	-13.05	0.002
52	61	545	1.5	9.860	0.0126	0.852	-12.97	0.002
53	60	550	1.5	9.620	0.0125	0.865	-12.88	0.002
54	60	555	1.5	8.970	0.0093	0.877	-12.86	0.001
55	61	560	1.5	8.960	0.0182	0.889	-12.77	0.001
56	60	550	1.5	5.670	0.0069	0.896	-13.11	0.002
57	60	540	3	3.630	0.0059	0.901	-13.53	0.000
58	60	530	3	2.410	0.0058	0.904	-13.90	0.000
59	60	520	3	1.650	0.0029	0.907	-14.25	0.000
60	60	510	1.5	1.130	0.0033	0.908	-14.61	0.000

Table 2.2 cont

61	61	500	1.5	0.786	0.0032	0.909	-14.97	0.000
62	61	510	1.5	1.050	0.0025	0.910	-14.67	0.000
63	61	520	1.5	1.410	0.0037	0.912	-14.36	0.000
64	60	530	1.5	2.080	0.0044	0.915	-13.92	0.000
65	60	540	1.5	2.900	0.0049	0.919	-13.55	0.000
66	60	550	3	3.590	0.0070	0.924	-13.29	0.000
67	60	560	1.5	4.080	0.0069	0.929	-13.09	0.000
68	61	570	1.5	4.500	0.0057	0.935	-12.93	0.000
69	61	580	3	5.500	0.0080	0.942	-12.63	0.000
70	60	590	1.5	6.530	0.0090	0.951	-12.30	0.000
71	61	600	3	10.100	0.0118	0.964	-11.64	0.000
72	61	610	1.5	7.490	0.0103	0.974	-11.62	0.000
73	61	620	1.5	5.360	0.0112	0.981	-11.63	0.000
74	61	610	1.5	2.460	0.0060	0.985	-12.15	0.000
75	61	600	1.5	1.340	0.0036	0.986	-12.60	0.000
76	61	590	1.5	0.823	0.0019	0.987	-12.98	0.000
77	60	580	1.5	0.515	0.0025	0.988	-13.37	0.000
78	60	570	1.5	0.355	0.0009	0.989	-13.69	0.000
79	60	560	1.5	0.245	0.0013	0.989	-14.03	0.000
80	60	550	1.5	0.174	0.0012	0.989	-14.35	0.000
81	60	540	1.5	0.118	0.0022	0.989	-14.72	0.000

Aliquot C015-24
Location Hall Peninsula

Step #	Time (min)	Average T (°C)	±	He (ncc)	±	f	ln(D/a^2)	±
1	**61**	**300**	**1.5**	**13.340**	**0.0157**	**0.030**	**-17.64**	**0.165**
2	**61**	**315**	**1.5**	**10.966**	**0.0201**	**0.055**	**-16.77**	**0.168**
3	**60**	**330**	**1.5**	**12.902**	**0.0151**	**0.084**	**-16.07**	**0.088**
4	**60**	**345**	**1.5**	**15.355**	**0.0218**	**0.119**	**-15.49**	**0.056**
5	**61**	**360**	**1.5**	**18.519**	**0.0147**	**0.161**	**-14.97**	**0.036**
6	61	375	1.5	21.686	0.0271	0.210	-14.49	0.026
7	61	390	1.5	24.472	0.0322	0.266	-14.07	0.022
8	61	405	1.5	26.985	0.0458	0.327	-13.69	0.018
9	61	420	1.5	28.739	0.0319	0.392	-13.36	0.013
10	61	435	1.5	29.689	0.0357	0.459	-13.07	0.010
11	61	450	1.5	29.925	0.0247	0.527	-12.82	0.007
12	60	442	1.5	14.789	0.0236	0.560	-13.33	0.010
13	61	432	1.5	8.217	0.0167	0.579	-13.84	0.010
14	61	422	1.5	4.872	0.0091	0.590	-14.31	0.010

Table 2.2 cont

15	61	412	1.5	2.977	0.0059	0.597	-14.77	0.009
16	60	402	1.5	1.896	0.0044	0.601	-15.19	0.009
17	61	392	1.5	1.242	0.0032	0.604	-15.61	0.010
18	60	382	1.5	0.822	0.0030	0.606	-16.00	0.011
19	61	386	1.5	0.901	0.0026	0.608	-15.92	0.009
20	61	396	1.5	1.235	0.0030	0.611	-15.59	0.007
21	61	406	1.5	1.759	0.0051	0.615	-15.23	0.007
22	61	416	1.5	2.552	0.0053	0.620	-14.84	0.006
23	61	426	1.5	3.640	0.0073	0.629	-14.46	0.005
24	61	436	1.5	4.945	0.0088	0.640	-14.12	0.005
25	61	446	1.5	6.475	0.0122	0.654	-13.80	0.005
26	61	456	1.5	8.270	0.0109	0.673	-13.49	0.004
27	61	466	1.5	9.985	0.0131	0.696	-13.22	0.004
28	61	476	1.5	11.670	0.0195	0.722	-12.97	0.004
29	61	486	1.5	12.212	0.0162	0.750	-12.81	0.003
30	61	496	1.5	12.647	0.0135	0.779	-12.64	0.003
31	60	488	1.5	7.369	0.0088	0.795	-13.05	0.003
32	61	478	1.5	4.422	0.0058	0.805	-13.51	0.003
33	61	468	1.5	2.759	0.0067	0.812	-13.94	0.003
34	61	458	1.5	1.781	0.0032	0.816	-14.35	0.004
35	61	448	1.5	1.168	0.0036	0.818	-14.75	0.004
36	61	450	1.5	1.216	0.0049	0.821	-14.69	0.004
37	61	460	1.5	1.694	0.0040	0.825	-14.34	0.003
38	61	470	1.5	2.361	0.0051	0.830	-13.98	0.002
39	61	480	1.5	3.166	0.0055	0.837	-13.65	0.002
40	61	485	1.5	3.481	0.0064	0.845	-13.50	0.002
41	61	490	1.5	3.702	0.0034	0.854	-13.39	0.002
42	61	495	1.5	3.963	0.0066	0.863	-13.26	0.002
43	61	500	1.5	4.057	0.0063	0.872	-13.16	0.002
44	61	505	1.5	4.148	0.0090	0.881	-13.06	0.002
45	61	510	1.5	4.168	0.0066	0.891	-12.97	0.002
46	61	515	1.5	4.722	0.0082	0.901	-12.77	0.000
47	61	520	1.5	4.262	0.0097	0.911	-12.77	0.000
48	61	525	1.5	4.147	0.0071	0.920	-12.69	0.000
49	61	530	1.5	3.991	0.0059	0.929	-12.61	0.000
50	61	535	1.5	3.776	0.0078	0.938	-12.54	0.000
51	61	540	1.5	3.599	0.0060	0.946	-12.45	0.000
52	61	545	1.5	3.259	0.0082	0.954	-12.41	0.000
53	60	549	4.5	2.870	0.0048	0.960	-12.37	0.000

Table 2.2 cont

54	61	555	1.5	2.648	0.0046	0.966	-12.31	0.000
55	61	560	1.5	2.320	0.0050	0.971	-12.28	0.000
56	61	550	1.5	1.325	0.0036	0.974	-12.70	0.000
57	61	540	1.5	0.828	0.0026	0.976	-13.08	0.000
58	60	530	1.5	0.529	0.0020	0.977	-13.44	0.000
59	61	520	1.5	0.355	0.0017	0.978	-13.81	0.000
60	61	510	3	0.235	0.0014	0.979	-14.20	0.000
61	61	500	3	0.156	0.0019	0.979	-14.58	0.000
62	61	510	3	0.211	0.0013	0.980	-14.26	0.000
63	61	520	1.5	0.290	0.0015	0.980	-13.92	0.000
64	61	530	3	0.378	0.0022	0.981	-13.62	0.000
65	61	540	3	0.476	0.0027	0.982	-13.33	0.000
66	61	550	1.5	0.591	0.0026	0.983	-13.05	0.000
67	61	560	1.5	0.693	0.0022	0.985	-12.80	0.000
68	61	570	1.5	0.773	0.0032	0.987	-12.58	0.000
69	*61*	*573*	*60*	*0.785*	*0.0027*	*0.989*	*-12.43*	*0.000*
70	61	590	1.5	0.832	0.0031	0.990	-12.21	0.000
71	61	600	1.5	0.780	0.0027	0.992	-12.08	0.000
72	61	610	1.5	0.693	0.0030	0.994	-11.99	0.000
73	61	620	1.5	0.581	0.0027	0.995	-11.93	0.000
74	61	610	1.5	0.298	0.0018	0.996	-12.41	0.000
75	61	600	1.5	0.172	0.0017	0.996	-12.83	0.000
76	61	590	1.5	0.107	0.0020	0.996	-13.22	0.000
77	61	580	3	0.072	0.0011	0.997	-13.57	0.000
78	61	570	3	0.049	0.0011	0.997	-13.91	0.000
79	61	560	3	0.035	0.0009	0.997	-14.23	0.000
80	60	550	1.5	0.024	0.0007	0.997	-14.57	0.000
81	61	540	3	0.017	0.0007	0.997	-14.89	0.000

Aliquot C015-27

Location Hall Peninsula

Step #	**Time (min)**	**Average T (°C)**	**±**	**He (ncc)**	**±**	**f**	**ln(D/a^2)**	**±**
1	60	300	9	3.163	0.0112	0.006	-20.75	1.124
2	61	300	6	1.745	0.0093	0.010	-20.42	1.395
3	61	300	6	1.363	0.0063	0.013	-20.34	1.093
4	61	300	6	1.156	0.0052	0.015	-20.30	0.898
5	**61**	**315**	**4.5**	**1.908**	**0.0081**	**0.019**	**-19.59**	**0.613**
6	**61**	**330**	**6**	**3.181**	**0.0116**	**0.025**	**-18.81**	**0.473**
7	**61**	**345**	**6**	**4.968**	**0.0165**	**0.035**	**-18.04**	**0.352**

Table 2.2 cont

8	**61**	**359**	**6**	**7.097**	**0.0189**	**0.049**	**-17.34**	**0.250**
9	**61**	**375**	**6**	**9.815**	**0.0150**	**0.069**	**-16.66**	**0.158**
10	**61**	**390**	**7.5**	**12.821**	**0.0445**	**0.094**	**-16.05**	**0.131**
11	**61**	**405**	**7.5**	**16.316**	**0.0454**	**0.127**	**-15.48**	**0.104**
12	**61**	**420**	**9**	**19.522**	**0.0411**	**0.166**	**-14.99**	**0.071**
13	61	435	1.5	21.993	0.0590	0.210	-14.58	0.055
14	61	450	1.5	24.779	0.0647	0.260	-14.19	0.044
15	61	442	1.5	12.963	0.0178	0.286	-14.65	0.052
16	61	432	4.5	7.598	0.0261	0.301	-15.09	0.043
17	61	422	1.5	4.604	0.0130	0.310	-15.54	0.048
18	61	412	9	2.857	0.0106	0.316	-15.98	0.046
19	60	402	1.5	1.799	0.0130	0.319	-16.41	0.058
20	61	392	1.5	1.179	0.0071	0.322	-16.84	0.067
21	61	382	6	0.759	0.0058	0.323	-17.27	0.067
22	61	386	6	0.851	0.0081	0.325	-17.15	0.059
23	61	396	7.5	1.251	0.0076	0.328	-16.75	0.047
24	61	406	9	1.826	0.0082	0.331	-16.36	0.036
25	61	416	1.5	2.465	0.0113	0.336	-16.04	0.034
26	61	426	1.5	3.612	0.0145	0.343	-15.64	0.031
27	61	436	1.5	4.927	0.0149	0.353	-15.29	0.028
28	61	446	1.5	6.498	0.0209	0.366	-14.97	0.026
29	61	456	1.5	8.397	0.0247	0.383	-14.65	0.024
30	61	466	1.5	10.508	0.0431	0.404	-14.36	0.025
31	61	476	1.5	16.310	0.0590	0.437	-13.81	0.021
32	61	486	1.5	17.612	0.0488	0.472	-13.61	0.020
33	61	496	1.5	18.249	0.0685	0.508	-13.45	0.018
34	61	488	1.5	8.366	0.0262	0.525	-14.14	0.028
35	61	478	1.5	4.684	0.0164	0.535	-14.67	0.022
36	61	468	1.5	3.234	0.0159	0.541	-15.01	0.021
37	61	458	1.5	2.169	0.0064	0.545	-15.39	0.022
38	61	448	3	1.416	0.0069	0.548	-15.81	0.020
39	61	450	7.5	1.462	0.0094	0.551	-15.76	0.020
40	60	460	1.5	1.947	0.0059	0.555	-15.45	0.015
41	60	470	1.5	2.765	0.0170	0.561	-15.08	0.015
42	61	480	1.5	3.837	0.0111	0.568	-14.75	0.014
43	61	485	1.5	4.305	0.0141	0.577	-14.60	0.013
44	60	490	1.5	4.577	0.0152	0.586	-14.49	0.013
45	61	495	1.5	5.044	0.0110	0.596	-14.38	0.011
46	*60*	*496*	*27*	*5.697*	*0.0156*	*0.608*	*-14.20*	*0.010*

Table 2.2 cont

47	61	505	1.5	6.717	0.0167	0.621	-14.01	0.010
48	61	510	1.5	6.134	0.0145	0.633	-14.05	0.010
49	61	515	1.5	6.793	0.0178	0.647	-13.90	0.009
50	60	520	1.5	7.254	0.0229	0.661	-13.77	0.009
51	61	525	1.5	7.770	0.0221	0.677	-13.66	0.009
52	61	530	1.5	7.929	0.0240	0.693	-13.57	0.009
53	61	535	1.5	8.127	0.0310	0.709	-13.49	0.009
54	61	540	1.5	7.917	0.0198	0.725	-13.45	0.008
55	60	545	1.5	7.458	0.0262	0.740	-13.42	0.007
56	60	550	1.5	7.951	0.0274	0.756	-13.29	0.007
57	60	555	1.5	8.142	0.0184	0.772	-13.19	0.006
58	60	560	1.5	7.769	0.0277	0.788	-13.16	0.006
59	61	550	1.5	4.968	0.0166	0.797	-13.56	0.007
60	60	540	1.5	3.068	0.0146	0.804	-13.98	0.008
61	60	530	1.5	2.050	0.0058	0.808	-14.36	0.007
62	61	520	1.5	1.437	0.0085	0.811	-14.71	0.007
63	60	510	1.5	0.996	0.0049	0.813	-15.05	0.008
64	60	500	1.5	0.657	0.0064	0.814	-15.45	0.010
65	61	510	1.5	0.845	0.0063	0.816	-15.21	0.008
66	61	520	1.5	1.205	0.0101	0.818	-14.84	0.007
67	61	530	1.5	1.613	0.0084	0.821	-14.54	0.006
68	61	540	1.5	2.259	0.0107	0.826	-14.18	0.005
69	61	550	1.5	2.851	0.0122	0.831	-13.91	0.005
70	61	560	1.5	4.165	0.0137	0.840	-13.49	0.004
71	61	570	1.5	4.605	0.0135	0.849	-13.33	0.004
72	60	580	1.5	5.312	0.0130	0.860	-13.10	0.003
73	61	590	1.5	6.098	0.0225	0.872	-12.89	0.003
74	60	600	1.5	6.667	0.0167	0.885	-12.67	0.003
75	60	610	1.5	7.460	0.0196	0.900	-12.45	0.000
76	61	620	1.5	7.601	0.0192	0.915	-12.30	0.000
77	60	610	1.5	4.043	0.0123	0.923	-12.78	0.000
78	60	600	1.5	2.717	0.0112	0.929	-13.09	0.000
79	60	590	1.5	1.754	0.0090	0.932	-13.46	0.000
80	60	580	1.5	1.166	0.0067	0.935	-13.83	0.000
81	60	570	1.5	0.792	0.0077	0.936	-14.18	0.000
82	61	560	1.5	0.570	0.0099	0.937	-14.51	0.000
83	61	550	1.5	0.413	0.0040	0.938	-14.82	0.000
84	60	540	1.5	0.280	0.0039	0.939	-15.18	0.000

Table 2.2 cont

Aliquot C015-28

Location Hall Peninsula

Step #	Time (min)	Average T (°C)	±	He (ncc)	±	f	ln(D/a^2)	±
1	61	300	1.5	9.692	0.0143	0.018	-18.68	0.382
2	61	300	13.5	5.347	0.0238	0.028	-18.32	0.569
3	60	300	12	3.897	0.0127	0.035	-18.30	0.466
4	61	300	12	3.184	0.0141	0.041	-18.32	0.370
5	**61**	**315**	**4.5**	**4.949**	**0.0128**	**0.050**	**-17.69**	**0.227**
6	**60**	**329**	**6**	**7.266**	**0.0216**	**0.064**	**-17.06**	**0.173**
7	**61**	**345**	**1.5**	**10.212**	**0.0201**	**0.083**	**-16.47**	**0.128**
8	**61**	**360**	**3**	**14.039**	**0.0357**	**0.109**	**-15.87**	**0.097**
9	**61**	**375**	**1.5**	**17.635**	**0.0319**	**0.141**	**-15.35**	**0.073**
10	**60**	**389**	**7.5**	**21.544**	**0.0243**	**0.181**	**-14.84**	**0.048**
11	**60**	**404**	**7.5**	**25.543**	**0.0474**	**0.229**	**-14.39**	**0.038**
12	61	420	7.5	29.353	0.0656	0.283	-13.99	0.033
13	61	434	7.5	31.575	0.0557	0.342	-13.66	0.026
14	60	450	1.5	35.132	0.0619	0.407	-13.28	0.019
15	60	442	1.5	17.952	0.0528	0.440	-13.77	0.027
16	61	432	6	10.180	0.0238	0.459	-14.26	0.025
17	60	421	7.5	6.114	0.0212	0.470	-14.69	0.023
18	61	412	4.5	3.950	0.0122	0.478	-15.11	0.024
19	61	401	9	2.546	0.0118	0.482	-15.53	0.025
20	61	392	3	1.616	0.0072	0.485	-15.97	0.028
21	61	382	1.5	1.044	0.0060	0.487	-16.40	0.029
22	61	386	1.5	1.179	0.0067	0.489	-16.27	0.023
23	*61*	*396*	*3*	*0.252*	*0.0071*	*0.490*	*0.00*	*0.000*
24	61	406	3	2.483	0.0063	0.494	-15.51	0.012
25	61	415	7.5	3.488	0.0103	0.501	-15.15	0.013
26	60	426	9	4.898	0.0157	0.510	-14.77	0.014
27	60	436	1.5	6.518	0.0144	0.522	-14.45	0.012
28	61	446	3	8.625	0.0179	0.538	-14.13	0.011
29	61	456	1.5	11.407	0.0352	0.559	-13.79	0.011
30	60	466	1.5	16.132	0.0348	0.589	-13.33	0.010
31	61	476	1.5	17.946	0.0326	0.622	-13.13	0.009
32	61	486	1.5	18.875	0.0315	0.657	-12.96	0.007
33	61	496	1.5	19.313	0.0344	0.693	-12.80	0.007
34	61	488	1.5	11.110	0.0215	0.714	-13.24	0.008
35	61	478	1.5	6.532	0.0229	0.726	-13.70	0.009
36	61	468	1.5	4.106	0.0180	0.734	-14.12	0.010

Table 2.2 cont

37	61	458	1.5	2.657	0.0141	0.738	-14.53	0.011
38	61	448	1.5	1.759	0.0071	0.742	-14.93	0.011
39	61	450	1.5	1.832	0.0081	0.745	-14.87	0.008
40	61	460	1.5	2.494	0.0125	0.750	-14.54	0.007
41	61	470	1.5	3.381	0.0095	0.756	-14.22	0.006
42	61	480	1.5	4.431	0.0170	0.764	-13.91	0.006
43	61	485	1.5	4.826	0.0192	0.773	-13.79	0.006
44	61	490	1.5	5.201	0.0142	0.783	-13.67	0.006
45	61	495	1.5	5.396	0.0296	0.793	-13.58	0.006
46	61	500	1.5	5.643	0.0203	0.803	-13.48	0.006
47	61	505	1.5	5.790	0.0268	0.814	-13.40	0.006
48	61	510	1.5	6.294	0.0255	0.826	-13.25	0.005
49	61	515	1.5	6.348	0.0180	0.837	-13.17	0.004
50	61	520	1.5	6.199	0.0200	0.849	-13.12	0.004
51	61	525	1.5	6.162	0.0155	0.860	-13.04	0.003
52	61	530	1.5	5.988	0.0227	0.871	-12.98	0.003
53	61	535	1.5	5.768	0.0190	0.882	-12.93	0.003
54	61	540	1.5	5.418	0.0187	0.892	-12.89	0.003
55	61	545	1.5	5.233	0.0192	0.902	-12.86	0.000
56	61	550	1.5	4.947	0.0246	0.911	-12.82	0.000
57	61	555	1.5	4.718	0.0190	0.920	-12.76	0.000
58	61	560	1.5	4.464	0.0133	0.928	-12.71	0.000
59	60	550	1.5	2.674	0.0088	0.933	-13.12	0.000
60	61	540	1.5	1.767	0.0090	0.936	-13.49	0.000
61	61	530	1.5	1.196	0.0066	0.939	-13.83	0.000
62	61	520	1.5	0.818	0.0061	0.940	-14.18	0.000
63	61	510	1.5	0.565	0.0102	0.941	-14.53	0.000
64	60	500	1.5	0.401	0.0038	0.942	-14.84	0.000
65	60	510	1.5	0.518	0.0082	0.943	-14.57	0.000
66	60	520	1.5	0.683	0.0050	0.944	-14.28	0.000
67	61	530	1.5	0.891	0.0054	0.946	-14.00	0.000
68	61	540	1.5	1.151	0.0049	0.948	-13.71	0.000
69	60	550	1.5	1.423	0.0092	0.950	-13.44	0.000
70	61	560	1.5	1.749	0.0093	0.954	-13.19	0.000
71	61	570	1.5	2.025	0.0079	0.957	-12.96	0.000
72	60	580	1.5	2.225	0.0099	0.962	-12.76	0.000
73	60	590	1.5	2.331	0.0101	0.966	-12.60	0.000
74	61	600	1.5	2.384	0.0112	0.970	-12.47	0.000
75	60	610	1.5	2.319	0.0086	0.975	-12.33	0.000

Table 2.2 cont

76	61	620	1.5	2.132	0.0107	0.979	-12.27	0.000
77	60	610	1.5	1.157	0.0056	0.981	-12.73	0.000
78	61	600	1.5	0.742	0.0051	0.982	-13.10	0.000
79	60	590	1.5	0.495	0.0060	0.983	-13.42	0.000
80	61	580	1.5	0.342	0.0041	0.984	-13.76	0.000
81	61	570	1.5	0.242	0.0042	0.984	-14.07	0.000
82	61	560	1.5	0.172	0.0032	0.984	-14.39	0.000
83	61	550	1.5	0.118	0.0028	0.985	-14.75	0.000
84	60	540	1.5	0.089	0.0024	0.985	-15.00	0.000

Aliquot Dalam-1

Location Grasberg Igneous Complex

Step #	**Time (min)**	**Average T (°C)**	**±**	**He (ncc)**	**±**	**f**	**ln(D/a^2)**	**±**
1	91	400	1.5	0.116	0.0033	0.020	-18.86	1.778
2	91	400	1.5	0.114	0.0039	0.040	-17.76	1.646
3	**91**	**400**	**1.5**	**0.039**	**0.0028**	**0.047**	**-18.46**	**2.078**
4	**91**	**410**	**1.5**	**0.048**	**0.0028**	**0.055**	**-18.07**	**1.514**
5	**91**	**420**	**1.5**	**0.058**	**0.0028**	**0.065**	**-17.72**	**1.291**
6	**91**	**430**	**1.5**	**0.068**	**0.0025**	**0.077**	**-17.38**	**1.062**
7	**91**	**440**	**1.5**	**0.073**	**0.0028**	**0.089**	**-17.14**	**0.934**
8	**91**	**450**	**1.5**	**0.089**	**0.0040**	**0.105**	**-16.77**	**0.842**
9	**91**	**460**	**1.5**	**0.096**	**0.0026**	**0.121**	**-16.54**	**0.726**
10	**91**	**470**	**1.5**	**0.108**	**0.0039**	**0.140**	**-16.25**	**0.602**
11	**90**	**480**	**1.5**	**0.109**	**0.0042**	**0.159**	**-16.08**	**0.604**
12	120	482	1.5	0.115	0.0051	0.179	-16.17	0.561
13	121	472	1.5	0.069	0.0035	0.191	-16.59	0.694
14	121	462	1.5	0.041	0.0028	0.198	-17.05	0.741
15	121	452	1.5	0.026	0.0027	0.203	-17.46	0.846
16	121	442	1.5	0.018	0.0026	0.206	-17.82	0.999
17	121	432	1.5	0.012	0.0023	0.208	-18.22	1.189
18	121	422	1.5	0.007	0.0023	0.209	-18.79	1.553
19	121	412	1.5	0.005	0.0024	0.210	-19.15	1.822
20	121	402	1.5	0.003	0.0024	0.211	-19.46	2.083
21	121	405	1.5	0.003	0.0023	0.211	-19.46	2.064
22	121	420	1.5	0.007	0.0023	0.212	-18.73	1.468
23	121	435	1.5	0.012	0.0027	0.214	-18.16	1.134
24	121	450	1.5	0.023	0.0028	0.218	-17.52	0.822
25	121	465	1.5	0.036	0.0027	0.225	-17.03	0.613
26	121	480	1.5	0.057	0.0030	0.234	-16.52	0.453

Table 2.2 cont

27	120	495	1.5	0.080	0.0044	0.248	-16.11	0.419
28	120	510	1.5	0.129	0.0052	0.271	-15.54	0.338
29	121	525	1.5	0.122	0.0043	0.292	-15.50	0.337
30	121	540	1.5	0.133	0.0036	0.315	-15.32	0.264
31	120	536	1.5	0.094	0.0033	0.331	-15.57	0.296
32	120	526	1.5	0.044	0.0026	0.339	-16.27	0.424
33	120	516	1.5	0.027	0.0024	0.344	-16.76	0.490
34	121	506	1.5	0.017	0.0026	0.346	-17.22	0.645
35	150	496	1.5	0.014	0.0025	0.349	-17.57	0.697
36	151	486	1.5	0.010	0.0025	0.351	-17.94	0.871
37	151	476	1.5	0.007	0.0024	0.352	-18.29	1.060
38	151	466	1.5	0.004	0.0024	0.353	-18.78	1.376
39	151	456	1.5	0.002	0.0023	0.353	-19.38	1.818

Aliquot Dalam-2

Location Grasberg Igneous Complex

Step #	Time (min)	Average T (°C)	±	He (ncc)	±	f	ln(D/a^2)	±
1	*91*	*379*	*19.5*	*0.067*	*0.0050*	*0.012*	*-19.92*	*2.945*
2	90	400	1.5	0.089	0.0056	0.028	-18.40	2.457
3	90	400	1.5	0.061	0.0047	0.038	-18.27	2.308
4	**90**	**410**	**1.5**	**0.065**	**0.0048**	**0.050**	**-17.90**	**1.888**
5	**90**	**420**	**1.5**	**0.069**	**0.0046**	**0.062**	**-17.60**	**1.645**
6	**91**	**430**	**1.5**	**0.074**	**0.0050**	**0.075**	**-17.32**	**1.451**
7	**91**	**440**	**1.5**	**0.076**	**0.0048**	**0.088**	**-17.10**	**1.305**
8	**91**	**450**	**1.5**	**0.076**	**0.0047**	**0.102**	**-16.94**	**1.176**
9	**91**	**460**	**1.5**	**0.081**	**0.0050**	**0.116**	**-16.73**	**1.050**
10	**91**	**470**	**1.5**	**0.085**	**0.0047**	**0.131**	**-16.54**	**0.946**
11	**91**	**480**	**1.5**	**0.090**	**0.0049**	**0.147**	**-16.35**	**0.838**
12	**121**	**482**	**1.5**	**0.095**	**0.0047**	**0.163**	**-16.46**	**0.756**
13	121	472	1.5	0.051	0.0049	0.172	-16.98	1.016
14	121	462	1.5	0.032	0.0046	0.178	-17.41	1.187
15	120	452	1.5	0.019	0.0046	0.181	-17.88	1.450
16	121	442	1.5	0.012	0.0044	0.184	-18.34	1.751
17	120	432	1.5	0.008	0.0044	0.185	-18.68	1.996
18	120	422	1.5	0.005	0.0043	0.186	-19.19	2.422
19	120	412	1.5	0.003	0.0043	0.186	-19.64	2.806
20	120	402	1.5	0.001	0.0043	0.187	-20.65	3.766
21	120	405	1.5	0.002	0.0043	0.187	-20.12	3.247
22	120	420	1.5	0.004	0.0044	0.188	-19.31	2.510

Table 2.2 cont

23	120	435	1.5	0.008	0.0044	0.189	-18.68	1.974
24	120	450	1.5	0.014	0.0046	0.192	-18.15	1.579
25	121	465	1.5	0.024	0.0047	0.196	-17.56	1.192
26	121	480	1.5	0.034	0.0048	0.202	-17.18	0.995
27	121	495	1.5	0.049	0.0045	0.211	-16.79	0.791
28	121	510	1.5	0.064	0.0052	0.222	-16.46	0.675
29	121	524	3	0.071	0.0053	0.234	-16.30	0.650
30	*120*	*519*	*28.5*	*0.070*	*0.0048*	*0.247*	*-16.23*	*0.616*
31	121	529	13.5	0.056	0.0054	0.257	-16.41	0.686
32	121	526	1.5	0.037	0.0047	0.263	-16.79	0.843
33	121	516	1.5	0.022	0.0046	0.267	-17.26	1.040
34	121	506	1.5	0.015	0.0047	0.270	-17.64	1.248
35	150	496	1.5	0.013	0.0049	0.272	-17.97	1.334
36	151	486	1.5	0.009	0.0045	0.273	-18.40	1.634
37	151	476	1.5	0.005	0.0045	0.274	-18.84	1.939
38	150	466	1.5	0.003	0.0043	0.275	-19.44	2.447
39	151	456	1.5	0.002	0.0043	0.275	-19.82	2.759

Aliquot MGI-1

Location Grasberg Igneous Complex

Step #	Time (min)	Average T (°C)	±	He (ncc)	±	f	ln(D/a^2)	±
1	120	400	1.5	1.385	0.0038	0.073	-16.55	0.168
2	120	400	1.5	0.311	0.0020	0.090	-17.17	0.446
3	**120**	**400**	**1.5**	**0.251**	**0.0023**	**0.103**	**-17.21**	**0.265**
4	**120**	**410**	**1.5**	**0.297**	**0.0015**	**0.119**	**-16.89**	**0.184**
5	**120**	**420**	**1.5**	**0.347**	**0.0017**	**0.137**	**-16.57**	**0.132**
6	**120**	**430**	**1.5**	**0.385**	**0.0026**	**0.158**	**-16.31**	**0.128**
7	120	440	1.5	0.401	0.0025	0.179	-16.12	0.120
8	120	450	1.5	0.373	0.0020	0.199	-16.05	0.104
9	120	460	1.5	0.335	0.0027	0.216	-16.05	0.104
10	120	470	1.5	0.279	0.0040	0.231	-16.14	0.137
11	121	480	1.5	0.247	0.0027	0.244	-16.20	0.139
12	181	482	1.5	0.247	0.0018	0.257	-16.53	0.097
13	181	472	1.5	0.123	0.0015	0.264	-17.18	0.136
14	180	462	1.5	0.072	0.0013	0.268	-17.69	0.166
15	180	452	1.5	0.047	0.0009	0.270	-18.09	0.179
16	180	442	1.5	0.031	0.0008	0.272	-18.49	0.199
17	180	432	1.5	0.021	0.0009	0.273	-18.86	0.265
18	180	422	1.5	0.015	0.0008	0.274	-19.25	0.351

Table 2.2 cont

19	180	412	1.5	0.010	0.0007	0.274	-19.62	0.421
20	181	402	1.5	0.007	0.0005	0.275	-19.95	0.458
21	180	405	1.5	0.007	0.0005	0.275	-19.94	0.394
22	180	420	1.5	0.012	0.0007	0.276	-19.46	0.306
23	180	435	1.5	0.020	0.0008	0.277	-18.89	0.238
24	180	450	1.5	0.038	0.0010	0.279	-18.28	0.173
25	181	465	1.5	0.057	0.0015	0.282	-17.87	0.158
26	181	480	1.5	0.093	0.0012	0.287	-17.35	0.110
27	180	495	1.5	0.143	0.0038	0.294	-16.88	0.125
28	181	510	1.5	0.220	0.0055	0.306	-16.41	0.139
29	181	525	1.5	0.282	0.0019	0.321	-16.11	0.092
30	181	539	3	0.346	0.0028	0.339	-15.83	0.054
31	181	536	1.5	0.268	0.0029	0.353	-16.02	0.073
32	181	526	1.5	0.160	0.0044	0.362	-16.50	0.127
33	181	516	1.5	0.105	0.0014	0.367	-16.88	0.142
34	181	506	1.5	0.068	0.0013	0.371	-17.30	0.111
35	181	496	1.5	0.047	0.0009	0.374	-17.67	0.125
36	181	486	1.5	0.034	0.0011	0.375	-17.98	0.146
37	181	476	1.5	0.024	0.0010	0.377	-18.33	0.201
38	180	466	1.5	0.019	0.0008	0.378	-18.52	0.202
39	181	456	1.5	0.014	0.0007	0.378	-18.88	0.234

Aliquot MGI-2

Location Grasberg Igneous Complex

Step #	Time (min)	Average T (°C)	±	He (ncc)	±	f	ln(D/a^2)	±
1	121	400	1.5	0.102	0.0013	0.016	-19.54	1.227
2	121	400	1.5	0.045	0.0007	0.024	-19.46	1.626
3	121	400	1.5	0.044	0.0013	0.031	-19.15	1.280
4	121	410	1.5	0.056	0.0010	0.040	-18.64	1.031
5	**121**	**420**	**1.5**	**0.075**	**0.0011**	**0.052**	**-18.09**	**0.725**
6	**121**	**430**	**1.5**	**0.091**	**0.0011**	**0.067**	**-17.63**	**0.560**
7	**121**	**440**	**1.5**	**0.104**	**0.0018**	**0.084**	**-17.25**	**0.493**
8	**121**	**450**	**1.5**	**0.110**	**0.0018**	**0.102**	**-16.96**	**0.452**
9	121	460	1.5	0.113	0.0015	0.120	-16.75	0.369
10	120	470	1.5	0.124	0.0022	0.140	-16.47	0.315
11	120	480	1.5	0.123	0.0030	0.160	-16.31	0.343
12	181	482	1.5	0.146	0.0030	0.183	-16.40	0.290
13	180	472	1.5	0.088	0.0011	0.198	-16.77	0.306
14	181	462	1.5	0.056	0.0008	0.207	-17.16	0.239

Table 2.2 cont

15	181	452	1.5	0.037	0.0007	0.213	-17.54	0.255
16	181	442	1.5	0.025	0.0008	0.217	-17.88	0.321
17	181	432	1.5	0.016	0.0007	0.220	-18.32	0.435
18	181	422	1.5	0.011	0.0005	0.221	-18.69	0.479
19	181	412	1.5	0.008	0.0006	0.223	-19.06	0.579
20	181	402	0.75	0.004	0.0005	0.223	-19.59	0.796
21	181	405	1.5	0.006	0.0006	0.224	-19.25	0.614
22	181	420	1.5	0.010	0.0006	0.226	-18.71	0.450
23	181	435	1.5	0.017	0.0007	0.229	-18.19	0.315
24	181	450	1.5	0.028	0.0009	0.233	-17.68	0.248
25	181	465	1.5	0.044	0.0009	0.241	-17.20	0.197
26	181	480	1.5	0.064	0.0012	0.251	-16.79	0.166
27	181	495	1.5	0.090	0.0011	0.266	-16.38	0.130
28	181	510	1.5	0.114	0.0015	0.284	-16.07	0.115
29	180	525	1.5	0.130	0.0013	0.305	-15.84	0.104
30	180	540	1.5	0.147	0.0015	0.329	-15.62	0.089
31	180	536	1.5	0.092	0.0022	0.344	-16.01	0.144
32	181	526	1.5	0.056	0.0010	0.353	-16.47	0.173
33	180	516	1.5	0.040	0.0014	0.360	-16.75	0.167
34	181	506	1.5	0.027	0.0008	0.364	-17.13	0.207
35	181	496	1.5	0.019	0.0007	0.367	-17.48	0.197
36	181	486	1.5	0.015	0.0007	0.370	-17.69	0.217
37	181	476	1.5	0.011	0.0005	0.371	-18.01	0.252
38	181	466	1.5	0.008	0.0005	0.373	-18.32	0.288
39	181	456	1.5	0.005	0.0006	0.373	-18.85	0.454

Aliquot MGI-3

Location Grasberg Igneous Complex

Step #	**Time (min)**	**Average T (°C)**	**±**	**He (ncc)**	**±**	**f**	**ln(D/a^2)**	**±**
1	120	400	1.5	0.052	0.0011	0.026	-18.58	1.348
2	*121*	*52*	*133.5*	*0.002*	*0.0006*	*0.028*	*0.00*	*0.000*
3	121	400	1.5	0.030	0.0011	0.043	-18.16	1.271
4	121	410	1.5	0.033	0.0025	0.059	-17.66	1.429
5	121	420	1.5	0.035	0.0011	0.077	-17.30	1.175
6	120	430	1.5	0.036	0.0014	0.095	-17.01	0.850
7	*121*	*34*	*60*	*0.001*	*0.0005*	*0.096*	*0.00*	*0.000*
8	121	450	1.5	0.060	0.0020	0.126	-16.23	0.456
9	121	460	1.5	0.050	0.0019	0.152	-16.16	0.627

Table 2.2 cont

10	121	470	9	0.048	0.0013	0.176	-16.03	0.497
11	**121**	**480**	**1.5**	**0.045**	**0.0012**	**0.198**	**-15.95**	**0.398**
12	**181**	**482**	**1.5**	**0.046**	**0.0012**	**0.222**	**-16.17**	**0.338**
13	**181**	**472**	**7.5**	**0.025**	**0.0009**	**0.234**	**-16.69**	**0.457**
14	**180**	**462**	**1.5**	**0.016**	**0.0010**	**0.242**	**-17.08**	**0.513**
15	**181**	**452**	**1.5**	**0.009**	**0.0007**	**0.247**	**-17.61**	**0.661**
16	**181**	**442**	**1.5**	**0.005**	**0.0007**	**0.249**	**-18.29**	**0.894**
17	**181**	**432**	**1.5**	**0.004**	**0.0005**	**0.251**	**-18.39**	**0.854**
18	**181**	**422**	**1.5**	**0.002**	**0.0006**	**0.252**	**-18.93**	**1.093**
19	181	412	1.5	0.002	0.0006	0.253	-19.29	1.327
20	181	402	1.5	0.001	0.0005	0.254	-19.91	1.785
21	181	405	1.5	0.001	0.0005	0.254	-19.55	1.479
22	181	420	1.5	0.002	0.0006	0.255	-18.99	1.109
23	181	435	1.5	0.003	0.0006	0.257	-18.60	0.940
24	181	450	1.5	0.006	0.0006	0.260	-18.03	0.665
25	181	465	1.5	0.008	0.0007	0.264	-17.63	0.523
26	181	480	1.5	0.012	0.0008	0.270	-17.21	0.429
27	180	495	1.5	0.016	0.0009	0.278	-16.91	0.386
28	181	510	1.5	0.021	0.0011	0.288	-16.60	0.342
29	181	525	1.5	0.021	0.0009	0.299	-16.52	0.327
30	181	540	1.5	0.021	0.0010	0.310	-16.47	0.302
31	181	536	1.5	0.013	0.0010	0.317	-16.90	0.438
32	0	508	133.5	0.132	0.0011	0.383	65535.00	65535.000

Table 2.3 Diffusion kinetics estimated from ^{4}He-only step-heating experiments (Table 2.2). Bolded lines are D_{init}, representing our best estimates of the initial, undisturbed diffusion kinetics before the onset of decreasing diffusivities. Other diffusion kinetics estimates are provided to demonstrate changes in diffusion kinetics during step-heating.

P=prograde R=retrograde	**Starting Step#**	**Ending Step#**	**Tc (°C)**	**±**	**Ea (kcal/mol)**	**±**	**ln(D0/r2)**	**±**	**D0(cm2/s)**	**±**
09GS05-3	Sinai Peninsula									
P	**10**	**20**	**181**	**17.5**	**39.7**	**7.59**	**8.8**	**4.97**	**1.1E-01**	**6.02E-02**
R	28	37	190	6.8	40.8	2.91	9.1	1.81	1.4E-01	2.88E-02
P	38	50	184	4.2	39.3	1.76	8.0	1.08	5.0E-02	6.71E-03
ERB48-1	Sinai Peninsula									
P	**10**	**19**	**152**	**1.4**	**40.6**	**0.74**	**13.1**	**0.50**	**2.8E+01**	**1.06E+00**
R	28	37	189	1.6	45.4	0.76	14.4	0.48	1.1E+02	3.58E+00
P	38	49	133	0.9	33.9	0.43	6.8	0.27	5.6E-02	2.19E-03
R	56	59	236	7.7	50.0	3.26	14.2	1.86	8.9E+01	1.16E+01
ERB48-2	Sinai Peninsula									
P	**10**	**20**	**169**	**1.7**	**41.9**	**0.82**	**12.5**	**0.55**	**4.4E+01**	**1.93E+00**
R	28	37	193	1.6	45.1	0.76	13.6	0.48	1.2E+02	4.41E+00
P	38	50	139	0.8	33.8	0.39	6.1	0.24	7.3E-02	2.84E-03
R	53	59	253	6.2	55.3	2.69	17.8	1.56	8.4E+03	7.35E+02
B099-7	Hall Peninsula									
P	10	24	154	8.6	44.1	4.90	17.0	4.04	2.5E+03	5.95E+02
R	25	29	105	14.7	31.4	8.75	6.8	7.31	8.8E-02	9.56E-02
P	30	49	122	2.1	35.5	1.20	10.1	0.95	2.5E+00	2.36E-01

Table 2.3 cont

R		**50**	**58**	**118**	**5.4**	**34.6**	**3.12**	**9.4**	**2.44**	**1.3E+00**	**3.33E-01**
P		66	98	112	0.8	33.2	0.45	8.3	0.32	4.2E-01	1.62E-02
R		99	120	164	2.3	43.2	1.19	14.6	0.84	2.3E+02	1.32E+01
R		149	156	200	4.7	47.7	2.23	15.7	1.37	6.7E+02	5.80E+01
P		158	183	199	1.6	47.4	0.75	15.3	0.45	4.8E+02	1.39E+01
B099-11	Hall Peninsula										
P		**4**	**9**	**44**	**0.7**	**26.8**	**0.89**	**7.6**	**0.70**	**2.1E-01**	**1.96E-02**
R		14	18	128	3.1	40.9	1.96	16.4	1.42	1.4E+03	1.22E+02
P		19	23	54	0.9	26.4	0.84	5.6	0.59	2.9E-02	3.05E-03
R		29	36	154	1.8	41.6	0.97	13.9	0.67	1.2E+02	5.56E+00
P		37	44	111	0.9	32.5	0.51	7.4	0.33	1.7E-01	7.69E-03
R		50	58	266	2.6	60.4	1.18	21.2	0.71	1.7E+05	5.52E+03
P		59	65	225	2.3	48.2	0.98	13.5	0.58	7.6E+01	3.27E+00
R		66	72	261	3.7	56.7	1.62	18.2	0.96	8.7E+03	4.57E+02
C013-11	Hall Peninsula										
P		13	20	133	65.3	31.9	31.13	4.3	26.10	3.1E-03	1.86E-02
R		21	26	145	80.6	34.8	38.54	6.8	33.22	3.6E-02	1.77E-01
P		33	49	158	11.6	38.8	5.67	10.2	4.04	1.1E+00	4.37E-01
R		**50**	**58**	**141**	**15.3**	**34.9**	**7.55**	**7.3**	**5.53**	**6.3E-02**	**4.78E-02**
P		61	89	140	1.4	35.1	0.71	7.6	0.44	8.5E-02	4.89E-03
R		90	99	168	2.2	39.5	1.02	10.0	0.64	8.9E-01	5.68E-02
P		100	116	165	1.4	38.7	0.64	9.3	0.39	4.6E-01	1.95E-02

Table 2.3 cont

C015-14	Hall Peninsula									
P	30	49	160	26.0	38.4	12.38	9.4	9.72	5.9E-01	6.11E-01
P	64	77	156	34.3	38.3	16.66	9.7	13.02	7.8E-01	1.05E+00
P	**78**	**99**	**162**	**4.8**	**39.5**	**2.31**	**10.6**	**1.55**	**2.0E+00**	**2.86E-01**
R	100	109	165	5.7	39.8	2.75	10.7	1.88	2.1E+00	3.71E-01
P	110	117	160	17.6	38.7	8.47	9.9	6.09	1.0E+00	6.10E-01
P	124	149	135	1.2	33.9	0.62	6.7	0.38	4.1E-02	2.32E-03
R	150	156	212	6.4	48.4	2.88	15.1	1.74	1.7E+02	1.99E+01
P	169	187	168	2.2	39.1	1.01	9.5	0.58	6.3E-01	3.87E-02
C015-20	Hall Peninsula									
P	**2**	**9**	**89**	**1.8**	**30.9**	**1.26**	**8.0**	**0.95**	**3.4E-01**	**3.99E-02**
R	12	16	135	3.5	39.4	2.01	13.6	1.45	9.0E+01	9.62E+00
P	19	29	94	0.7	30.7	0.45	7.0	0.32	1.2E-01	5.70E-03
R	31	35	148	3.6	40.1	1.93	12.8	1.31	4.2E+01	4.30E+00
P	36	40	102	2.0	30.9	1.21	6.4	0.83	6.7E-02	8.63E-03
R	56	61	146	2.7	36.4	1.32	8.6	0.83	5.9E-01	5.71E-02
P	62	73	94	0.6	27.8	0.36	3.0	0.22	2.2E-03	1.59E-04
R	74	81	188	2.2	42.0	0.98	10.6	0.58	4.7E+00	2.58E-01
C015-21	Hall Peninsula									
P	**1**	**11**	**108**	**1.3**	**34.2**	**0.82**	**10.1**	**0.60**	**2.5E+00**	**1.48E-01**
R	12	18	123	2.3	36.9	1.34	11.8	0.97	1.3E+01	1.11E+00
P	19	30	90	0.8	30.2	0.51	6.8	0.36	8.7E-02	4.61E-03
R	31	35	161	6.7	43.2	3.54	15.0	2.43	3.2E+02	5.18E+01
P	36	40	119	3.5	34.1	1.97	8.7	1.34	5.8E-01	8.95E-02

Table 2.3 cont

Table 2.3 cont

P		41	53	22	0.4	20.3	0.53	-0.5	0.33	6.0E-05	-4.13E-05
R		56	61	194	3.8	47.1	1.81	15.7	1.14	6.4E+02	4.64E+01
P		62	66	195	5.8	47.1	2.79	15.6	1.75	5.8E+02	6.50E+01
P		67	70	162	5.7	39.8	2.76	10.9	1.64	5.1E+00	7.73E-01
R		75	81	214	3.1	49.3	1.40	15.8	0.84	6.9E+02	3.68E+01
C015-24	Hall Peninsula										
P		**1**	**5**	**77**	**2.3**	**31.1**	**1.82**	**9.8**	**1.49**	**1.6E+00**	**2.50E-01**
R		13	18	132	2.4	39.9	1.46	14.6	1.08	2.6E+02	1.90E+01
P		19	28	102	0.9	32.9	0.55	9.2	0.39	1.2E+00	4.97E-02
R		31	35	170	4.1	46.3	2.21	17.5	1.50	4.8E+03	4.06E+02
P		36	42	124	2.4	35.7	1.35	10.1	0.91	3.0E+00	2.65E-01
R		56	61	193	4.9	47.9	2.40	16.6	1.50	1.8E+03	1.65E+02
P		62	69	140	2.5	36.3	1.28	9.1	0.79	1.0E+00	9.05E-02
R		75	81	214	3.8	48.8	1.72	15.3	1.02	5.0E+02	3.32E+01
C015-27	Hall Peninsula										
P		**5**	**12**	**116**	**6.3**	**35.4**	**3.80**	**10.8**	**2.94**	**4.2E+00**	**1.15E+00**
R		15	21	148	3.7	41.3	2.04	14.4	1.49	1.6E+02	1.61E+01
P		22	33	123	1.3	35.2	0.74	9.7	0.51	1.5E+00	7.61E-02
R		35	38	154	7.2	40.2	3.75	12.3	2.55	1.9E+01	3.92E+00
P		39	45	128	3.4	34.6	1.84	8.3	1.23	3.6E-01	5.36E-02
R		59	64	199	3.6	47.2	1.72	15.3	1.08	3.8E+02	2.67E+01
P		65	70	186	3.4	43.8	1.59	13.0	0.99	3.7E+01	2.85E+00
R		77	84	219	2.6	49.4	1.15	15.4	0.68	4.1E+02	1.83E+01

Table 2.3 cont

C015-28	Hall Peninsula										
P		**5**	**11**	**76**	**3.1**	**29.5**	**2.41**	**7.5**	**1.91**	**1.8E-01**	**4.49E-02**
R		15	21	139	2.6	41.0	1.52	15.0	1.11	3.2E+02	2.35E+01
P		22	29	115	1.5	35.1	0.90	10.5	0.64	3.4E+00	2.09E-01
R		33	37	171	4.2	46.1	2.22	17.2	1.51	2.8E+03	2.43E+02
P		38	41	121	4.1	34.7	2.36	9.3	1.61	1.0E+00	1.76E-01
R		58	63	180	3.3	44.0	1.58	13.7	1.00	8.7E+01	6.31E+00
P		64	71	134	1.6	34.7	0.81	7.8	0.50	2.2E-01	1.41E-02
R		76	83	207	2.4	46.9	1.09	13.9	0.65	1.0E+02	4.86E+00
Dalam-1	Grasberg Igneous Complex										
P		**3**	**11**	**108**	**25.8**	**29.3**	**13.89**	**3.5**	**9.59**	**3.6E-03**	**9.78E-03**
R		13	20	180	40.9	42.5	19.19	12.1	13.34	1.9E+01	2.07E+01
P		21	28	160	19.8	37.8	9.27	8.7	6.14	6.4E-01	4.49E-01
R		32	39	225	36.1	49.5	15.79	14.8	10.18	2.9E+02	2.00E+02
Dalam-2	Grasberg Igneous Complex										
P		**4**	**12**	**40**	**17.7**	**19.9**	**17.60**	**-3.1**	**12.06**	**4.9E-06**	**-1.93E-05**
R		13	20	201	65.8	46.9	30.57	14.7	21.19	2.6E+02	3.73E+02
P		21	29	126	28.9	30.4	13.73	3.0	9.00	2.1E-03	6.41E-03
R		32	39	229	67.0	49.4	28.69	14.3	18.53	1.7E+02	2.22E+02
MGI-1	Grasberg Igneous Complex										
P		**3**	**6**	**89**	**13.0**	**27.9**	**8.06**	**3.7**	**5.85**	**9.2E-03**	**1.45E-02**
R		13	19	186	10.7	42.5	4.88	11.4	3.38	2.1E+01	6.32E+00
P		21	30	146	3.3	33.5	1.51	5.0	0.99	3.3E-02	6.63E-03

Table 2.3 cont

R		32	38	193	8.9	41.5	3.77	9.5	2.45	3.2E+00	8.22E-01
MGI-2	Grasberg Igneous Complex										
P		**5**	**8**	**148**	**52.3**	**36.4**	**25.63**	**8.4**	**18.13**	**7.2E-01**	**1.55E+00**
R		13	20	167	15.0	39.3	7.01	9.7	4.89	2.7E+00	1.34E+00
P		21	29	114	4.7	29.0	2.33	2.6	1.53	2.1E-03	1.24E-03
R		32	38	169	11.5	36.9	4.97	6.7	3.23	1.3E-01	6.41E-02
MGI-3	Grasberg Igneous Complex										
P		**2**	**11**	**18**	**194.7**	**31.4**	**46.01**	**14.7**	**14.36**	**1.0E+01**	**1.92E+02**
R		1	19	26	114.5	16.1	28.48	7.9	1.75	5.2E+00	6.41E-04

Table 2.4 Step-heating data tables for ^{4}He/^{3}He experiments on Hall Peninsula zircons.

Aliquot Step #	Time (min)	T (°C)	±	10,000/T	±	4He (ncc)	±	fraction 4He	4He ln(D/a2)	±	3He (pcc)	±	fraction 3He	3He ln(D/a2)	±
B106-1															
1	60	400	0.5	14.86	0.01	192.49	2.898	0.164	-14.25	0.31	9.90	0.154	0.690	-11.37	0.09
2	60	400	0.5	14.86	0.01	69.84	1.053	0.223	-14.23	0.47	0.57	0.010	0.729	-12.54	0.32
3	60	400	0.5	14.86	0.01	48.50	0.740	0.264	-14.32	0.26	0.32	0.006	0.752	-12.99	0.05
4	60	380	0.5	15.31	0.01	19.21	0.290	0.281	-15.10	0.32	0.12	0.003	0.760	-13.92	0.07
5	90	360	0.4	15.79	0.01	12.27	0.185	0.291	-15.89	0.23	0.08	0.002	0.765	-14.73	0.05
6	120	340	0.4	16.31	0.01	7.03	0.106	0.297	-16.70	0.23	0.04	0.001	0.768	-15.59	0.06
7	120	350	0.7	16.05	0.02	9.91	0.149	0.305	-16.33	0.15	0.06	0.002	0.772	-15.26	0.04
8	120	370	0.5	15.55	0.01	19.98	0.302	0.322	-15.57	0.12	0.11	0.002	0.780	-14.59	0.03
9	120	390	0.4	15.08	0.01	37.24	0.563	0.354	-14.84	0.11	0.19	0.004	0.793	-14.00	0.03
10	120	410	0.5	14.64	0.01	47.13	0.711	0.394	-14.46	0.11	0.22	0.005	0.808	-13.75	0.03
11	120	430	0.4	14.22	0.01	90.66	1.365	0.471	-13.58	0.08	0.40	0.007	0.836	-13.05	0.02
12	120	450	0.4	13.83	0.01	104.11	1.567	0.560	-13.15	0.07	0.43	0.008	0.866	-12.78	0.02
B106-2															
1	60	400	0.4	14.86	0.01	80.95	1.221	0.180	-14.06	0.29	4.95	0.078	0.873	-10.90	0.07
2	60	400	0.4	14.86	0.01	24.35	0.368	0.234	-14.24	0.49	0.08	0.002	0.888	-12.54	0.40
3	60	400	0.4	14.86	0.01	16.75	0.253	0.272	-14.37	0.25	0.04	0.002	0.896	-13.07	0.03
4	60	380	0.4	15.31	0.01	6.34	0.096	0.286	-15.22	0.32	0.02	0.001	0.899	-14.07	0.05
5	90	360	0.4	15.79	0.01	3.79	0.057	0.294	-16.09	0.23	0.01	0.001	0.900	-15.02	0.00
6	120	340	0.4	16.31	0.01	2.02	0.030	0.299	-16.98	0.24	0.00	0.000	0.901	-15.95	0.00
7	120	350	0.4	16.05	0.01	2.75	0.041	0.305	-16.64	0.15	0.01	0.000	0.903	-15.55	0.00
8	120	370	0.4	15.55	0.01	5.87	0.088	0.318	-15.84	0.12	0.01	0.001	0.905	-14.87	0.00
9	120	390	0.4	15.08	0.01	11.92	0.179	0.344	-15.05	0.11	0.03	0.001	0.909	-14.20	0.00
10	90	410	0.5	14.64	0.01	16.39	0.247	0.381	-14.31	0.12	0.04	0.001	0.916	-13.52	0.00
11	90	430	0.3	14.22	0.01	26.65	0.401	0.440	-13.64	0.09	0.05	0.002	0.925	-13.04	0.00
12	120	450	0.4	13.83	0.01	44.70	0.673	0.540	-13.12	0.07	0.08	0.002	0.940	-12.69	0.00
B106-3															
1	60	420	0.9	14.43	0.02	63.54	1.086	0.565	-11.77	0.13	10.94	0.184	0.990	-10.65	0.07
2	60	420	0.4	14.43	0.01	6.87	0.139	0.626	-12.55	0.34	0.02	0.001	0.992	-12.08	0.00
3	60	420	0.4	14.43	0.01	4.17	0.086	0.663	-12.87	0.09	0.01	0.001	0.993	-12.55	0.00
4	60	405	0.4	14.75	0.01	1.97	0.030	0.680	-13.51	0.09	0.01	0.001	0.993	-12.90	0.00
5	60	390	0.5	15.08	0.01	0.90	0.014	0.688	-14.25	0.08	0.00	0.000	0.993	-13.83	0.00
6	90	375	0.5	15.43	0.01	0.67	0.010	0.694	-14.92	0.06	0.00	0.000	0.994	-14.74	0.00
7	90	360	0.4	15.79	0.01	0.34	0.005	0.697	-15.59	0.07	0.00	0.000	0.994	-15.17	0.00
8	120	345	0.4	16.18	0.01	0.19	0.005	0.699	-16.44	0.07	0.00	0.000	0.994	-15.64	0.00
9	120	330	0.3	16.58	0.01	0.10	0.003	0.700	-17.05	0.09	0.00	0.000	0.994	-16.57	0.00
10	120	350	0.4	16.05	0.01	0.23	0.005	0.702	-16.25	0.04	0.00	0.000	0.994	-16.24	0.00
11	120	370	0.4	15.55	0.01	0.53	0.010	0.706	-15.38	0.04	0.00	0.000	0.994	-15.02	0.00

Table 2.4 cont

12	120	390	0.4	15.08	0.01	1.19	0.033	0.717	-14.54	0.04	0.00	0.000	0.994	-14.09	0.00
13	120	410	0.4	14.64	0.01	2.22	0.061	0.737	-13.86	0.04	0.01	0.000	0.995	-13.63	0.00
14	90	430	0.4	14.22	0.01	2.67	0.078	0.760	-13.29	0.05	0.01	0.000	0.995	-13.12	0.00
15	90	450	0.4	13.83	0.01	3.87	0.106	0.795	-12.78	0.04	0.01	0.001	0.996	-12.51	0.00
B106-6															
1	60	420	0.8	14.43	0.02	49.66	0.752	0.141	-14.54	0.36	2.31	0.037	0.702	-11.34	0.09
2	60	420	0.8	14.43	0.02	15.64	0.237	0.186	-14.72	0.60	0.06	0.002	0.720	-13.29	0.62
3	60	420	0.7	14.43	0.01	10.75	0.163	0.216	-14.85	0.32	0.04	0.001	0.732	-13.71	0.07
4	60	405	0.8	14.75	0.02	5.00	0.076	0.230	-15.49	0.35	0.02	0.001	0.737	-14.45	0.09
5	90	390	0.7	15.08	0.02	3.64	0.055	0.241	-16.15	0.26	0.01	0.001	0.741	-15.24	0.09
6	90	375	0.6	15.43	0.01	1.80	0.027	0.246	-16.81	0.31	0.00	0.000	0.742	-16.09	0.14
7	120	360	1	15.79	0.02	1.23	0.019	0.249	-17.46	0.26	0.00	0.000	0.744	-16.38	0.10
8	120	345	0.5	16.18	0.01	0.59	0.009	0.251	-18.18	0.31	0.00	0.000	0.744	-16.99	0.15
9	180	330	0.6	16.58	0.02	0.47	0.007	0.252	-18.80	0.24	0.00	0.000	0.745	-17.99	0.20
C015-2															
1	60	400	0.5	14.86	0.01	125.07	1.882	0.127	-14.75	0.39	1.13	0.019	0.349	-12.74	0.19
2	60	400	0.4	14.86	0.01	45.21	0.681	0.173	-14.78	0.60	0.13	0.003	0.389	-13.79	0.61
3	60	400	2.8	14.86	0.06	31.16	0.469	0.205	-14.89	0.34	0.08	0.002	0.412	-14.19	0.22
4	60	400	2.8	14.86	0.06	24.22	0.365	0.230	-14.97	0.28	0.05	0.002	0.429	-14.46	0.20
5	60	380	0.5	15.31	0.01	10.01	0.210	0.240	-15.76	0.38	0.02	0.001	0.437	-15.24	0.27
6	60	360	0.4	15.79	0.01	4.55	0.089	0.244	-16.51	0.38	0.01	0.001	0.440	-16.08	0.33
7	90	340	4.5	16.31	0.12	2.53	0.049	0.247	-17.48	0.33	0.01	0.001	0.441	-17.08	0.37
8	90	365	0.5	15.67	0.01	6.87	0.110	0.254	-16.46	0.16	0.01	0.001	0.446	-16.15	0.20
9	90	390	0.44	15.08	0.01	15.60	0.254	0.270	-15.58	0.15	0.03	0.001	0.456	-15.29	0.15
10	90	415	0.4	14.53	0.01	32.86	0.494	0.303	-14.72	0.14	0.07	0.002	0.476	-14.50	0.11
11	90	440	0.4	14.02	0.01	56.82	0.854	0.361	-13.98	0.12	0.12	0.003	0.512	-13.84	0.10
12	90	465	0.5	13.55	0.01	78.01	1.173	0.440	-13.39	0.10	0.16	0.003	0.561	-13.39	0.09
13	60	490	0.5	13.10	0.01	65.09	0.981	0.507	-12.90	0.10	0.13	0.004	0.602	-12.99	0.10
14	60	515	0.3	12.69	0.00	77.60	1.168	0.586	-12.46	0.07	0.17	0.004	0.656	-12.55	0.07
15	60	500	0.5	12.93	0.01	31.38	0.485	0.618	-13.17	0.10	0.08	0.002	0.679	-13.24	0.11
16	90	485	0.5	13.19	0.01	22.75	0.352	0.641	-13.80	0.06	0.06	0.002	0.696	-13.88	0.08
17	90	470	0.5	13.46	0.01	11.80	0.183	0.653	-14.39	0.07	0.03	0.001	0.704	-14.58	0.11
18	90	455	0.4	13.73	0.01	6.58	0.102	0.659	-14.94	0.07	0.01	0.001	0.708	-15.20	0.12
19	90	440	0.4	14.02	0.01	3.69	0.063	0.663	-15.50	0.07	0.01	0.001	0.711	-15.63	0.13
20	90	425	0.5	14.32	0.01	2.10	0.036	0.665	-16.05	0.07	0.00	0.001	0.713	-16.21	0.17
C015-3															
1	60	400	0.5	14.86	0.01	26.42	0.410	0.061	-16.21	0.69	0.29	0.005	0.095	-15.34	0.60
2	60	400	0.5	14.86	0.01	10.83	0.167	0.087	-16.22	0.89	0.07	0.002	0.119	-15.79	1.13
3	60	400	0.5	14.86	0.01	8.09	0.125	0.105	-16.17	0.61	0.05	0.002	0.137	-15.94	0.70
4	60	385	0.5	15.19	0.01	3.56	0.054	0.114	-16.85	0.70	0.02	0.001	0.143	-16.76	0.88
5	60	370	0.5	15.55	0.01	1.84	0.028	0.118	-17.45	0.61	0.01	0.001	0.146	-17.60	0.97
6	60	355	0.5	15.92	0.01	1.05	0.016	0.120	-17.98	0.57	0.01	0.001	0.148	-17.97	1.00

Table 2.4 cont															
7	60	340	0.4	16.31	0.01	0.59	0.009	0.122	-18.54	0.57	0.00	0.000	0.149	-18.73	1.26
8	90	325	0.5	16.72	0.01	0.46	0.007	0.123	-19.18	0.48	0.00	0.000	0.150	-19.76	1.33
9	90	345	0.5	16.18	0.01	0.90	0.014	0.125	-18.49	0.34	0.00	0.000	0.151	-18.68	0.78
10	90	365	28.3	15.67	0.67	1.10	0.017	0.128	-18.28	0.39	0.01	0.000	0.153	-18.34	0.78
11	60	385	0.5	15.19	0.01	3.88	0.059	0.137	-16.56	0.28	0.02	0.001	0.161	-16.48	0.45
12	60	405	0.6	14.75	0.01	4.96	0.075	0.148	-16.23	0.34	0.03	0.001	0.172	-16.08	0.49
13	60	425	0.4	14.32	0.01	8.95	0.135	0.169	-15.51	0.27	0.06	0.001	0.191	-15.44	0.37
14	60	445	0.5	13.92	0.01	14.12	0.216	0.202	-14.88	0.24	0.10	0.002	0.225	-14.72	0.29
15	60	465	0.5	13.55	0.01	20.20	0.304	0.249	-14.28	0.20	0.14	0.003	0.272	-14.15	0.25
16	60	485	0.5	13.19	0.01	24.47	0.368	0.306	-13.83	0.17	0.18	0.004	0.332	-13.67	0.21
17	60	505	0.5	12.85	0.01	28.29	0.426	0.371	-13.42	0.14	0.21	0.004	0.400	-13.26	0.17
18	60	480	0.5	13.28	0.01	8.66	0.130	0.391	-14.43	0.25	0.06	0.002	0.421	-14.29	0.31
19	60	455	0.4	13.73	0.01	3.35	0.050	0.399	-15.33	0.20	0.02	0.001	0.429	-15.18	0.29
20	90	430	0.5	14.22	0.01	1.73	0.026	0.403	-16.37	0.17	0.01	0.001	0.433	-16.18	0.29
21	120	405	0.5	14.75	0.01	0.92	0.014	0.405	-17.28	0.16	0.01	0.000	0.435	-17.20	0.39
22	120	380	0.4	15.31	0.01	0.33	0.005	0.406	-18.31	0.21	0.00	0.000	0.436	-18.51	0.66
C015-4															
1	60	400	0.5	14.86	0.01	54.71	0.823	0.104	-15.16	0.46	0.96	0.015	0.297	-13.06	0.22
2	60	400	0.5	14.86	0.01	22.03	0.332	0.146	-15.08	0.65	0.16	0.003	0.346	-13.78	0.56
3	60	400	0.5	14.86	0.01	15.69	0.236	0.176	-15.14	0.39	0.09	0.002	0.375	-14.15	0.24
4	60	385	0.05	15.19	0.00	7.57	0.136	0.190	-15.72	0.43	0.04	0.002	0.388	-14.83	0.29
5	60	370	0.4	15.55	0.01	3.92	0.071	0.197	-16.31	0.42	0.02	0.001	0.394	-15.63	0.35
6	60	355	0.5	15.92	0.01	2.05	0.037	0.201	-16.92	0.40	0.01	0.000	0.397	-16.34	0.35
7	90	340	0.4	16.31	0.01	1.63	0.029	0.204	-17.54	0.32	0.01	0.001	0.399	-16.98	0.32
8	90	325	0.5	16.72	0.01	0.86	0.015	0.206	-18.16	0.39	0.00	0.000	0.401	-17.54	0.43
9	60	350	0.5	16.05	0.01	1.42	0.023	0.209	-17.24	0.22	0.01	0.000	0.402	-16.70	0.28
10	60	375	0.5	15.43	0.01	3.60	0.055	0.216	-16.28	0.19	0.01	0.001	0.407	-15.82	0.22
11	60	400	0.5	14.86	0.01	8.62	0.133	0.232	-15.35	0.18	0.04	0.001	0.418	-14.92	0.16
12	60	425	0.5	14.32	0.01	18.64	0.285	0.267	-14.44	0.16	0.07	0.002	0.440	-14.15	0.13
13	60	450	0.5	13.83	0.01	32.47	0.493	0.329	-13.65	0.14	0.13	0.003	0.479	-13.48	0.12
14	60	475	0.5	13.37	0.01	45.68	0.692	0.416	-13.00	0.11	0.17	0.005	0.533	-12.98	0.11
15	60	500	0.6	12.93	0.01	53.08	0.804	0.517	-12.50	0.09	0.22	0.004	0.600	-12.56	0.09
16	60	485	1.1	13.19	0.02	19.28	0.290	0.553	-13.27	0.13	0.08	0.003	0.626	-13.34	0.15
17	60	470	0.5	13.46	0.01	9.36	0.141	0.571	-13.90	0.10	0.04	0.002	0.638	-14.05	0.16
18	60	455	0.5	13.73	0.01	5.10	0.077	0.581	-14.46	0.09	0.02	0.001	0.644	-14.62	0.15
19	60	440	0.3	14.02	0.01	2.73	0.041	0.586	-15.06	0.09	0.01	0.001	0.648	-15.13	0.15
Y080-1															
1	60	400	0.6	14.86	0.01	113.49	1.707	0.527	-11.91	0.11	1.29	0.021	0.901	-10.84	0.08
2	60	400	1.3	14.86	0.03	20.23	0.304	0.621	-12.19	0.20	0.03	0.001	0.922	-11.90	0.00
3	60	400	0.9	14.86	0.02	6.26	0.094	0.650	-13.14	0.11	0.01	0.001	0.928	-13.02	0.00
4	120	380	0.5	15.31	0.01	9.57	0.152	0.694	-13.27	0.04	0.01	0.001	0.938	-13.08	0.00
5	120	360	0.6	15.79	0.01	4.03	0.064	0.713	-14.01	0.07	0.01	0.000	0.942	-13.86	0.00
6	150	340	0.6	16.31	0.02	1.64	0.026	0.721	-15.08	0.07	0.00	0.000	0.944	-15.03	0.00

Table 2.4 cont															
7	180	320	0.5	16.86	0.01	0.23	0.004	0.722	-17.20	0.15	0.00	0.000	0.944	-16.41	0.00
8	180	330	0.5	16.58	0.01	0.49	0.007	0.724	-16.44	0.03	0.00	0.000	0.944	-16.41	0.00
9	180	350	0.5	16.05	0.01	0.76	0.011	0.728	-15.99	0.03	0.00	0.000	0.945	-16.08	0.00
10	180	370	0.5	15.55	0.01	2.27	0.034	0.738	-14.87	0.02	0.00	0.000	0.947	-14.85	0.00
11	180	390	0.6	15.08	0.01	1.35	0.020	0.745	-15.35	0.05	0.00	0.000	0.948	-15.27	0.00
12	180	410	0.5	14.64	0.01	5.51	0.083	0.770	-13.87	0.02	0.01	0.000	0.954	-13.83	0.00
13	180	430	0.5	14.22	0.01	8.97	0.135	0.812	-13.22	0.02	0.01	0.001	0.962	-13.24	0.00
Y080-2															
1	60	400	0.4	14.86	0.01	28.07	0.428	0.049	-16.68	0.81	0.92	0.015	0.115	-14.95	0.47
2	60	400	0.5	14.86	0.01	13.25	0.201	0.071	-16.52	0.95	0.30	0.005	0.152	-15.12	0.77
3	60	400	0.6	14.86	0.01	10.01	0.152	0.089	-16.52	0.63	0.21	0.004	0.179	-15.23	0.45
4	60	380	0.4	15.31	0.01	3.98	0.060	0.096	-17.30	0.77	0.08	0.002	0.188	-16.10	0.61
5	90	360	0.5	15.79	0.01	2.42	0.037	0.100	-18.14	0.60	0.04	0.002	0.194	-17.03	0.55
6	90	370	0.4	15.55	0.01	3.43	0.052	0.106	-17.66	0.44	0.06	0.001	0.201	-16.69	0.35
7	90	390	0.5	15.08	0.01	6.95	0.105	0.118	-16.86	0.37	0.13	0.003	0.218	-15.80	0.24
8	90	410	0.6	14.64	0.01	12.84	0.193	0.140	-16.09	0.33	0.25	0.005	0.250	-15.04	0.22
9	90	430	0.6	14.22	0.01	21.12	0.318	0.176	-15.36	0.28	0.41	0.007	0.301	-14.35	0.18
10	90	450	0.5	13.83	0.01	30.65	0.462	0.229	-14.69	0.23	0.57	0.009	0.372	-13.75	0.14
11	90	470	0.5	13.46	0.01	39.42	0.594	0.298	-14.12	0.18	0.69	0.012	0.458	-13.25	0.12
12	90	370	0.4	15.55	0.01	0.91	0.014	0.299	-17.73	1.63	0.01	0.001	0.459	-17.27	1.60
13	90	390	0.5	15.08	0.01	1.71	0.026	0.302	-17.09	0.13	0.02	0.001	0.462	-16.50	0.14
14	90	410	0.5	14.64	0.01	3.33	0.050	0.308	-16.40	0.13	0.05	0.002	0.468	-15.75	0.12
15	90	430	0.6	14.22	0.01	6.39	0.096	0.319	-15.71	0.12	0.10	0.003	0.480	-14.98	0.10
16	90	450	0.5	13.83	0.01	11.82	0.178	0.339	-15.03	0.12	0.19	0.004	0.504	-14.26	0.08
17	90	470	0.5	13.46	0.01	19.80	0.298	0.374	-14.40	0.11	0.33	0.006	0.545	-13.60	0.07

Table 2.5 Diffusion kinetics estimates from ^{4}He and ^{3}He step-heating regressions. In all cases, D_{init} is the first regression.

Aliquot		**4He results**								**3He results**							
Starting Step#	**Ending Step#**	**Tc (°C)**	**±**	**Ea (kcal/mol)**	**±**	**ln(D0/r2)**	**±**	**D0(cm2s-1)**	**±**	**Tc (°C)**	**±**	**Ea (kcal/mol)**	**±**	**ln(D0/r2)**	**±**	**D0(cm2s-1)**	**±**
B106-1																	
3	6	91	6.4	32.6	4.56	10.0	3.60	3.9E+02	3.75E+02	96	1.5	35.6	1.10	13.6	0.86	1.4E+04	7.80E+03
7	12	71	1.4	28.5	1.14	6.7	0.84	1.4E+01	8.14E+00	21	0.2	21.8	0.32	2.5	0.24	2.1E-01	4.38E-02
B106-2																	
3	6	107	6.8	35.6	4.54	12.3	3.57	2.8E+03	2.74E+03	112	0.8	39.0	0.54	16.0	0.43	1.2E+05	4.26E+04
7	12	89	1.6	31.5	1.13	8.9	0.82	9.6E+01	5.37E+01	52	0.1	26.2	0.12	5.7	0.09	4.0E+00	3.46E-01
B106-3																	
3	9	117	1.4	39.1	0.90	15.5	0.70	8.4E+04	4.26E+04	109	0.3	38.0	0.18	15.1	0.14	5.7E+04	7.26E+03
10	15	83	0.6	31.1	0.46	8.9	0.35	1.2E+02	3.56E+01	86	0.2	31.9	0.16	9.8	0.12	3.0E+02	3.23E+01
B106-6																	
3	9	120	5.0	36.3	2.99	11.5	2.35	7.5E+02	6.76E+02	122	2.0	38.7	1.29	14.3	0.98	1.2E+04	7.79E+03
C015-2																	
4	7	103	9.7	34.0	6.33	10.4	4.93	4.3E+02	4.31E+02	105	8.7	35.2	5.80	11.9	4.48	1.9E+03	1.87E+03
8	14	60	1.0	25.9	0.86	4.1	0.59	8.0E-01	3.58E-01	33	0.7	22.4	0.89	1.8	0.61	7.7E-02	3.55E-02
15	20	150	2.5	40.4	1.33	13.0	0.92	5.7E+03	3.45E+03	163	4.1	43.2	2.15	14.8	1.45	3.4E+04	2.58E+04
C015-3																	
3	8	100	11.5	31.3	7.16	7.2	5.72	1.1E+01	1.11E+01	135	22.3	39.2	12.85	13.3	10.03	5.0E+03	5.02E+03
9	17	90	2.5	29.3	1.62	5.6	1.12	2.4E+00	1.61E+00	92	4.0	29.9	2.56	6.2	1.75	4.2E+00	3.45E+00
18	22	142	5.0	37.8	2.67	10.8	1.93	4.2E+02	3.57E+02	152	9.9	40.3	5.23	12.7	3.69	2.8E+03	2.74E+03
C015-4																	
3	8	96	7.4	32.3	4.92	9.0	3.92	5.5E+01	5.40E+01	114	6.3	37.6	4.10	13.9	3.21	7.5E+03	7.16E+03
9	14	94	2.2	31.6	1.45	8.3	1.04	2.8E+01	1.84E+01	66	1.9	27.3	1.58	5.4	1.13	1.6E+00	1.08E+00
16	19	153	6.4	41.9	3.48	14.5	2.40	1.4E+04	1.27E+04	156	9.0	42.5	4.88	14.8	3.34	1.9E+04	1.83E+04
Y080-1																	
4	7	117	2.0	41.7	1.42	19.0	1.12	1.5E+06	1.01E+06	120	0.7	42.9	0.49	20.1	0.40	4.7E+06	1.53E+06
8	13	61	0.3	27.5	0.30	6.4	0.23	5.2E+00	1.08E+00	74	0.2	29.7	0.19	8.0	0.14	2.6E+01	3.49E+00

Table 2.5 cont

Y080-2																	
3	5	118	32.6	34.5	18.41	9.3	14.21	1.4E+02	1.36E+02	125	24.6	38.2	14.97	13.3	11.49	7.7E+03	7.70E+03
6	11	114	5.7	33.6	3.38	8.6	2.39	7.3E+01	6.67E+01	94	3.5	31.5	2.35	8.1	1.66	4.4E+01	3.57E+01
12	17	113	3.3	33.0	1.90	8.0	1.35	3.7E+01	2.74E+01	121	2.8	35.7	1.63	10.6	1.15	5.2E+02	3.53E+02

submission, however, it is unclear why these zircons yield no low-*f* anomalies. Due to the unusual nature of these Arrhenius relationships, we argue that the use of low-*f* diffusivities in estimating initial diffusion kinetics is a valid approach for these results.

Hall Peninsula, ^{4}He-only step-heating results

Zircons from Archean Hall Peninsula rocks (Fig. 2.2) are relatively abundant, large euhedral tetragonal prisms with bipyramidal terminations with appearances varying from clear to hazy to nearly opaque, from colorless to white, light red, crimson, smoky, dark purple, brownish-black, and opaque black. Bulk U and Th concentrations range from 91 to 790 ppm and 32 to 124 ppm, respectively and ZHe ages from 1110 to 80 Ma, markedly decreasing with increasing eU (Fig. 2.1). A range of Raman ν3 peaks (Table 2.1) suggests a mix of low radiation damage to fully metamict states. Sample B099-11 showed no discernable ν3 or ν1 peak, indicative of complete metamictization.

Figure 2.6 shows Arrhenius diagrams from Hall Peninsula ^{4}He step-heating experiments with depth-profiled U and Th concentrations and relevant sample information. Nominal D_{init} closure temperatures for these zircons range from 44 to 183°C, systematically decreasing with increasing eU. D_{init} activation energies show a similar correlation with increasing eU, decreasing from 40 to 30 kcal/mol (Fig. 2.6; Table 2.3). The majority of experiments show a strong and consistent decrease in diffusivities, starting at ~430-460°C for 0.5 – 2 hr (C015-24 and B099-11 yield rollovers <400°C). Only the two lowest eU samples (C015-14 and C013-11) show linear diffusivities at higher temperatures, C015-14 only deviating from linearity at >600°C and at very high release fractions (>90% releases in many experiments yields anomalous diffusivities, likely due to depletion of the diffusant).

Through depth profiling analysis, all zircons were found to be moderately to strongly zoned (Fig. 2.6 insets), with absolute U and Th pit concentrations deviating significantly from bulk U and Th concentrations derived from whole-grain dissolution. Parent nuclide concentrations show the presence of thin low-concentration outer rims, with deeper U and Th concentrations reaching a peak, and then decreasing again with depth. In cases where more than one LA-ICP-MS measurement were made on the same zircon (C015-27, C015-20, B099-7), concentration profiles exhibit similar topologies, but marked absolute concentration variations >100 ppm at similar depths suggest that zonation is only concentric to a first order.

Sinai Peninsula step-heating results

Zircons from the Pan-African basement granite of the Sinai Peninsula (Fig. 2.3; Table 2.1) are euhedral, elongate tetragonal bipyramidal zircons. Most are clear, with a small fraction showing shades of gray, red or opaque white. Bulk parent concentrations for three analyzed span a limited range of 106 to 237 ppm U and 58 to 113 ppm Th, with ZHe ages from 366 to 480 Ma (Table 2.1). Other ZHe analyses from these samples show a greater range of parent nuclide concentrations (29-1950 ppm U and 13-710 ppm Th) with ZHe ages ranging from 580 to 16.7 Ma (Fig. 2.1). Raman spectra for these three grains yield a similarly limited range: ν3 peak shifts at <1000 cm^{-1} and FWHM from 6.6 to 10.8 cm^{-1} suggest high to moderate crystallinity (Table 2.1). Arrhenius diagrams from these diffusion experiments are shown in Figure 2.7. Nominal D_{init} closure temperatures range from 152 to 183°C, decreasing with increasing eU (Table 2.3). Activation energies exhibit a limited range from 40 to 42 kcal/mol. The same behavior of decreasing diffusivities observed in the Hall Peninsula (Fig. 2.6) is also evident from all three Sinai samples, starting at ~500-530°C/1 hr, but with only minor effects on the lowest-eU zircon (09GS05-3).

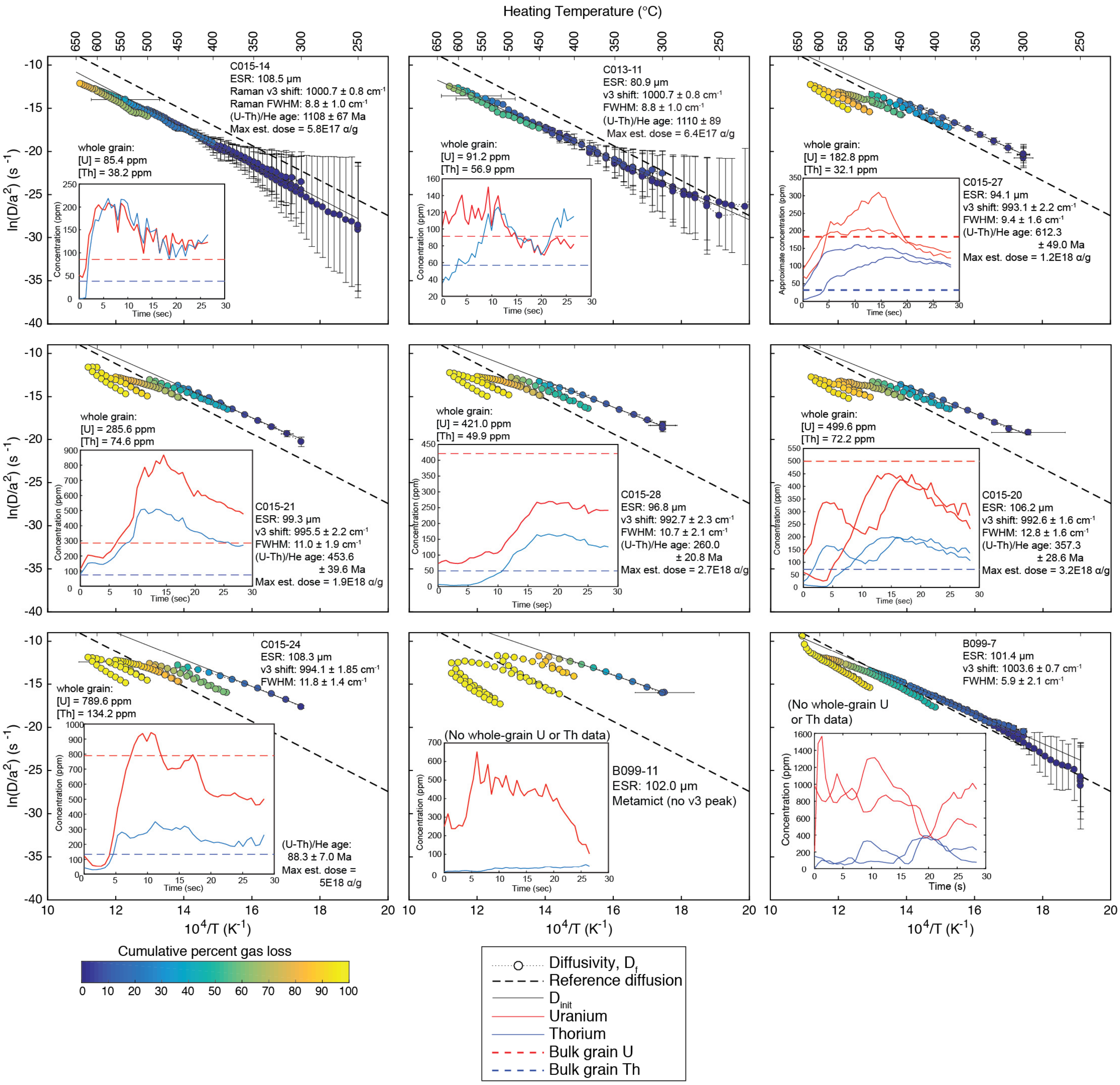

Figure 2.6 Arrhenius results of D_f including aliquot information for Hall Peninsula zircons, organized by increasing bulk eU concentration (right to left, top to bottom, excepting B099-11 and B099-7 for which no bulk U and Th data are available). Data are colored to represent cumulative percent of gas loss. Thin black lines indicate the measured representative diffusivity D_{init} (Fig. 6). Dashed lines indicate a reference set of diffusion kinetics from moderately damaged zircon, taken from Reiners et al. (2005): $E_A = 40.1$ kcal/mol, $D_0 = 0.46$ cm^2/s^{-1}, with a = 100 μm (this is the same diffusion kinetics and grain size used for many of the simulations in Chapter 1). Inset figures show outer U and Th concentration profiles from LA-ICP-MS trace element analyses, with U in red and Th in blue. Dashed lines on inset plots indicate the whole-grain average concentration.

Grasberg Igneous Complex step-heating results

Young, low-damage zircons from the GIC (Fig. 2.4) were euhedral tetragonal crystals with bipyramidal terminations, with a- and c-axis dimensions of up to 243 µm and 580 µm, respectively. They were clear with a pinkish hue. Bulk U and Th concentrations range from 99 to 313 ppm and 38 to 162 ppm, respectively. Arrhenius relationships (Fig. 2.8) are somewhat erratic, due in part to low gas releases and high analytical uncertainties. Although diffusivities decrease with increasing fractional losses, a correlation with T-t conditions similar to previous experiments (Figs. 2.6 - 2.7) is less obvious. D_{init} closure temperatures vary widely from 195 to 48°C, decreasing strongly with increasing eU; activation energies similarly decrease over a wide range from 46 to 20 kcal/mol (Fig. 2.6; Table 2.3).

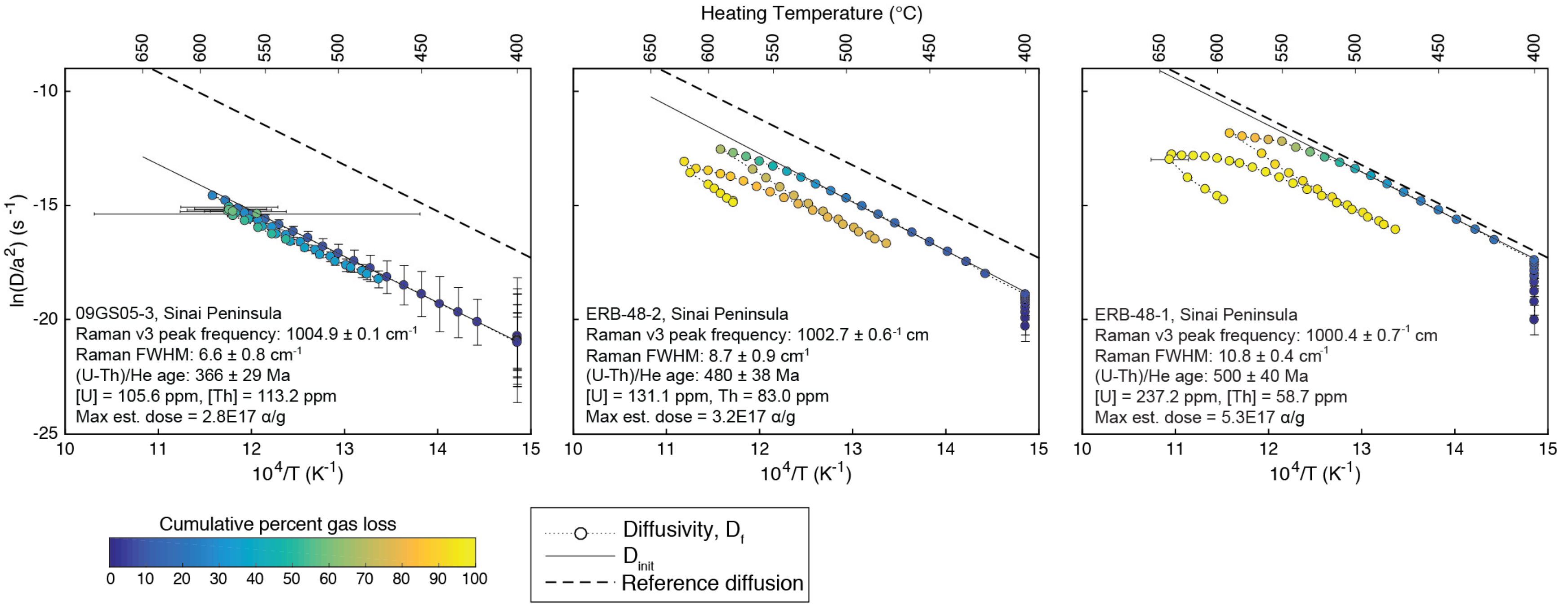

Figure 2.7 Arrhenius diagrams and aliquot information from Sinai Peninsula zircons. Data are shaded to represent cumulative percent of gas loss, with thin black lines representing 'initial' diffusivity $ln(D/a^2)_0$. From left to right, eU increases. Dashed lines indicate a reference set of diffusion kinetics from moderately damaged zircon, taken from Reiners et al. (2005): E_A = 40.1 kcal/mol, D_0 = 0.46 cm^2/s^{-1}, with a = 100 µm.

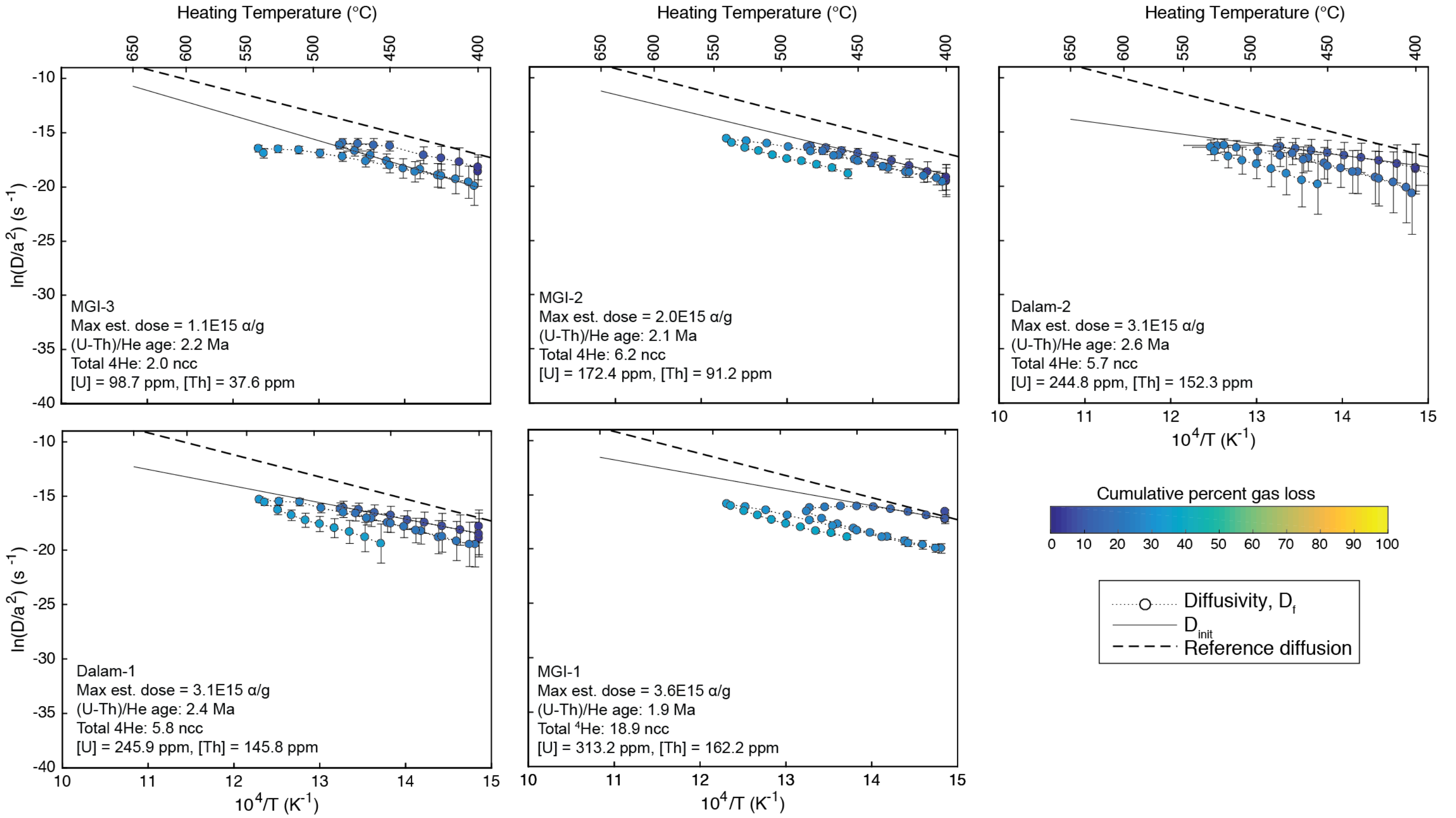

Figure 2.8 Cycled step-heating results from the young, rapidly-cooled zircons sampled from the Grasberg Igneous Complex. See explanations in previous two figures for symbology. From left to right, top to bottom, eU increases. Dashed lines indicate a reference set of diffusion kinetics from moderately damaged zircon, taken from Reiners et al. (2005): $E_A = 40.1$ kcal/mol, $D_0 = 0.46$ cm^2/s^{-1}, with a = 100 μm.

Hall Peninsula, ^{4}He/^{3}He step-heating results

The zircons selected from irradiated samples, with appearances similar to those described above (Section 2.5.1.1), trend toward the high-eU, high-damage side of the Hall Peninsula dataset (Fig. 2.1; Table 2.1). They span a wide range of U and Th concentrations, 82 to 1683 ppm and 7 to 431 ppm respectively (Table 2.1) with ZHe ages from 440 to 6.4 Ma (Fig. 2.1). Arrhenius diagrams are presented in Figure 2.9. Nominal closure temperature estimates range from 91 to 120 °C for ^{3}He, and 96 to 135 °C for ^{4}He, and decrease with increasing eU. Activation energies for ^{3}He range from 42 to 31 kcal/mol, with ^{4}He from 42 to 35 kcal/mol, but lack a clear correlation with eU, similar to $\ln(D_0/a^2)$ measurements. In some grains, diffusivities estimated from both isotopes appear tightly matched, even at low fractional losses (i.e. C015-2, C015-3, Y080-1, B106-3); in others, ^{4}He is initially low relative to ^{3}He. Another noteworthy behavior is that ^{3}He diffuses much faster in the earliest heating steps in some experiments: samples Y080-1, B106-1, B106-2, B106-3, and B106-6 see >60% of total ^{3}He loss after the first heating step. High initial ^{4}He releases >50% are only observed in Y080-1 and B106-3, both of which released >99% of ^{3}He during the first hour of heating.

2.5.2 Annealing Experiments

Results of annealing experiments are summarized as a function of heating times and temperatures in Figure 2.10 and Table 2.6. Although ν3 peak parameter changes show little consistency overall, most samples whose peak shifts begin below ~995 cm^{-1} before heating tend toward more moderate values. In some cases, peak shift values decrease towards lower values,

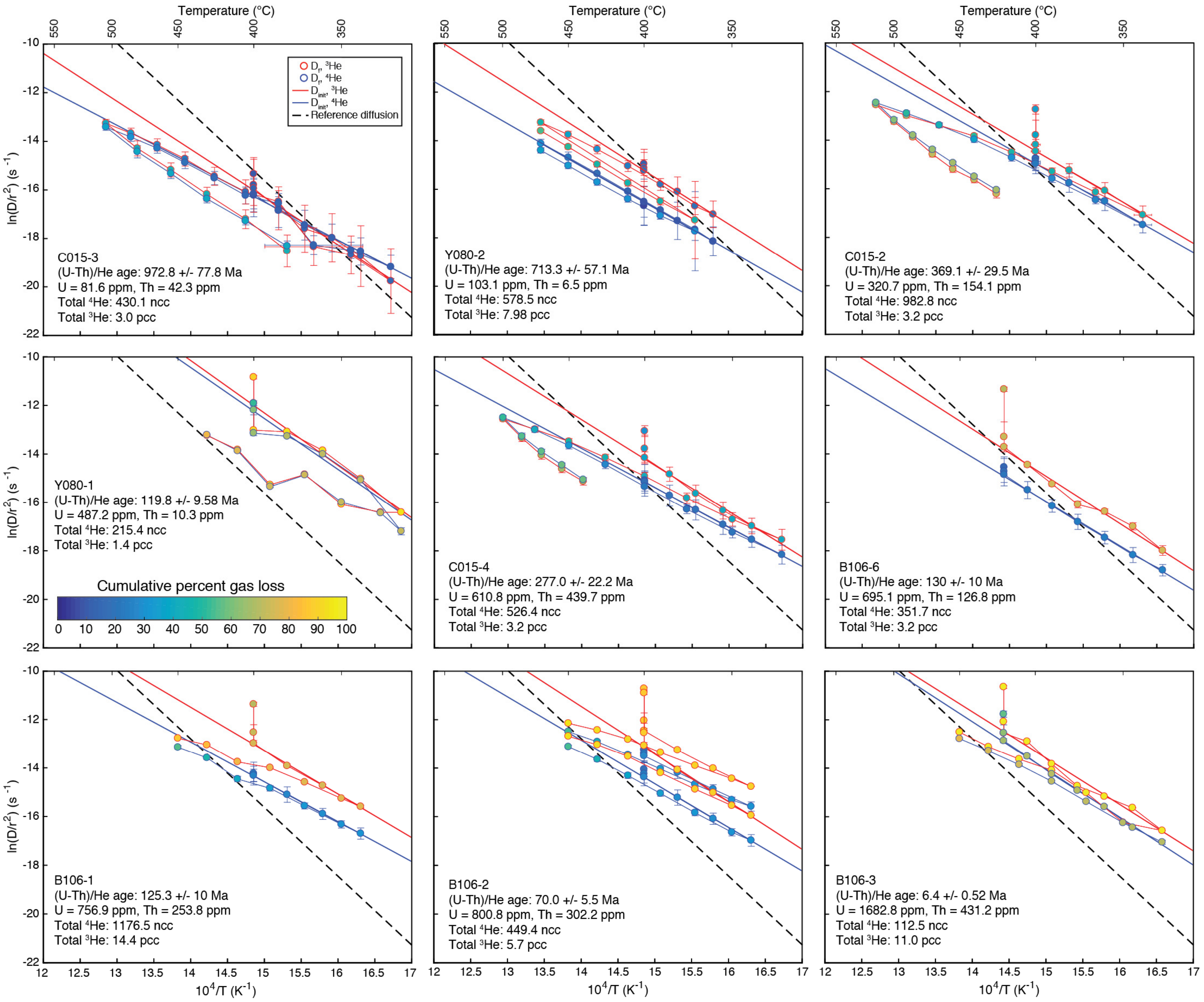

Figure 2.9 Arrhenius plots from ^{4}He/^{3}He cycled step-heating experiments for proton irradiated zircons from the Hall Peninsula. Red circles and lines connecting data indicate ^{3}He results, blue represents ^{4}He results. Straight red and blue lines represent the regression for which $\ln(D/a^2)_0$ diffusion kinetics were chosen. Plots also display relevant sample information, with data fill color indicating percent of total gas released as in previous figures. Dashed lines indicate a reference set of diffusion kinetics from moderately damaged zircon, taken from Reiners et al. (2005): $E_A = 40.1$ kcal/mol, $D_0 = 0.46$ cm^2/s^{-1}, with a = 100 μm.

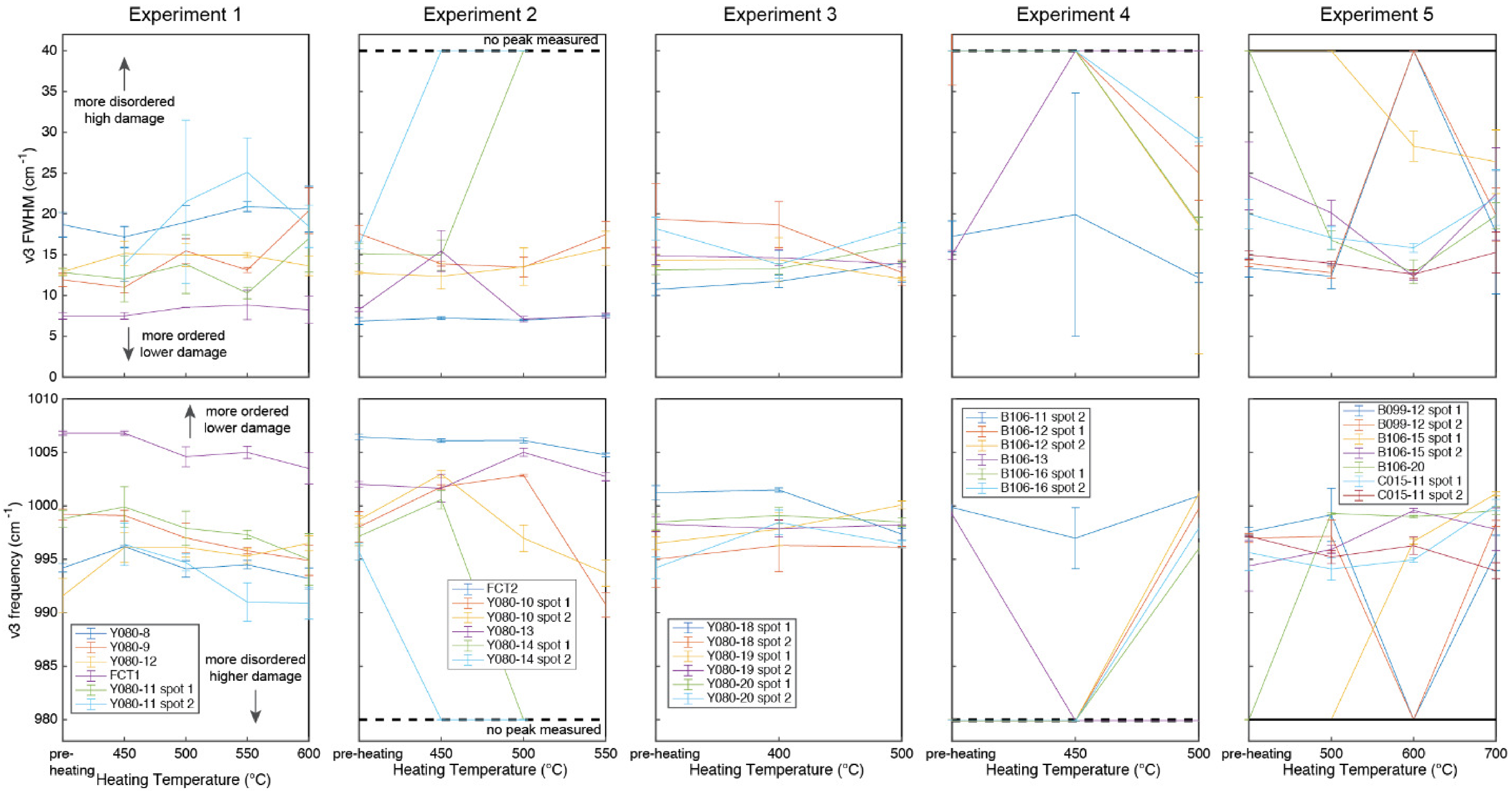

Figure 2.10 Results of annealing experiments. See Table 7 for an explanation of Tt conditions. On the top row, increasing FWHM indicates a decrease in atomic symmetry; on the bottom, decreasing peak shifts indicate the same. Zircons with no discernable v3 peaks are given arbitrary values (FWHM = 40 cm^{-1} and peak shift = 980 cm^{-1}) and plotted along the dotted line for visual reference. Counterintuitively, many experiments appear to indicate increasing disorder with increasing Tt conditions. In other experiments, e.g. Experiment 5, both spots measured on B099-12, go from values suggesting moderate crystallinity to having no discernable peak at all, suggestive of total metamictization. In some cases, after further heating, peaks reappear again.

Table 2.6 Tables containing Raman measurements for spots on crystalline faces of zircons before and after heating in conditions identical to 4He-only step-heating experiments, except the 700 degree heating in experiment 5. 'NP' (no peak) indicates spectra whose peaks were either missing or questionable (i.e. significantly influenced by background noise and/or fluorescence, very large (>30) FWHM, indistinguishable from the v1 peak at 970 cm-1, etc). 'L' indicates that the zircon was lost. Experiments 3 and 4 were both heated to 550 C, similar to experiment 2, however, all grains were either lost or destroyed before Raman measurements could be completed.

Experiment 1	Pre-Heating				450 C 1 hr				500 C 1 hr				550 C 1 hr				600 C 1 hr			
Sample	FWHM	+/-	v3	+/-	FWHM	+/-	v3	+/-	FWHM	+/-	v3	+/-	FWHM	+/-	v3	+/-	FWHM	+/-	v3	+/-
Y080-8	18.7	1.5	994.2	0.4	17.2	1.3	996.2	0.1	19.0	2	994.1	0.8	20.9	0.6	994.5	0.4	20.6	2.8	993.2	1.0
Y080-9	11.9	0.8	999.2	0.5	11.0	0.7	999.1	0.5	15.5	1.5	997	1.4	13.1	0.3	995.8	0.3	20.4	2.8	994.9	1.4
Y080-12	12.9	0.4	991.6	1.6	15.2	1.5	996.1	1.4	15.0	1.4	996.1	0.9	15.0	0.3	995.3	0.7	13.6	1.2	996.5	0.7
FCT1	7.5	0.4	1006.8	0.2	7.5	0.4	1006.8	0.2	8.5	1	1004.6	0.9	8.8	1.8	1005	0.6	8.2	1.7	1003.5	1.5
Y080-11 spot 1	12.8	0.5	998.8	0.8	12.0	2.8	999.9	1.9	13.8	3.6	997.9	1.6	10.3	0.7	997.3	0.4	17.0	4.1	995	2.4
Y080-11 spot 2	18.6	2.6	990.9	1.5	13.8	2.1	996.4	2.0	21.5	10	994.7	0.8	25.1	4.2	991	1.8	18.5	2.6	990.9	1.5

Experiment 2	Pre-Heating				400,410,…,450 C, 1 hr each				460,470,…,500 C, 1 hr each				510,520,…,550 C, 1 hr each			
Sample	FWHM	+/-	v3	+/-	FWHM	+/-	v3	+/-	FWHM	+/-	v3	+/-	FWHM	+/-	v3	+/-
FCT2	6.9	0.4	1006.5	0.3	7.2	0.2	1006.1	0.2	7.0	0.1	1006.1	0.2	7.5	0.1	1004.8	0.2
Y080-10 spot 1	17.6	1.0	998.0	1.4	13.9	0.3	1001.8	0.2	13.5	1.2	1002.9	0.1	17.5	1.6	990.7	1.2
Y080-10 spot 2	12.8	0.2	998.7	0.4	12.3	1.5	1003.0	0.3	13.5	2.3	997.0	1.2	15.8	2.1	993.7	1.2
Y080-13	8.3	0.2	1002.0	0.3	15.5	2.5	1001.6	1.3	7.1	0.3	1005.0	0.4	7.5	0.3	1002.7	0.4
Y080-14 spot 1	15.1	1.2	997.1	0.9	14.9	1.86634081	1000.6	0.86408507	NP	NP	NP	NP	L	L	L	L
Y080-14 spot 2	16.1	0.4	995.7	0.8	NP	NP	NP	NP	NP	NP	NP	NP	L	L	L	L

Experiment 3	Pre-Heating				400,410,…,450 C, 1 hr each				460,470,…,500 C, 1 hr each			
Sample	FWHM	+/-	v3	+/-	FWHM	+/-	v3	+/-	FWHM	+/-	v3	+/-
Y080-18 spot 1	10.7	0.7	1001.2	0.7	11.7	0.8	1001.5	0.2	14.0	2.4	997.3	0.6
Y080-18 spot 2	19.4	4.3	995.0	2.6	18.7	2.8	996.3	2.4	12.8	1.6	996.1	0.1
Y080-19 spot 1	14.3	0.7	996.5	0.6	14.4	2.7	997.8	1.6	12.0	0.2	1000.1	0.4
Y080-19 spot 2	14.8	1.1	998.3	0.7	14.6	1.0	997.9	0.8	13.8	0.4	998.2	0.0
Y080-20 spot 1	13.1	0.6	998.5	0.7	13.3	0.6	999.1	0.8	16.2	2.1	998.5	0.4
Y080-20 spot 2	18.2	1.4	994.2	1.0	13.8	1.7	998.4	1.2	18.3	0.6	996.4	0.3

Experiment 4	Pre-Heating				400,410,…,450 C, 1 hr each				460,470,…,500 C, 1 hr each			
Sample	FWHM	+/-	v3	+/-	FWHM	+/-	v3	+/-	FWHM	+/-	v3	+/-
B106-11 spot 1	11.8	1.5	1001.3	0.7	13.7	1.5	1000.0	0.4	21.0	18.5	999.1	0.4
B106-11 spot 2	17.2	1.9	999.1	0.3	19.9	14.9	996.3	2.7	12.2	0.6	1000.1	0.4
B106-12 spot 1	NP	NP	NP	NP	NP	NP	NP	NP	25.0	3.3	999.0	1.4
B106-12 spot 2	NP	NP	NP	NP	NP	NP	NP	NP	18.6	15.7	1000.3	0.3
B106-13	15.0	0.6	998.5	0.2	NP	NP	NP	NP	NP	NP	NP	NP

Table 2.6 cont

B106-16 spot 1	NP	NP	NP	NP	NP	NP	NP	NP	18.8	0.7	995.4	0.5				
B106-16 spot 2	NP	NP	NP	NP	NP	NP	NP	NP	29.1	0.3	997.2	0.9				

Experiment 5	Pre-Heating				400,410,…,500 C, 1 hr each				500,510,…,600 C, 1 hr each				700 C, 1 hr			
Sample	FWHM	+/-	v3	+/-	FWHM	+/-	v3	+/-	FWHM	+/-	v3	+/-	FWHM	+/-	v3	+/-
B099-12 spot 1	13.4	1.1	997.6	0.4	12.3	1.5	999.2	2.5	NP	NP	NP	NP	17.8	7.6	995.6	1.64874781
Y080-10 spot 1	13.9	0.4	997.0	0.4	12.8	0.7	997.1	1.5	NP	NP	NP	NP	19.9	3.3	998.4	0.27515814
Y080-10 spot 2	NP	NP	NP	NP	NP	NP	NP	NP	28.3	1.8	996.7	0.3	26.4	3.9	1001.1	0.19697716
Y080-13	24.6	4.2	994.4	2.4	20.1	1.5	995.9	0.4	12.3	0.4	999.6	0.2	22.4	5.7	997.8	1.99064068
Y080-14 spot 1	NP	NP	NP	NP	16.8	1.1	999.3	0.1	12.9	1.5	999.0	0.1	19.8	1.6	999.6	0.37511909
Y080-14 spot 2	20.0	1.8	995.6	1.7	17.1	1.4	994.1	1.0	15.8	0.5	994.9	0.2	22.0	3.4	1000.1	0.52957184
Y080-18 spot 1	15.0	0.5	997.2	0.1	13.9	0.3	995.2	0.6	12.6	0.5	996.3	0.8	15.3	2.5	993.9	0.74671972

indicating a somewhat counterintuitive *increase* in apparent crystalline disorder with heating. Overall those zircons whose peak shift and FWHM measured in the ‘moderate’ range remain there during the course of heating. The low-damage Fish Canyon Tuff zircons analyzed during experiments 1 and 2 also mostly remain unchanged. In some instances, measurements go from moderate to metamict (no discernable ν3 peak), only to return to ‘normal’ values after further heating. The source of this behavior is unclear, but it may be related to the large spot size (30 μm), and/or natural variations on the surface of the grain.

Zircon grains selected for annealing experiments were from the same analyses as other Hall Peninsula zircons, and as such reveal a variety of colors. We observed that all grains whose original color was red turned purple/black after the first round of heating; color has been suggested to be correlated with radiation damage in zircon (Riley, 2004).

2.6 DISCUSSION

2.6.1 Summary of step-heating results

The topologies of Arrhenius data calculated from fractional loss experiments in this study are predominately characterized by initial linear data arrays, followed by a thermally activated pattern of progressively decreasing diffusivities, which we term ‘rollover’. The onset of this behavior appears to occur at temperatures of ~400-400 – 530°C for heating times of 0.5-2 hr, and its intensity is greater in zircons with higher parent concentrations. In many ^{4}He-only experiments, we have chosen D_{init} as the linear, pre-rollover prograde steps; this assumes that rollover represents an alteration to the initial, undisturbed diffusional mechanics.

D_{init} results are shown against bulk eU concentrations in Figure 2.11, and against Raman ν3 peak parameters in Figure 2.12 (Sinai Peninsula and Hall Peninsula ^{4}He-only). In both cases,

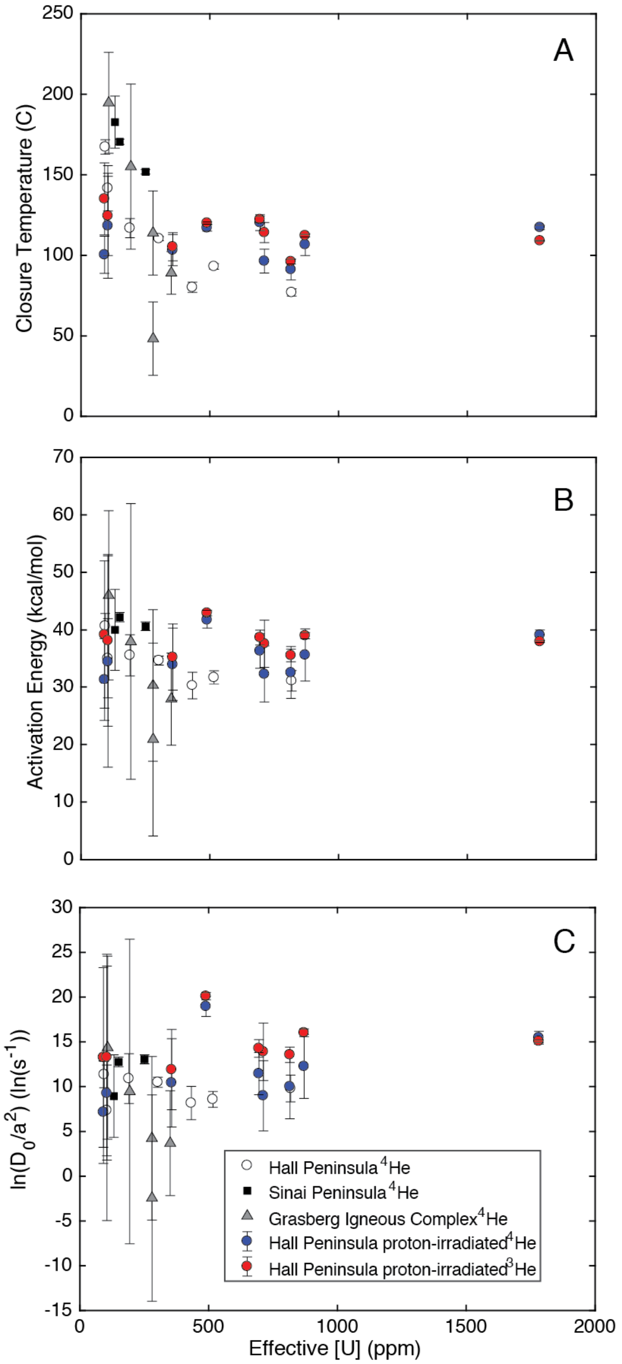
A
B
C
Closure Temperature (C)
Activation Energy (kcal/mol)
$\ln(D_0/a^2)$ ($\ln(s^{-1})$)
Effective [U] (ppm)
250
200
150
100
50
0
70
60
50
40
30
20
10
0
30
25
20
15
10
5
0
-5
-10
-15
0
500
1000
1500
2000
Hall Peninsula ^{4}He
Sinai Peninsula ^{4}He
Grasberg Igneous Complex ^{4}He
Hall Peninsula proton-irradiated ^{4}He
Hall Peninsula proton-irradiated ^{3}He

Figure 2.11

Figure 2.11 D_{init} closure temperatures (A) and diffusion kinetics (B,C) from Arrhenian regressions (Tables 2-6; Figs. 6-10), as a function of bulk eU concentration. D_{init} represents our best estimates of the original, undisturbed diffusion kinetics of the zircon analyzed. All zircons show a clearly defined decrease in Tc with increasing eU (A); activation energies yield a similar decrease for Hall Peninsula and GIC ^{4}He only zircons, but are lacking in ^{4}He/^{3}He data. The intercept term, $\ln(D_0/a^2)$, lacks a correlation with eU.

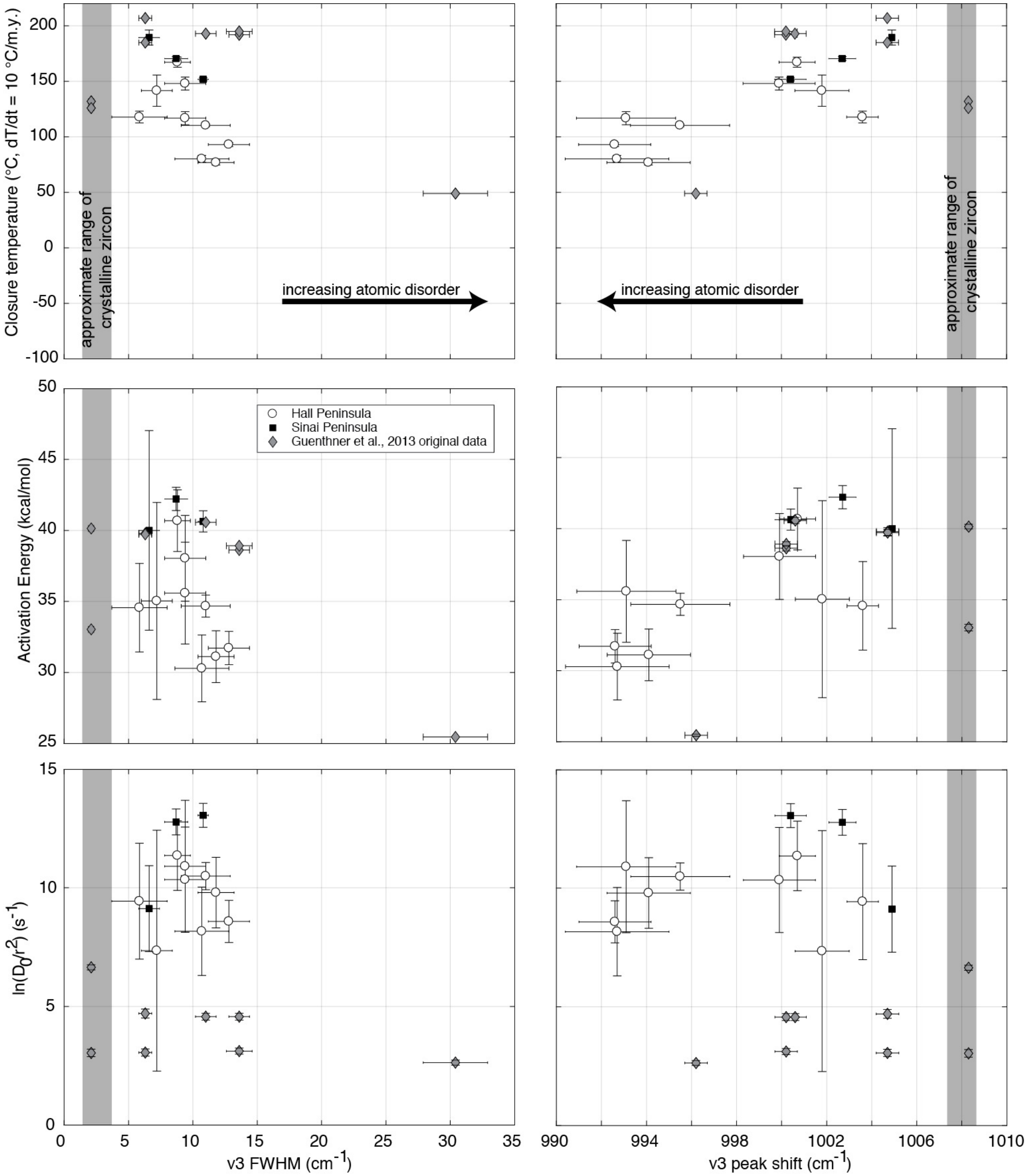
Closure temperature (°C, dT/dt = 10 °C/m.y.)
Activation Energy (kcal/mol)
ln(D_0/r^2) (s^{-1})
approximate range of crystalline zircon
increasing atomic disorder
Hall Peninsula
Sinai Peninsula
Guenthner et al., 2013 original data
v3 FWHM (cm^{-1})
v3 peak shift (cm^{-1})
200
150
100
50
0
-50
-100
45
40
35
30
25
15
10
5
0
5
10
15
20
25
30
35
990
994
998
1002
1006
1010

Figure 2.12

Figure 2.12 D_{init} diffusion kinetics for ^{4}He-only Sinai and Hall Peninsula against averaged measurements of the Raman ν3 peak for each grain. We have also included the dataset of Guenthner et al. (2013) for comparison to our own. Although the complex effects of thermal annealing on ν3 peak parameters (Geisler et al., 2001, 2003) makes comparison of absolute peak shift or FWHM values between regional datasets ambiguous, both Hall Peninsula zircons and those of Guenthner et al. (2013) show a consistent decreasing TC and EA with increasing damage. The relationship between damage and ln(D0/a2) is less clear in our own dataset, which may be due to the lack of crystallographically-oriented slabs. Hall Peninsula zircons yield lower closure temperatures and activation energies, with higher ln(D0/a2), overall.

we see correlations between T_C, E_A and proxies for radiation damage, defined mostly by the Hall Peninsula zircons which span a wide range of damage states. For high-damage zircon, this behavior is in general agreement with the predictions of ZRDAAM, that high-damage zircons yield lower closure temperatures with increased damage (Guenthner et al., 2013).

2.6.2 Damage and diffusion

Diffusion kinetics are similar to previous studies (Table 2.7) but with a wider range: D_{init} closure temperatures range from 44 to 193 °C (dT/dt = 10 °C/m.y.); activation energies range from 26.8 to 46 kcal/mol. In all datasets, T_C and E_A appear inversely correlated with increasing damage, although the Hall Peninsula defines this trend most clearly (Figs. 2.10 - 2.11). Negative correlations between T_C and high-damage zircons are expected, but low-damage zircons should yield positive correlations according to ZRDAAM. Unfortunately, erratic Arrhenius relationships from GIC zircons (Fig. 2.8) yield widely variable diffusion kinetics that are difficult to interpret. That the intercept term, $\ln(D_0/a^2)$, does not appear to correlate with eU or Raman ν3 peak parameters (Figs. 2.10 – 2.11) is unsurprising for two reasons: first, D_0 appears related to anisotropy in a way that whole-grain diffusion experiments may not capture (Farley, 2007; Reich et al., 2007; Cherniak et al., 2009; Guenthner et al., 2013); second, in zoned zircon, the relationship between radiation damage zones with different diffusivities may be more complex than a single diffusion domain *a* may capture (Anderson et al., 2017; Danišík et al., 2017).

To compare D_{init} results to each other and to other datasets, the traditional approach is to approximate the damage state using a single α-dose (Guenthner et al., 2013). Estimated doses for zircons in this study are provided in Table 2.1. This calculation is straightforward with GIC zircons, given their well-constrained rapid-cooling history (Wafforn, 2017), and assumes total retention of α-damage since their zircon U-Pb crystallization ages of 3.2 Ma (MGI) and 3.4 Ma (Dalam). An estimation is more difficult in the Hall and Sinai Peninsulas, whose thermal histories

Table 2.7 Empirically measured diffusion kinetics of zircon from available published literature. 'nr' indicates that the measurement, or sufficient information to make the calculation, was not reported. Doses are estimated based on damage accumulation since the (U-Th)/He age, similar to the ZRDAAM parameterization Guenthner et al. (2013), except Fish Canyon Tuff zircons (FCT) for which we used an age of 28 Ma (Reiners et al., 2004).

Ea (kcal/mol)	D0 (cm2/s)	Orientation	Dose	Sample	Citation
37.1	nr	whole grain	3.69E+16	FCT1 prograde	Reiners et al., 2002
44.1	nr	whole grain	3.69E+16	FCT1 retrograde	Reiners et al., 2002
37.3	nr	whole grain	nr	FCT44-7a prograde	Reiners et al., 2002
43.2	nr	whole grain	nr	FCT44-7a retrograde	Reiners et al., 2002
29.4	nr	whole grain	nr	MH-10 prograde	Reiners et al., 2002
36.6	nr	whole grain	nr	MH-10 retrograde	Reiners et al., 2002
29.2	nr	whole grain	6.97E+15	98PRGB4 prograde	Reiners et al., 2002
34.6	nr	whole grain	6.97E+15	98PRGB4 retrograde	Reiners et al., 2002
36.9	nr	whole grain	1.76E+17	98PRGB18 retrograde	Reiners et al., 2002
41.2	8.39E-01	whole grain	nr	01CS15z 40 um post high-T steps	Reiners et al., 2004
41.1	1.51E+00	whole grain	nr	01CS15z 56 um post high-T steps	Reiners et al., 2004
39	3.08E-01	whole grain	nr	01CS15z 66 um post high-T steps	Reiners et al., 2004
40.7	5.60E-01	whole grain	1.97E+18	M146 100 um post high-T steps	Reiners et al., 2004
40	9.27E-02	whole grain	1.97E+18	M146 38 um post high-T steps	Reiners et al., 2004
41.6	2.70E-01	whole grain	1.97E+18	M146 isothermal	Reiners et al., 2004
34.9	6.25E-02	c-axis normal	1.28E+16	DR	Cherniak et al., 2009
35.4	1.67E-01	c-axis parallel	2.80E+16	Mud Tank & DR	Cherniak et al., 2009
43.74	6.00E-01	whole grain	9.31E+15	ZKTB1516-DE	Wolfe and Stockli, 2010
38.241	4.00E-02	whole grain	8.90E+16	ZKTB4050-DE	Wolfe and Stockli, 2010
40.1	1.11E+02	c-axis normal	1.22E+16	MudTank	Guenthner et al., 2013
33.0	2.73E-02	c-axis parallel	1.22E+16	MudTank	Guenthner et al., 2013
39.8	2.01E-01	c-axis normal	4.67E+17	RB140	Guenthner et al., 2013
39.7	2.30E-02	c-axis parallel	4.67E+17	RB140	Guenthner et al., 2013
40.6	2.30E-01	c-axis normal	1.21E+18	BR231	Guenthner et al., 2013
38.6	2.65E-02	c-axis normal	1.48E+18	M127	Guenthner et al., 2013
38.9	2.65E-01	c-axis parallel	1.48E+18	M127	Guenthner et al., 2013
25.5	4.19E-03	c-axis normal	4.04E+18	G3	Guenthner et al., 2013
34.9	1.70E-02	whole grain	nr	TH62Z	Guenthner et al., 2013
16.9	6.37E-03	whole grain	8.21E+18	N17	Guenthner et al., 2013

are regionally defined but locally unresolved. Because several studies have observed damage-induced changes in age or closure temperatures at doses lower than ZRDAAM predictions (Pik et al., 2016; Powell et al., 2016; Anderson et al., 2017), we opted to err on the side of overestimation: our calculations assume Sinai Peninsula zircons have retained all α-damage since their U-Pb crystallization age of 610 Ma. In the Hall Peninsula, doses are estimated since the time of the youngest published muscovite K/Ar age, 1610 Ma, with a closure temperature higher than at which fission tracks can accumulate in zircon (T_C ~420 °C; Skipton et al., 2015 and references therein). We have also estimated radiation doses from other literature measurements, which are given in Table 2.7. In many cases, we have used the ZHe age as the starting point for damage accumulation, in accordance with the approach of Guenthner and others (2013) when defining the parameterization for the ZRDAAM; in the case of Fish Canyon Tuff zircons (FCT), we have used 28 Ma (Reiners et al., 2004).

Our data are shown alongside other literature measurements as a function of estimated dose in Figure 2.13. Although the overall trend of decreasing T_C with increasing dose appears clearly in the Hall Peninsula zircons, they define a very different trend from ZRDAAM. We see these decreases occur at doses as low as 2-5 × 10^{17} α/g—significantly lower than sharp decrease at ~1-2 × 10^{18} α/g predicted by ZRDAAM. This discrepancy is particularly interesting given that our doses are almost certainly overstated. Interestingly, our data closely agree with those of Anderson and others (2017), whose modeled closure temperatures define a similar trend. These trends define a major discrepancy with ZRDAAM, and investigation of the Arrhenian behavior displayed by these data may help explain these differences.

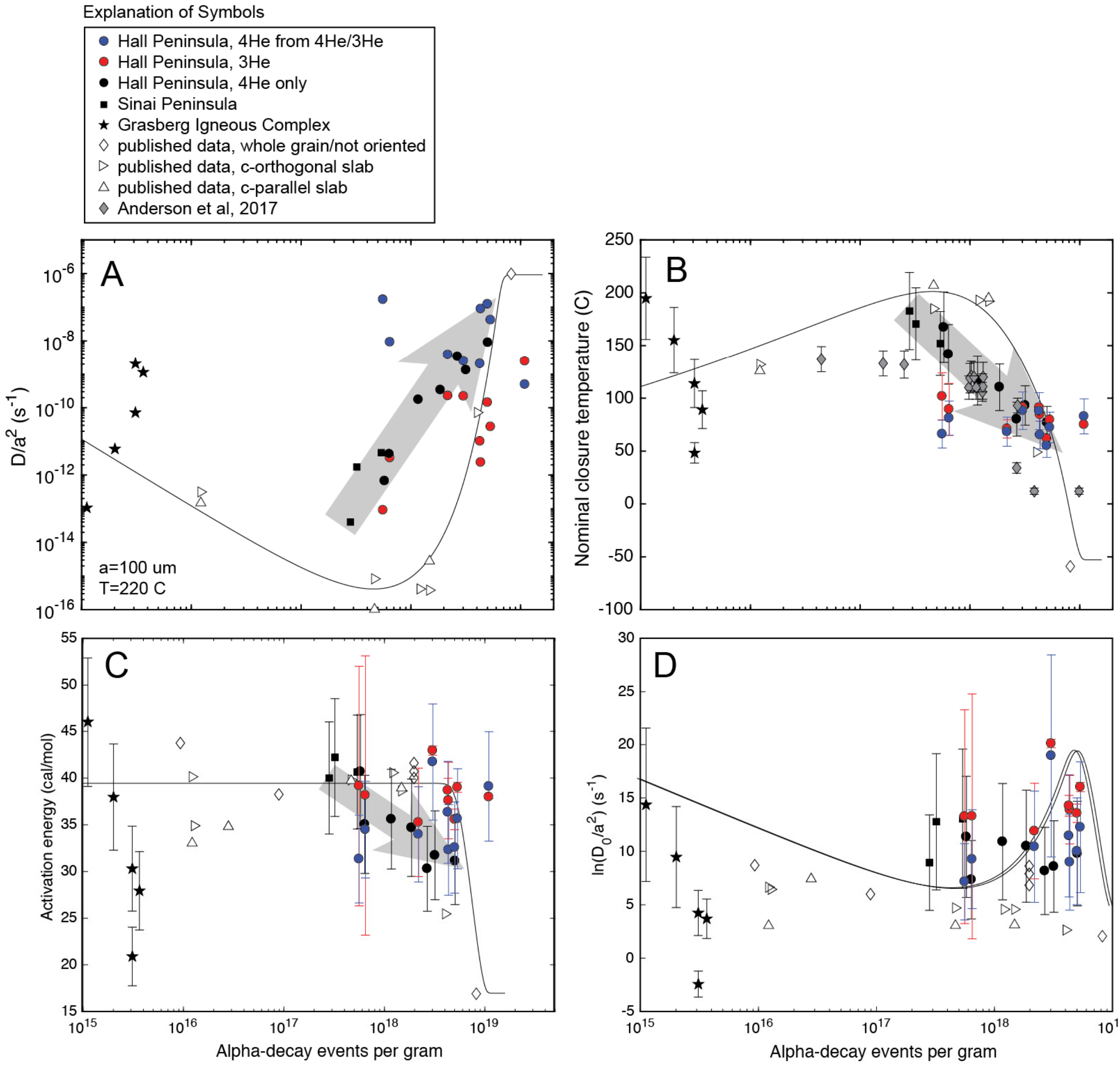
Explanation of Symbols
Hall Peninsula, 4He from 4He/3He
Hall Peninsula, 3He
Hall Peninsula, 4He only
Sinai Peninsula
Grasberg Igneous Complex
published data, whole grain/not oriented
published data, c-orthogonal slab
published data, c-parallel slab
Anderson et al, 2017
A
D/a^2 (s^{-1})
10^{-6}
10^{-8}
10^{-10}
10^{-12}
10^{-14}
10^{-16}
a=100 um
T=220 C
B
Nominal closure temperature (C)
250
200
150
100
50
0
-50
-100
C
Activation energy (cal/mol)
55
50
45
40
35
30
25
20
15
10^{15}
10^{16}
10^{17}
10^{18}
10^{19}
Alpha-decay events per gram
D
ln(D$_0$/a^2) (s^{-1})
30
25
20
15
10
5
0
-5
10^{15}
10^{16}
10^{17}
10^{18}
10^{19}
Alpha-decay events per gram

Figure 2.13

Figure 2.13 Results in terms of diffusivity D/a^2, nominal closure temperature T_C, activation energy, and frequency factor. Other published data are also included, when available (Reiners et al., 2002, 2004; Cherniak et al., 2009; Wolfe and Stockli, 2010; Table 7); not all parameters are available for all published data. Thin black lines show the ZRDAAM parameterization curve; the thick arrows show the trends defined by our data. (A) Diffusivity at 220°C for a 100-µm grain size. Our results show higher diffusivities overall per equivalent dose compared to the ZRDAAM data and parameterization. Closure temperatures (B) show a similar trend. Our results are broadly compatible with the dataset of Anderson et al. (2017) (gray diamonds, only Tc values are provided), with closure temperatures decreasing well before a dose of 10^{18} α/g and at a slower rate compared to ZRDAAM. Activation energy results (C) are also scattered, but overall ^{4}He-only experiments show a clear trend of decreasing E_a at ~$2x10^{17}$ α/g. Trends for $\ln(D_0/r^2)$ (D) are difficult to decipher due to high scatter and large error bars. Because of the erratic nature of the Grasberg zircon Arrhenius relationships (Fig. 2.8), we caution the reader against attaching much significance to these low-damage results.

2.6.3 ^{4}He heterogeneity and diffusivity

In Chapter 1, we explore the effects of alpha ejection, diffusional rounding, zoning, and annealing on ^{4}He diffusivity estimations from fractional losses. These results, exemplified in Figure 2.14, predict that the depletion of ^{4}He at the grain boundary caused by alpha ejection and diffusional rounding would result in strongly underestimated diffusivities due to depletion at the grain boundary, even in the case of severely high rim ^{4}He enrichment (10x). This results in very low initial *D* estimates which rapidly approach 'true' values (Fig. 2.14). Only two ^{4}He-only experiment display a similar pattern: C015-14 and B099-7 (Fig. 2.6), and only with total gas releases <1%, at temperatures <300°C (Table 2.2). Arrhenius relationships also lack a correlation with zonation, suggesting that heterogeneity plays a far smaller role in measured diffusivities than predicted by modeling (Chapter 1).

Several ^{4}He/^{3}He experiments yield ^{4}He diffusivities lower than ^{3}He, in apparent agreement with model predictions (Y080-2, C015-4, B106-1,2,3,6; Fig. 2.9). Interpreting these datasets is not straightforward given the disparities in release fractions between ^{4}He and ^{3}He. Many experiments release a majority of ^{3}He (>80%) during the first one to three hours of heating; only B106-3 and Y080-1 show similarly high ^{4}He fractions (>50%) (Table 2.4). Recent evidence of ^{4}He heterogeneity associated with U and Th variation in zircon (Danišík et al., 2017) may point to an explanation: some zones within our zircons may be highly damaged, and connected to the outside of the grain, while others are more retentive. The damaged zones may have previously been depleted in ^{4}He due to diffusive loss during the latter portion of their geological history, and thus contain a disproportionately small amount of ^{4}He relative to uniformly generated ^{3}He. Sufficient damage in these zones would also be expected to cause the ^{3}He generated within them to be lost quickly in the step-heating experiment. To test for this, we re-analyzed our data for these experiments but omitting the ^{3}He released during the first hour of heating (Fig. 2.15)—this approach also omits an unknown volume of ^{3}He released from the zircon by lattice diffusion during

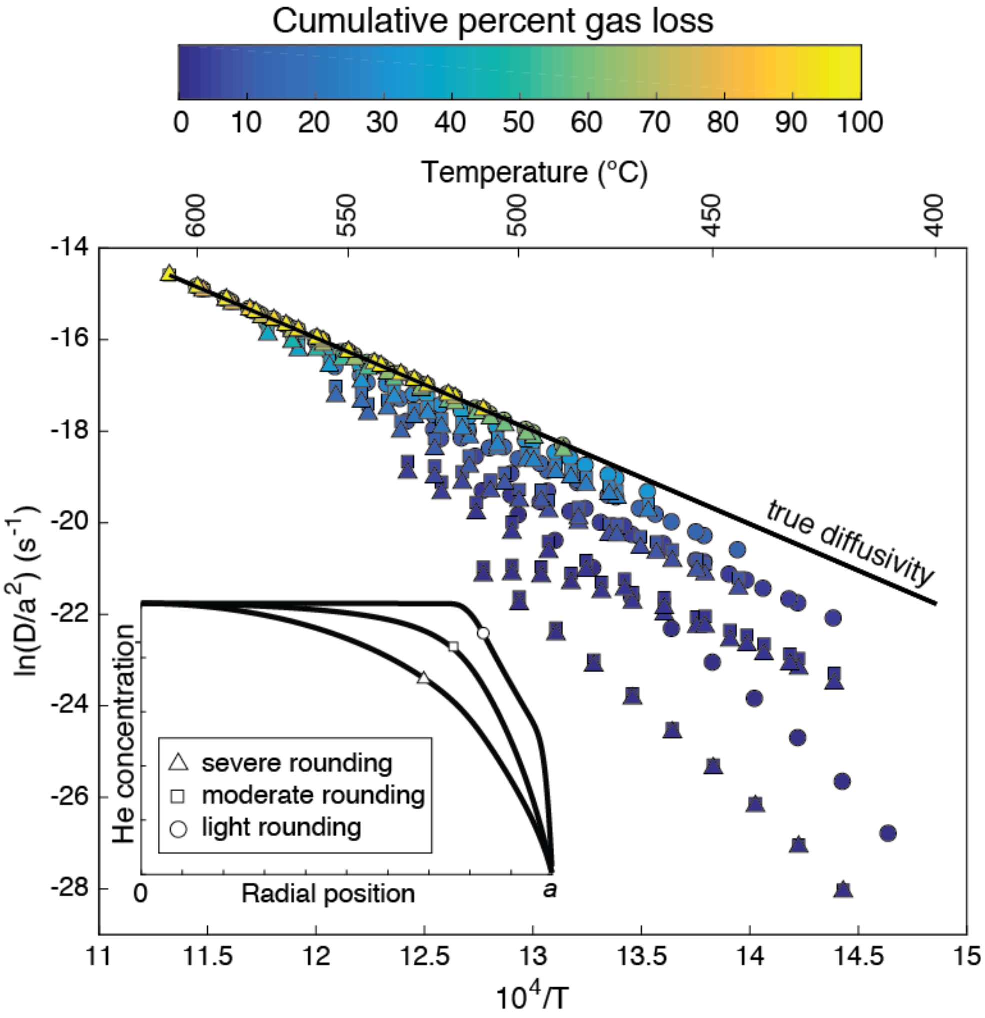

Figure 2.14 Modified from Chapter 1. The results of heterogeneous gas concentrations caused by alpha ejection and diffusional rounding (inset) on diffusivity estimates, as predicted by a 1D spherical finite difference model. The result is a dramatic underestimation of true diffusivity at low fractional losses, due to depletion of helium near the grain boundary, which rises to near "true" diffusivity values by ~50% gas loss. Further results suggest that depletion of U and Th near the grain boundary, like that observed in almost all Hall Peninsula zircons (Fig. 6 insets), exacerbates this effect.

this step, which lowers estimated diffusivities relative to “true” values by an unknown amount. This yields overlapping ^{4}He and ^{3}He diffusivities for three of the five zircons showing high ^{3}He releases; in the other two, ^{3}He plots lower than ^{4}He although results are still within ^{3}He uncertainty. If this re-calculation is valid, seven of our nine ^{4}He/^{3}He experiments would yield largely negligible differences in diffusivities for ^{4}He and ^{3}He. This would also help explain why diffusion kinetics derived from ^{4}He/^{3}He experiments yields a larger degree of scatter than those of ^{4}He-only experiments (Figs. 2.11, 2.13), although it fails to explain very high (>30%) ^{4}He release during the initial step which is not seen in ^{4}He-only experiments. It is possible that proton irradiation alters the crystal lattice and thereby the diffusion kinetics, either in the form of induced damage or annealing. In light of these complications, we urge the reader to interpret the diffusion kinetics of ^{4}He/^{3}He with caution; results have been presented in Figure 2.13 as they are calculated from Figure 2.9 for the sake of completion (that is, without removing the gas from the initial step), however, it is possible that these calculations incorporate diffusional anomalies which are difficult to quantitatively correct.

Lastly, the effects of alpha ejection, rounding, and zonation on diffusion rates are absent or appear subtle relative to model predictions, calling into question fundamental assumptions about He diffusional mechanics. Diffusion appears to behave more like it originated from a homogeneous concentration than previously thought (Chapter 1); these results are particularly striking in light of maps of ^{4}He concentrations in zircons, in which concentrations are far more heterogeneous than 1D models can capture (Danišík et al., 2017).

2.6.4 Rollover and radiation damage annealing

The trend of decreasing diffusivities, which we have termed ‘rollover’, dominates our Arrhenian results (Figs. 2.6 - 2.9). It appears to be thermally activated, with an onset of ~370 – 450 °C in the Hall Peninsula and 500 - 530 °C in the Sinai Peninsula for 0.5 – 2 hr of heating (such

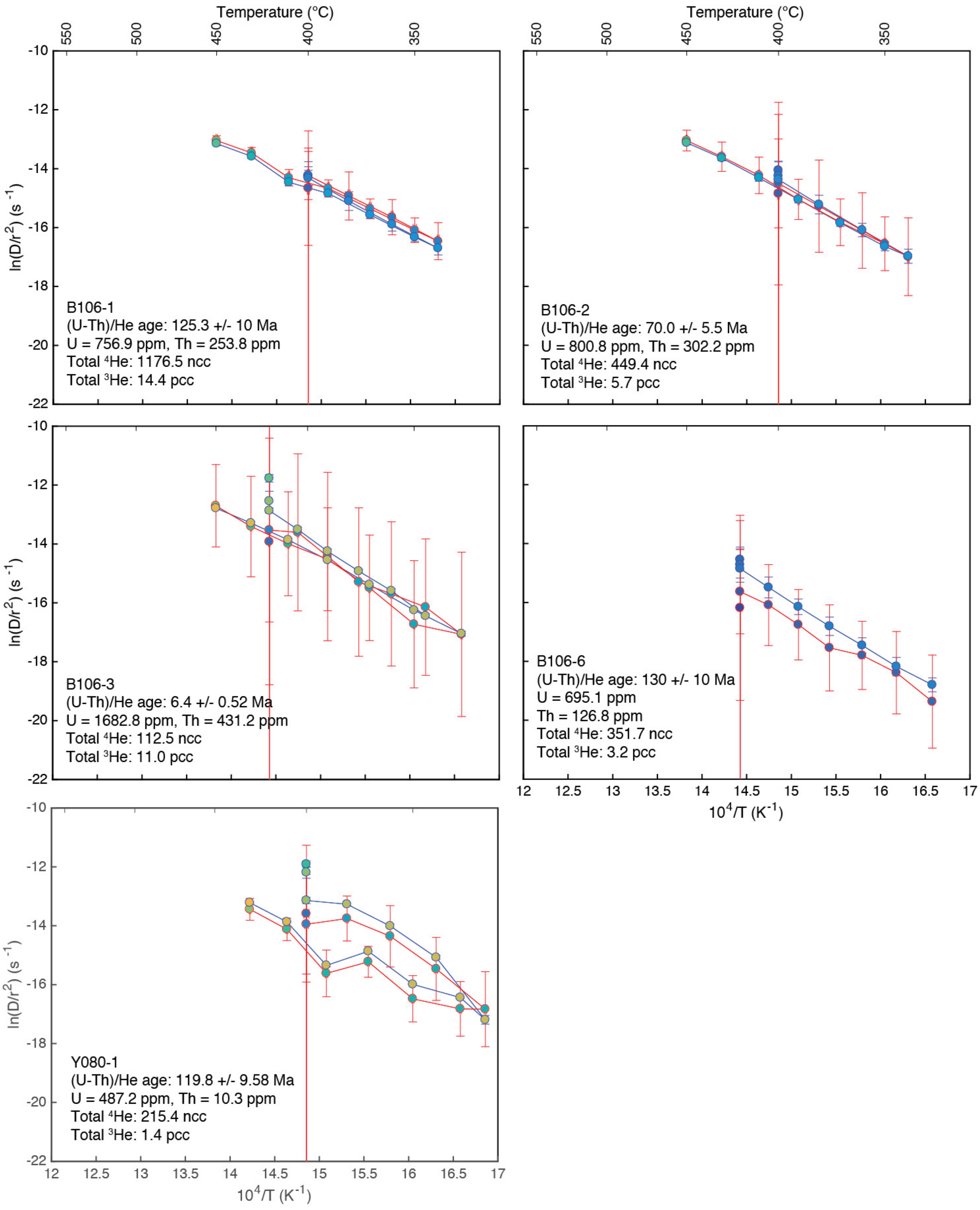

Figure 2.15 Results of five ^{4}He/^{3}He diffusion experiments yielding exceptionally high ^{3}He volumes during the first heating step, with diffusivities recalculated by removing the gas volumes from the first hour of heating from fractional loss calculations. This tests whether the first portion of gas released during heating contained extraneous ^{3}He, not associated with lattice diffusion from the zircon. Results show that, for three of five samples, ^{4}He/^{3}He diffusivities match each other tightly.

thresholds in the Grasberg data are less clear). Below these temperatures, diffusivities are predominantly linear. The intensity of rollover is loosely correlated with bulk eU, yielding stronger effects in higher-eU zircons than lower. Visually, it may appear that rollover primarily decreases the intercept term ($\ln(D_0/a^2)$) while slope (activation energy) remains relatively constant; however, plotting retrograde results of ^{4}He-only experiments (Table 2.3) as a function of total gas loss (Fig. 2.16) reveals that activation energies increase significantly over most experiments. Although increases in both terms have counteracting effects of increasing (E_A) and decreasing ($\ln(D_0/a^2)$) diffusivities respectively, the result is an overall increase in T_C with heating.

Two non-mutual explanations for this behavior are the effects of multiple diffusion domains, and radiation damage annealing. The former is capable of recording complex thermal histories, e.g. in K-feldspar (Richter et al., 1991). Although it is possible that diffusion proceeds within multiple effective domains (e.g. zones with significantly different radiation damage densities, or a network of fast-diffusion pathways induced by interconnected radiation damage zones), this is an unsatisfactory explanation: minerals with multiple diffusion domains typically only yield non-linear behavior during the "switch" from one domain to another (Richter et al., 1991). The changes in diffusivity observed herein are, in contrast, relatively smooth and continuous.

Radiation damage annealing offers a more coherent explanation, given the thermally activated nature of rollover, in conjunction with the observation that higher-eU grains appear more strongly affected (Figs. 2.6, 2.7, 2.9). Furthermore, 1D diffusion-annealing models based on ZRDAAM show a similar behavior at doses $>1 \times 10^{18}$ α/g (Fig. 2.17; see also Chapter 1). Below this dose, however, models predict that annealing *increases* diffusivities, particularly at $T > 600$ °C. This behavior is not observed in any of our experiments (Figs. 2.6-2.9) nor in any published data that we are aware of, although few step-heating experiments venture into such temperatures.

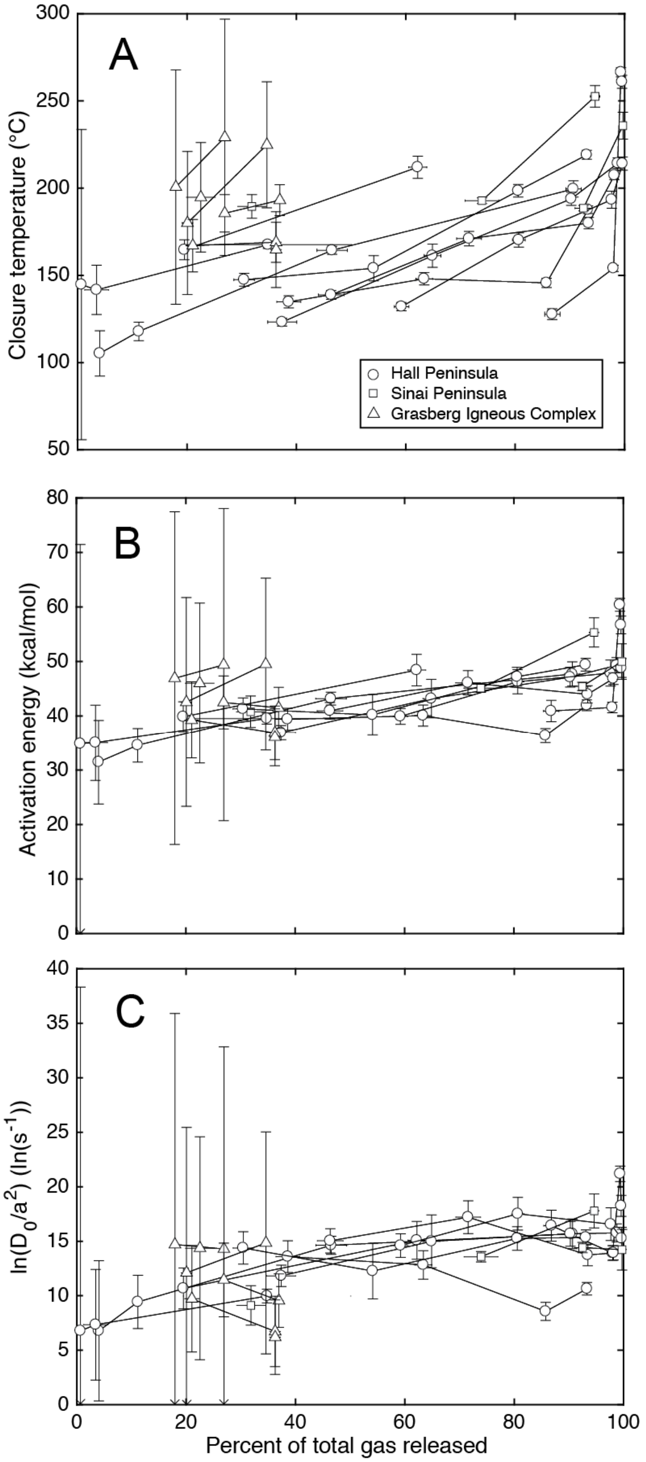
A
B
C
Closure temperature (°C)
300
250
200
150
100
50
Hall Peninsula
Sinai Peninsula
Grasberg Igneous Complex
Activation energy (kcal/mol)
80
70
60
50
40
30
20
10
0
ln(D0/a2) (ln(s-1))
40
35
30
25
20
15
10
5
0
0
20
40
60
80
100
Percent of total gas released

Figure 2.16

Figure 2.16 The effects of rollover on apparent diffusion kinetics, shown by plotting the results of regressions over retrograde heating for ^{4}He-only experiments (Tables 2.2 - 2.3). Retrograde heating is shown exclusively here because most prograde heating steps yield a strong rollover with anomalous diffusivities, while retrograde heating minimizes these effects. Horizontal “error” bars represent the span of gas release over which the regression was made; for example, if during an experiment 10% of the total gas was released by the end of the first step of a retrograde heating sequence, and 15% on the last step of the retrograde sequence, the datum would lie at 12.5% and display a horizontal bar from 10-15%. Both empirically measured diffusivity parameters, E_A (B) and $ln(D_0/a^2)$ (C), are observed to increase over the course of most experiments, but increases in E_A are more consistent overall. The result is an overall increase in T_C.

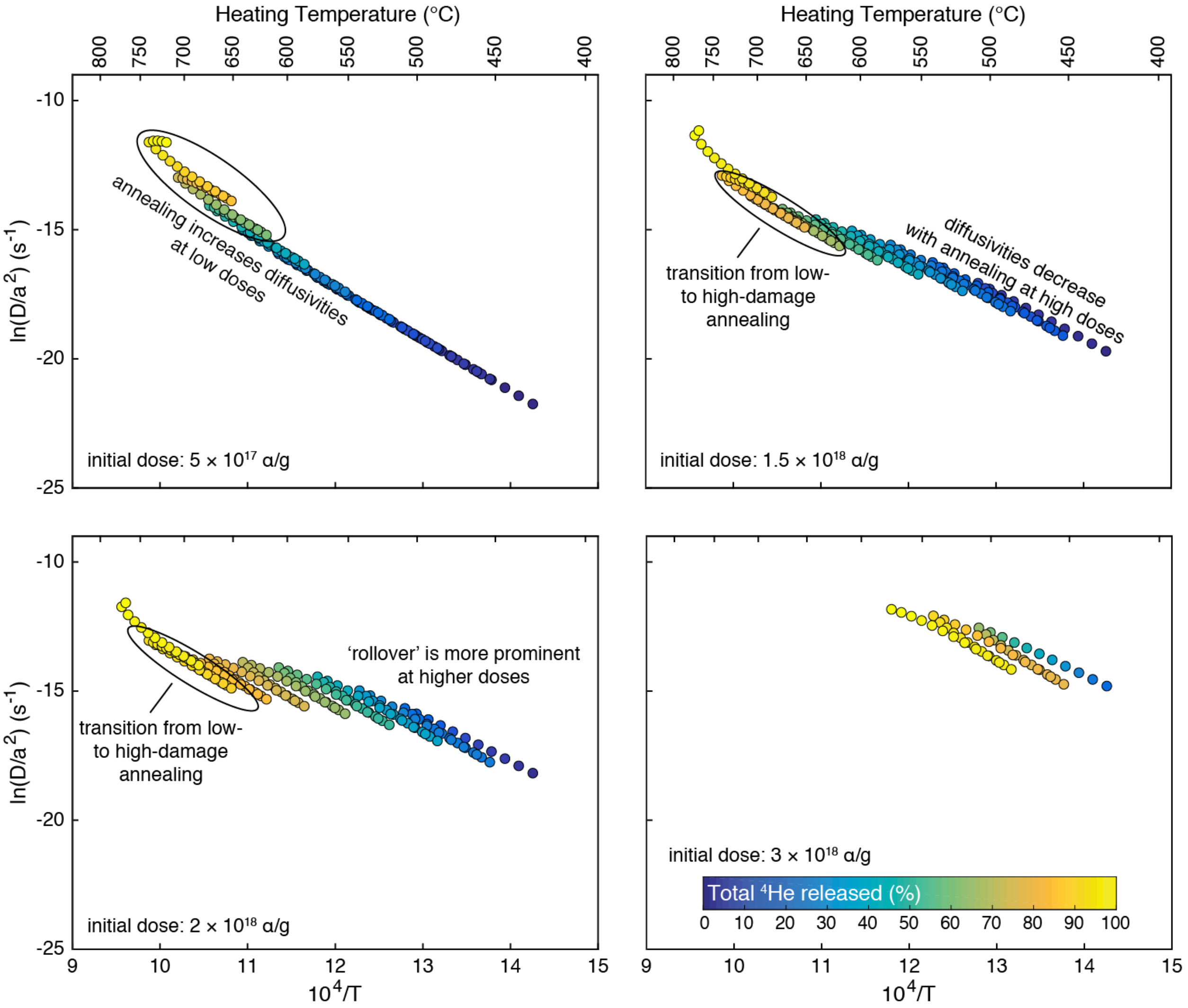

Figure 2.17 Modified from Chapter 1. 1D spherical finite difference diffusion modeling of the damage-diffusivity and annealing relationships defined by the ZRDAAM. He concentrations are homogeneous, to isolate effects of damage annealing from gas heterogeneities. Damage is annealed as a single population with no prior annealing history, for simplicity. Approaching the threshold of metamictization, exposure to Tt conditions similar to those of step-heating schedules yields rollover in a similar manner to that observed herein (Figs. 2.6-2.9), with the notable exception that below effective doses of 1 × 10^{18} α/g, damage annealing yields *increases* in diffusivity. No such effect in our experiments.

The idea that rollover is caused by damage annealing is complicated by several factors. First and foremost is the lack of consistent changes in Raman spectra at similar Tt conditions (Fig. 2.11): although some measurements show increasing crystallinity as expected, most are chaotic and inconsistent. These experiments operated at lower temperatures than prior similar studies (Zhang et al., 2000; Nasdala et al., 2001; Marsellos and Garver, 2010), and are the first to measure Raman spectra on natural grain surfaces. It is possible that the response of the natural grain boundary differs from that of a polished surface—or perhaps Raman is not ideal for measuring the changes in crystalline structure that affect diffusion. Some researchers have observed that low-temperature (<1000 °C) annealing in zircon forms a unique semi-crystalline state through relaxation of damage-induced stresses, but falling short of epitaxial recrystallization (Nasdala et al., 2004 and references therein). It is possible that these Tt conditions yield 'relaxation annealing', rather than the formation of crystalline zircon to which the ν3 peak is sensitive. The well-studied and variably damaged Sri Lankan megacrystic zircons yield ν3 peak widths and shifts similar to our own (Fig. 2.12; Guenthner et al., 2013 and references therein), but are known to contain significant volumes of semi-annealed or 'relaxed' material (Nasdala et al., 2004). Another observation of note is the color change from red zircons to purple/black after the first heating phases, suggesting that some transformation is occurring within these crystals. Secondly, no other similar diffusion experiments on zircon have consistently shown this rollover behavior, even high-damage Sri Lankan megacrystic zircons (Guenthner et al., 2013). We have already discussed the idea that many zircons from Sri Lanka contain a significant volume of a 'relaxed' crystalline state formed by low-temperature annealing (Nasdala et al., 2004). Some Sri Lankan zircons have also yielded a ZFT age of 40 Ma (Garver, 2002), an unusual result given the stated He age of 440 Ma (the closure temperature of the ZFT system is higher than ZHe). These observations indicate that Sri Lankan zircons have already experienced significant changes to their crystalline state besides radiation damage, and so may be 'pre-annealed' to not yield significant rollover at the lower temperature conditions of their experiments. Sinai Peninsula zircons, with their complex and varied thermal history, may have also been partially annealed and so rollover at higher temperatures than Hall Peninsula zircons. On the other hand, it is unlikely that such behavior would afflict the Grasberg zircons after ~3 myr of damage accumulation, but not the Sri Lankan zircons after 40 myr.

Thus, the final issue with interpreting rollover as annealing is its appearance in the low-damage Grasberg zircons. Research shows that low-damage zircon anneals differently than high-damage (Colombo and Chrosch, 1998; Nasdala et al., 2001; Marsellos and Garver, 2010). It is possible that decreases in diffusivity in these zircons are caused by a different process than in high-damage datasets (Figs. 2.7, 2.8 and 2.9), or a confluence of processes like annealing and anisotropic diffusion (Reich et al., 2007; Cherniak et al., 2009; Guenthner et al., 2013). Unfortunately, diffusivities and the diffusion kinetics measured from them yield results which are widely variable and difficult to decipher. Due to the erratic nature of the Arrhenius relationships derived from the Grasberg zircons, we strongly caution the reader against interpreting our 'best fit' lines from these data as real diffusion kinetics. We have presented these data for the sake of completion, however, further research into these or other low-damage zircons is needed to resolve these issues.

2.6.5 Implications for zircon (U-Th)/He thermochronometry

The idea that low-temperature annealing represents a transformation rather than recrystallization (Section 2.2) is reflected in the difference between our high-damage experimental data (Figures 2.6, 2.7, 2.9), and the predictions of ZRDAAM (Figure 2.17). In the model defined by Guenthner et al. (2013), diffusivity is defined by the confluence of two sets of diffusion kinetics, representing crystalline and amorphous fractions; in the case of annealing, the amorphous fraction being annealed is returned to the crystalline fraction. Our observations, however, indicate that low-temperature annealing may *decrease* diffusivity in zircon but not *increase* it: this supports a model in which the amorphous fraction does not return to a crystalline state, but rather is transformed into a partially annealed state that may be inadequately described by the confluence of only two sets of diffusion kinetics.

Although some researchers have used ZRDAAM with success (Guenthner et al., 2014, 2015; Orme et al., 2015, 2016), others have found discrepancies with other measurements or geological reality (Powell et al., 2016; Anderson et al., 2017; Chapter 3). A possible explanation for these discrepancies is that the quantification of the high-damage end of the dose-diffusivity relationship was based heavily on measurements of Sri Lankan megacrystic zircons. The radiation damage of these zircons has been quite extensively studied—in fact, much of the published research on the effects of damage in zircon utilize these gem-quality crystals (Nasdala et al., 2004 and references therein; Guenthner et al., 2013). The presence of a significant quantity of ‘relaxed’ material, which we interpret as causing decreasing diffusivities, may a yield mis-calibration of ZRDAAM for high-damage zircon. Moreover, if our hypothesis is correct that rollover is the result of the *in situ* formation of one or more intermediate, low-diffusivity regions within the grain, a single α-dose is inadequate to describe the damage states of zircon as they relate to diffusion.

Due to incomplete knowledge of the Hall Peninsula’s thermal history, and knowing that the Sinai Peninsula has experienced several major, local tectonic events since the formation of its basement rock, we cannot assume that no such annealing has occurred in our own samples. Attempts were made to obtain ZFT ages of Hall Peninsula zircons, but large portions of many grains dissolved under normal etching conditions (Garver, 2003); those that survived yielded FT densities far too high to count. Given these and other potential complications such as zonation effects, it is difficult to say what threshold marks the transition to increasing diffusivities.

Excluding the very low-damage Grasberg zircons, our lowest-dose estimate comes from aliquot 09GS05-3 from the Sinai Peninsula which yields a very slight roll-over, indicating that radiation damage plays a role at lower doses than our lowest high-damage estimate. The two Hall Peninsula samples with the lowest dose estimates show no or very little rollover, but these exceed our dose estimate of 09GS05-3. With these complications in mind, we posit that increases in ^{4}He diffusion in zircon due to radiation damage occur, at minimum, ~2-5 × 10^{17} α/g. Interestingly, this overlaps with the percolation threshold of non-clustered α-recoil damage zones, or α-recoil tracks which do not share a common endpoint as they would in a natural decay chain, at approximately 3 × 10^{17} α/g (Ketcham et al., 2013). This "no chain" model may represent a case where tip-to-tip intersection along chains is insufficient for creating high-diffusivity pathways, perhaps due to a lack of amorphization at track tips, thus requiring a greater degree of intersection to create a network.

2.7 CONCLUSIONS

A careful analysis of diffusion kinetics and Arrhenian behavior from 26 zircons, from low to high damage raises significant questions about fundamental assumptions of helium diffusion mechanics in zircon, calling into question the approach of simplifying the damage states of zircon into a single α-dose. These data also provide a window into the annealing kinetics of zircon, showing that significant changes to diffusion may occur at relatively low temperature-time conditions. Our results support a model in which low-temperature annealing of zircon does not cause a return to a crystalline state, but rather modifies the crystal lattice in a way that significantly decreases diffusion. In particular, the high closure temperatures obtained in several experimental data sets, including those underlying ZRDAAM, may be due to analysis of partially annealed material. Such an overprint in turn may have masked the threshold at which diffusivity begins to rise with increasing dose, which we estimate to be ~2-5 × 10^{17} α/g. Our interpretation implies that the relationship between radiation damage, diffusivity, gas heterogeneity, and annealing is considerably more complex than previously appreciated, and is not encompassed by a single dose-diffusivity curve. Heterogeneity of 4He also appears to play a far less significant role than predicted by 1D spherical diffusion models, similar to those which underlie most inverse modeling approaches.

Lastly, we recommend that researchers seeking to improve the ZHe forward model be cognizant of the effects of low-temperature annealing, both in selecting zircons for experiments and in step-heating schedule design. These results will be critical in moving forward with the investigation of diffusional mechanics in zircon and in the creation of a new, more accurate forward model for the zircon (U-Th)/He system.

Chapter 3: Age-eU relationships in zircon (U-Th)/He dating, and the effects of radiation damage on thermal history recovery

ABSTRACT

The interpretation of zircon (U-Th)/He (ZHe) ages from slowly cooled cratons with complex thermal histories is both aided and complicated by the phenomenon of over-dispersed ages, in which zircon ages from the same rock sample show a strong and often negative correlation to effective U concentration (eU = [U] + 0.2378*[Th]) spanning up to hundreds of millions of years. Because the relationship between ZHe age and eU is often a sensitive function of thermal history, such datasets theoretically allow for the recovery of robust thermal histories. The recovery of such thermal histories is achieved by the use of a model which integrates radiation damage into ^{4}He diffusivity calculations (ZRDAAM; Guenthner et al., 2013, Am. Journ. Sci.); however, several studies have shown discrepancies between observed age-eU relationships and model predictions, suggesting that the model radiation dose at which ages begin to decrease with increasing eU (aka increasing dose) is too high. We use ZHe dating in conjunction with inverse modeling, Raman spectroscopy, and laser ablation ICP-MS to characterize discrepancies between real ages and model predictions with respect to radiation damage and zonation. Our inverse modeling approach, featuring 'age envelopes', is optimized for large datasets and allows for visualization of differences between model-predicted and observed age populations. Our results support observations indicating that the threshold dose of ~1 – 2 × 10^{18} α/g, beyond which closure temperatures and ages are predicted to increase by the ZRDAAM, is too high. Although modeling of zonation represents a second order improvement, predictions still fail to match first-order age-eU relationships. Results suggest that a more reasonable estimate for a critical damage threshold is <7 × 10^{17} α/g; however, when interpreted in the context of Chapter 2, results suggest that the use of a single α-dose may be an oversimplification in describing the dynamic diffusion kinetics of zircon.

3.1 INTRODUCTION

Thermochronology is a powerful tool for constraining the timing and thermal evolution of tectonic, geomorphic, and erosional processes. These systems record exhumation or cooling across a range of temperatures over geologic time using information about the concentration and distribution of parent isotopes, and the thermally-activated loss of a radiogenic daughter product either by diffusion (e.g. ^{4}He, ^{40}Ar) or annealing (fission tracks). Each thermochronometric system gives researchers unique ways of recovering information about the thermal history of its host rock. For example, in ^{40}Ar/^{39}Ar and proton irradiated ^{4}He/^{3}He analyses, the shape of the daughter isotope's concentration profile is sensitive to the timing and magnitude of thermal events (Fechtig and Kalbitzer, 1966; Shuster and Farley, 2005); in fission track dating, similar information can be found in the distribution of etched track lengths (Gleadow et al., 1986; Ketcham et al., 2009). In whole-grain (U-Th)/He analysis, parent and daughter concentrations are typically measured in bulk (Farley, 2002), so that the nuances of the temperature-time (Tt) path are obscured within a single age. These studies therefore rely on arrays of single- or multi-grain analyses, from which thermal histories may be inferred based on relationships between age, grain size, bulk parent concentration, and distance along a transect (Stockli, 2005; Reiners, 2005; Dunai, 2005).

The interpretation of thermal histories from thermochronometric datasets is straightforward only if the rate of cooling is either known and constant, or rapid relative to daughter production (Dodson, 1973). Excepting volcanic or hypabyssal magmatism, this information is rarely available; conversely, the purpose of such studies is usually to resolve the timing and speed of cooling of the host rock. Furthermore, rocks may experience multiple cycles of heating and cooling which may alter a thermochronometric system without fully resetting the mineral. The complexities in quantitatively interpreting non-monotonically cooled thermochronometers necessitate the use of a *forward model*, a numerical description of how the system behaves, primarily as a function of temperature and time. Such models predict the age yielded by a mineral grain for a hypothetical, user-input temperature-time (Tt) path. When manually fitting forward models to real data, however, multitudes of thermal histories may accurately account for a given dataset within the bounds of uncertainty. *Inverse* modeling, therefore, explores a series of random Tt paths within the range of geologic constraints, and retains those that are most consistent with the data. One example of such a model is the Radiation Damage Accumulation and Annealing Model (RDAAM), which describes the production and diffusion of ^{4}He in apatite as a function of temperature, time, and radiation damage (Flowers et al., 2009). As radiation damage increases, so does the effective closure temperature (T_C; Dodson, 1973). This effect is caused by a reduction in diffusivity due to damage zones, hypothesized to act as helium traps which require a greater activation energy for ^{4}He diffusion than undamaged crystal lattice (Shuster et al., 2006a, 2006b).

The accuracy of thermal histories calculated this way relies not only on the quality of data, but also on the validity of the assumptions in the forward model. In (U-Th)/He thermochronology, significant attention is given to improving the accuracy of thermal histories derived by modeling through increasingly nuanced quantification of zonation and alpha ejection corrections (Anderson et al., 2017; Danišík et al., 2017; Gautheron et al., 2012; Ketcham et al., 2011; Farley et al., 2011; Hourigan et al., 2005; Orme et al., 2015). The improvements yielded by such efforts are, however, effectively negated if the diffusion parameters of the underlying model do not accurately describe of the kinetics of the system. The issue is compounded when one considers that an erroneous or mis-calibrated forward model may discover Tt paths which are mathematically acceptable but have no real geological significance, particularly in regions where independent thermal constraints are lacking or ambiguous.

3.2 ZIRCON (U-TH)/HE THERMOCHRONOLOGY AND ZRDAAM

The most recent forward model for the zircon (U-Th)/He (or ZHe) system is ZRDAAM (Zircon Radiation Damage Accumulation and Annealing Model; Guenthner et al., 2013). This model is the first attempt to fully quantify the relationship between radiation damage and helium diffusion in zircon, a topic of scientific interest for over a century (e.g. Strutt, 1910; Hurley, 1952). Even since the development of the modern ZHe system (Reiners, 2005; Reiners et al., 2004, 2002), it has been recognized that high radiation doses (>2 × 10^{18} α/g) increase the rate of ^{4}He diffusion from zircon, in some cases beyond the point of bulk helium retention at surface temperatures (e.g. Nasdala et al., 2004). The relationship between diffusivity and dose, according to ZRDAAM, is shown on Figure 3.1 in terms of closure temperature: T_C begins low, increases with increasing damage, but drops rapidly to effectively zero beyond ~1 - 2 × 10^{18} α/g.

This model was formulated, in part, to address the increasingly common observation of negative age-eU correlations in ZHe datasets. The strongest of such correlations, with potential age variations up to hundreds of millions of years, are the result of partial resetting in rocks whose zircons have accumulated large amounts of differential radiation damage. The example thermal history shown in Figure 3.2 is one type of Tt path which contains the necessary ingredients: an initial phase of exhumation to temperatures at which radiation damage is annealed; a significant length of time below annealing temperatures during which damage accumulates; and an additional event or events which variably reset the zircons based on their differential degrees of damage. The result can be envisioned as three distinct populations on an age-eU plot, which we denote as: population 1, unaffected by the second thermal event; population 2, partially reset by the second event; and population 3, fully reset by the second event. We refer to the threshold between populations 1 and 2, or the dose at which ZHe ages begin to decrease with increasing eU, as the decreasing age threshold or DAT; the threshold between partially and fully reset ages (populations 2 and 3) is termed the full resetting threshold, or FRT. Although the DAT is, hypothetically, a constant dose threshold independent of the characteristics of an individual grain, the ages of populations 1 and 3 and the eU values corresponding to DAT and FRT for a given sample set are sensitive to the timing and magnitude of partial resetting.

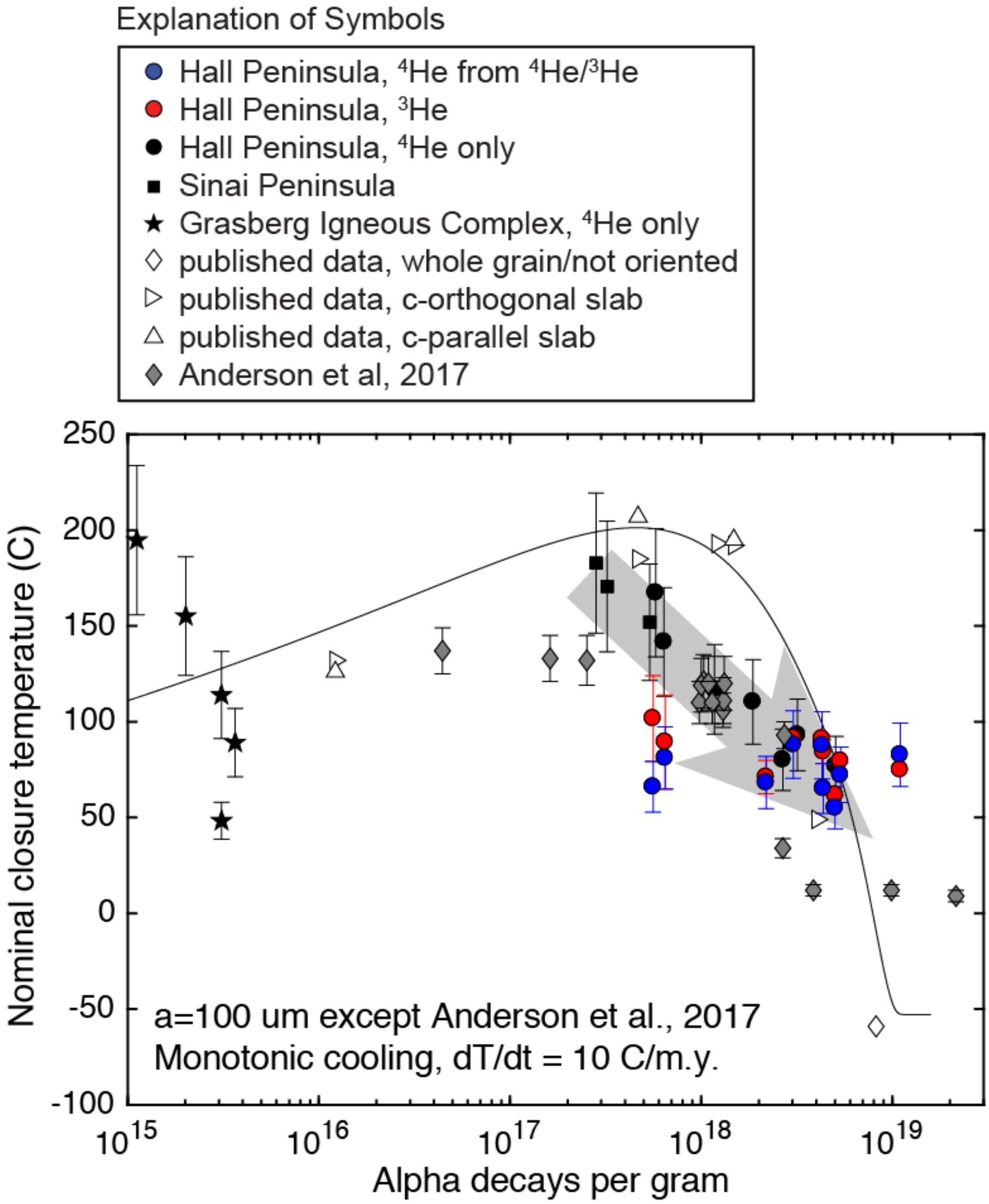

Figure 3.1 Modified from Chapter 2. Zircon closure temperatures as a function of radiation dose in α/g. Data are from Chapter 2 (Hall Peninsula, Sinai Peninsula, and Grasberg Igenous Complex zircons), calculated from other empirical diffusion kinetics data (triangles and diamonds; Cherniak et al., 2009; Guenthner et al., 2013 and references therein), and derived from thermal history modeling (gray diamonds, Anderson et al., 2017; because diffusion kinetics do not exist for these data they cannot be normalized to 100 µm). Some measured closure temperatures (gray arrow) decrease at lower doses than model predictions (black line).

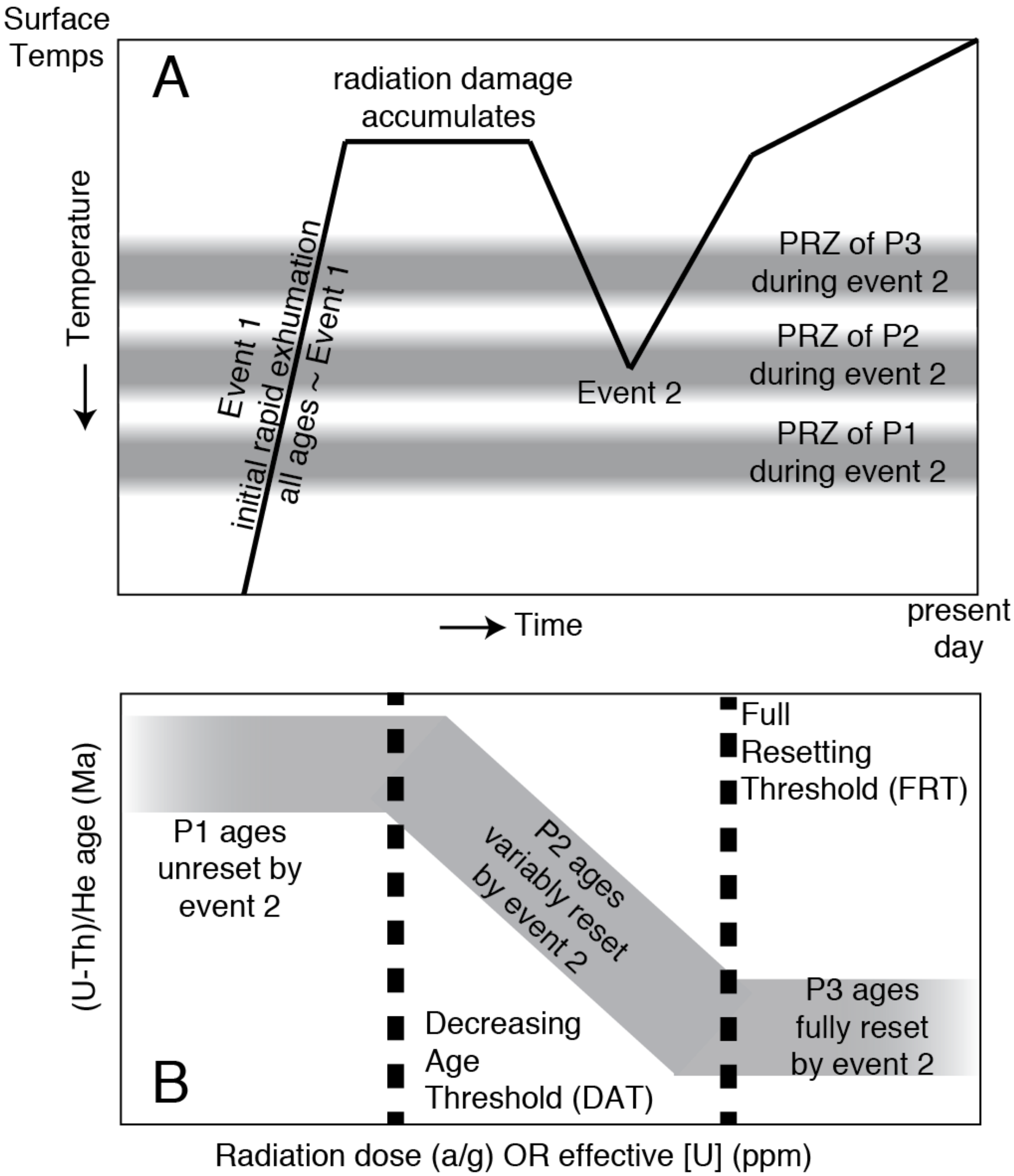
Surface Temps
A
radiation damage accumulates
Temperature
Event 1
initial rapid exhumation
all ages ~ Event 1
PRZ of P3 during event 2
PRZ of P2 during event 2
Event 2
PRZ of P1 during event 2
Time
present day
B
(U-Th)/He age (Ma)
P1 ages unreset by event 2
P2 ages variably reset by event 2
Decreasing Age Threshold (DAT)
Full Resetting Threshold (FRT)
P3 ages fully reset by event 2
Radiation dose (a/g) OR effective [U] (ppm)

Figure 3.2

Figure 3.2 (A) An example Tt path capable of producing the age-eU relationship described in (B). Three critical elements are: an initial exhumation event which resets all zircons in the host rock (Event 1); a phase wherein a high radiation damage differential accumulates between low- and high-eU zircons; and a second heating event which variably resets zircons based on differential damage (Event 2). A high damage differential yields zircons with widely variable diffusion kinetics, resulting in variations in the PRZ and a significantly different response to Event 2 (in reality, PRZs overlap, however, we have illustrated them separately here for clarity). Resulting ages fall within three populations: P1 ages are unaffected by the second heating event; P2 ages are variably affected by the second event; and P3 ages are fully reset by the second event. Populations are separated by two distinct thresholds, at which eU first beings to decrease (DAT) and at which ages no longer decrease (FRT).

Although some authors have employed ZRDAAM to achieve geologically reasonable results (Guenthner et al., 2014, 2015, Orme et al., 2016, 2015), others have experienced difficulties in using the model to fit geologically reasonable scenarios. For example, Powell et al., (2016) show that detrital zircons from the McKenzie Mountains in the northern Canadian Cordillera yield the effects of the DAT (decreasing ages with increasing eU) at estimated doses one billion years short of the stated ZRDAAM threshold. Anderson et al., 2016 show that closure temperatures modeled from the well-constrained and rapidly cooled McClure Mountain (Fig. 3.1), including measurements of in-situ laser ablation (U-Th)/He, are also in disagreement with the current model's predictions. Their study showed T_C decreasing from radiation damage in the range of 10^{17} α/g, with some zircons reliably retaining helium at doses $>1 \times 10^{19}$ α/g. The results presented in chapter 2 measuring diffusion kinetics in natural zircon also shows a very different trend, with radiation damage consistently yielding increased diffusivity at doses approx. 4-7 × 10^{17} α/g, significantly lower than the 1-2 × 10^{18} α/g threshold used in ZRDAAM. Notably, the DAT of ZRDAAM is similar to the threshold of metamictization in zircon, approx. 2-4 × 10^{18} α/g; (Nasdala et al., 2004; Balan et al., 2001; Woodhead et al., 1991), and to the estimated percolation threshold of fission track damage (Ketcham et al., 2013).

This study employs ZHe dates of crystalline basement rock from two localities, the Sinai Peninsula of Egypt and the Hall Peninsula of Baffin Island, Canada, to test the viability of ZRDAAM to invert reasonable thermal histories. In addition, we have included complementary estimates of radiation damage via Raman spectroscopic measurements, and measurement of the degree of rim to core zonation via trace element laser ablation ICP-MS (LA-ICP-MS). This research demonstrates that ZRDAAM has significant issues fitting real data, which cannot be reconciled by a consideration of zonation alone. We also hypothesize a mechanism which explains these discrepancies, based on the results of Chapter 2, in which we use cycled step-heating diffusion from these datasets shows that low-temperature annealing may play a critical and previously underappreciated role in shaping diffusion kinetics.

3.2 CASE STUDIES

3.2.1 Sinai Peninsula

The geologic history of the western coast of the Sinai Peninsula, along the Gulf of Suez, Egypt, is thoroughly characterized due to a well-preserved sedimentary record, lack of vegetation, and abundant hydrocarbon exploration-motivated research (e.g. Bosworth and McClay, 2001; Bosworth et al., 2005). Regional crystalline basement rock is composed of syn-tectonic granites and granodiorites, gneisses, and metavolcanics, formed and variably metamorphosed during the Pan African orogeny (~700 – 570 Ma). Zircon U-Pb ages from regional basement rocks range from 623 - 610 Ma, with post-tectonic dikes having ages of 591 Ma (Stern and Manton, 1987). Since crustal formation, the region has experienced a range of different tectonic regimes: Late Devonian-Early Carboniferous Hercynian tectonism (e.g., Frizon de Lamotte et al., 2013), early Mesozoic Neo-Tethyan rifting (Bosworth and McClay, 2001), Santonian inversion (Guiraud and Bosworth, 1997; Guiraud, 1998; Bosworth and McClay, 2001; Bosworth et al., 2005), and Cenozoic extension resulting from rifting between the African and Arabian plates (Bosworth et al., 2005; Kohn et al., 1993; Bosworth et al., 2015). Regional thermal history reconstructions from apatite fission track dating (AFT) and K-feldspar $^{40}Ar/^{39}Ar$ thermochronometry (Kohn et al., 1997) indicate rapid post-crystallization cooling followed by reheating during the Late D-Early C (Frizon de Lamotte et al., 2013) and holding at approx. 110 – 170 °C prior to Miocene extension from 23 - 14 Ma (Bosworth and McClay, 2001; Bosworth and Stockli, 2016).

Zircons in this study are taken from undeformed granitic samples (Fig. 3.3): 08GZ17 and 09GS05 are surface samples taken from Gebel Samra, while ERB47 and ERB48 are taken from an industry borehole (ERB-B-2X) a depth of approx. 1.6 km. All samples are likely from the same pluton, offset by faulting. Zircons are are mostly euhedral tetragonal bipyramidal crystals, with equivalent spherical radii from ~40 – 125 µm. Their color is mostly clear, with light yellow and colorations being rare.

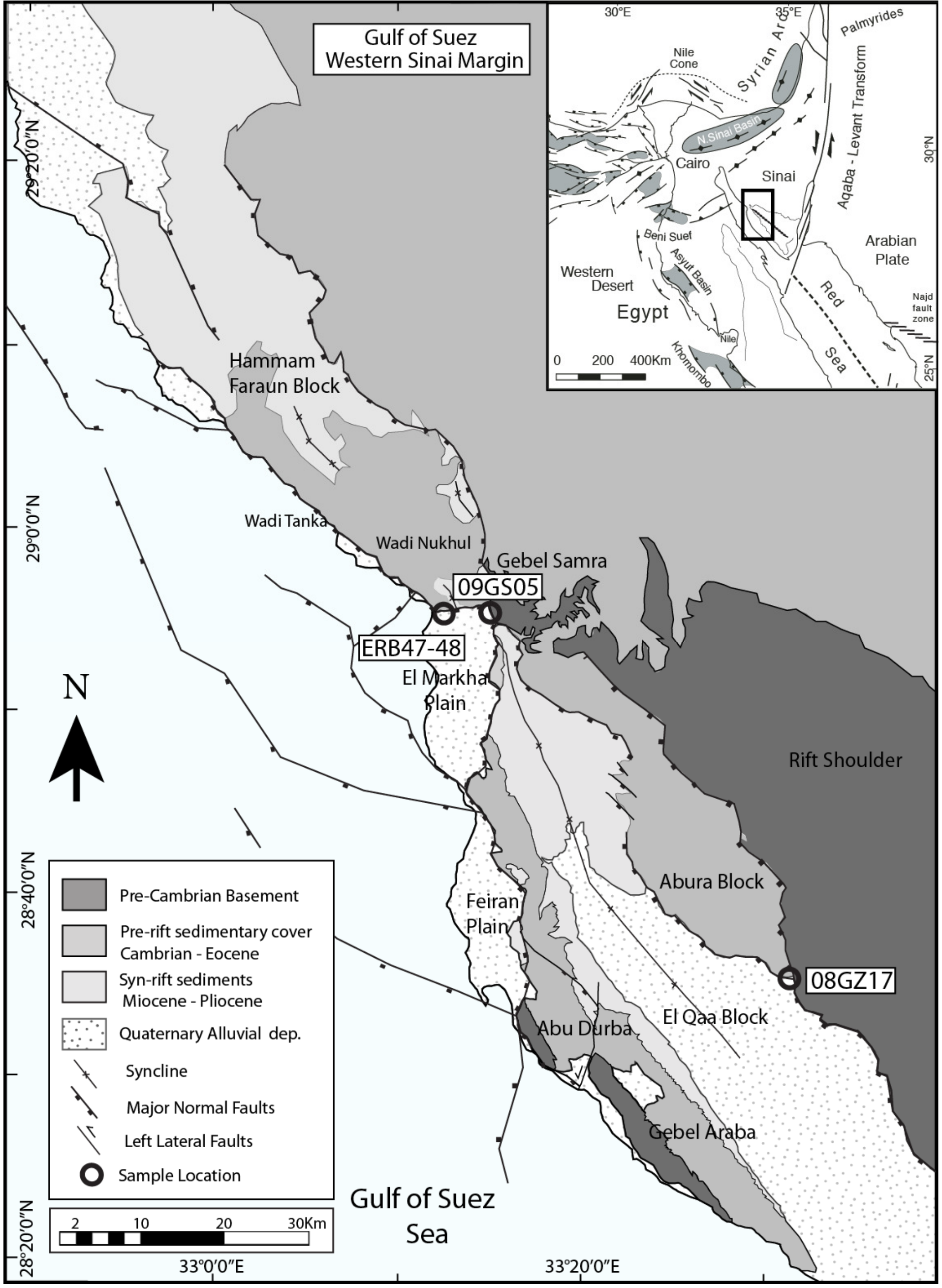

Figure 3.3 Sample locations within the Sinai Peninsula/Gulf of Suez region, on top of a geologic map modified from Pujols, 2011. 08GZ17 and 09GS05 are surface samples from Gebel Samra, and the two ERB samples are taken from the ERB-B-2X borehole by Apache Egypt at approx. 1620 m depth. All samples are granites likely from the same formation, offset by faulting.

3.2.2 Hall Peninsula geologic setting and sample description

The Hall Peninsula of Baffin Island (Fig. 3.4) is composed of an Archean tonalite-orthogneiss complex (2.7 – 2.8 Ga, zircon U/Pb and Pb/Pb) which was variably metamorphosed during the Trans-Hudson orogeny from 2.0 – 1.8 Ga (Scott, 1999, 1996). Following regional metamorphism, the complex remained at mid-crustal temperatures for an extended time as recorded by muscovite K/Ar ages (T_C ~420 °C) of 1.69 - 1.62 Ga (Skipton et al., 2015 and references therein). The geologic record through the Proterozoic and Phanerozoic is sparse, and is mainly constrained by the presence of conodonts from limestone xenoliths recovered from kimberlites, identified by Zhang and Pell (2014) as Ordovician. This suggests a period of active sedimentation and Phanerozoic burial of unknown depth. The region was affected by rifting and exhumation from 228 – 140 Ma as Greenland separated from North America, and again from 80 – 64 Ma during the opening of the Labrador Sea (McGregor et al., 2013 and references therein). The degree to which the Archean block was affected by these events is loosely constrained regionally, but locally unresolved.

Rock samples from the Hall Peninsula were collected and provided by the Canada-Nunavut Geoscience Office; more information on the geologic context of these samples is provided by Creason, 2015. Zircons from Hall Peninsula separates are abundant, euhedral, and larger on average than their Sinai Peninsula counterparts, with colors ranging from clear, yellow, rose, red, crimson, and purple.

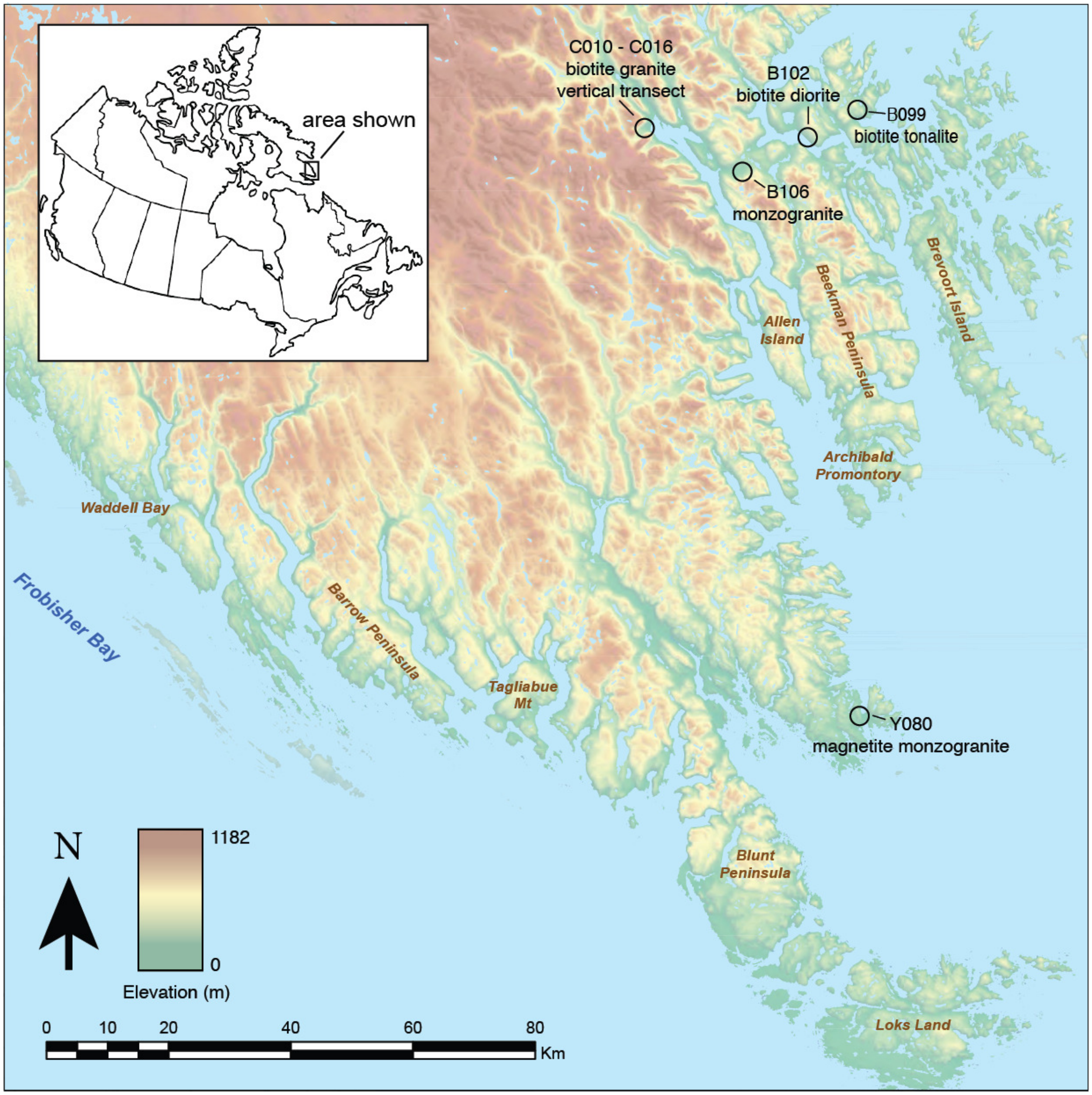

Figure 3.4 Elevation map showing locations and host-rock lithologies of Hall Peninsula samples. These rocks are taken from an Archean tonalite-orthogneiss complex which was metamorphosed during the Trans-Hudson orogeny. Samples were collected and provided by the Canada-Nunavut Geoscience Office. Modified from Creason, 2015.

3.3 METHODOLOGY

3.3.1 Overview of workflow

This study combines whole-grain (U-Th)/He analyses and inverse thermal history modeling with Raman spectroscopy, to obtain an independent measure of radiation damage, and trace element analyses via laser ablation, to obtain information about U and Th zonation. Standard practice for these and similar types of analyses is to embed zircons into epoxy or a similar material, and then polish away a portion of the grains so that the interiors are exposed for analysis (Nasdala et al., 2003; Košler and Sylvester, 2003). Because the (U-Th)/He technique used herein requires dissolution of the whole zircon, however, we are restricted to whole-grain analyses prior to dissolution. Figure 3.5 illustrates our workflow, which involves analyzing a natural surface of the grain perpendicular to the c-axis.

3.3.2 Raman spectroscopy

Raman spectroscopy is a well-documented technique for assessing the degree of atomic disorder in zircon (Nasdala et al., 1995; Geisler et al., 2001; Nasdala et al., 2004; Marsellos and Garver, 2010). With increasing disorder, primarily caused by radiation damage, the ν3 Si-O anti-symmetric stretching peak widens and its peak moves to lower wavenumbers. In this study, Raman spectroscopy represents an independent measure of radiation damage.

Measurements for Sinai Peninsula zircons were made at the University of Kansas on a Renishaw system, at 512 nm with a 5 µm diameter circular spot size. Hall Peninsula zircons were measured at The University of Texas at Austin Mineral Physics lab, using a 523.13 nm laser with a 30 μm^2 square spot size. Baselines for Raman spectra were fitted by hand and subtracted, after

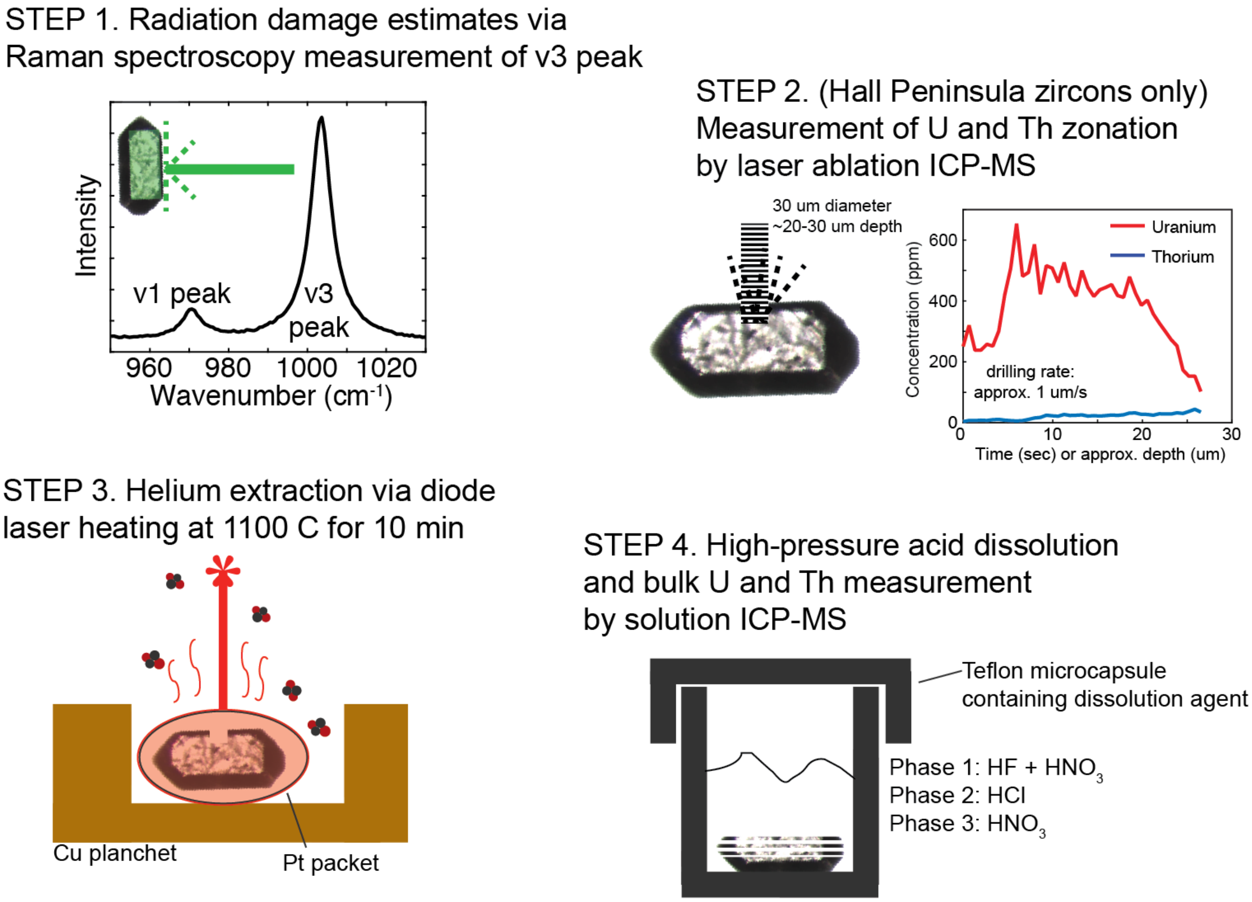

STEP 1. Radiation damage estimates via Raman spectroscopy measurement of v3 peak

STEP 2. (Hall Peninsula zircons only) Measurement of U and Th zonation by laser ablation ICP-MS

STEP 3. Helium extraction via diode laser heating at 1100 C for 10 min

STEP 4. High-pressure acid dissolution and bulk U and Th measurement by solution ICP-MS

Figure 3.5 An illustration of the workflow for each zircon: (1) whole-grain Raman spectroscopic analysis, to obtain an independent estimation of radiation damage for each zircon; (2) LA-ICP-MS pit-profiling analyses to observe zonation on the outside of the zircon; (3) diode laser heating to release and measure ^{4}He; and (4) dissolution and measurement of whole-grain average U and Th concentrations ($U_{bulkavg}$ and $Th_{bulkavg}$).

which the ν3 SiO4 antisymmetric stretching peak was fitted to a Voigt profile using the program *fityk* (Wojdyr, 2010), with the resulting full-width at half max (FWHM) corrected for spectral resolution (Nasdala et al., 2001 and references therein). Each reported measurement is an average over three individual spots from natural, unpolished (100) crystal faces, with errors reported as 1σ. Because no effort was made to ensure that both systems yield comparable measurements with zircons, it is possible that discrepancies between datasets may exist due to the difference in wavelength and spot size.

3.3.3 Laser ablation trace element analysis

Parent nuclide concentrations in zircon are commonly heterogeneous, and the degree of heterogeneity has consequences for measurement of ages and recovery of thermal histories which have been extensively discussed in literature (Hourigan et al., 2005; Anderson et al., 2017; Danišík et al., 2017 and references therein). To observe variations in parent nuclide distributions on the outer surface of the zircon, we use laser ablation ICP-MS depth profiling analyses (Ault and Flowers, 2012; Smye and Stockli, 2014; Anderson et al., 2017) on Hall Peninsula zircons. An excimer laser in a large format HELEX cell was used to ablate a circular 30 μm diameter pit of ~18-28 μm depth into a (100) crystal face of each zircon, and a ThermoFisher Element2 single-collector magnetic sector ICP-MS was used to determine parent nuclide concentrations. Washout time is <0.3s, yielding a down-hole resolution of <1 μm (Smye and Stockli, 2014). Measurements were calibrated to either NIST612 glass or to natural samples of GJ1 zircon (Jackson et al., 2004).

3.3.4 (U-Th)/He dating

(U-Th)/He ages are obtained following the procedures of Wolfe and Stockli (2010): ^{4}He was liberated from zircons by diode laser heating at 1300 °C, spiked with ^{3}He, cryogenically concentrated purified, and measured by isotope dilution using a Balzers Prisma 200 quadrupole mass spectrometer (Wolfe and Stockli, 2010). Zircons were then dissolved in high-pressure digestion vessels with a spike containing ^{235}U, ^{230}Th, and ^{149}Sm, with bulk concentrations determined using a ThermoFisher Element2 single-collector magnetic sector ICP-MS using isotope dilution and a gravimetric standard solution. Uncertainties on whole-grain concentrations are <1%.

3.3.5 Thermal history inverse modeling

To explore the ability of the ZRDAAM to recreate the overall age-eU relationships observed in both settings, we use an inverse modeling approach which simulates all zircons in a given dataset (Appendix A). Each zircon is modeled with a 1D spherical approximation using 250 grid nodes, homogeneous production rates based on bulk U and Th measurements, and a time step length of 0.25 myr (Ketcham, 2005). 'Best' Tt paths are defined by those which have the highest number of modeled ages falling within 12% of the measured age (1.5x the standard error of zircon, 8%, to encourage more fits; Reiners, 2005), and the age-eU relationship of the best paths are shown as 'age envelopes' (Fig. 3.6). Inspired by the concept of inheritance envelopes (Guenthner et al., 2015) but for zircons from crystalline rocks lacking inheritance, age envelopes show the bounds within which fall all modeled ages for a given dataset using and time-temperature path, by using ages modeled from the maximum and minimum grain sizes across the range of parent concentrations. Age envelopes allow an easy visual comparison of observed vs modeled age-eU relationships.

Our approach of modeling multiple samples with a single thermal history is admittedly a considerable simplification, as sample locations from each region vary both laterally and vertically. For example, in the Hall Peninsula, sample Y080 was taken approx. 100 km from samples C010 – C016, which themselves are from a 250 m vertical transect (Fig. 3.3). In the Sinai Peninsula, sample 08GZ17 sits along the boundary of a major normal fault, 50 km from the

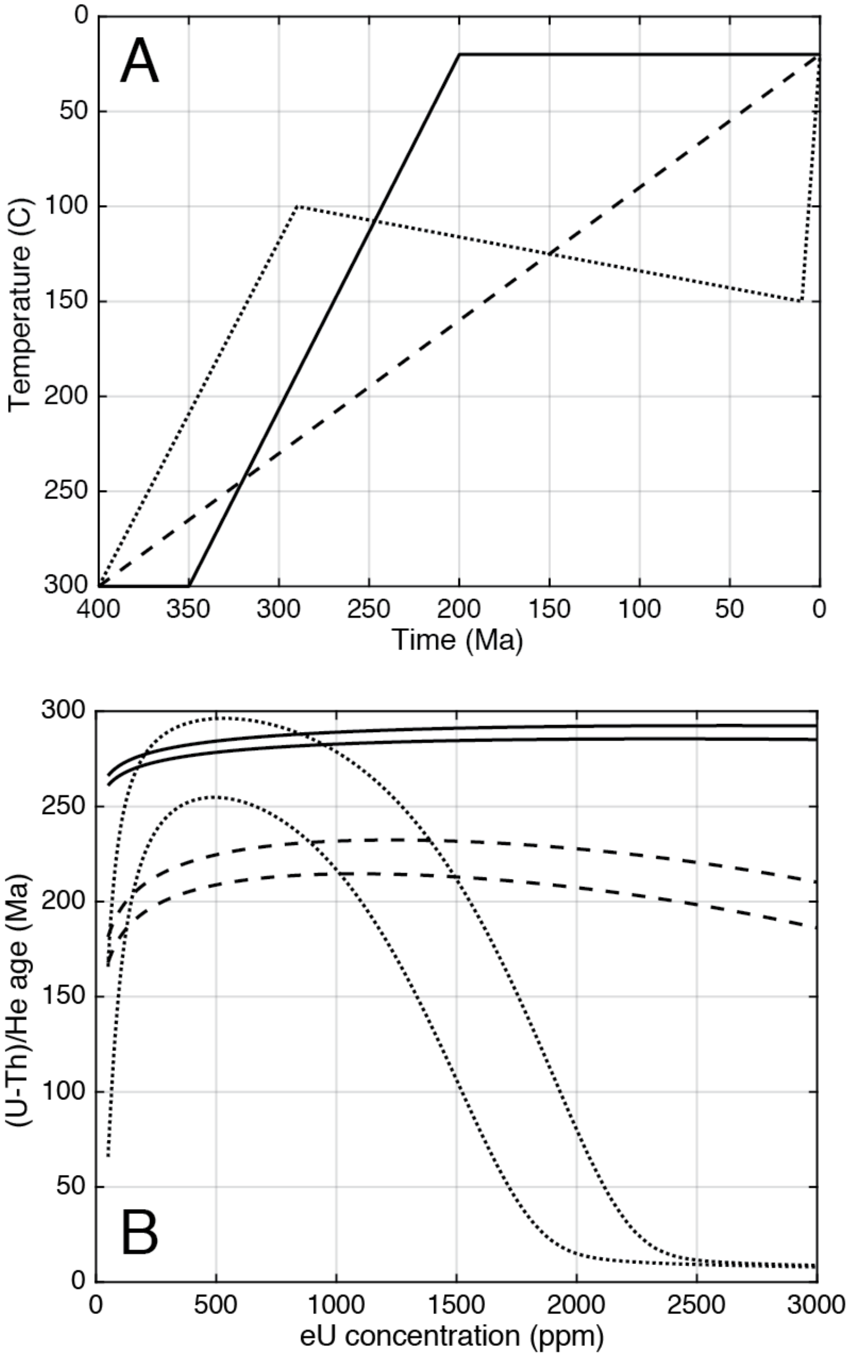
A
Temperature (C)
0
50
100
150
200
250
300
400
350
300
250
200
150
100
50
0
Time (Ma)
B
(U-Th)/He age (Ma)
300
250
200
150
100
50
0
0
500
1000
1500
2000
2500
3000
eU concentration (ppm)

\

Figure 3.6

Figure 3.6 (A) Example Tt paths for demonstrating age envelopes. The solid line represents steady monotonic cooling at 6.6 °C/myr; the dashed line represents slower cooling at 0.8 °C/myr; the dotted line cools initially to 100 °C, is slowly reheated to 150 °C, and rapidly cooled at ~10 Ma. (B) Model-predicted age envelopes for a sample set containing 50 – 3000 ppm eU, and a range of grain sizes between 60 and 120 µm (equivalent spherical radii). The upper line in each pair represents the ages predicted for the matching Tt path at the largest grain size, and the lower line represents the smallest grain size; all modeled ages from a given dataset occur between these two lines. At dT/dt = 6.6 °C/myr (solid lines) and 0.8 °C/myr (dashed lines), the differences in grain size play a minimal role, with ages tightly recording initial cooling. At low doses, the model predicts a slight decrease in ages (Fig. 3.1). The Tt path with reheating (dotted lines) reveals widely variable ages similar to those described on Figure 2. In model predictions, the low-damage population 1 is replaced by a trend of decreasing ages with decreasing eU. Real data (below) yield a more consistent low-eU population. The effects of radiation damage on diffusion kinetics are mild when recording a single cooling event, but when partially reset zircons display age-eU relationships as a sensitive function of thermal history.

ERB-B-2X borehole (Fig. 3.4), wherein ERB47 and ERB48 were retrieved from a depth of 1.6 km. The details of thermal histories among regional samples are expected to vary, however, when plotted together, our ages display relatively consistent and complete age-eU trends (see below), with most samples having ages in at least two of the three populations. This degree of overlap suggests that differences in thermal history across the sampling areas have only second-order effects on their ZHe ages, and that using a single thermal history is a reasonable simplification.

3.4 RESULTS

3.4.1 Sinai Peninsula

Table 3.1 contains all Sinai Peninsula zircon sample data including ZHe ages and Raman ν3 peak values. Bulk average U concentrations vary from 66 to 2125 ppm, with Th concentrations from 19.6 to 701 ppm. Figure 3.7 shows zircon (U-Th)/He ages against eU, yielding a well-defined negative age-eU trend, indicative of radiation damage effects (Guenthner et al., 2013, 2014; Powell et al., 2016; Anderson et al., 2017). Ages range from 563 to 17 Ma. The majority of low-eU ages cluster between the end of the Neoproterozoic Pan-African orogeny and the beginning of the Late Devonian thermal event. Beyond 300 – 400 ppm eU, ZHe ages decrease with increasing eU. Above 600 – 700 ppm eU, all ages but one are below 100 Ma.

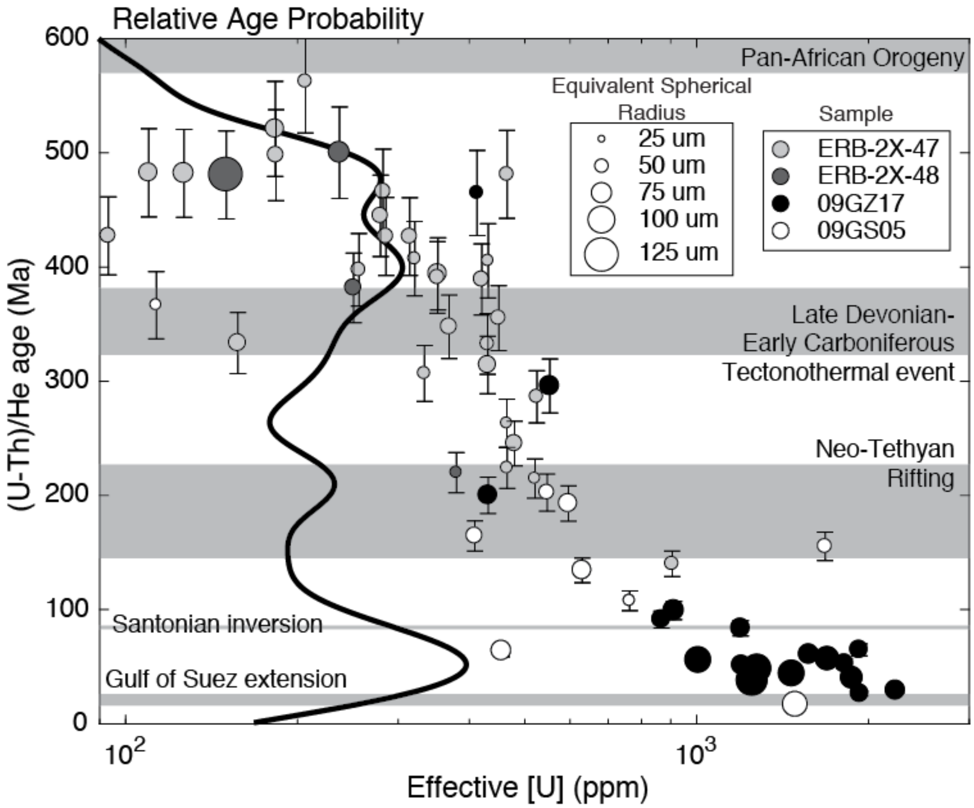

Figure 3.7 Zircon (U-Th)/He ages from the Sinai Peninsula plotted against eU, alongside a kernel density estimate of ages (black line). Relevant tectonic events are highlighted. A distinct negative age-eU trend is observed with the highest age densities occuring at approx 480 – 400 Ma for low eU zircons, prior to the Late D-Early C event; and at ~50 Ma in high eU zircons, between Santonian inversion and Gulf of Suez extension. A small increase in age density also occurs near the onset of Neo-Tethyan rifting. Despite widely variable geographical locations (Fig. 3.3), all ages appear to define a single age-eU ‘curve’.

Table 3.1 Zircon sample information for Sinai Peninsula zircons (Fig. 3.4), including grain size (as equivalent spherical radius) U and Th concentrations, ZHe age, and Raman ν3 peak width parameters.

Sample	Aliquot	ESR (um)	U (ppm)	Th (ppm)	eU (ppm)	ZHe age (Ma)	+/-	v3 FWHM (cm-1)	+/-	v3 peak shift	+/-
ERB-47	11	55.6	393.3	117.7	420.4	389	31.1	11.5	0.4	1001.6	1.3
ERB-47	12	44.8	306.5	117.9	333.6	307	24.5	14.6	2.3	998.6	1.4
ERB-47	14	63.3	106.7	219.8	157.3	333	26.7	8.4	0.1	1003.8	0.3
ERB-47	15	55.9	263.5	82.5	282.5	466	37.3	10.2	1.5	1002	1.3
ERB-47	16	50.5	433.6	139.1	465.6	481	38.5	11.0	0.1	1001	0.1
ERB-47	17	40.2	440.1	109.3	465.2	263	21.0	17.6	1.8	1000.7	0.2
ERB-47	18	68.3	330.2	95.9	352.3	394	31.5	15.4	0.9	999.4	0.4
ERB-47	19	44.8	303	77.6	320.8	407	32.6	13.7	0.4	999.5	0.4
ERB-47	20	41.5	395.9	154.1	431.3	405	32.4	15.6	1	998.9	0.4
ERB-47	21	52.8	330.1	93.9	351.7	391	31.3	11.4	0.4	1002.4	0.3
ERB-47	22	50.5	251.6	19.6	256.1	398	31.8	10.8	1.8	1003.2	0.3
ERB-47	23	59.1	323.1	198.2	368.7	348	27.8	10.5	0.3	1001.3	0.3
ERB-47	24	67.5	166.1	72.9	182.9	521	41.7	12.9	0.3	1000.3	0.9
ERB-47	25	49.1	840.9	281.8	905.7	140	11.2	14.7	1.5	998.9	0.4
ERB-47	26	49.7	400.5	130.4	430.5	333	26.6	16.8	1	999	0.4
ERB-47	27	48.6	477.4	206.4	524.9	286	22.9	11.4	0.7	1001.4	0.4
ERB-47	28	53.1	418.1	138.8	450.0	355	28.4	11.9	0.5	1000.5	0.3
ERB-47	29	55.5	287.1	119	314.5	427	34.1	12.3	0.4	1001.5	0.2
ERB-47	30	54.8	266.9	82.2	285.8	427	34.1	11.9	0.5	1001.2	0.3
ERB-47	31	63.2	399.4	136.5	430.8	314	25.1	10.4	0.1	1002.6	0.2
ERB-47	32	59.6	443.9	155.9	479.8	245	19.6	15.3	1.6	999.1	0.5
ERB-47	33	56.4	238.4	178.9	279.5	445	35.6	10.1	0.6	1002.1	0.5
ERB-47	34	48.8	182.7	103.4	206.5	563	45.0	9.1	0.1	1003.8	0.1

Table 3.1 cont

ERB-47	35	54.7	66.4	116.8	93.3	427	34.2	7.0	0.1	1004.7	0.3
ERB-47	36	41.0	455.2	285.7	520.9	215	17.2	13.5	0.2	999.7	0.4
ERB-47	37	57.6	157.5	112.6	183.4	498	39.8	8.6	0.4	1003	0.3
ERB-47	38	67.0	96.3	58.6	109.8	483	38.6	8.6	1.4	1004.3	0.3
ERB-47	40	73.8	109	76.2	126.5	482	38.6	13.6	1.2	1000	0.5
ERB-47	42	42.9	437.9	121.2	465.8	224	17.9	12.8	1.1	1002	0.6
09GS05	1	68.8	594.1	158.5	630.6	134	10.7	11.5	4.1	1002.1	1.1
09GS05	2	67.0	551.6	194.1	596.2	193	15.4	7.7	7.5	1001.5	0.9
09GS05	3	39.9	105.6	32.9	113.2	367	29.3	6.6	0.8	1004.9	0.1
09GS05	5	40.8	692	309.6	763.2	108	8.6	16.6	1.4	999.6	0.9
09GS05	6	91.7	1399.6	395.1	1490.5	17	1.3	23.7	1.8	997.2	1
09GS05	7	72.2	431.6	104.6	455.7	64	5.1	18.9	1.3	997.6	0.2
09GS05	8	51.0	1568.6	479.1	1678.8	155	12.4	15.2	4.4	999.8	1.2
09GS05	9	58.4	381	120.9	408.8	165	13.2	20.2	0.9	999.2	0.2
09GS05	10	54.1	509.7	162.8	547.1	203	16.2	14.8	0.7	999.2	0.8
09GZ17	5	47.2	380.9	136.9	412.4	465	37.2	12.1	0.9	1002.7	1.5
09GZ17	6	71.2	504.4	212.9	553.4	296	23.7	16.8	0.1	999.1	0.3
09GZ17	7	72.1	2125.3	460.2	2231.1	29	2.3	16.6	0.7	999.4	0.3
09GZ17	8	66.1	1832.9	425.6	1930.8	26	2.1	6.8	0.6	1006.3	0.4
09GZ17	9	75.4	839.2	320.2	912.8	99	7.9	14.4	1.4	1000.4	1.4
09GZ17	10	88.1	1577.9	515.5	1696.5	57	4.5	17.1	3.1	999.4	0.9
09GZ17	11	105.7	1222.9	242	1278.6	48	3.8	8.8	0.2	1005.3	0.4
09GZ17	12	67.1	1654.6	700.7	1815.8	53	4.2	19.5	1.1	999.2	0.1
09GZ17	13	96.7	1409.3	260.3	1469.2	44	3.5	10.5	1.3	1004.1	0.4
09GZ17	14	65.3	1858.4	294.9	1926.2	65	5.2	12.1	1	1000.4	0.8
09GZ17	15	73.1	1506.8	288.2	1573.1	61	4.9	13.4	1.4	1000.4	0.6
09GZ17	16	115.8	1191.4	267.3	1252.9	38	3.0	10.5	4.2	999.5	0.7

Table 3.1 cont

09GZ17	17	70.2	1143.4	243.1	1199.3	51	4.1	11.6	1.8	1001.2	0.4
09GZ17	18	96.7	979	125.9	1008.0	56	4.4	8.2	0.5	1002.6	0.6
09GZ17	20	66.1	818	216.5	867.8	91	7.3	8.8	2.5	999.9	3.1
09GZ17	21	69.6	1129.4	284.1	1194.7	84	6.7	13.7	0.6	999	0.5
09GZ17	22	70.5	409.7	94.3	431.4	200	16.0	9.9	0.6	1002	1.3
09GZ17	23	81.5	1786.8	370	1871.9	40	3.2	6.4	0.9	1004.7	0.4
ERB-48	1	76.9	213.5	102	237.0	500	40.0	10.6	0.4	1000.4	0.7
ERB-48	2	125.7	131.5	80.9	150.1	481	38.4	8.6	0.9	1002.7	0.6
ERB-48	3	42.0	349.3	131.8	379.6	220	17.6	13.5	0.2	999.2	0.3
ERB-48	5	59.7	237.2	58.8	250.7	382	30.5	7.3	0.9	1002.3	0.7

Sinai Peninsula inverse modeling

The results of inverse modeling are given in Figure 3.8, using reasonable geologic constraints. Initial exhumation from post-orogenic cooling occurs during Cambrian-Devonian times, followed by an increase in temperature in the Late Devonian-Early Carboniferous (Frizon de Lamotte et al., 2013). This is followed by a relatively quiescent period with temperatures between 110 and 170 °C, in accordance with cooling ages from K-feldspar $^{40}Ar/^{39}Ar$, apatite fission track (AFT), and zircon fission track (ZFT) (Kohn et al., 1997). A final phase of exhumation occurs during Gulf of Suez spreading in the Miocene (Kohn et al., 1993, 1997; Bosworth and McClay, 2001). Age envelopes from best fit paths deviate from the observed age-eU trend strongly, fitting the P1 but missing most P2 ages. Although model results provide a reasonable approximation of P3 ages, model ages are tightly restricted at high damage, yielding a lack of acceptable fits. Observed ages decrease at a significantly lower eU than predicted by ZRDAAM at these Tt paths.

In Figure 3.9, we have expanded the range of possibilities to allow exhumation to begin anytime between post-tectonic dike formation (591 Ma; Stern and Manton, 1987) and 1,000 Ma, long before the rocks' Pan-African origins. Allowing earlier exhumation gives radiation damage more time to accumulate. We have also allowed a wider range of possible Devonian to Cretaceous temperatures which allows for either a higher or lower degree of partial resetting, and have widened the window of possible Gulf of Suez exhumation to improve the model's ability to fit high-eU grains. Given a geologically unreasonable length of time to accumulate damage, the ZRDAAM yields a significantly better fit with observed data.

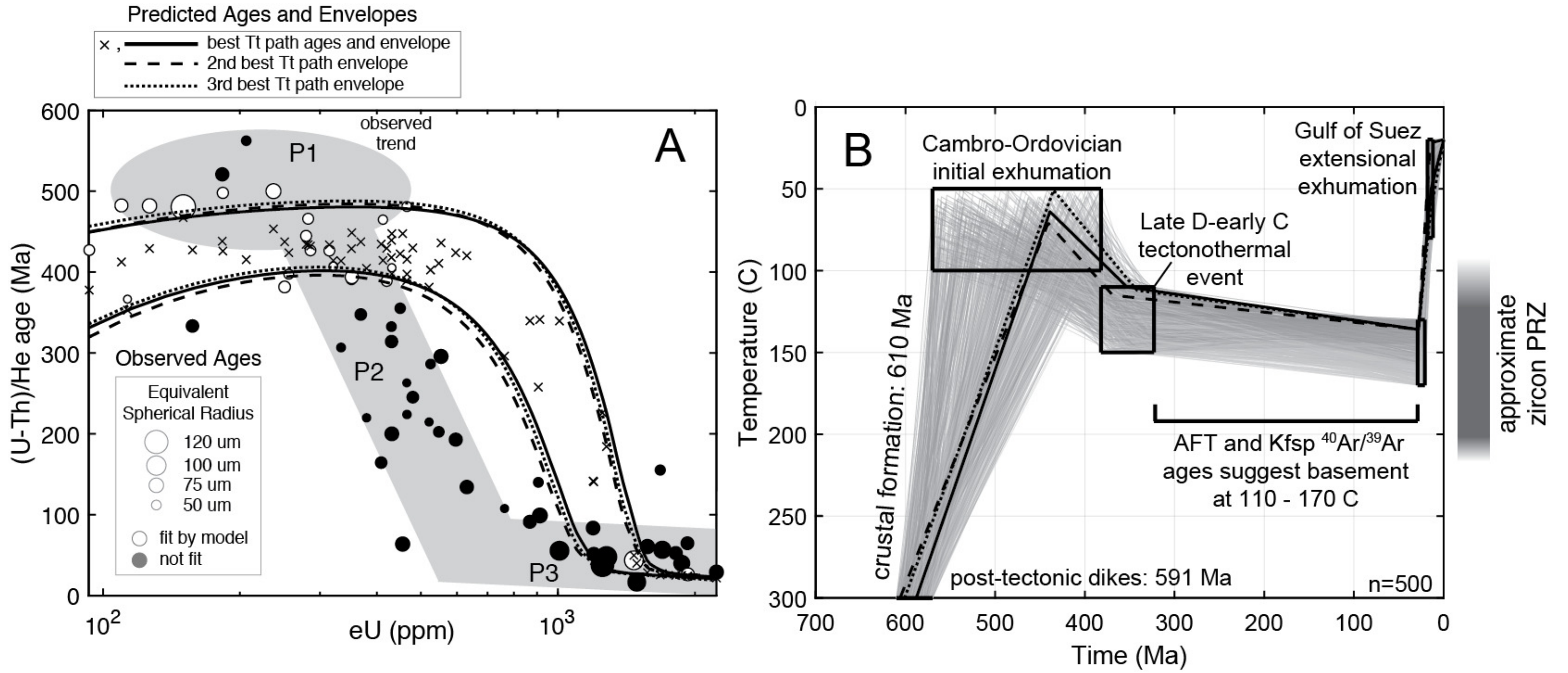

Figure 3.8 (A) Inverse modeling results, as x's for the best fitting Tt path, and as age envelopes for the top three paths. Age populations (P1-P3; Fig 3.2) are highlighted. Although the wide geographical distribution of these samples (Fig. 3.3) may yield some disparities between samples real thermal histories, the coherence of the age-eU relationship (Fig. 3.9) suggests that this approach is justified. Models produce Tt paths and age envelopes which deviate strongly from real data, with the 'best' (highest scoring) paths underestimating P1 ages and failing to fit any P2 ages. Real ages decrease at much lower eU concentrations (~300 ppm) than model ages. (B) Models used 500 randomly generated paths with a time step length of 0.5 myr and 500 grid nodes per zircon (Appendix). All paths are lightly transparent, and better scoring paths are darker shades of gray. The three highest scoring paths are shown as thick solid, dashed, and dotted lines respectively.

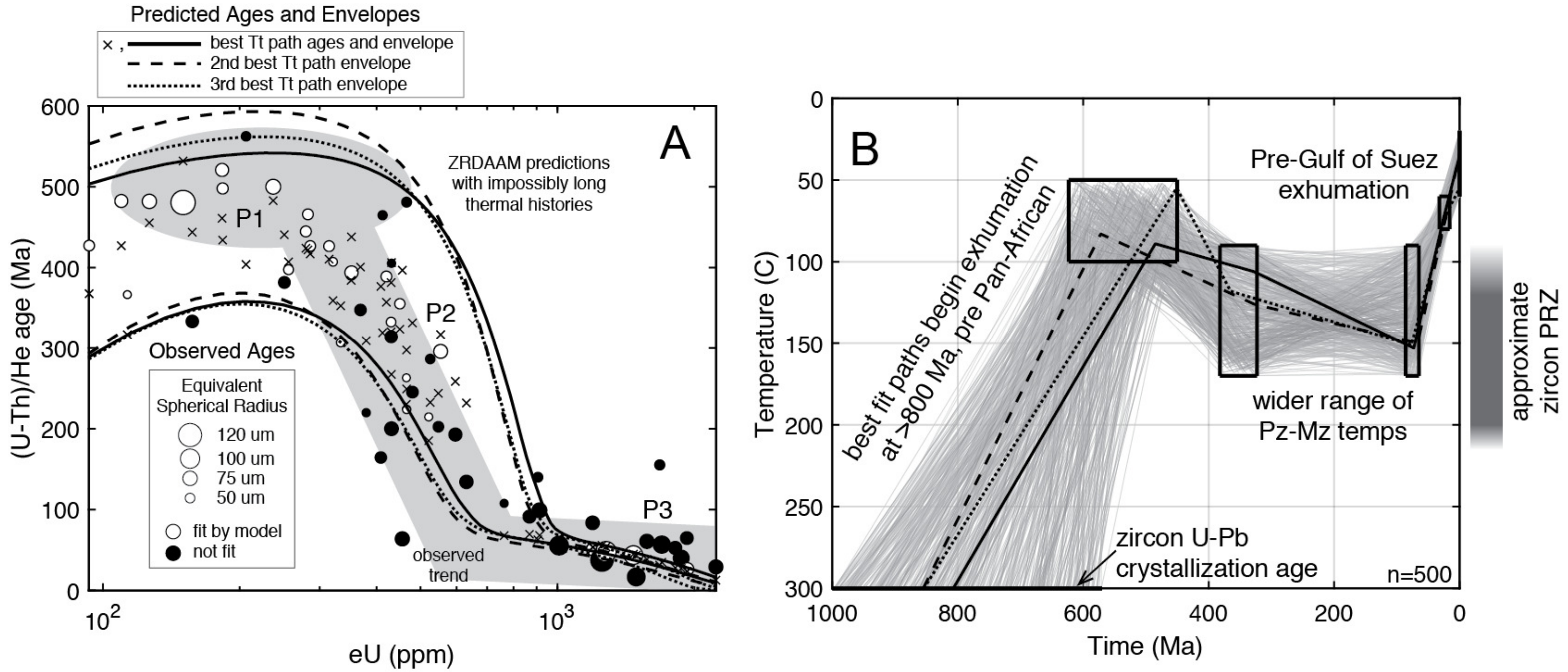

Figure 3.9 Inverse modeling results from the Sinai Peninsula similar to Figure 3.10, but with a wider window of initial exhumation times. This adjustment allows for a better fit to the data (A), but is geologically unrealistic as exhumation for best-fit paths begins at >800 Ma (B), long before the Pan-African orogeny which formed these rocks. These results demonstrate how the ZRDAAM may give preference to Tt paths which are mathematically agreeable but geologically impossible, when not properly constrained.

3.4.2 Hall Peninsula

Zircon sample data and results from the Hall Peninsula are presented in Table 3.2. U concentrations range from 29 to 1747 ppm, with Th concentrations from 13 to 200 ppm. Results of ZHe dating from this region are shown in Figure 3.10: ages below ~120 ppm eU cluster around 800 – 1050 Ma, coinciding with late and post-Grenville tectonism. Above 120 ppm eU, ages decrease with increasing eU. Many high-eU (>500 ppm) ages coincide with the Late Cretaceous opening of the Labrador Sea. There are several outlier ages in this dataset, namely three pre-Grenville ages, and the Paleozoic ages which occur at low and high-eU

The results of laser ablation ICP-MS analyses are shown in Figure 3.11. Overall, zircons in this dataset show a trend of U and Th enrichment.

Hall Peninsula inverse modeling

Because the thermal history of the Hall Peninsula is less well constrained than that of the Sinai Peninsula, our inverse modeling constraints allow for a generous degree of variation in Tt paths (Fig. 3.12). Exhumation begins between 1,600 Ma – 1,400 Ma at 300 °C, in accordance with regional muscovite K/Ar ages of 1.69 – 1.62 Ga (T_C ~420 °C; Skipton et al. 2015 and references therein), with exhumation occurring during the Grenville orogeny. After the initial phase of exhumation, Tt paths are allowed to take several different routes, with optional exhumation or burial during the Paleozoic and Greenland rifting. Final exhumation occurs during the spreading of the Labrador Sea, in accordance with observed ages (Fig. 3.10). Age envelopes capture most P1 ages but overestimate a majority of P2 ages, similar to Sinai Peninsula results (Fig. 3.8). Also similar to previous results, P3 ages are well approximated by model results, but restricted to a very narrow range.

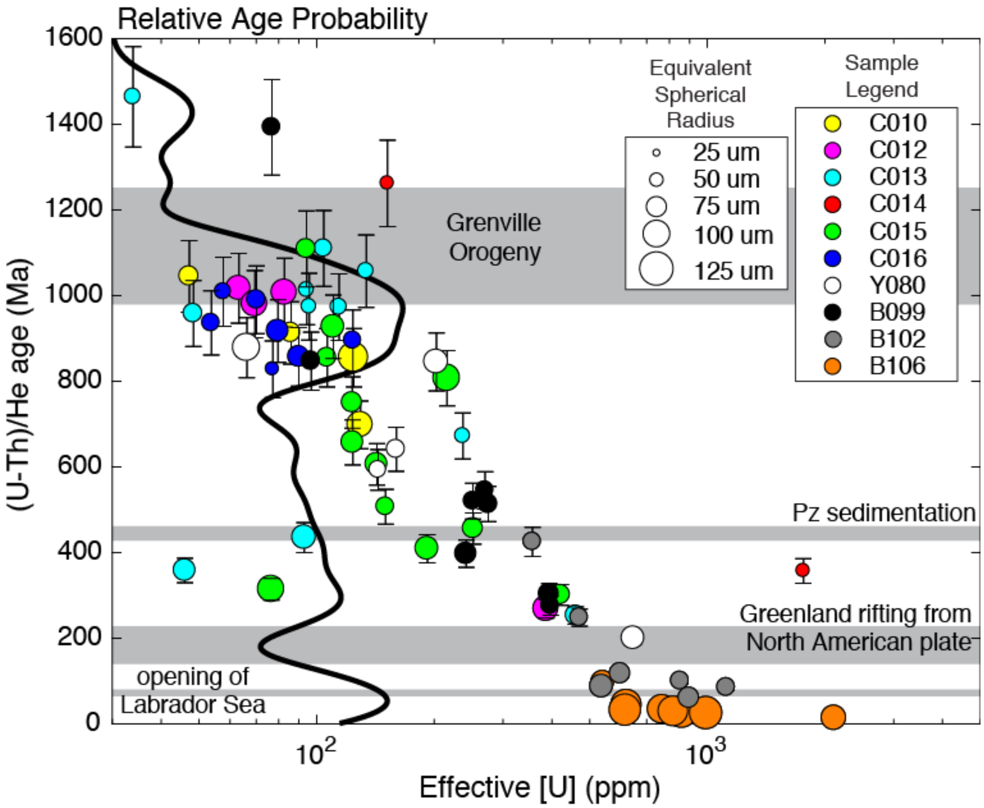

Figure 3.10 Zircon (U-Th)/He ages from Hall Peninsula samples (Fig. 3.4), with a kernel density estimate of ages (black line) regional tectonism highlighted. Despite being from a wide geographical distribution and from a range of lithologies (Fig. 3.4), the negative age-eU trend is very clearly defined by all samples. The majority of low-eU cooling ages occur at approx. 1100 – 800 Ma, coinciding with the end of the Grenville orogeny. High-eU ages cluster around ~50 Ma, coinciding with Labrador Sea spreading. A small number of ages cluster around ~400 Ma in apparent disagreement with the overall age-eU trend; similarly, three ages appear to record pre-Grenville cooling.

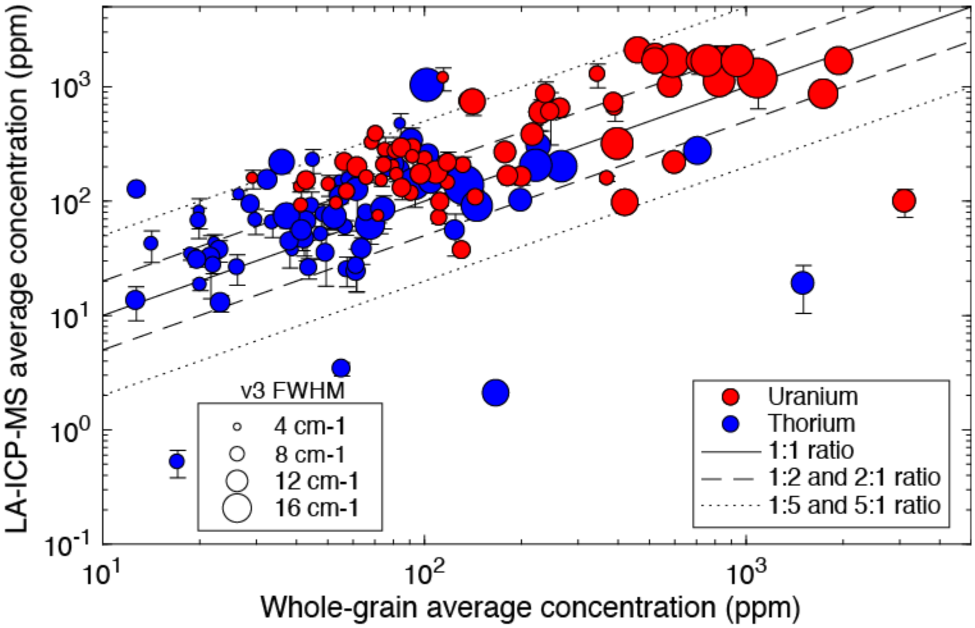

Figure 3.11 Whole-grain average concentrations of U (red) and Th (blue) vs average concentrations measured over laser ablation pits for Hall Peninsula zircons. The solid, dashed, and dotted lines represent core-to-rim (and vice-versa) concentration ratios of 1:1, 1:2, and 1:5 respectively. Marker sizes represent mean FWHM. We observe an overall trend of rim enrichment, with FWHM increasing with increasing concentrations as expected.

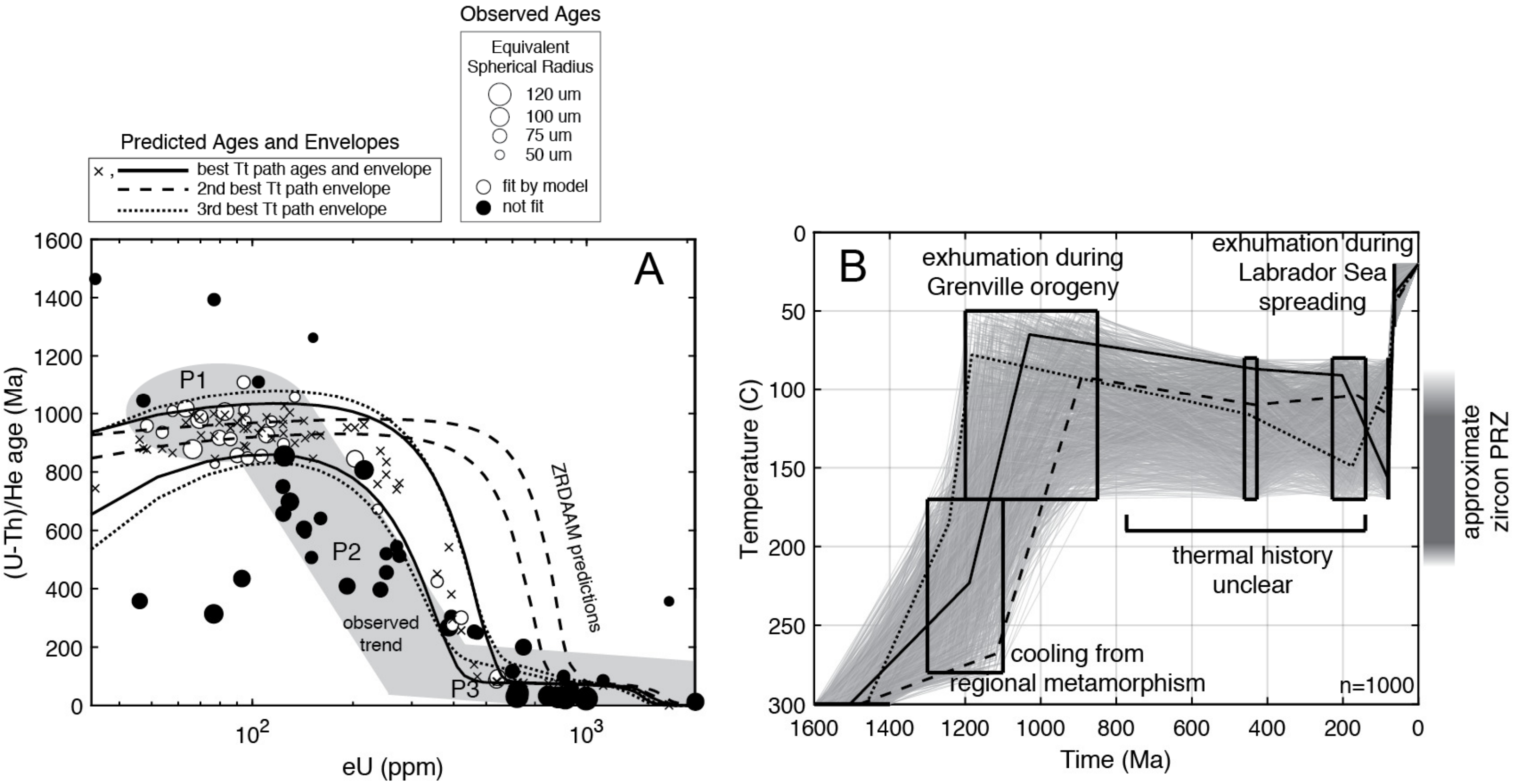

Figure 3.12 Inverse modeling results from the Hall Peninsula, with identical methodology from Figs. 3.10-3.11 but with 1000 Tt paths. (A) The ZRDAAM provides Tt paths which fit the relatively large population of low-eU ages, but misses P2 ages in a manner similar to Sinai Peninsula results (Fig. 3.10). (B) The main phase of exhumation occurs during the Grenville orogeny, after which the thermal history is locally unresolved. We have provided a range of possible post-Grenville Tt paths coinciding with regional tectonism, followed by a second exhumational phase during Labrador Sea spreading.

Table 3.2 Zircon sample information for Hall Peninsula zircons, including grain size (as equivalent spherical radius), U and Th concentrations, ZHe age, and Raman ν3 peak width parameters.

Sample	Aliquot	ESR (um)	U (ppm)	Th (ppm)	eU (ppm)	ZHe age (Ma)	+/-	v3 FWHM (cm-1)	+/-	v3 peak shift	+/-
C010	2	93.9	118.5	47.8	129.5	698	55.8	8.1	1.8	1000.5	1.7
C010	3	109.1	111.4	57.4	124.6	855	68.4	8.8	1.3	999.5	1.9
C010	4	72.2	75.6	45.1	86.0	913	73.0	7.8	3.2	1002.5	0.5
C010	5	71.0	41.1	26.6	47.2	1045	83.6	6.4	0.8	1004.5	0.3
C012	1	93.2	370.3	73	387.1	268	21.4	7.8	1.6	1000.1	0.3
C012	3	93.7	73.8	39	82.8	1007	80.6	7.0	0.5	1002.8	0.6
C012	4	89.3	56.6	28.9	63.2	1017	81.4	10.1	2.0	1000.6	2.0
C012	5	95.1	62	32.6	69.5	980	78.4	11.2	2.2	992.8	4.8
C013	1	87.7	80.4	55	93.1	435	34.8	6.7	0.3	1003.8	0.4
C013	2	58.6	29.3	20	33.9	1464	117.1	6.1	0.1	1003.8	0.3
C013	3	54.6	82.3	52.6	94.4	1013	81.0	7.5	0.5	1003.1	0.7
C013	4	55.3	217.7	83.3	236.9	672	53.8	12.5	0.9	998.0	0.1
C013	5	59.7	100.7	58.5	114.2	973	77.8	8.6	0.7	1003.1	0.2
C013	6	68.9	41.5	29.9	48.4	958	76.6	7.8	2.2	1002.6	1.1
C013	7	53.9	81.5	62.1	95.8	974	77.9	8.5	0.3	1002.3	0.8
C013	9	56.9	114.6	84.3	134.0	1057	84.6	6.2	1.1	1003.5	0.3
C013	11	64.4	91.2	56.9	104.3	1110	88.8	8.6	2.0	1001.8	1.2
C013	13	80.9	43.1	12.8	46.0	358	28.6	10.2	2.2	1002.1	1.4
C013	15	71.6	422.1	167.5	460.6	253	20.2	14.8	2.1	992.4	1.2
C014	1	49.1	137.8	61.5	151.9	1262	101.0	10.7	1.1	996.4	1.6
C014	2	49.1	1746.9	68.1	1762.6	357	28.6	16.4	1.2	991.7	0.6
C015	1	99.2	201	64	215.7	807	64.6	11.1	1.1	1001.4	0.3
C015	2	98.1	68.9	33.7	76.7	314	25.1	8.0	1.9	1003.0	1.4

Table 3.2 cont

C015	4	69.8	92.3	61.5	106.4	855	68.4	9.3	1.6	1001.7	1.4
C015	6	80.6	112.4	49.4	123.8	657	52.6	10.0	0.6	1001.2	0.3
C015	7	74.5	109.2	61.8	123.4	750	60.0	12.8	0.6	998.2	0.4
C015	8	74.1	230.7	91.4	251.7	456	36.5	12.9	1.5	1000.1	0.3
C015	9	81.2	132.4	44.6	142.7	606	48.5	8.8	1.9	1002.0	0.6
C015	10	85.1	182.3	42.3	192.0	409	32.7	11.4	1.1	1000.3	0.3
C015	12	71.6	399.9	93.4	421.4	301	24.1	17.8	2.2	985.7	1.8
C015	13	84.5	97.7	54.9	110.3	927	74.2	11.4	0.1	998.1	0.5
C015	14	69.8	85.4	38.2	94.2	1109	88.7	10.2	1.0	1000.7	0.8
C015	17	65.7	141.9	36.2	150.2	507	40.6	14.2	2.8	986.0	0.8
C016	1	48.8	72.1	22.3	77.2	828	66.2	6.5	1.9	1002.3	1.7
C016	2	80.7	75.1	19.9	79.7	917	73.4	8.7	2.1	1001.3	2.0
C016	3	63.8	118.6	23.1	123.9	895	71.6	10.0	0.6	999.9	0.2
C016	4	77.4	85.1	21.7	90.1	857	68.6	10.7	0.5	1000.0	0.7
C016	5	59.2	53.4	18.8	57.7	1009	80.7	7.1	0.1	1003.9	0.5
C016	6	68.4	66.3	17.1	70.2	990	79.2	8.1	0.3	1002.9	0.7
C016	7	64.9	50.5	14.2	53.8	936	74.9	7.7	0.8	1000.7	1.2
Y080	1	61.9	131	55.4	143.7	593	47.4	10.0	2.7	995.8	5.6
Y080	2	84.6	600.8	199.7	646.7	200	16.0	12.8	2.2	991.1	5.1
Y080	3	101.2	57.6	37.9	66.3	878	70.2	8.9	1.6	1001.7	1.6
Y080	4	88.8	179	103.1	202.7	845	67.6	12.1	2.6	998.0	2.5
Y080	5	67.1	144.7	66.1	159.9	641	51.3	9.2	1.5	998.8	1.8
B099	1	64.9	391.5	22.1	396.6	276	22.1	8.9	0.6	1002.3	1.1
B099	2	65.4	70.8	26.2	76.8	1393	111.4	8.8	2.3	1001.2	1.1
B099	3	73.9	388.4	23.3	393.8	303	24.2	10.9	0.2	1000.5	0.6
B099	4	64.3	260	43.8	270.1	545	43.6	9.4	0.9	1001.1	1.2

Table 3.2 cont

B099	5	69.9	265.2	43.1	275.1	513	41.0	10.9	0.8	1001.3	0.5
B099	6	79.1	238.6	12.7	241.5	397	31.8	10.6	3.8	1000.6	1.4
B099	9	68.8	92.2	20.1	96.8	847	67.8	7.5	0.9	1002.6	0.7
B099	10	65.6	246.8	19.7	251.3	520	41.6	10.2	1.5	1002.1	0.7
B102	1	64.3	345.9	48.6	357.1	425	34.0	8.5	1.2	1002.6	0.8
B102	2	64.9	462.3	37.5	470.9	248	19.8	14.6	2.1	996.6	1.8
B102	3	66.1	843.2	41.7	852.8	100	8.0	11.4	2.5	1002.2	0.6
B102	4	75.9	870.1	124.7	898.8	60	4.8	11.1	1.3	999.2	1.8
B102	5	75.7	582.1	74.7	599.3	117	9.4	13.5	1.8	996.0	0.8
B102	7	84.6	525.2	52.7	537.3	87	7.0	13.6	0.5	997.8	0.6
B102	10	65.7	1088.9	133.5	1119.6	85	6.8	22.2	1.5	995.9	1.5
B106	1	116.3	829.2	146.4	862.9	26	2.1	17.5	0.3	993.8	0.5
B106	3	112.8	598.3	105.1	622.5	43	3.4	13.5	0.4	999.9	1.6
B106	4	117.3	594.9	102.3	618.4	31	2.5	18.7	1.6	992.7	0.8
B106	5	105.9	715.4	227.2	767.7	33	2.6	13.7	1.0	997.2	1.2
B106	6	91.0	1950.2	710.2	2113.5	13	1.0	15.6	1.5	993.8	1.5
B106	7	84.5	523.1	79	541.3	96	7.7	14.5	2.1	996.8	1.0
B106	9	110.7	759	267.9	820.6	28	2.2	17.7	1.5	991.9	1.5
B106	10	121.0	944.4	223.1	995.7	24	1.9	18.2	1.3	993.7	0.6

In Figure 3.13, we have expanded the thermal history constraints to allow for pre-Grenville cooling to >300 °C, in spite of muscovite K/Ar ages (Skipton et al., 2015, and references therein), giving far more time for radiation damage to accumulate than would be geologically possible. This approach yields age envelopes which encompasses more ages overall, and shows a threshold of decreasing ages closer to that observed in real data.

3.4.3 Effects of U and Th zonation

Because parent nuclide zonation may exert significant effects on measured ages (e.g. Hourigan et al., 2005; Orme et al., 2015), we use forward modeling of zoned zircons to show age-eU curves as effected by 3x U and Th enrichment or depletion near the grain boundary (Fig. 3.14). In both cases, zonation brings the age-eU curve closer to (but not overlapping) P2 ages by reducing the apparent dose at which ages begin to decrease. This is the result of enriched zones reaching doses beyond which ages decrease faster than when averaged out over the whole grain. The overall effect, however, is not enough to bring model predictions in line with the observed age-eU relationship.

3.5 DISCUSSION

3.5.1 Sinai Peninsula

In Figure 3.14, the Sinai age-eU relationship is seen alongside radiation dose estimates and the age envelopes from Figure 3.8. Dose are maximum estimates of present-day doses, assuming total damage accumulation since the measured U-Pb age of 610 Ma. This likely constitutes an overestimation; the closure temperature of the U-Pb system in zircon (>900 °C) is far higher than that of the zircon fission track system (ZFT, nominal Tc ~280 °C), however, the relatively short

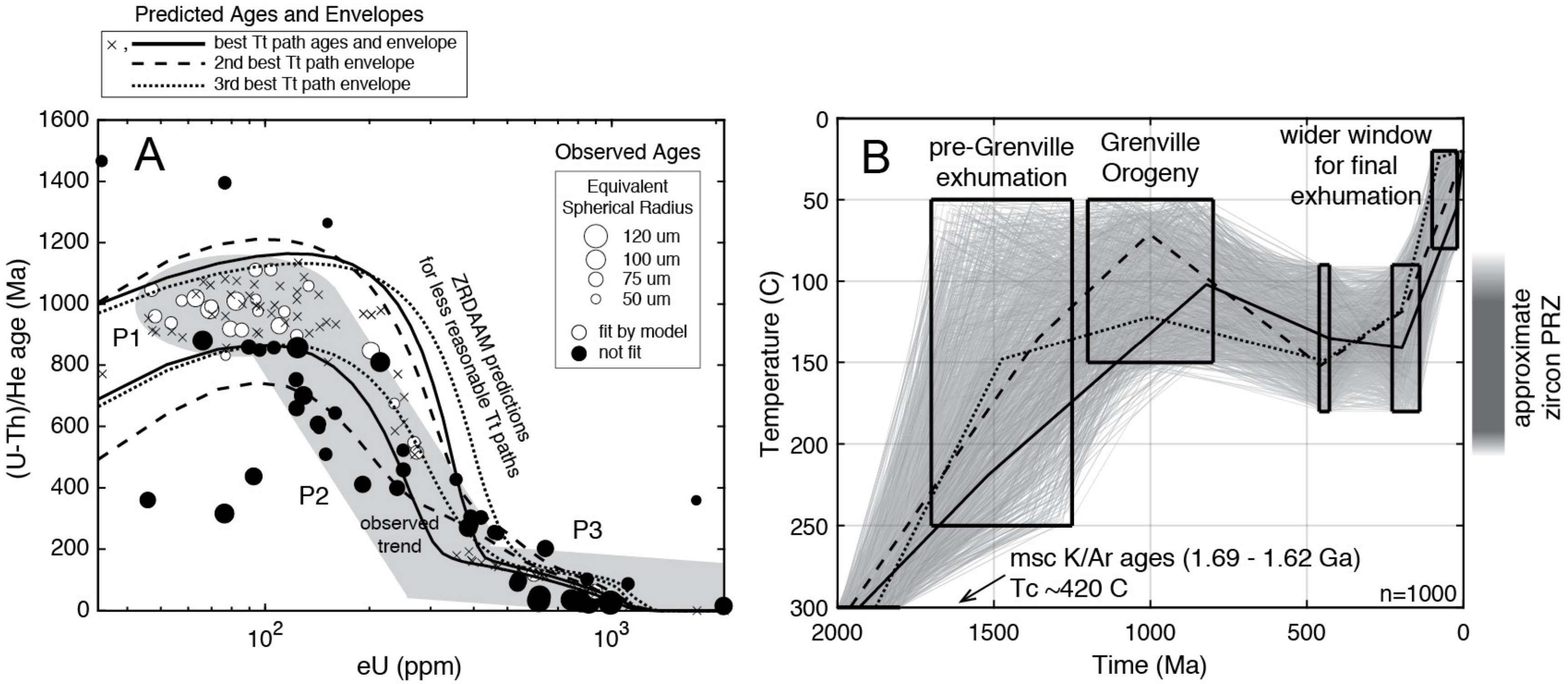

Figure 3.13 Inverse models from the Hall Peninsula, but with Tt paths adjusted to allow for exhumation to begin during the Trans-Hudson Orogeny (2.0 – 1.8 Ga). These models also have expanded the windows of final exhumation. These Tt paths are geologically unlikely, given muscovite K/Ar ages (T_C ~ 420 °C) from 1.69 – 1.62 Ga (Skipton et al., 2015 and references therein), however, they do produce a generally better fit to the overall age-eU curve than the previous model (Fig. 3.13). These results, in conjunction with Sinai Peninsula modeling results (Figs. 3.10-3.11), suggest that the ZRDAAM may give preference to geologically unreasonable paths.

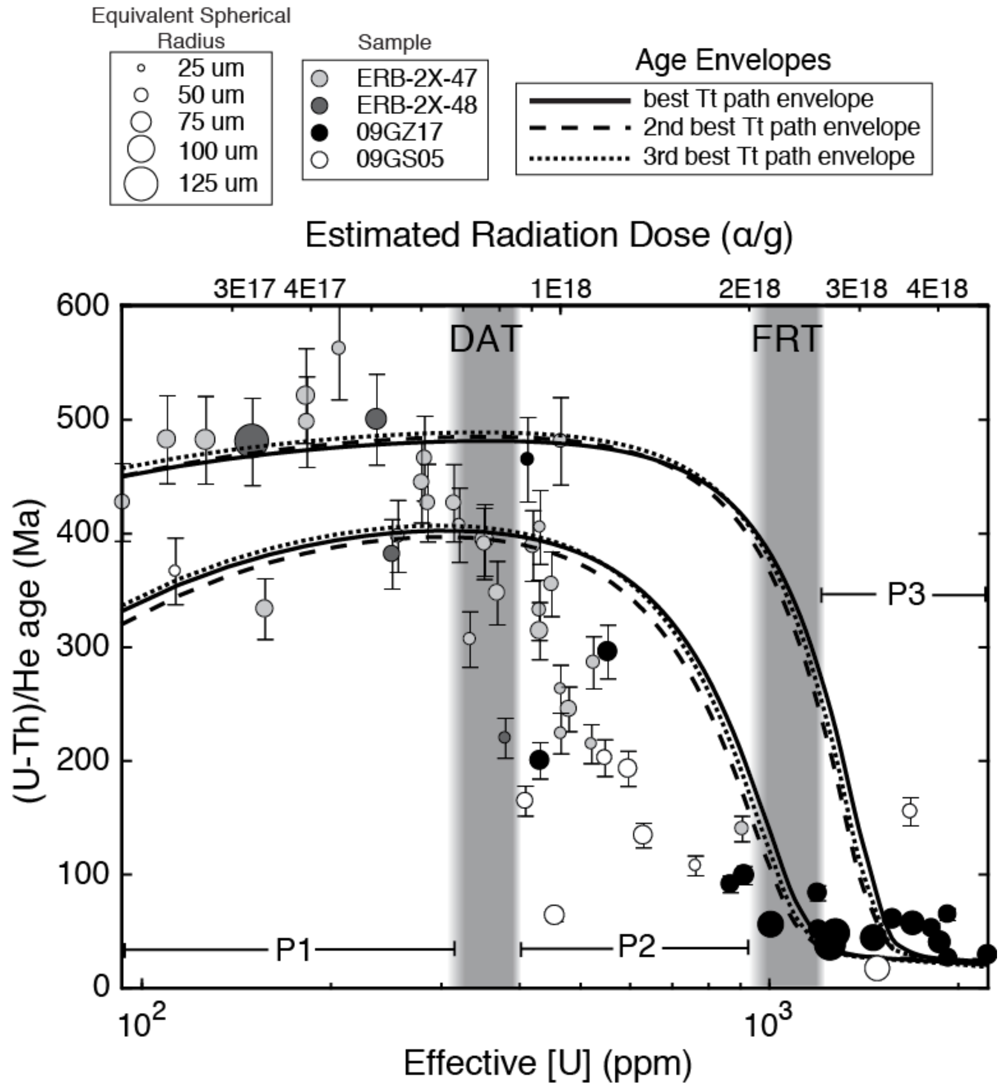

Figure 3.14 ZHe age-eU plot of Sinai Peninsula zircons with age envelopes from Figure 3.10, including present day radiation dose estimates (top). Doses are likely an overestimation, based on continuous damage accumulation since the measured zircon U-Pb crystallization age of 610 Ma. We have also denoted each population P1-P3, and the Decreasing Age and Full Resetting Threshold (Fig. 3.2). The ZRDAAM predicts the onset of decreasing ages occurs between 1 – 2 × 10^{18} α/g (Fig. 3.1), however, these results suggest that threshold is too high. In terms of present day estimated doses day, the DAT occurs at approx. 7-9 × 10^{17} α/g, with the FRT occurring between 2-3 × 10^{18} α/g. Using present-day doses causes a further overestimation, as the relevant doses are those over which time partial resetting occurred.

amount of time between crystallization (610 Ma), post-tectonic diking (591 Ma), and the oldest ZHe age (562 Ma) indicate that cooling was relatively rapid. In spite of this overestimation, our data place the DAT at 7 – 9 × 10^{17} α/g in terms of present day doses, lower than the 1 – 2 × 10^{18} α/g predicted by the model. Furthermore, when calculated this way, the observed DAT is likely to be far greater than the 'true' DAT for two reasons: first, we have admitted to using overestimated doses in lieu of a more accurate approach; and second, because the relevant doses are those during partial resetting, not present day doses, which are likely to be higher. Because the relevant temperatures and times are not sufficiently resolved, and further complicated by the unknown degree of annealing experienced by these zircons, it is difficult to estimate how much higher our dose estimates are than the relevant dose values. As such, our results suggest that the true DAT in zircon occurs at a maximum of <7 – 9 × 10^{17} α/g.

3.5.2 Hall Peninsula

Figure 3.15 shows the age-eU relationship between zircons from the Hall Peninsula, zonation, and model age envelopes. Radiation doses are estimated assuming total damage retention since the youngest muscovite K/Ar age of 1610 Ma. Given that the closure temperature of Ar in muscovite is ~420 °C, much higher than the ZFT total annealing threshold, this is probably an overestimation; however, the pre-Grenville thermal history of the Archean block is poorly constrained. Attempts were made to obtain ZFT ages on these zircons, however, most dissolved entirely under normal etching conditions (Garver, 2003); portions of grains which survived yielded FT densities too high to be counted. Ages in these zircons decrease at approx. 120 ppm eU, corresponding to present day doses of ~7 × 10^{17} a/g, similar to Sinai Peninsula results (Fig. 3.14).

Although zonation is known to be a significant factor in (U-Th)/He dating (Hourigan et al., 2005; Farley et al., 2011; Ault and Flowers, 2012; Anderson et al., 2017; Danišík et al., 2017), the relationship between age and degree of zonation appears lacking in Hall Peninsula zircons.

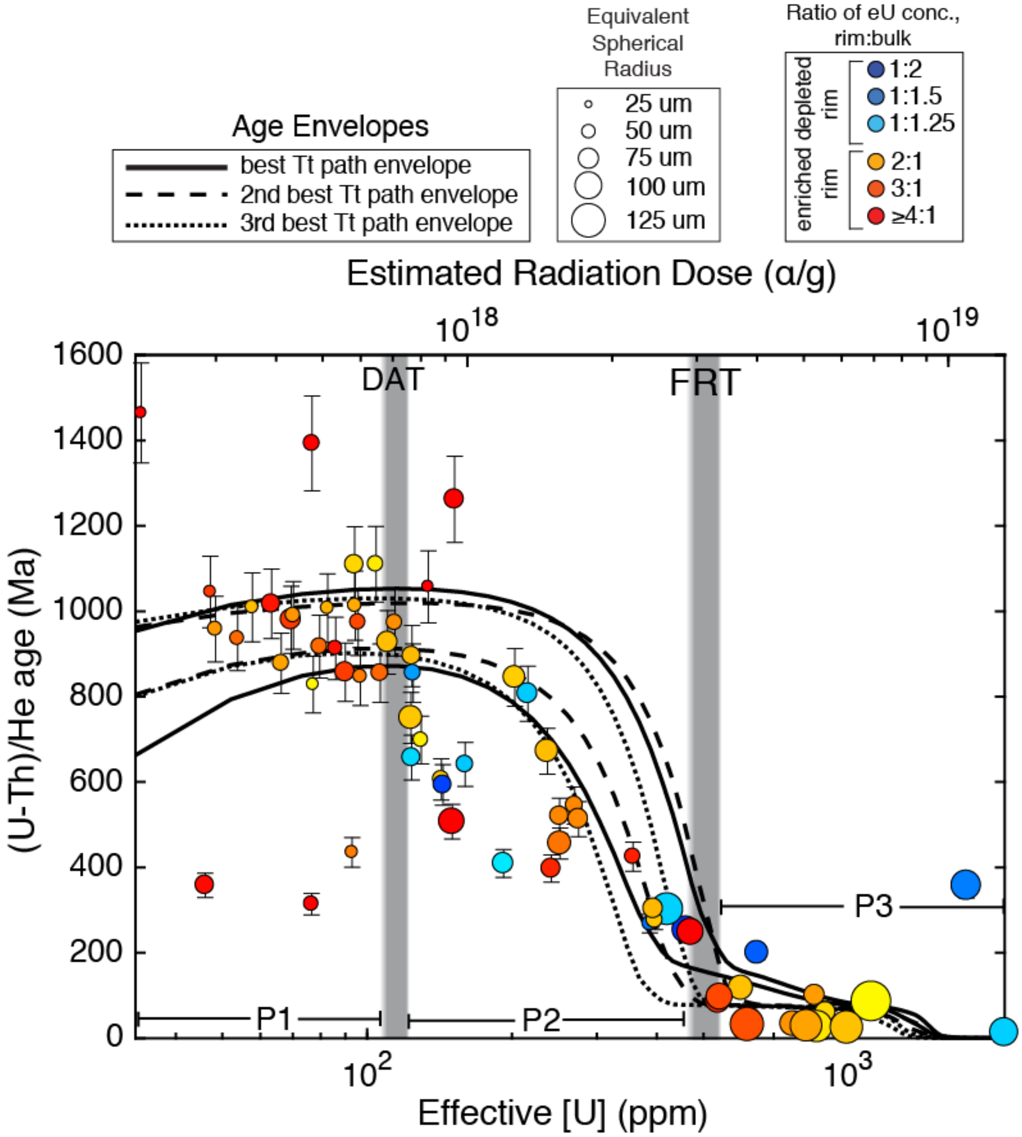

Figure 3.15 ZHe age-eU plot of Hall Peninsula zircons with best age envelopes from Figure 3.13 and present day estimated doses (top). Doses are likely overestimated, assuming damage accumulation since 1.62 Ga (corresponding to the youngest muscovite K/Ar cooling ages with a T_C of ~420 °C; Fig. 3.13). The DAT occurs in ages with present day doses estimated at 7×10^{17} α/g, with the FRT occurring at approx. 3×10^{18} α/g. Although age envelopes do encompass some P2 ages, the ZRDAAM still has significant issues reproducing the age-eU curve for these data.

Although P1 zircons have enriched rims, few other consistencies are seen between age and the degree of zonation.

3.5.3 The role of zonation

Significant attention has been given to quantifying the effects of zonation on ZHe ages, since it is perhaps the most obvious source of error between an idealized model and bulk (U-Th)/He ages: the heterogeneous ingrowth of helium constitutes a violation of the assumptions of the FT correction (Chapter 1; Farley et al., 1996), and variable degrees of damage yield variable diffusion kinetics (Guenthner et al., 2013; Danišík et al., 2017; Anderson et al., 2017). Complications arising from zonation have even been suggested as a direct cause of discrepancies with the ZRDAAM model (Orme et al., 2015). On the other hand, Anderson et al. (2017) used in-situ laser ablation (U-Th)/He on discrete sections of zoned grains to show that zircons from the McClure Mountain syenite still yield a different T_C vs dose relationship than ZRDAAM (Fig 3.1). Furthermore, results from Chapter 2 suggest that zonation plays a minimal role in diffusion rates. In Figure 3.16, we have also explored the effects of zonation on age-eU predictions. U and Th heterogeneities will usually lead to enriched zones becoming damaged faster than depleted zones, which has an effect of decreasing ages overall. Our results show that, in terms of thermal history estimates, the effect of zonation plays a second-order role at best; given the large difference between the observed DAT and that predicted by the model, it is unlikely that zonation would ‘correct’ the discrepancies between observed and modeled ages.

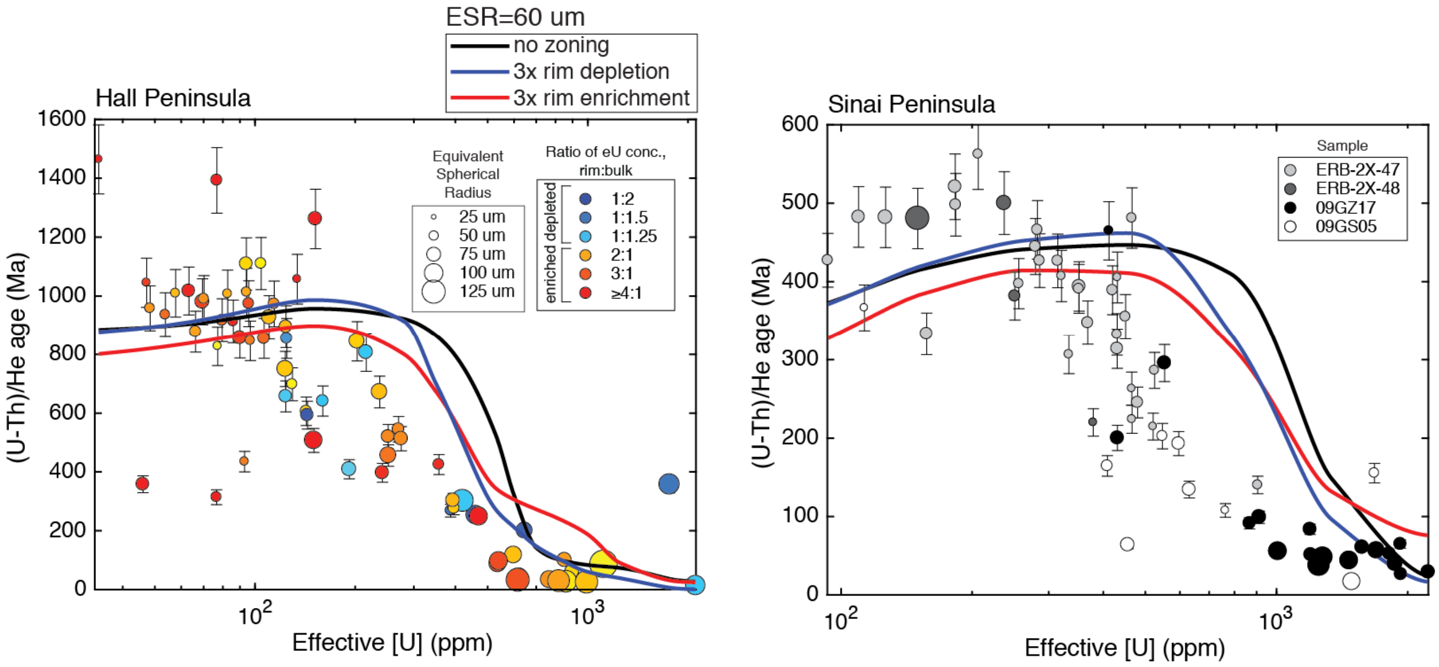

Figure 3.16 ZHe ages for both settings over eU concentration, alongside with model-generated age-eU curves demonstrating the effects of U and Th zonation for a 60 µm grain with no zonation (black line), with 3x parent nuclide enrichment near the grain rim (red line), and with 3x parent nuclide depletion near the grain rim (blue line). Results are generated using the highest scoring Tt paths from Figures 3.10 and 3.13, using HeFTy (Ketcham, 2005) to account for inter-grain diffusivity variations resulting from zonation. Hall Peninsula data are colored to represent the ratio of the U and Th concentration averages of laser ablation pits (e.g. the rim) to the whole-grain (Fig. 3.7). Low-eU zircons consistently yield high-eU rims, although few other correlations between zonation and age are seen. In both settings, enrichment and depletion bring the age-eU curve closer to the observed values, likely a result of faster metamictization within enriched regions of the grains. In the Hall Peninsula, however, ages still decrease at significantly lower eU concentrations than predicted by the models. In the Sinai Peninsula, the concentration at which ages decrease is similar for real and zoned data, however, models still overshoot the observed decreasing age-eU relationship.

3.5.4 Implications for zircon (U-Th)/He thermochronology

The suggestion that the ZRDAAM does not fit observed age-eU relationships due to decreasing ages at doses lower than model predictions is supported by other studies with similar conclusions (Powell et al., 2016; Anderson et al., 2017). In Chapter 2, we propose that the DAT occurs at approx. 3-5 × 10^{17} α/g, and that the discrepancies observed between these data and model predictions may be explained by low-temperature annealing. Several studies have directly observed the formation of an 'intermediate' phase, in which damage-induced strains are relaxed but crystallinity is not restored (Nasdala et al., 2004; Capitani et al., 2000; Ewing et al., 2003; Geisler et al., 2001; Geisler, 2002; Colombo and Chrosch, 1998), although the relationship of this state to diffusivity is unclear, Chapter 2 posits that its formation represents a significant alteration to diffusional mechanics which is unaccounted for by the ZRDAAM. An alternative or complementary possibility is that annealing could cause a decrease in the interconnectivity of damage zones, the percolation of which is a potential cause of increasing diffusivity at high doses (Ketcham et al., 2013; Guenthner et al., 2013). Furthermore, the ZRDAAM's high-damage parameterization was based primarily on Sri Lankan zircons, in which significant portions of 'intermediate' material have been observed (Nasdala et al., 2004; Capitani et al., 2000; Ewing et al., 2003; Geisler et al., 2001; Geisler, 2002; Colombo and Chrosch, 1998; Guenthner et al., 2013). In conjunction with our inverse modeling results, these observations imply that the ZRDAAM may be maladjusted to model high-damage datasets, either failing to fit age-eU relationships when well constrained (Figs. 3.8-3.9), and favoring unrealistic Tt paths when loosely constrained (Figs. 3.12-3.13).

It is possible that a parameterization based on an empirical fit of the data in Chapter 2, corroborated by the modeled closure temperatures of Anderson et al. (2017), may be an improvement over ZRDAAM, particularly in the range of 10^{17} – 10^{18} α/g. If such discrepancies are indeed the result of low-temperature annealing, however, then the use of a single dose-diffusivity curve would be too simple to accurately describe the kinetics of ^{4}He diffusion, and a model based on a single dose-diffusivity curve would only be valid for zircons which have experienced the same degree of partial annealing. While the ZRDAAM's determination of diffusivity is based on the presence of relative fractions of crystalline and amorphous materials, our results suggest that an improved approach would include (at least) a third fraction dedicated to the 'intermediate' phase.

A further complication in using these data to retrofit a new model, we cannot be sure that zircons from either locality have experienced such low temperature annealing. In fact, the location of the apparent DAT for each dataset—approx. 7-8 × 10^{17} α/g, much higher than the predicted 2-3 × 10^{17} α/g (Figs. 3.15 – 3.16)—could be suggestive of annealing (or, that our dose estimations are too high). A comparison of Raman results between the two datasets (Fig. 3.17) shows that, while both yield comparable FWHM, Hall Peninsula zircons occupy a much larger range of peak widths. Research has suggested that a trend like the Hall Peninsula's may be indicative of annealing effects, whereas Sinai Peninsula zircons show more of an un-annealed trend (Geisler et al., 2001; Geisler and Pidgeon, 2002). This interpretation is in conflict with Chapter 2, in which we interpret the onset of annealing effects at relatively higher temperatures in Sinai Peninsula zircons to be due to previous partial annealing. Furthermore, we cannot rule out that such differences may be due to differences in equipment.

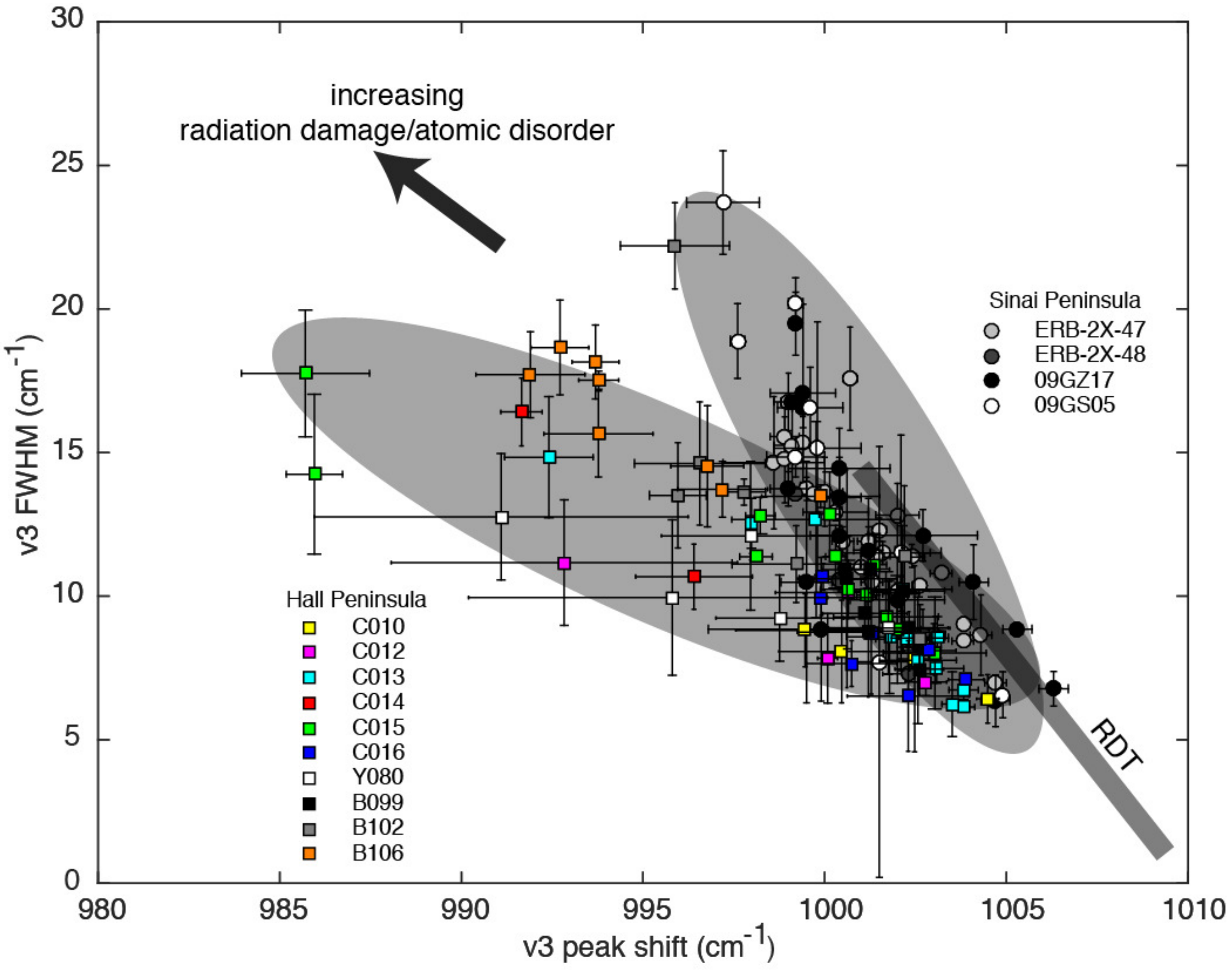

Figure 3.17 A comparison of the Raman v3 SiO_4 anti-symmetric stretching peaks of both Sinai (circles) and Hall Peninsula (squares) datasets, presented as peak shift vs FWHM. Although the two overlap in the low damage range, the Hall Peninsula tends towards lower peak shift values per FWHM. The trend of the Hall Peninsula zircons may be indicative of some ‘relaxation’ annealing (Geisler and Pidgeon, 2002). The thick line represents the radiation damage trend (RDT) of damage accumulation with no annealing observed by Nasdala et al (1998).

3.6 CONCLUSIONS

In this study, we have demonstrated that ZRDAAM fails to predict the age-eU curves observed in two different geologic settings with very different histories. Inverse modeling shows that in both settings, given a generous range of realistic thermal histories, the model is incapable of reproducing the shape of the observed age-eU curve; in the Sinai Peninsula in particular, the model requires unrealistic thermal histories and cannot reproduce the data with geologically reasonable ones. The main source of model's inability to accurately fit these age-eU trends is that ages decrease with increasing dose at lower damage levels than the ZRDAAM DAT of 1×10^{18} α/g. These results, in conjunction with the results of Chapters 1 and 2, Powell et al. (2016), and Anderson et al. (2017), shows that ZRDAAM does not accurately describe the diffusion kinetics of the ZHe system in some cases. Further work is needed to develop a more accurate model which will not only help recover more accurate thermal histories, but will also fully explain the discrepancies between these data and those which appear to be accurately modeled by ZRDAAM.

Appendices

APPENDIX A. 1D MODELING CODE AND RELATED FUNCTIONS

```
%%% FDM_diffusion %%%
% finite difference He diffusion modeling for step-heating simulations

clear; close all

% input model parameters
variable_a = [50 100 150];
variable_alpha = [1 1 1]; % 1=ejection correction, 0=no ejection correction
variable_marker = {'^','s','o'};
nexp = length(variable_a); % length(variable_a); % number of experiments to run
f_cutoff = 0.99;

% the "outer loop" which collects data at various parameters from the model
% for comparison
for c = 1:nexp
    %% experimental parameters %%
    alpha = variable_alpha(c); % apply alpha ejection profile
    Ti = 420 + 273.15; % initial temperature in K
    a = variable_a(c); % radius in um
    Ttsim = 'prograde'; % starts the script off at 'prograde' or 'retrograde' heating
    nr = 0; % a counter for the number of retrograde heating paths

    % model parameters
    t = 3600; % heating step length in sec, increases by 1.5x each transition to retrograde
    dt = 10; % timestep length (sec), 10 sec recommended, lower dt = lower error, longer run
    Ng = a * 60; % number of grid nodes, 60 per um recommended
    [r,Vshell] = SFDgeometry(a,Ng);

    % concentration profile
```

```
v = ones(Ng,1); % flat
if alpha == 1
    [~,RF] = FT(a,18,r);
    v=v.*RF;
end

% calculate initial volume
fVi = ppcreate(r,v.*Vshell,'pchip');
Vi  = integral(fVi,0,a);

% diffusivity constants
Ea = 40100; % activation energy in cal/mol
D0 = 0.46 * 1E8; % pre-exponential factor in um^2/s
Tc_ideal = closure_temp(Ea,0,log(D0/a^2),0,10); % closure temp, ideal
R  = 1.9872041; % gas constant cal/mol.K

% preallocate matrices, set counters
b = zeros(Ng,1); % 'b' vector as in A*x = b
u = zeros(Ng,1); % u is diffusing quantity times radial position
prograde = 0; % counter for Tt schedule loop
retrograde = 0; % counter for Tt schedule loop
i = 0; % loop counter
release_trigger = 0; % while loop release trigger

%% begin simulation %%
while release_trigger == 0 % loop through the time/temperature schedule
    i = i+1; % increment the loop counter

    %%% automatic temperature-time step-heating schedule %%%
    if i == 1
        T(i) = Ti;
    else
        switch Ttsim
            case 'prograde'
                T(i) = T(i-1) + 8; % increment T by whatever degrees
                if prograde > 9
```

```
                        Ttsim = 'retrograde'; % switch to retrograde
                        prograde = 0; % reset the counter
                    else
                        prograde = prograde + 1; % increment the counter
                    end
                case 'retrograde'
                    T(i) = T(i-1) - 5; % decrement temperature by whatever C
                    if retrograde == 0
%                         t = t * 2;6
                        retrograde = retrograde + 1;
                        nr = nr + 1; % retrograde step counter
                    elseif retrograde > 9
                        Ttsim = 'prograde';
                        retrograde = 0;
                    else
                        retrograde = retrograde + 1;
                    end
            end
        end

        %% simulation %%%
        Da(i) = D0 * exp(-Ea / (R*T(i)));  % calculate the D (ideal diffusivity via Arrhenius equation)
        for k = 1:(t/dt) % step through time
            v = Hediff(Da(i),dt,r,v,0);
        end % exiting time loop to measure profile

        % tsum = vector of cumulative time in hours
        if i == 1
            tsum(i) = t/3600;
        else
            tsum(i) = tsum(i-1) + t/3600;
        end

        %%% calculate fractional loss %%%
        fVi = ppcreate(r,v.*Vshell,'pchip');
        V  = integral(fVi,0,a);
        f(i) = 1 - V/Vi;
```

```
if f(i) > f_cutoff % when gas is depleted beyond the predetermined threshold
    release_trigger = 1; % release the while loop when all gas is gone
end

% calculate F, step release fraction
if i == 1
    F(i) = f(i);
else
    F(i) = f(i) - f(i-1);
end

%%% calculate diffusivity and error from fractional release results %%%
% fechtig & kalbitzer 1966 equations
if i == 1
    Dfa2(1) = NaN;
else
    if f(i) <= .86
        Dfa2(i) = 1/(pi^2 * t) * ((-pi^2/3) * (f(i) - f(i-1)) - ...
            2*pi*(sqrt(1-f(i) * pi/3) - sqrt(1-f(i-1) * pi/3)));
    elseif f(i) > .86
        Dfa2(i) = (pi^2 * t)^-1 * log((1-f(i-1))/(1-f(i)));
    end
end
Df(i) = Dfa2(i) * a^2;
logDf(i) = log(Dfa2(i)); % convert model values into arrhenius space
logD(i)  = log(Da(i)/a^2); % convert ideal D values into arrhenius space
ama(i) = 0.5 * (logD(i) - logDf(i)); % ln(r/r0)

%%% calculate and store diffusivity parameters from D(f) %%%
if retrograde == 1 && strcmp(Ttsim,'retrograde') == 1
    retro_f_start(nr) = f(i); % fractional release at beginning of retrograde rn
    retro_f_start_i = i;
elseif retrograde > 9 || release_trigger == 1
    retro_mean_f(nr)  = (retro_f_start(nr) + f(i)) / 2; % mean fractional release of retrograde
rn
```

```
                  retro_regress = polyfit(1./T(retro_f_start_i:i),logDf(retro_f_start_i:i),1);
                  Ea_retro(nr) = retro_regress(1) * -R / 1000 ; % activation energy of retrograde rn in
kcal/mol
                  D0_retro(nr) = exp(retro_regress(2)) * a^2 / 1E8; % frequency factor of retrograde rn in
cm2s-1
                  Tc_retro(nr) = closure_temp(Ea_retro(nr)*1000,0,log(D0_retro(nr)/a^2*1E8),0,10);
              end
              if f(i) > f_cutoff % when gas is depleted
                  release_trigger = 1; % release the while loop when all gas is gone
              end
          end % thus ends the simulation
```

Next, an example of a step-heating model with radiation damage annealing.

```
      %%% FDM_auto_annealing %%%
      % finite difference He step-heating diffusion modeling with damage annealing

      clear; close all
      tic % start the timer

      % name the figures
      initial_dose = [5E17 1.5E18 2E18 3E18];
      grain_sizes = [100 100 100 100];
      ejection_switch = [0 0 0 0]; % 1=apply ejection profile
      Nx = length(initial_dose); % number of experiments to run
      floss_cutoff = 0.99; % fractional loss at which to exit the diffusion loop
      t = 3600; % heating step length in sec
      dt = 10; % model timestep length (sec)
      R  = 1.9872041; % gas constant cal/mol.K

      for z = 1:Nx % loop over the number of experiments to run
          %% experimental parameters %%
          Ti            = 420 + 273.15; % initial temperature in K
          a             = grain_sizes(z); % radius in um
          Tcycle        = 'prograde'; % starts heating with prograde
          Ng            = a * 60; % number of grid nodes per um
```

```
[r,Vshell]    = SFDgeometry(a,Ng); % calculate grid node spacing
annealed_dose = initial_dose(z);

% concentration profile and volume
v = ones(Ng,1); % homogeneous concentration profile
if ejection_switch(z) == 1 % apply ejection profile
    [~,retained_fraction] = FT(a,18,r); % use FT.m to calculate the retained fraction vector
    v=v.*retained_fraction;
end
Vi = integral(ppcreate(r,v.*Vshell,'pchip'),0,a); % calculate initial volume

% preallocate matrices, (re)set counters
i = 0; % loop counter
prograde = 0; % heating counter
retrograde = 0; % "
release_trigger = 0; % while-loop release trigger
while release_trigger == 0 % loop through the time/temperature schedule
    i = i+1; % increment the loop counter

    % set heating temperature
    if i == 1
        T(i) = Ti;
    else
        switch Tcycle
            case 'prograde'
                T(i) = T(i-1) + 8; % increment T by whatever degrees
                if prograde > 9 % for however many steps
                    Tcycle = 'retrograde'; % switch to retrograde
                    prograde = 0; % reset the counter
                else
                    prograde = prograde + 1; % increment the counter
                end
            case 'retrograde'
                T(i) = T(i-1) - 5; % decrement temperature by whatever C
                if retrograde == 0
                    retrograde = retrograde + 1;
                elseif retrograde > 9 % for however many steps
```

```
                              Tcycle = 'prograde';
                              retrograde = 0;
                          else
                              retrograde = retrograde + 1;
                          end
                  end
              end

              % calculate diffusivity
              if i == 1
                  D(i) = ZRDAAM(T(i),initial_dose(z));
              else
                  D(i) = ZRDAAM(T(i),annealed_dose(i-1));
              end
              for k = 1:(t/dt) % begin heating/diffusing/annealing
                  % diffuse and generate a new He profile with Hediff.m
                  v = Hediff(D(i),dt,r,v,0);
              end % exiting time loop to measure profile
               % calculate annealing parameters
              if i == 1
                  [annealed_dose(i),length_reduction(i)] = Zanneal(initial_dose(z),T(i),t,0);
              else
                  [annealed_dose(i),length_reduction(i)]                                                    =
Zanneal(initial_dose(z),T(i),t,length_reduction(i-1));
              end
              %%% calculate fractional loss %%%
              fVi = ppcreate(r,v.*Vshell,'pchip');
              V  = integral(fVi,0,a);
              f(i) = 1 - V/Vi;

              if f(i) > floss_cutoff % when gas is depleted beyond the predetermined threshold
                  release_trigger = 1; % release the while loop when all gas is gone
              end

              %%% calculate diffusivity and error from fractional release results %%%
              % fechtig & kalbitzer 1966 equations
              if i == 1
```

```
                  Dfa2(1) = NaN;
              else
                  if f(i) <= .86
                      Dfa2(i) = 1/(pi^2 * t) * ((-pi^2/3) * (f(i) - f(i-1)) - ...
                          2*pi*(sqrt(1-f(i) * pi/3) - sqrt(1-f(i-1) * pi/3)));
                  elseif f(i) > .86
                      Dfa2(i) = (pi^2 * t)^-1 * log((1-f(i-1))/(1-f(i)));
                  end
              end
              Df(i) = Dfa2(i) * a^2;
              logDf(i) = log(Dfa2(i)); % convert model values into arrhenius space
          end % thus ends the simulation
          clearvars -except t dt initial_dose aliquot exp_type floss_cutoff grain_sizes experiment_marker
ejection_switch Nx z variable_color
      end
```

APPENDIX B. INVERSE MODELING CODE AND RELATED FUNCTIONS

```
%% inverse_model.m
% author: Adam Goldsmith
% inverse modeling of thermal histories from zircon (U-Th)/He datasets
% and presentation of age envelopes for the top three paths.

clear
close all

% load sample data
% ZHe is (U-Th)/He age, ZHe_ is uncertainty
% U, Th, and eU are concentrations in ppm
% ESR is equivalent spherical radius in um
load zheman_baffin.mat ZHe ZHe_ U Th eU ESR

% temperature-time constraints in a matrix Nx4 where column 1 is the minimum time of each constraint,
column 2 is the max time, and columns 3 and 4 are min/max temperatures.
load('constraints_baffin'); % input temperatures in C, time in myr

% model parameters
Ns    = 30; % number of points in each age envelope curve
Ng    = 200; % number of grid nodes to use
Np    = 5; % number of Tt paths to try
Nz    = length(ZHe); % number of zircons in dataset
dt_Ma = 0.5; % timestep size in myr

% sort the ages and eU values by eU for interpolation
[eU,eU_sort] = sort(eU);
ZHe = ZHe(eU_sort);
U   = U(eU_sort);
Th  = Th(eU_sort);
ESR = ESR(eU_sort);

%% geometry
```

```
% predefine radial grid node and He concentration matrices
% rows represent grid nodes, columns represent zircons
v = zeros(Ng,Nz); % concentration profiles
r = zeros(Ng,Nz); % radial position vectors
Vshell = zeros(Ng,Nz); % volume of subshells
S = 18; %alpha ejection radius
% populate r and Vshell matrices, generate rf (retained fraction) matrix and FT correction factor (FTc) for
each grain
for i = 1:Nz
    % get grid nodes and subshell volumes from SFDgeometry.m
    [r(:,i),Vshell(:,i)] = SFDgeometry(ESR(i),Ng);
    % get FT correction and retained fraction vectors from FT.m
    [FTc(i),rf(:,i)] = FT(ESR(i),S,r(:,i)); %#ok<SAGROW>
end

%% radioactivity and time constants/calculations
% constants
my2sec = 1E6 * 365 * 24 * 3600; % number of seconds in a million years
dc238  = 4.916E-18;  % decay constant of uranium-238 in s-1
dc235  = 3.12E-17;   % decay constant of uranium-235 in s-1
dc232  = 1.57E-18;   % decay constant of thorium-232 in s-1

% one-liners
dt   = dt_Ma * my2sec; % dt in seconds
age = zeros(Nz,1); % preallocate age vector
% convert parent concentrations from ppm to atoms/g
U238  = U * 0.9927 * 6.022E+23 / (238.0508 * 10^6);
U235  = U * 0.0073 * 6.022E+23 / (235.0439 * 10^6);
Th232 = Th * 6.022E+23 / (232.0381 * 10^6);

% generate a set of random Tt paths
[times,Temps] = randTt(Np,Tt_input);
times = times * my2sec; % convert from m.y. to sec
Temps = Temps + 273.15; % convert from C to K
Nc       = size(Tt_input,2); % number of constraints

% predefine Tt path scoring variables
```

```
pscore = zeros(Np,1); % score for the path
pscore_plot = zeros(Np,1); % for plotting
zscore = zeros(Nz,Np); % score for individual ZHe age

% start the model
for p = 1:Np % loop through the random Tt paths
    Nt = max(times(:,p))/dt; % number of timesteps in Tt path p
    t  = wrev(linspace(0,max(times(:,p)),Nt+1)); % timestep vector for p
    T  = interp1(times(:,p),Temps(:,p),t,'linear'); % interpolated temperatures for path p

    % reset/predefine dose and annealing variables before starting time loop
    annealed_doses = zeros(Nt,Nz); % doses generated at each time step and annealed independently
    LR             = zeros(Nt,1); % length reduction for each damage pop
    HeProd         = zeros(Nt,Nz);

    for i = 1:Nt % loop over timesteps
        % calculate helium production
        HeProd(i,:) = 8*U238*(exp(dc238 * t(i)) - exp(dc238 * t(i+1))) ...
            + 7*U235*(exp(dc235 * t(i)) - exp(dc235 * t(i+1))) ...
            + 6*Th232*(exp(dc232 * t(i)) - exp(dc232 * t(i+1)));
        % damage accumulation and annealing (Zanneal) and diffusion (Hediff)
        [annealed_doses(1:i,:),LR(1:i,:)] = Zanneal(HeProd(i,:),T(i),dt,LR(1:i,:));
        v = Hediff(ZRDAAM(T(i),sum(annealed_doses(1:i,:))),dt,r,v,HeProd(i,:).*rf);
    end

    for z = 1:Nz % calculate ages
        V238 = integral(ppcreate(r(:,z),U238(z)*Vshell(:,z),'pchip'),0,ESR(z));
        V235 = integral(ppcreate(r(:,z),U235(z)*Vshell(:,z),'pchip'),0,ESR(z));
        V232 = integral(ppcreate(r(:,z),Th232(z)*Vshell(:,z),'pchip'),0,ESR(z));
        V4He  = integral(ppcreate(r(:,z),v(:,z).*Vshell(:,z),'pchip'),0,ESR(z))/FTc(z);

        % calculate an age based on final concentrations
        age(z) = Heage(V4He,V238,V235,V232);

        %% calculate the pscore of each path
        % ZHe uncertainty
```

```
        ZHe_hi = ZHe(z) + ZHe(z) * 0.15;
        ZHe_lo = ZHe(z) - ZHe(z) * 0.15;
        if ZHe_lo <= age(z) && age(z) <= ZHe_hi
            zscore(z,p) = 1;
            pscore(p) = pscore(p) + 1;
        end
    end

    % shading value of Tt path line
    pscore_plot(p) = 3/4 * (1 - pscore(p) / Nz);
end

%% grab the best paths and calculate their age envelopes
% sort pscore so that the best Tt paths are first in the vector
[pscore,psort] = sort(pscore);
pscore = wrev(pscore);
psort  = wrev(psort);

% create matrices containing best path times and temps
bestTemps = [Temps(:,psort(1)) Temps(:,psort(2)) Temps(:,psort(3))];
besttimes = [times(:,psort(1)) times(:,psort(2)) times(:,psort(3))];
bestTempsC  = bestTemps - 273.15;
besttimesMa = besttimes / my2sec;

% round down and up to the min and max U,Th concentrations
U_agenv  = logspace(log10(floor(min(U))),log10(ceil(max(U))),Ns);
Th_agenv = logspace(log10(floor(min(Th))),log10(ceil(max(Th))),Ns);

% age envelope simulation U and Th concentrations
ae238 = U_agenv * 0.9927 * 6.022E+23 / (238.0508 * 10^6); % convert ppm to atoms/g, U238
ae235 = U_agenv * 0.0073 * 6.022E+23 / (235.0439 * 10^6); % convert ppm to atoms/g, U235
ae232 = Th_agenv * 6.022E+23 / (232.0381 * 10^6); % convert ppm to atoms/g, Th232

% effective U concentrations
eU_agenv    = U_agenv + 0.23*Th_agenv; % total eU per grain
```

```
eUint = linspace(floor(min(eU_agenv)),ceil(max(eU_agenv)),100); % vector across eU concentrations for
interp
Neu = length(eUint);

% grab r and Vshell from the highest and lowest ESR
[~,ESRsort] = sort(ESR);
r_hi = r(:,ESRsort(end));
r_lo = r(:,ESRsort(1));
Vshi = Vshell(:,ESRsort(end));
Vslo = Vshell(:,ESRsort(1));
rf_hi = rf(:,ESRsort(end));
rf_lo = rf(:,ESRsort(1));
FT_hi = FTc(ESRsort(end));
FT_lo = FTc(ESRsort(1));

% predefine some vectors for speed
AgeEnvHi = zeros(Ns,3); % high line
AgeEnvLo = zeros(Ns,3); % low line
AgeEnvHiInterp = zeros(Neu,3);
AgeEnvLoInterp = zeros(Neu,3);
linestyle = {'-','--',':'};
v_hi = zeros(Ng,Ns);
v_lo = zeros(Ng,Ns);

% create age envelopes from the best 3 paths
for p = 1:3
    % number of timesteps in the path
    Nt = max(besttimes(:,p))/dt;

    % timestep vector t and t+1 vector t_1
    t  = wrev(linspace(0,max(besttimes(:,p)),Nt+1));

    % interpolate temperature at each timestep
    T  = interp1(besttimes(:,p),bestTemps(:,p),t,'linear');

    % reset dose and annealing variables
```

```
LR = zeros(Nt,Ns); % lenght reduction for each damage pop
annealed_doses = zeros(Nt,Ns);
HeProd = zeros(Nt,Ns);

for i = 1:Nt % loop over timesteps in Tt path 'it'
    % calculate helium production vectors for each grain
    HeProd(i,:) = 8*ae238*(exp(dc238 * t(i)) - exp(dc238 * t(i+1))) ...
        + 7*ae235*(exp(dc235 * t(i)) - exp(dc235 * t(i+1))) ...
        + 6*ae232*(exp(dc232 * t(i)) - exp(dc232 * t(i+1)));

    % calculate damage production, annealing, and diffusion
    [annealed_doses(1:i,:),LR(1:i,:)] = Zanneal2(HeProd(1:i,:),T(1:i)',t(1:i)',LR(1:i,:));
    v_hi = Hediff(ZRDAAM(T(i),sum(annealed_doses)),dt,r_hi,v_hi,HeProd(i,:).*rf_hi);
    v_lo = Hediff(ZRDAAM(T(i),sum(annealed_doses)),dt,r_lo,v_lo,HeProd(i,:).*rf_lo);

    % at the last timestep...
    if i == Nt
        for g = 1:Ns % loop over the zircons
            %% calculate the age
            % calculate volume of parent and daughter by interpolating
            % a piecewise poly function and integrating it over 0 to a
            V238hi  = integral(ppcreate(r_hi,ae238(g)*Vshi,'pchip'),0,max(ESR));
            V235hi  = integral(ppcreate(r_hi,ae235(g)*Vshi,'pchip'),0,max(ESR));
            V232hi  = integral(ppcreate(r_hi,ae232(g)*Vshi,'pchip'),0,max(ESR));
            V4Hehi  = integral(ppcreate(r_hi,v_hi(:,g).*Vshi,'pchip'),0,max(ESR))/FT_hi;
            V238lo  = integral(ppcreate(r_lo,ae238(g)*Vslo,'pchip'),0,min(ESR));
            V235lo  = integral(ppcreate(r_lo,ae235(g)*Vslo,'pchip'),0,min(ESR));
            V232lo  = integral(ppcreate(r_lo,ae232(g)*Vslo,'pchip'),0,min(ESR));
            V4Helo  = integral(ppcreate(r_lo,v_lo(:,g).*Vslo,'pchip'),0,min(ESR))/FT_lo;

            % convert the symbolic solution to a numerical one
            AgeEnvHi(g,p) = Heage(V4Hehi,V238hi,V235hi,V232hi);
            AgeEnvLo(g,p) = Heage(V4Helo,V238lo,V235lo,V232lo);
        end
        % interpolate for plotting
        AgeEnvHiInterp(:,p) = pchip(eU_agenv,AgeEnvHi(:,p),eUint);
```

```
            AgeEnvLoInterp(:,p) = pchip(eU_agenv,AgeEnvLo(:,p),eUint);
        end
    end % end Tt path
end % end best paths
% fin




%% function SFDgeometry.m
% creates a node spacing scheme suitable for finite difference diffusion
% models (i.e. Hediff.m)
%
% INPUTS:
% a  = radial width of diffusion domain
% Ng = number of grid nodes desired
%
% OUTPUTS:
% r, vector containing radial location of grid nodes
% Vshell, volume of each subshell defined by grid nodes

function [r,Vshell] = SFDgeometry(a,Ng)
    r = zeros(Ng,1);
    dr = a/(Ng+1/2);
    for i = 1:Ng
        r(Ng-i+1) = a - (dr*i);
    end
    Vshell = 4/3 * pi * r.^2 * dr;
end



%% function FT.m
% calculates ejection correction and retained fraction vectors for one or
% multiple grains
% Farley et al., 1996
%
```

```
% inputs:
% a: grain radius
% S: ejection radius
% r:  grid node vector
%
% outputs:
% FTcorrection: the FT correction for the grain
% RF: a retained fraction vector that can be applied to a helium production
% vector

function [FTcorrection,RF] = FT(a,S,r)

    FTcorrection = 1 - (3*S)/(4*a) ...
        + S^3/(16*a^3);

    Ng = length(r); % number of grid nodes
    X = zeros(Ng,1); % X-star in literature
    RF = zeros(Ng,1); % retainedfraction
    if Ng > 1
        for j = 1:Ng % loop over grid nodes
            X(j) = (r(j)^2 + a^2 - S^2) / (2 * r(j)); % sphere of ejection
            RF(j) = 0.5 + (X(j) - r(j))/(2*S); % fraction retained
            RF(RF>1) = 1; % otherwise funky things happen
        end
    else
        RF = NaN;
    end
end


%% randTt.m
% generate random time temperature paths within given geologic constraints
%
% INPUTS:
% N: number of paths to generate
% Tt_paths: a 4xNc matrix, where Nc is # of constraints:
```

```
% [times_min times_max Temps_min Temps_max]
%
% OUTPUTS
% [time_matrix,Temp_matrix]
% two Nc x N matrices, where N is the number of requested paths and Nc is
% the number of constraints given.
%
% example:
% to add a constraint of 110 C - 200 C between 100 Ma and 80 Ma,
% as well as between 120 - 140 C between 40 Ma and 45 Ma:
% [80 100 110 200]
% [40 45 120 140]
% make sure Temp1 and time2 are the lower of the two values
% paths can overlap in time without going backwards

function [time_out,Temp_out] = randTt(N,Tt_paths)

    % number of constraints
    Nc = size(Tt_paths,1);

    % make the variables readable
    time1 = Tt_paths(:,1);
    time2 = Tt_paths(:,2);
    Temp1 = Tt_paths(:,3);
    Temp2 = Tt_paths(:,4);

    time_out = zeros(Nc,N); % preallocate for speed
    Temp_out = zeros(Nc,N); % preallocate for speed

    % generate the Tt paths
    for i = 1:N  % loop over requested number of Tt paths
        Temp_out(1,i) = randi([Temp1(1),Temp2(1)]);
        time_out(1,i) = randi([time1(1),time2(1)]);

        for j = 2:Nc % loop over number of nodes in Tt path
            % calculate a random time and temp in the constraints
```

```
            Temp_out(j,i) = randi([Temp1(j),Temp2(j)]);

            % make sure the paths aren't going backwards in time
            if time1(j) <= time_out(j-1,i)
                time_out(j,i) = randi([time_out(j-1,i)+1,time2(j)]);
            else
                time_out(j,i) = randi([time1(j),time2(j)]);
            end

        end
    end
end
```

```
% Zanneal.m
% ZRDAAM annealing model with equivalent time calculation
% assumes that
% see Guenthner et al, 2013, Am. Journ. Sci.
%
% INPUTS:
% raw_dose = unannealed dose per step, a/g
% Temp     = heating temperature in K
% time     = time over which heating occurs, in seconds
% LR       = length reduction matrix (time, grains)
%
% OUTPUTS:
% annealed_dose = dose after equivalent time annealing
% new_LR        = new length reduction term to pass on to next iteration
%
function [annealed_dose,LRnew] = Zanneal(raw_dose,Temp,time,LR)
    % constants
    B     = -0.05721;
    C0    =  6.24534;
    C1    = -0.11977;
    C2    = -314.937;
```

```
    C3    = -14.2868;

    % equivalent time: figure out the amount of time required to
    % produce all prior annealing as though it were produced at the
    % current temperature
    eqtime = exp((((1./LR-1).^B - C0)/C1) * (log(1/Temp) - C3)+C2);
    eqtime(size(LR,1),:) = zeros(1,size(LR,2)); % set to 0 for current timestep (does not return 0 when LR
= 0)

    % calculate new length reduction value based on equivalent time
    LRnew = ((C0 + C1 * ((log(time+eqtime)-C2)./(log(1/Temp)- C3))).^(1/B) + 1).^(-1);
    % calculate new annealed alpha dose
    annealed_dose = raw_dose .* (1.25 * (LRnew - 0.2));
end


%% Hediff.m
% Generate a new He concentration profile curve, v, after production and
% diffusion over timestep dt.
%
% Can either calculate v for a single grain or multiple grains at once.
% If submitting multiple grains, each grain's data should be stored in
% separate columns with rows representing grid nodes. If Nr is the number
% of grid nodes, and Ng is the number of grains,
% * r and v should be Nr x Ng
% * D and HeProd should be 1 x Ng
% * dt is a scalar
%
% INPUTS
% D  = diffusivity, e.g. cm2/s, 1xNg
% dt = timestep length, scalar
% r  = radial grid nodes, Nr x Ng
% v_input = initial concentration profile curves, Nr x Ng
% HeProd  = helium production per timestep, ejection corrected, 1 x Ng
%
% OUTPUT
```

```
% v_output, a new He concentration profile matrix
%
% TROUBLESHOOTING
% do not input logD or D/a^2 instead of D
% make sure your units are consistent:
%    D and dt units need to be consistent
%    D and r units need to be consistent
%    v and HeProd units need to be consistent
%    HeProd is total production over dt, not a production rate
% ensure that your node spacing is correct:
%    the innermost node must be 1/2 dr away from the grain center
%    the outermost node must be 1 full dr away from the grain center
%    see Ketcham et al 2005

function v_output = Hediff(D,dt,r,v_input,HeProd)
    % preallocate & define matrices
    [Nr,Ng] = size(v_input); % Ng=number of 'grains', Nr=number of nodes
    b = zeros(Nr,Ng); % right-hand side of tridiag eq, e.g. A*x = 'b'
    e = zeros(Nr,Ng); % used in tri-diagonal solution

    % reshape HeProd to a matrix if scalar
    if HeProd == 0; HeProd = zeros(Nr,Ng); end

    % preliminary tridiagonal stuff
    beta = (2 * (r(1,:)*2).^2) ./ (D * dt); % equation simplifying term
    main_diagonal = -2-beta; % tridiagonal system main diagonal value
    main_diag_Nmb = -3-beta; % special Neumann boundary condition value

    % Crank-Nicholson finite difference/populate tridiagonal matrix
    u = v_input .* r;
    He_term = HeProd .* r .* beta;
    b(1,:) = (3-beta) .* u(1,:) - u(2,:) - He_term(1,:); % Neumann boundary (grain center)
    for i = 2:Nr-1
        b(i,:) = (2-beta) .* u(i,:) - u(i-1,:) - u(i+1,:) - He_term(i,:); % solve for b at each node
    end
    b(Nr,:) = (2-beta) .* u(Nr,:) - u(Nr-1,:) - He_term(Nr,:); % Dirichlet boundary (grain edge)
```

```
    % tridiagonal solution
    q = main_diag_Nmb;
    u(1,:) = b(1,:)./q;
    for i=2:Nr
        e(i-1,:) = 1./q;
        q = main_diagonal - e(i-1,:);
        u(i,:) = (b(i,:) - u(i-1,:))./q;
    end
    for i=Nr-1:-1:1
        u(i,:) = u(i,:) - e(i,:).*u(i+1,:);
    end
    v_output = u ./ r; % convert u back to v
end


%% ZRDAAM.m
% Calculates zircon He diffusivities as a function of temperature and dose
% Based on Guenthner et al., 2013, Am. Journ. Sci.
%
% INPUTS:
% * Temperature (T) in K
% * timestep length (dt) in seconds
% * alpha dose (input_dose) in decays/g
% * He_production over the given timestep (atoms/g)
% NOTE: He_production is used as a proxy for alpha damage accumulation
% Do not input the production rate. only the concentration produced over dt
% Do not input FT corrected values or you will be underestimating your dose
%
% OUTPUTS:
% * D, diffusivity in um2/s (NOT cm2/s)
% * density_reduction, annealing factor
%
% TROUBLESHOOTING:
% * make sure you are inputting He production as a concentration, not rate
% * make sure alpha dose and He production have the same mass units (/g)
```

```
% * output diffusivity is NOT domain-size normalized (D not D/a^2)!
function D = ZRDAAM(T,alpha_dose)
    % constants
    Ba    = 5.48E-19; % mass of amorphous material produced per alpha decay event in g/a
    SV    = 1.669; % surface to volume ratio of damage capsules nm-1
    lint0 = 45920; % mean intercept length of zircon with dose of 1E14 a/g in nm
    R     = 1.9872041; % gas constant cal/mol.K
    phi   = 3; % empirical fitting factor
    % crystalline zircon diffusional parameters
    Eaz = 39435.9; % activation energy cal/mol
    D0z = 193188 * 1E8; % frequency factor, um2/sec
    % metamict zircon diffusional parameters
    Eam = 16969.4; % activation energy cal/mol
    D0m = 6.367E-3 * 1E8; % frequency factor, um2/sec

    % calculations
    fa   = 1-exp(-Ba * alpha_dose); % amorphous fraction
    fap  = 1-exp(-Ba * alpha_dose * phi); % amorphous fraction, prime
    fc   = 1-fap; % crystalline fraction
    lint = 4.2 ./ (SV * fa) - 2.5; % length until a particule intercepts a damage zone
    tau  = (lint0 ./ lint).^2; % tortuosity
    Dz   = D0z * exp(-Eaz/(R*T)); % diffusivity of crystalline zircon
    Dm   = D0m * exp(-Eam/(R*T)); % diffusivity of metamict zircon
    % diffusivity calculation:
    D = (fc ./(1./tau .* (Dz ./ fc.^2)) + fap ./ (Dm ./ fap.^2)).^-1;
end


%% Heage.m
% symbolically calculate a helium age from concentrations of
% helium, uranium, and thorium
%
% for best results, input FT-corrected He concentration

function age = Heage(He4,U238,U235,Th232)
    dc238  = 4.916E-18;   % decay constant of uranium-238 in s-1
```

```
    dc235  = 3.12E-17;   % decay constant of uranium-235 in s-1
    dc232  = 1.57E-18;   % decay constant of thorium-232 in s-1
    my2sec = 1E6 * 365 * 24 * 3600; % number of seconds in a million years

    % symbolic variable used to calculate age
    syms age_x

    % symbolic age equation
    age_eqn = He4 == 8*U238*(exp(dc238 * age_x) - 1) + ...
        7*U235*(exp(dc235 * age_x) - 1) + ...
        6*Th232*(exp(dc232 * age_x) - 1);

    % convert symbolic solution to numeric value
    age = double(vpasolve(age_eqn,age_x))/my2sec;
end
```

Works Cited

Chapter 1

Ault, A.K., and Flowers, R.M., 2012, Is apatite U–Th zonation information necessary for accurate interpretation of apatite (U–Th)/He thermochronometry data? Geochimica et Cosmochimica Acta, v. 79, p. 60–78.

Carslaw, H.S., and Jaeger, J.C., 1959, Conduction of heat in solids: Oxford: Clarendon Press, 1959, 2nd ed.

Colombo, M., and Chrosch, J., 1998, Annealing of natural metamict zircons. I low degree of radiation damage: Radiation Physics and Chemistry, v. 53, p. 555–561.

Danišík, M., McInnes, B.I., Kirkland, C.L., McDonald, B.J., Evans, N.J., and Becker, T., 2017, Seeing is believing: Visualization of He distribution in zircon and implications for thermal history reconstruction on single crystals: Science Advances, v. 3, p. e1601121.

Farley, K.A., Wolf, R.A., and Silver, L.T., 1996, The effects of long alpha-stopping distances on (U-Th)/He ages: Geochimica et cosmochimica acta, v. 60, p. 4223–4229.

Fechtig, H., and Kalbitzer, S., 1966, The diffusion of argon in potassium-bearing solids, *in* Potassium argon dating, Springer, p. 68–107

Gautheron, C., and Tassan-Got, L., 2010, A Monte Carlo approach to diffusion applied to noble gas/helium thermochronology: Chemical Geology, v. 273, p. 212–224.

Gautheron, C., Tassan-Got, L., Ketcham, R.A., and Dobson, K.J., 2012, Accounting for long alpha-particle stopping distances in (U–Th–Sm)/He geochronology: 3D modeling of diffusion, zoning, implantation, and abrasion: Geochimica et Cosmochimica Acta, v. 96, p. 44–56.

Geisler, T., 2002, Isothermal annealing of partially metamict zircon: evidence for a three-stage recovery process: Physics and Chemistry of Minerals, v. 29, p. 420–429, doi: 10.1007/s00269-002-0249-3.

Geisler, T., Pidgeon, R.T., van Bronswijk, W., and Pleysier, R., 2001, Kinetics of thermal recovery and recrystallization of partially metamict zircon: a Raman spectroscopic study: European Journal of Mineralogy, v. 13, p. 1163–1176, doi: 10.1127/0935-1221/2001/0013-1163.

Guenthner, W.R., Reiners, P.W., Ketcham, R.A., Nasdala, L., and Giester, G., 2013, Helium diffusion in natural zircon: Radiation damage, anisotropy, and the interpretation of zircon (U-Th)/He thermochronology: American Journal of Science, v. 313, p. 145–198.

Hanchar, J.M., and Miller, C.F., 1993, Zircon zonation patterns as revealed by cathodoluminescence and backscattered electron images: implications for interpretation of complex crustal histories: Chemical geology, v. 110, p. 1–13.

Hourigan, J.K., Reiners, P.W., and Brandon, M.T., 2005, U-Th zonation-dependent alpha-ejection in (U-Th)/He chronometry: Geochimica et Cosmochimica Acta, v. 69, p. 3349–3365.

Hurley, P.M., 1952, Alpha ionization damage as a cause of low helium ratios: Eos, Transactions American Geophysical Union, v. 33, p. 174–183.

Ketcham, R.A., 2005, Forward and Inverse Modeling of Low-Temperature Thermochronometry Data: Reviews in Mineralogy and Geochemistry, v. 58, p. 275–314, doi: 10.2138/rmg.2005.58.11.

Ketcham, R.A., Gautheron, C., and Tassan-Got, L., 2011, Accounting for long alpha-particle stopping distances in (U–Th–Sm)/He geochronology: refinement of the baseline case: Geochimica et Cosmochimica Acta, v. 75, p. 7779–7791.

Lovera, O.M., and Richter, F.M., 1989, The 40Ar/39Ar Thermochronometry for Slowly Cooled Samples: Journal of Geophysical Research, v. 94, p. 17–917.

Marsellos, A.E., and Garver, J.I., 2010, Radiation damage and uranium concentration in zircon as assessed by Raman spectroscopy and neutron irradiation: American Mineralogist, v. 95, p. 1192–1201, doi: 10.2138/am.2010.3264.

McDougall, I., and Harrison, T.M., 1999, Geochronology and Thermochronology by the 40Ar/39Ar Method: Oxford University Press on Demand.

Meesters, A., and Dunai, T.J., 2002, Solving the production–diffusion equation for finite diffusion domains of various shapes: Part II. Application to cases with α-ejection and nonhomogeneous distribution of the source: Chemical Geology, v. 186, p. 347–363.

Nasdala, L., Reiners, P.W., Garver, J.I., Kennedy, A.K., Stern, R.A., Balan, E., and Wirth, R., 2004, Incomplete retention of radiation damage in zircon from Sri Lanka: American Mineralogist, v. 89, p. 219–231.

Reiners, P.W., 2005, Zircon (U-Th)/He Thermochronometry: Reviews in Mineralogy and Geochemistry, v. 58, p. 151–179, doi: 10.2138/rmg.2005.58.6.

Reiners, P.W., Farley, K.A., and Hickes, H.J., 2002, He diffusion and (U–Th)/He thermochronometry of zircon: initial results from Fish Canyon Tuff and Gold Butte: Tectonophysics, v. 349, p. 297–308.

Reiners, P.W., Spell, T.L., Nicolescu, S., and Zanetti, K.A., 2004, Zircon (U-Th)/He thermochronometry: He diffusion and comparisons with 40Ar/39Ar dating: Geochimica et Cosmochimica Acta, v. 68, p. 1857–1887, doi: 10.1016/j.gca.2003.10.021.

Shuster, D.L., and Farley, K.A., 2005, 4He/3He thermochronometry: theory, practice, and potential complications: Reviews in mineralogy and geochemistry, v. 58, p. 181–203.

Smye, A.J., and Stockli, D.F., 2014, Rutile U–Pb age depth profiling: A continuous record of lithospheric thermal evolution: Earth and Planetary Science Letters, v. 408, p. 171–182.

Strutt, R.J., 1908, Helium and radio-activity in rare and common minerals: Proceedings of the Royal Society of London. Series A, Containing Papers of a Mathematical and Physical Character, v. 80, p. 572–594.

Wolfe, M.R., and Stockli, D.F., 2010, Zircon (U–Th)/He thermochronometry in the KTB drill hole, Germany, and its implications for bulk He diffusion kinetics in zircon: Earth and Planetary Science Letters, v. 295, p. 69–82, doi: 10.1016/j.epsl.2010.03.025.

Zhang, M., Salje, E.K., Farnan, I., Graeme-Barber, A., Daniel, P., Ewing, R.C., Clark, A.M., and Leroux, H., 2000, Metamictization of zircon: Raman spectroscopic study: Journal of Physics: Condensed Matter, v. 12, p. 1915.

Chapter 2

Anderson, A.J., Hodges, K.V., and Van Soest, M.C., 2017, Empirical constraints on the effects of radiation damage on He diffusion kinetics in zircon: Geological Society of America Abstracts with Programs, v. 48, doi: 10.1130/abs/2016AM-279840.

Ault, A.K., and Flowers, R.M., 2012, Is apatite U–Th zonation information necessary for accurate interpretation of apatite (U–Th)/He thermochronometry data? Geochimica et Cosmochimica Acta, v. 79, p. 60–78.

Baughman, J.S., Flowers, R.M., Metcalf, J.R., and Dhansay, T., 2017, Influence of radiation damage on titanite He diffusion kinetics: Geochimica et Cosmochimica Acta, v. 205, p. 50–64.

Bernet, M., and Garver, J.I., 2005, Fission-track analysis of detrital zircon: Reviews in Mineralogy and Geochemistry, v. 58, p. 205–237.

Bojar, A.-V., Fritz, H., Kargl, S., and Unzog, W., 2002, Phanerozoic tectonothermal history of the Arabian–Nubian shield in the Eastern Desert of Egypt: evidence from fission track and paleostress data: Journal of African Earth Sciences, v. 34, p. 191–202.

Bosworth, W., Huchon, P., and McClay, K., 2005, The red sea and gulf of aden basins: Journal of African Earth Sciences, v. 43, p. 334–378.

Bosworth, W., and McClay, K., 2001, Structural and stratigraphic evolution of the Gulf of Suez rift, Egypt: a synthesis: Mémoires du Muséum national d'histoire naturelle, v. 186, p. 567–606.

Bosworth, W., and Stockli, D.F., 2016, Early magmatism in the greater Red Sea rift: timing and significance: Canadian Journal of Earth Sciences, v. 53, p. 1158–1176.

Bosworth, W., Stockli, D.F., and Helgeson, D.E., 2015, Integrated outcrop, 3D seismic, and geochronologic interpretation of Red Sea dike-related deformation in the Western Desert, Egypt–The role of the 23Ma Cairo "mini-plume": Journal of African Earth Sciences, v. 109, p. 107–119.

Capitani, G.C., Leroux, H., Doukhan, J.C., Ríos, S., Zhang, M., and Salje, E.K.H., 2000, A TEM investigation of natural metamict zircons: structure and recovery of amorphous domains: Physics and Chemistry of Minerals, v. 27, p. 545–556, doi:10.1007/s002690000100.

Cherniak, D.J., Watson, E.B., and Thomas, J.B., 2009, Diffusion of helium in zircon and apatite: Chemical Geology, v. 268, p. 155–166, doi:10.1016/j.chemgeo.2009.08.011.

Cloos, M., 1997, Anatomy of a mine: The discovery and development of Grasberg: Geotimes, v. 42, p. 16–20.

Cloos, M., Sapiie, B., van Ufford, A.Q., Weiland, R.J., Warren, P.Q., and McMahon, T.P., 2005, Collisional delamination in New Guinea: The geotectonics of subducting slab breakoff: Geological Society of America Special Papers, v. 400, p. 1–51.

Colombo, M., and Chrosch, J., 1998, Annealing of natural metamict zircons. I low degree of radiation damage: Radiation Physics and Chemistry, v. 53, p. 555–561.

Colombo, M., Chrosch, J., and Salje, E.K., 1999, Annealing Metamict Zircon: A Powder X-ray Diffraction Study of a Highly Defective Phase: Journal of the American Ceramic Society, v. 82, p. 2711–2716.

Creason, C., 2015, Phanerozoic Exhumation History of Hall Peninsula, Baffin Island: Insights from Apatite and Zircon (U-Th-Sm)/He Thermochronology and 3D Thermokinematic Modeling. Masteres Thesis, Dalhousie University

Danišík, M., McInnes, B.I., Kirkland, C.L., McDonald, B.J., Evans, N.J., and Becker, T., 2017, Seeing is believing: Visualization of He distribution in zircon and implications for thermal history reconstruction on single crystals: Science Advances, v. 3, p. e1601121.

Dodson, M.H., 1973, Closure temperature in cooling geochronological and petrological systems: Contributions to Mineralogy and Petrology, v. 40, p. 259–274.

Dunai, T.J., 2005, Forward modeling and interpretation of (U-Th)/He ages: Reviews in mineralogy and geochemistry, v. 58, p. 259–274.

Ewing, R.C., Meldrum, A., Wang, L., Weber, W.J., and Corrales, L.R., 2003, Radiation effects in zircon: Reviews in Mineralogy and Geochemistry, v. 53, p. 387–425.

Farley, K.A., 2007, He diffusion systematics in minerals: Evidence from synthetic monazite and zircon structure phosphates: Geochimica et Cosmochimica Acta, v. 71, p. 4015–4024, doi:10.1016/j.gca.2007.05.022.

Farley, K.A., Reiners, P.W., and Nenow, V., 1999, An apparatus for high-precision helium diffusion measurements from minerals: Analytical Chemistry, v. 71, p. 2059–2061.

Farley, K.A., Shuster, D.L., and Ketcham, R.A., 2011, U and Th zonation in apatite observed by laser ablation ICPMS, and implications for the (U–Th)/He system: Geochimica et Cosmochimica Acta, v. 75, p. 4515–4530.

Fechtig, H., and Kalbitzer, S., 1966, The diffusion of argon in potassium-bearing solids, *in* Potassium argon dating, Springer, p. 68–107

Flowers, R.M., Ketcham, R.A., Shuster, D.L., and Farley, K.A., 2009, Apatite (U–Th)/He thermochronometry using a radiation damage accumulation and annealing model: Geochimica et Cosmochimica Acta, v. 73, p. 2347–2365, doi:10.1016/j.gca.2009.01.015.

Frizon de Lamotte, D., Tavakoli-Shirazi, S., Leturmy, P., Averbuch, O., Mouchot, N., Raulin, C., Leparmentier, F., Blanpied, C., and Ringenbach, J.-C., 2013, Evidence for Late Devonian vertical movements and extensional deformation in northern Africa and Arabia: integration in the geodynamics of the Devonian world: Tectonics, v. 32, p. 107–122.

Garver, J.I., 2002, Discussion:" Metamictisation of natural zircon: accumulation versus thermal annealing of radioactivity-induced damage" by Nasdala et al. 2001 (Contributions to Mineralogy and Petrology 141: 125-144): Contributions to Mineralogy and Petrology, v. 143, p. 756–757.

Garver, J.I., 2003, Etching zircon age standards for fission-track analysis: Radiation Measurements, v. 37, p. 47–53.

Gautheron, C., Tassan-Got, L., Barbarand, J., and Pagel, M., 2009, Effect of alpha-damage annealing on apatite (U–Th)/He thermochronology: Chemical Geology, v. 266, p. 157–170.

Geisler, T., 2002, Isothermal annealing of partially metamict zircon: evidence for a three-stage recovery process: Physics and Chemistry of Minerals, v. 29, p. 420–429, doi:10.1007/s00269-002-0249-3.

Geisler, T., and Pidgeon, R.T., 2002, Raman scattering from metamict zircon: comments on “Metamictisation of natural zircon: accumulation versus thermal annealing of radioactivity-induced damage” by Nasdala et al. 2001 (Contribution to Mineralogy and Petrology)141: 125–144: Contributions to Mineralogy and Petrology, v. 143, p. 750–755, doi:10.1007/s00410-002-0378-1.

Geisler, T., Pidgeon, R.T., van Bronswijk, W., and Pleysier, R., 2001a, Kinetics of thermal recovery and recrystallization of partially metamict zircon: a Raman spectroscopic study: European Journal of Mineralogy, v. 13, p. 1163–1176, doi:10.1127/0935-1221/2001/0013-1163.

Geisler, T., Rashwan, A.A., Rahn, M.K.W., Poller, U., Zwingmann, H., Pidgeon, R.T., Schleicher, H., and Tomaschek, F., 2003, Low-temperature hydrothermal alteration of natural metamict zircons from the Eastern Desert, Egypt: Mineralogical Magazine, v. 67, p. 485–508, doi:10.1180/0026461036730112.

Geisler, T., Ulonska, M., Schleicher, H., Pidgeon, R.T., and van Bronswijk, W., 2001b, Leaching and differential recrystallization of metamict zircon under experimental hydrothermal conditions: Contributions to Mineralogy and Petrology, v. 141, p. 53–65, doi:10.1007/s004100000202.

Guenthner, W.R., Reiners, P.W., DeCelles, P.G., and Kendall, J., 2015, Sevier belt exhumation in central Utah constrained from complex zircon (U-Th)/He data sets: Radiation damage and He inheritance effects on partially reset detrital zircons: Geological Society of America Bulletin, v. 127, p. 323–348.

Guenthner, W.R., Reiners, P.W., Ketcham, R.A., Nasdala, L., and Giester, G., 2013, Helium diffusion in natural zircon: Radiation damage, anisotropy, and the interpretation of zircon (U-Th)/He thermochronology: American Journal of Science, v. 313, p. 145–198.

Guenthner, W.R., Reiners, P.W., and Tian, Y., 2014, Interpreting date–eU correlations in zircon (U-Th)/He datasets: A case study from the Longmen Shan, China: Earth and Planetary Science Letters, v. 403, p. 328–339.

Guiraud, R., 1998, Mesozoic rifting and basin inversion along the northern African Tethyan margin: an overview: Geological Society, London, Special Publications, v. 132, p. 217–229.

Guiraud, R., and Bosworth, W., 1997, Senonian basin inversion and rejuvenation of rifting in Africa and Arabia: synthesis and implications to plate-scale tectonics: Tectonophysics, v. 282, p. 39–82.

Holland, H.D., and Gottfried, D., 1955, The effect of nuclear radiation on the structure of zircon: Acta Crystallographica, v. 8, p. 291–300.

Hourigan, J.K., Reiners, P.W., and Brandon, M.T., 2005, U-Th zonation-dependent alpha-ejection in (U-Th)/He chronometry: Geochimica et Cosmochimica Acta, v. 69, p. 3349–3365.

Hurley, P.M., 1952, Alpha ionization damage as a cause of low helium ratios: Eos, Transactions American Geophysical Union, v. 33, p. 174–183.

Jackson, S.E., Pearson, N.J., Griffin, W.L., and Belousova, E.A., 2004, The application of laser ablation-inductively coupled plasma-mass spectrometry to in situ U–Pb zircon geochronology: Chemical Geology, v. 211, p. 47–69.

Ketcham, R.A., 2005, Forward and Inverse Modeling of Low-Temperature Thermochronometry Data: Reviews in Mineralogy and Geochemistry, v. 58, p. 275–314, doi:10.2138/rmg.2005.58.11.

Ketcham, R.A., Guenthner, W.R., and Reiners, P.W., 2013, Geometric analysis of radiation damage connectivity in zircon, and its implications for helium diffusion: American Mineralogist, v. 98, p. 350–360, doi:10.2138/am.2013.4249.

Kohn, B.P., Dal-Boni, M., and Eyal, M., 1993, Apatite fission track analysis of rift-related uplift in SW Sinai, Egypt: constraints on models for Gulf of Suez evolution: Nuclear Tracks and Radiation Measurements, v. 21, p. 628.

Leys, C.A., Cloos, M., New, B.T., and MacDonald, G.D., 2012, Copper-gold$\pm$molybdenum deposits of the Ertsberg-Grasberg District: Papua, Indonesia: Society of Economic Geologists, Special Publication, v. 16, p. 215–235.

Marsellos, A.E., and Garver, J.I., 2010, Radiation damage and uranium concentration in zircon as assessed by Raman spectroscopy and neutron irradiation: American Mineralogist, v. 95, p. 1192–1201, doi:10.2138/am.2010.3264.

Marsh, J.H., and Stockli, D.F., 2015, Zircon U–Pb and trace element zoning characteristics in an anatectic granulite domain: Insights from LASS-ICP-MS depth profiling: Lithos, v. 239, p. 170–185.

McDougall, I., and Harrison, T.M., 1999, Geochronology and Thermochronology by the 40Ar/39Ar Method: Oxford University Press on Demand.

McGregor, E.D., Nielsen, S.B., Stephenson, R.A., Petersen, K.D., and MacDonald, D.I.M., 2013, Long-term exhumation of a Palaeoproterozoic orogen and the role of pre-existing heterogeneous thermal crustal properties: a fission-track study of SE Baffin Island: Journal of the Geological Society, v. 170, p. 877–891.

Murakami, T., Chakoumakos, B.C., Ewing, R.C., Lumpkin, G.R., and Weber, W.J., 1991, Alpha-decay event damage in zircon: American Mineralogist;(United States), v. 76

Nasdala, L., Irmer, G., Wolf, D., and others, 1995, The degree of metamictization in zircons: a Raman spectroscopic study: European Journal of Mineralogy-Ohne Beihefte, v. 7, p. 471–478.

Nasdala, L., Reiners, P.W., Garver, J.I., Kennedy, A.K., Stern, R.A., Balan, E., and Wirth, R., 2004, Incomplete retention of radiation damage in zircon from Sri Lanka: American Mineralogist, v. 89, p. 219–231.

Nasdala, L., Wenzel, M., Vavra, G., Irmer, G., Wenzel, T., and Kober, B., 2001, Metamictisation of natural zircon: accumulation versus thermal annealing of radioactivity-induced damage: Contributions to Mineralogy and Petrology, v. 141, p. 125–144, doi:10.1007/s004100000235.

Omar, G.I., and Steckler, M.S., 1995, Fission track evidence on the initial rifting of the Red Sea: two pulses, no propagation: Science, v. 270, p. 1341–1344.

Omar, G.I., Steckler, M.S., Buck, W.R., and Kohn, B.P., 1989, Fission-track analysis of basement apatites at the western margin of the Gulf of Suez rift, Egypt: evidence for synchroneity of uplift and subsidence: Earth and Planetary Science Letters, v. 94, p. 316–328.

Orme, D.A., Guenthner, W.R., Laskowski, A.K., and Reiners, P.W., 2016, Long-term tectonothermal history of Laramide basement from zircon–He age-eU correlations: Earth and Planetary Science Letters, v. 453, p. 119–130.

Orme, D.A., Reiners, P.W., Hourigan, J.K., and Carrapa, B., 2015, Effects of inherited cores and magmatic overgrowths on zircon (U-Th)/He ages and age-eU trends from Greater Himalayan sequence rocks, Mount Everest region, Tibet: Geochemistry, Geophysics, Geosystems, v. 16, p. 2499–2507.

Palenik, C.S., Nasdala, L., and Ewing, R.C., 2003, Radiation damage in zircon: American Mineralogist, v. 88, p. 770–781.

Pik, R., Zimmermann, L., Bellahsen, N., Vacherat, A., Ternois, S., Mouthereau, F., and Ford, M., 2016, Damages dependent sensitivity of Zircon (U-Th)/He ages to thermal processes: the case of Pyrenean samples, *in* EGU General Assembly Conference Abstracts, v. 18, p. 13803.

Powell, J., Schneider, D., Stockli, D., and Fallas, K., 2016, Zircon (U-Th)/He thermochronology of Neoproterozoic strata from the Mackenzie Mountains, Canada: Implications for the Phanerozoic exhumation and deformation history of the northern Canadian Cordillera: Tectonics, v. 35, p. 663–689.

Pujols, E.J., 2011, Temporal and thermal evolution of extensional faulting in the central Gulf of Suez and detrital zircon (U-Th)/He constraints on the thermo-tectonic Paleozoic and Mesozoic history of the Sinai, Egypt. Masters Thesis, University of Kansas.

Reich, M., Ewing, R.C., Ehlers, T.A., and Becker, U., 2007, Low-temperature anisotropic diffusion of helium in zircon: Implications for zircon (U–Th)/He thermochronometry: Geochimica et Cosmochimica Acta, v. 71, p. 3119–3130, doi:10.1016/j.gca.2007.03.033.

Reiners, P.W., Spell, T.L., Nicolescu, S., and Zanetti, K.A., 2004, Zircon (U-Th)/He thermochronometry: He diffusion and comparisons with 40Ar/39Ar dating: Geochimica et Cosmochimica Acta, v. 68, p. 1857–1887, doi:10.1016/j.gca.2003.10.021.

Richter, F.M., Lovera, O.M., Harrison, T.M., and Copeland, P., 1991, Tibetan tectonics from 40 Ar/39 Ar analysis of a single K-feldspar sample: Earth and Planetary Science Letters, v. 105, p. 266–278.

Riley, B.C.D., 2004, Laramide exhumation and heating in southeastern Arizona: low-temperature thermal history and implications for zircon fission-track systematics. Dissertation, The University of Texas at Austin.

Salje, E.K.H., Chrosch, J., and Ewing, R.C., 1999, Is "metamictization" of zircon a phase transition? American Mineralogist, v. 84, p. 1107–1116.

Scott, D.J., 1996, Geology of the Hall Peninsula east of Iqaluit, southern Baffin Island: Geological Survey of Canada, Current Research, p. 83–91.

Scott, D.J., 1999, U–Pb geochronology of the eastern Hall Peninsula, southern Baffin Island, Canada: a northern link between the Archean of West Greenland and the Paleoproterozoic Torngat Orogen of northern Labrador: Precambrian Research, v. 93, p. 5–26.

Shuster, D.L., and Farley, K.A., 2005, 4He/3He thermochronometry: theory, practice, and potential complications: Reviews in mineralogy and geochemistry, v. 58, p. 181–203.

Skipton, D.R., Schneider, D.A., Kellett, D., and Joyce, N., 2015, New insights on the cooling history of Hall Peninsula, southern Baffin Island, Nunavut, using 40 Ar/39 Ar thermochronology on muscovite. Canada-Nunavut Geoscience Office Summary of Activities, 2014.

Skipton, D.R., and St-Onge, M.R., 2013, Paleoproterozoic deformation and metamorphism in metasedimentary rocks west of Okalik Bay: a field template for the evolution of eastern Hall Peninsula, Baffin Island, Nunavut: Summary of Activities, p. 63–72.

Smye, A.J., and Stockli, D.F., 2014, Rutile U–Pb age depth profiling: A continuous record of lithospheric thermal evolution: Earth and Planetary Science Letters, v. 408, p. 171–182.

Stern, R.J., and Manton, W.I., 1987, Age of Feiran basement rocks, Sinai: implications for late Precambrian crustal evolution in the northern Arabian–Nubian Shield: Journal of the Geological Society, v. 144, p. 569–575.

Stockli, D.F., 2005, Application of Low-Temperature Thermochronometry to Extensional Tectonic Settings: Reviews in Mineralogy and Geochemistry, v. 58, p. 411–448, doi:10.2138/rmg.2005.58.16.

St-Onge, M.R., Van Gool, J.A., Garde, A.A., and Scott, D.J., 2009, Correlation of Archaean and Palaeoproterozoic units between northeastern Canada and western Greenland: constraining the pre-collisional upper plate accretionary history of the Trans-Hudson orogen: Geological Society, London, Special Publications, v. 318, p. 193–235.

Strutt, R.J., 1908, Helium and radio-activity in rare and common minerals: Proceedings of the Royal Society of London. Series A, Containing Papers of a Mathematical and Physical Character, v. 80, p. 572–594.

Tagami, T., 2005, Fundamentals of Fission-Track Thermochronology: Reviews in Mineralogy and Geochemistry, v. 58, p. 19–47, doi:10.2138/rmg.2005.58.2.

Váczi, T., Nasdala, L., Wirth, R., Mehofer, M., Libowitzky, E., and Häger, T., 2009, On the breakdown of zircon upon "dry" thermal annealing: Mineralogy and Petrology, v. 97, p. 129–138.

Wafforn, S., 2017, Geo- and Thermochronology of the Ertsberg-Grasberg Cu-Au Mining District, west New Guinea, Indonesia. Dissertation, The University of Texas at Austin.

Willett, C.D., Fox, M., and Shuster, D.L., 2017, A helium-based model for the effects of radiation damage annealing on helium diffusion kinetics in apatite: Earth and Planetary Science Letters, v. 477, p. 195–204.

Wojdyr, M., 2010, Fityk: a general-purpose peak fitting program: Journal of Applied Crystallography, v. 43, p. 1126–1128.

Woodhead, J.A., Rossman, G.R., and Silver, L.T., 1991a, The metamictization of zircon: Radiation dose-dependent structural characteristics: American Mineralogist;(United States), v. 76.

Woodhead, J.A., Rossman, G.R., and Thomas, A.P., 1991b, Hydrous species in zircon: American Mineralogist, v. 76, p. 1533–1546.

York, D., Evensen, N.M., Martínez, M.L., and De Basabe Delgado, J., 2004, Unified equations for the slope, intercept, and standard errors of the best straight line: American Journal of Physics, v. 72, p. 367–375.

Zhang, S., and Pell, J., 2014, Conodonts recovered from the carbonate xenoliths in the kimberlites confirm the Paleozoic cover on the Hall Peninsula, Nunavut: Canadian Journal of Earth Sciences, v. 51, p. 142–155, doi:10.1139/cjes-2013-0171.

Zhang, M., Salje, E.K., Capitani, G.C., Leroux, H., Clark, A.M., Schlüter, J., and Ewing, R.C., 2000a, Annealing of-decay damage in zircon: a Raman spectroscopic study: Journal of Physics: Condensed Matter, v. 12, p. 3131.

Zhang, M., Salje, E.K.H., Ewing, R.C., Farnan, I., Ríos, S., Schlüter, J., and Leggo, P., 2000b, Alpha-decay damage and recrystallization in zircon: evidence for an intermediate state from infrared spectroscopy: Journal of Physics: Condensed Matter, v. 12, p. 5189.

Zhang, M., Salje, E.K., Farnan, I., Graeme-Barber, A., Daniel, P., Ewing, R.C., Clark, A.M., and Leroux, H., 2000c, Metamictization of zircon: Raman spectroscopic study: Journal of Physics: Condensed Matter, v. 12, p. 1915.

Chapter 3

Anderson, A.J., Hodges, K.V., and Van Soest, M.C., 2017, Empirical constraints on the effects of radiation damage on He diffusion kinetics in zircon: Geological Society of America Abstracts with Programs, v. 48, doi: doi: 10.1130/abs/2016AM-279840.

Ault, A.K., and Flowers, R.M., 2012, Is apatite U–Th zonation information necessary for accurate interpretation of apatite (U–Th)/He thermochronometry data? Geochimica et Cosmochimica Acta, v. 79, p. 60–78.

Balan, E., Neuville, D.R., Trocellier, P., Fritsch, E., Muller, J.-P., and Calas, G., 2001, Metamictization and chemical durability of detrital zircon: American Mineralogist, v. 86, p. 1025–1033.

Bosworth, W., Huchon, P., and McClay, K., 2005, The red sea and gulf of aden basins: Journal of African Earth Sciences, v. 43, p. 334–378.

Bosworth, W., and McClay, K., 2001, Structural and stratigraphic evolution of the Gulf of Suez rift, Egypt: a synthesis: Mémoires du Muséum national d'histoire naturelle, v. 186, p. 567–606.

Bosworth, W., and Stockli, D.F., 2016, Early magmatism in the greater Red Sea rift: timing and significance: Canadian Journal of Earth Sciences, v. 53, p. 1158–1176.

Bosworth, W., Stockli, D.F., and Helgeson, D.E., 2015, Integrated outcrop, 3D seismic, and geochronologic interpretation of Red Sea dike-related deformation in the Western Desert, Egypt–The role of the 23Ma Cairo "mini-plume": Journal of African Earth Sciences, v. 109, p. 107–119.

Capitani, G.C., Leroux, H., Doukhan, J.C., Ríos, S., Zhang, M., and Salje, E.K.H., 2000, A TEM investigation of natural metamict zircons: structure and recovery of amorphous domains: Physics and Chemistry of Minerals, v. 27, p. 545–556, doi: 10.1007/s002690000100.

Colombo, M., and Chrosch, J., 1998, Annealing of natural metamict zircons. I low degree of radiation damage: Radiation Physics and Chemistry, v. 53, p. 555–561.

Danišík, M., McInnes, B.I., Kirkland, C.L., McDonald, B.J., Evans, N.J., and Becker, T., 2017, Seeing is believing: Visualization of He distribution in zircon and implications for thermal history reconstruction on single crystals: Science Advances, v. 3, p. e1601121.

Dodson, M.H., 1973, Closure temperature in cooling geochronological and petrological systems: Contributions to Mineralogy and Petrology, v. 40, p. 259–274.

Dunai, T.J., 2005, Forward modeling and interpretation of (U-Th)/He ages: Reviews in mineralogy and geochemistry, v. 58, p. 259–274.

Ewing, R.C., Meldrum, A., Wang, L., Weber, W.J., and Corrales, L.R., 2003, Radiation effects in zircon: Reviews in Mineralogy and Geochemistry, v. 53, p. 387–425.

Farley, K.A., 2002, (U-Th)/He Dating: Techniques, Calibrations, and Applications: Reviews in Mineralogy and Geochemistry, v. 47, p. 819–844, doi: 10.2138/rmg.2002.47.18.

Farley, K.A., Shuster, D.L., and Ketcham, R.A., 2011, U and Th zonation in apatite observed by laser ablation ICPMS, and implications for the (U–Th)/He system: Geochimica et Cosmochimica Acta, v. 75, p. 4515–4530.

Farley, K.A., Wolf, R.A., and Silver, L.T., 1996, The effects of long alpha-stopping distances on (U-Th)/He ages: Geochimica et cosmochimica acta, v. 60, p. 4223–4229.

Fechtig, H., and Kalbitzer, S., 1966, The diffusion of argon in potassium-bearing solids, *in* Potassium argon dating, Springer, p. 68–107.

Flowers, R.M., Ketcham, R.A., Shuster, D.L., and Farley, K.A., 2009, Apatite (U–Th)/He thermochronometry using a radiation damage accumulation and annealing model: Geochimica et Cosmochimica Acta, v. 73, p. 2347–2365, doi: 10.1016/j.gca.2009.01.015.

Frizon de Lamotte, D., Tavakoli-Shirazi, S., Leturmy, P., Averbuch, O., Mouchot, N., Raulin, C., Leparmentier, F., Blanpied, C., and Ringenbach, J.-C., 2013, Evidence for Late Devonian vertical movements and extensional deformation in northern Africa and Arabia: integration in the geodynamics of the Devonian world: Tectonics, v. 32, p. 107–122.

Garver, J.I., 2003, Etching zircon age standards for fission-track analysis: Radiation Measurements, v. 37, p. 47–53.

Gautheron, C., Tassan-Got, L., Ketcham, R.A., and Dobson, K.J., 2012, Accounting for long alpha-particle stopping distances in (U–Th–Sm)/He geochronology: 3D modeling of diffusion, zoning, implantation, and abrasion: Geochimica et Cosmochimica Acta, v. 96, p. 44–56.

Geisler, T., 2002, Isothermal annealing of partially metamict zircon: evidence for a three-stage recovery process: Physics and Chemistry of Minerals, v. 29, p. 420–429, doi: 10.1007/s00269-002-0249-3.

Geisler, T., and Pidgeon, R.T., 2002, Raman scattering from metamict zircon: comments on "Metamictisation of natural zircon: accumulation versus thermal annealing of radioactivity-induced damage" by Nasdala et al. 2001 (Contribution to Mineralogy and Petrology)141: 125–144: Contributions to Mineralogy and Petrology, v. 143, p. 750–755, doi: 10.1007/s00410-002-0378-1.

Geisler, T., Pidgeon, R.T., van Bronswijk, W., and Pleysier, R., 2001, Kinetics of thermal recovery and recrystallization of partially metamict zircon: a Raman spectroscopic study: European Journal of Mineralogy, v. 13, p. 1163–1176, doi: 10.1127/0935-1221/2001/0013-1163.

Gleadow, A.J.W., Duddy, I.R., Green, P.F., and Lovering, J.F., 1986, Confined fission track lengths in apatite: a diagnostic tool for thermal history analysis: Contributions to Mineralogy and Petrology, v. 94, p. 405–415.

Guenthner, W.R., Reiners, P.W., DeCelles, P.G., and Kendall, J., 2015, Sevier belt exhumation in central Utah constrained from complex zircon (U-Th)/He data sets: Radiation damage and He inheritance effects on partially reset detrital zircons: Geological Society of America Bulletin, v. 127, p. 323–348.

Guenthner, W.R., Reiners, P.W., Ketcham, R.A., Nasdala, L., and Giester, G., 2013, Helium diffusion in natural zircon: Radiation damage, anisotropy, and the interpretation of zircon (U-Th)/He thermochronology: American Journal of Science, v. 313, p. 145–198.

Guenthner, W.R., Reiners, P.W., and Tian, Y., 2014, Interpreting date–eU correlations in zircon (U-Th)/He datasets: A case study from the Longmen Shan, China: Earth and Planetary Science Letters, v. 403, p. 328–339.

Guiraud, R., 1998, Mesozoic rifting and basin inversion along the northern African Tethyan margin: an overview: Geological Society, London, Special Publications, v. 132, p. 217–229.

Guiraud, R., and Bosworth, W., 1997, Senonian basin inversion and rejuvenation of rifting in Africa and Arabia: synthesis and implications to plate-scale tectonics: Tectonophysics, v. 282, p. 39–82.

Hourigan, J.K., Reiners, P.W., and Brandon, M.T., 2005, U-Th zonation-dependent alpha-ejection in (U-Th)/He chronometry: Geochimica et Cosmochimica Acta, v. 69, p. 3349–3365.

Hurley, P.M., 1952, Alpha ionization damage as a cause of low helium ratios: Eos, Transactions American Geophysical Union, v. 33, p. 174–183.

Jackson, S.E., Pearson, N.J., Griffin, W.L., and Belousova, E.A., 2004, The application of laser ablation-inductively coupled plasma-mass spectrometry to in situ U–Pb zircon geochronology: Chemical Geology, v. 211, p. 47–69.

Ketcham, R.A., Donelick, R.A., Balestrieri, M.L., and Zattin, M., 2009, Reproducibility of apatite fission-track length data and thermal history reconstruction: Earth and Planetary Science Letters, v. 284, p. 504–515, doi: 10.1016/j.epsl.2009.05.015.

Ketcham, R.A., Gautheron, C., and Tassan-Got, L., 2011, Accounting for long alpha-particle stopping distances in (U–Th–Sm)/He geochronology: refinement of the baseline case: Geochimica et Cosmochimica Acta, v. 75, p. 7779–7791.

Ketcham, R.A., Guenthner, W.R., and Reiners, P.W., 2013, Geometric analysis of radiation damage connectivity in zircon, and its implications for helium diffusion: American Mineralogist, v. 98, p. 350–360, doi: 10.2138/am.2013.4249.

Kohn, B.P., Dal-Boni, M., and Eyal, M., 1993, Apatite fission track analysis of rift-related uplift in SW Sinai, Egypt: constraints on models for Gulf of Suez evolution: Nuclear Tracks and Radiation Measurements, v. 21, p. 628.

Kohn, B.P., Feinstein, S., Foster, D.A., Steckler, M.S., and Eyal, M., 1997, Thermal history of the eastern Gulf of Suez, II. Reconstruction from apatite fission track and ^{40}Ar/^{39}Ar K-feldspar measurements: Tectonophysics, v. 283, p. 219–239.

Košler, J., and Sylvester, P.J., 2003, Present trends and the future of zircon in geochronology: laser ablation ICPMS: Reviews in mineralogy and geochemistry, v. 53, p. 243–275.

Marsellos, A.E., and Garver, J.I., 2010, Radiation damage and uranium concentration in zircon as assessed by Raman spectroscopy and neutron irradiation: American Mineralogist, v. 95, p. 1192–1201, doi: 10.2138/am.2010.3264.

McGregor, E.D., Nielsen, S.B., Stephenson, R.A., Petersen, K.D., and MacDonald, D.I.M., 2013, Long-term exhumation of a Palaeoproterozoic orogen and the role of pre-existing heterogeneous thermal crustal properties: a fission-track study of SE Baffin Island: Journal of the Geological Society, v. 170, p. 877–891.

Nasdala, L., Irmer, G., Wolf, D., and others, 1995, The degree of metamictization in zircons: a Raman spectroscopic study: European Journal of Mineralogy-Ohne Beihefte, v. 7, p. 471–478.

Nasdala, L., Reiners, P.W., Garver, J.I., Kennedy, A.K., Stern, R.A., Balan, E., and Wirth, R., 2004, Incomplete retention of radiation damage in zircon from Sri Lanka: American Mineralogist, v. 89, p. 219–231.

Nasdala, L., Wenzel, M., Vavra, G., Irmer, G., Wenzel, T., and Kober, B., 2001, Metamictisation of natural zircon: accumulation versus thermal annealing of radioactivity-induced damage: Contributions to Mineralogy and Petrology, v. 141, p. 125–144, doi: 10.1007/s004100000235.

Nasdala, L., Zhang, M., Kempe, U., Panczer, G., Gaft, M., Andrut, M., and Plötze, M., 2003, Spectroscopic methods applied to zircon: Reviews in Mineralogy and Geochemistry, v. 53, p. 427–467.

Orme, D.A., Guenthner, W.R., Laskowski, A.K., and Reiners, P.W., 2016, Long-term tectonothermal history of Laramide basement from zircon–He age-eU correlations: Earth and Planetary Science Letters, v. 453, p. 119–130.

Orme, D.A., Reiners, P.W., Hourigan, J.K., and Carrapa, B., 2015, Effects of inherited cores and magmatic overgrowths on zircon (U-Th)/He ages and age-eU trends from Greater Himalayan sequence rocks, Mount Everest region, Tibet: Geochemistry, Geophysics, Geosystems, v. 16, p. 2499–2507.

Powell, J., Schneider, D., Stockli, D., and Fallas, K., 2016, Zircon (U-Th)/He thermochronology of Neoproterozoic strata from the Mackenzie Mountains, Canada: Implications for the Phanerozoic exhumation and deformation history of the northern Canadian Cordillera: Tectonics, v. 35, p. 663–689.

Reiners, P.W., 2005, Zircon (U-Th)/He Thermochronometry: Reviews in Mineralogy and Geochemistry, v. 58, p. 151–179, doi: 10.2138/rmg.2005.58.6.

Reiners, P.W., Farley, K.A., and Hickes, H.J., 2002, He diffusion and (U–Th)/He thermochronometry of zircon: initial results from Fish Canyon Tuff and Gold Butte: Tectonophysics, v. 349, p. 297–308.

Reiners, P.W., Spell, T.L., Nicolescu, S., and Zanetti, K.A., 2004, Zircon (U-Th)/He thermochronometry: He diffusion and comparisons with 40Ar/39Ar dating: Geochimica et Cosmochimica Acta, v. 68, p. 1857–1887, doi: 10.1016/j.gca.2003.10.021.

Scott, D.J., 1996, Geology of the Hall Peninsula east of Iqaluit, southern Baffin Island: Geological Survey of Canada, Current Research, p. 83–91.

Scott, D.J., 1999, U–Pb geochronology of the eastern Hall Peninsula, southern Baffin Island, Canada: a northern link between the Archean of West Greenland and the Paleoproterozoic Torngat Orogen of northern Labrador: Precambrian Research, v. 93, p. 5–26.

Shuster, D.L., and Farley, K.A., 2005, 4He/3He thermochronometry: theory, practice, and potential complications: Reviews in mineralogy and geochemistry, v. 58, p. 181–203.

Shuster, D.L., Flowers, R.M., and Farley, K.A., 2006a, The influence of natural radiation damage on helium diffusion kinetics in apatite: Earth and Planetary Science Letters, v. 249, p. 148–161.

Shuster, D.L., Flowers, R.M., and Farley, K.A., 2006b, The influence of natural radiation damage on helium diffusion kinetics in apatite: Earth and Planetary Science Letters, v. 249, p. 148–161.

Skipton, D.R., Schneider, D.A., Kellett, D., and Joyce, N., 2015, New insights on the cooling history of Hall Peninsula, southern Baffin Island, Nunavut, using ^{40}Ar/^{39}Ar thermochronology on muscovite. Canada-Nunavut Geoscience Office Summary of Activities, 2014.

Smye, A.J., and Stockli, D.F., 2014, Rutile U–Pb age depth profiling: A continuous record of lithospheric thermal evolution: Earth and Planetary Science Letters, v. 408, p. 171–182.

Stern, R.J., and Manton, W.I., 1987, Age of Feiran basement rocks, Sinai: implications for late Precambrian crustal evolution in the northern Arabian–Nubian Shield: Journal of the Geological Society, v. 144, p. 569–575.

Stockli, D.F., 2005, Application of Low-Temperature Thermochronometry to Extensional Tectonic Settings: Reviews in Mineralogy and Geochemistry, v. 58, p. 411–448, doi: 10.2138/rmg.2005.58.16.

Strutt, R.J., 1910, The accumulation of helium in geological time. III: Proceedings of the Royal Society of London. Series A, Containing Papers of a Mathematical and Physical Character, v. 83, p. 298–301.

Wojdyr, M., 2010, Fityk: a general-purpose peak fitting program: Journal of Applied Crystallography, v. 43, p. 1126–1128.

Wolfe, M.R., and Stockli, D.F., 2010, Zircon (U–Th)/He thermochronometry in the KTB drill hole, Germany, and its implications for bulk He diffusion kinetics in zircon: Earth and Planetary Science Letters, v. 295, p. 69–82, doi: 10.1016/j.epsl.2010.03.025.

Woodhead, J.A., Rossman, G.R., and Silver, L.T., 1991, The metamictization of zircon: Radiation dose-dependent structural characteristics: American Mineralogist;(United States), v. 76.